COMPUTATIONAL ANALYSIS OF A PERMANENT MAGNET SYNCHRONOUS MACHINE USING NUMERICAL TECHNIQUES

DONG JING

A THESIS SUBMITTED

FOR THE DEGREE OF DOCTOR OF PHILOSOPHY

DEPARTMENT OF ELECTRICAL & COMPUTER ENGINEERING

NATIONAL UNIVERSITY OF SINGAPORE

2004

Acknowledgments

First of all, I would like to express my most sincere appreciation and thanks to my supervisor, Prof. Mohammed Abdul Jabbar, for his guidance and constant encouragement throughout my four years of postgraduate studies. His help and guidance have made my research work a very pleasant and fulfilling one. I am also grateful to my co-supervisor, Dr. Liu Zhejie, for providing me with many suggestions throughout the course of my work.

I would like to thank Dr. Fu Weinong from Data Storage Institute, for his valuable suggestions and discussions throughout this work. I am also thankful to Dr. Bi Chao, Senior Research Engineer in Data Storage Institute, for his suggestions and help in this work.

I would also like to express my appreciation to the laboratory technologists, Mr. Y. C. Woo and Mr. M. Chandra for their support and help, without which this research work would have been so much harder to complete.

I would also like to thank my colleagues in the EEM Lab - Ms. Qian Weizhe, Mr. Liu Qinghua, Mr. Zhang Yanfeng, Mr. Yeo See Wei, Mr. Anshuman Tripathi and Mr. S. K. Sahoo, for their valuable discussions, suggestions and helps throughout my work. Many thanks to all my friends in the EEM Lab - Ms. Hla Nu Phyu, Mr. Nay Lin Htun Aung, Mr. Azmi Bin Azeman, Ms. Wu Mei, Ms. Xi Yunxia,

Miss Wu Xinhui and Miss Wang Wei, who have made my research work in this lab a very pleasant one.

Finally, I would like to express my most heartfelt thanks and gratitude to my husband and my family, who have always provided me their support and encouragement. I thank them for their concerns and prayers.

Contents

Summary

This thesis deals with computational analysis of a line-start permanent magnet synchronous motor (PMSM) using finite element method (FEM). Electric machines receive power from external sources through electric circuits. The objective is to couple all the circuits directly with field calculations in order to make it a voltage source driven system as opposed to a current source driven system normally used in FEM computations. We studied both static as well as dynamic operations of this machine under various starting conditions for the dynamic analysis of PMSM. Motor parameters are important elements in the dynamic operations. We have studied many existing methods of parameter determinations and critically examined their suitability and shortcomings. We have developed two new methodologies for the determination of two-axis motor parameters using mathematical models and experimental measurements.

Field - circuit coupled time stepping FEM is used to study the dynamics of PMSM. In the computation, 2D models combined with various circuits are used. Maxwell's equation is used to model the 2D electromagnetic fields. The 3D effects due to the stator end windings and rotor end rings are simplified by circuit models. The parameters of these end effects, which are calculated by analytical methods, are included in the circuits. The semiconductor components in the external electric circuits are modelled as resistors with different resistance values depending on their operating status. Electric machines are electro-mechanical conversion devices;

hence mechanical movement of the machine governed by the kinetic equation is also included in our computational process.

Finite element method is implemented for the field equations. The space dependent quantities in the equations are formulated by the principle of weighted residuals. The time dependent quantities are evaluated by the backward Euler's method. Various circuit equations are assembled and solved simultaneously with the field equations. The nonlinearities brought along by permanent magnets and the soft magnetic materials are handled by Newton-Raphson's method, and cubic splines are used to represent the characteristics of the nonlinear materials. The resultant global system of equations is non-symmetric; and a bi-conjugate gradient method is used to get the solution of these equations in each Newton-Raphson iteration. With the electromagnetic field solutions, the motor torque at each instant of time step is calculated using the method of Maxwell stress tensor. The dynamics of the PMSM is computed using a step by step procedure.

The starting process is complicated by the asynchronous torque and rapidly changing slip. This has been computed using co-ordinate transformation and through eddy current modelling. Both the process of self-starting and the starting under controls are computed. The control schemes included the V/f control and the vector control. The good match of the computational results with the experimental results suggests that the time stepping FEM with coupled circuits can be a good tool for computing the dynamics of a PMSM.

In the determination of PMSM parameters, experimental methods used recently by many researchers have been reviewed. These methods include the DC current decay method, sensorless no-load test method and the load test method.

Analysis and experimentations show many shortcomings and inaccuracies involved in those methods. Some methods cannot provide complete parameter information; some involved complicated and weak experimental procedures that bring inaccuracies in the results. To overcome the drawbacks of the previous methods, two new methods have been proposed based on the load test method. Linear regression model and Hopfield neural network are used in combination with the load test to determine the machine parameters. Results obtained by these new methods are compared with those obtained by other researchers. The comparison shows great improvements made by these new methods in the parameter determination.

FEM is also applied to calculate the parameters. The saturation effects of stator current on the parameters are taken into account in the calculations as well. The agreement between the FEM results and the experimental results indicates that FEM is useful and applicable in predicting the PMSM parameters.

List of Symbols

A	magnetic vector potential
B	flux density
H	external applied field intensity
M	magnetization vector
μ	magnetic permeability
μ_0	magnetic permeability in the free space
μ_r	relative permeability
$\nu = 1/\mu$	magnetic reluctivity
χ_m	magnetic susceptibility
B_r	remanent flux density
H_c	magnetic coercive force or coercivity
J	current density
E	electric field intensity
σ	electric conductivity
i_s	stator phase current
i_a, i_b, i_c	phase a, b and c stator currents
s	cross section area of one turn of phase windings
t	time
V_s	applied stator phase voltage
R_s	total stator resistance
N_s	equivalent number of turns per phase
L_e	inductance of stator end windings
l	axil length of stator iron core
Ω^+, Ω^-	total areas of positively and negatively oriented coil sides of the phase conductors

i_{bk}, V_{bk}	the k_{th} bar current and bar voltage
$(k = 1, 2, ..., n)$	
i_{ek}, R_{ek}, L_{ek}	the k_{th} end ring current, resistance and inductance
J_r	moment inertia of the rotor
θ_m	mechanical rotor position
ω_m	mechanical rotor speed
T_{em}	electromagnetic torque
T_L	load torque
B_f	friction coefficient
ω_e	electrical rotor speed
θ_e	electrical rotor position
Δt	time step
λ	flux linkage
p	pole pairs
X_d	direct-axis reactance
X_q	quadrature-axis reactance
E_0	phase voltage due to permanent magnet excitation
suffixes $_{d,q}$	$d-$ and $q-$ axis quantities of the stator
suffixes $_{D,Q}$	$d-$ and $q-$ axis quantities of the rotor
L_d, L_q	$d-$ and $q-$ axis inductance
δ	torque angle
ψ	power factor angle
β	angle between the stator flux linkage and the permanent magnet flux linkage
v_{ab}, v_{bc}, v_{ca}	line to line voltage of three phases

List of Figures

List of Tables

Chapter 1

Introduction

1.1 Permanent Magnet Machines

Electrical machines are electromagnetic devices used for electromechanical energy conversion. Most machines have two principal parts: a non-moving part called the stator and a moving part called the rotor. In order to enable the rotor to rotate, two magnetic fluxes are needed to establish the air gap magnetic field. One flux is from the rotor and the other is from the stator. Two methods are usually used to generate flux, electromagnetic excitation and permanent magnet excitation. The former method is used in conventional DC and synchronous machines, and the latter one is used in permanent magnet(PM) machines. Permanent magnet machines are broadly classified into three categories [1, 2]:

- Synchronous machines (PMSMs): The PMSM owes its origin to the replacement of the exciter of the wound synchronous machine with permanent magnets. These machines have a uniformly rotating stator field as in induction machines. The stator is fed with 3-phase sinusoidal shaped currents. All phase windings conduct current at a time with phase differences.

- Brushless DC machines(BLDC): The BLDC owes its origin to an attempt to invert the brushed DC machine to remove the need for the commutator and brush gear. Rectangular-shaped phase currents are applied to the stator.

The field excitation in the rotor is provided in the form of permanent magnet excitation. Only two phase windings out of three conduct current at any given instant of time. The structures of PMSM and BLDC are shown in Figs. 1.1 and 1.2.

- Brushed DC machines (PMDC): The construction of a PMDC commutator machine is similar to a conventional DC machine with the electromagnetic excitation system replaced by permanent magnets. A PMDC commutator motor can be compared with a separately excited DC motor. The only difference is in the excitation flux in the air gap: for PMDC commutator motor excitation flux is constant whilst a separately excited DC motor's excitation flux can be controlled. The structures of a conventional DC machine and a PMDC commutator machine are shown in Fig. 1.3.

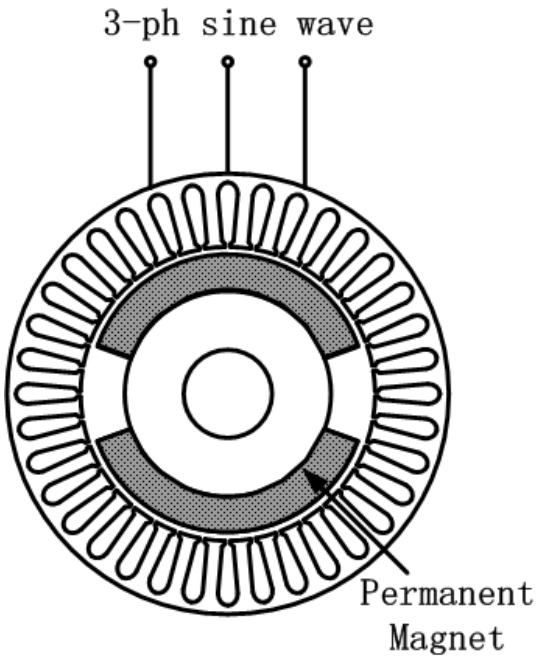

Figure 1.1: Typical Configurations of PMSM Machine

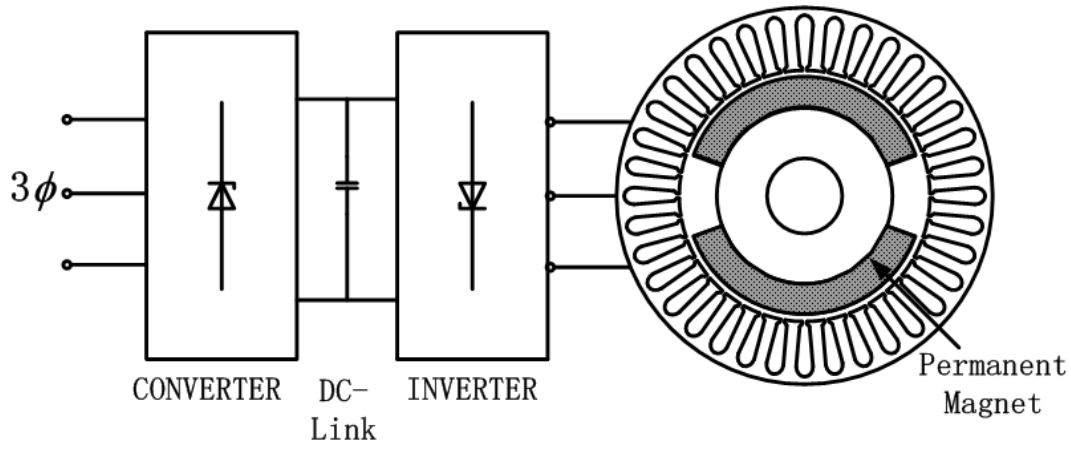

Figure 1.2: Typical Configurations of BLDC Machine

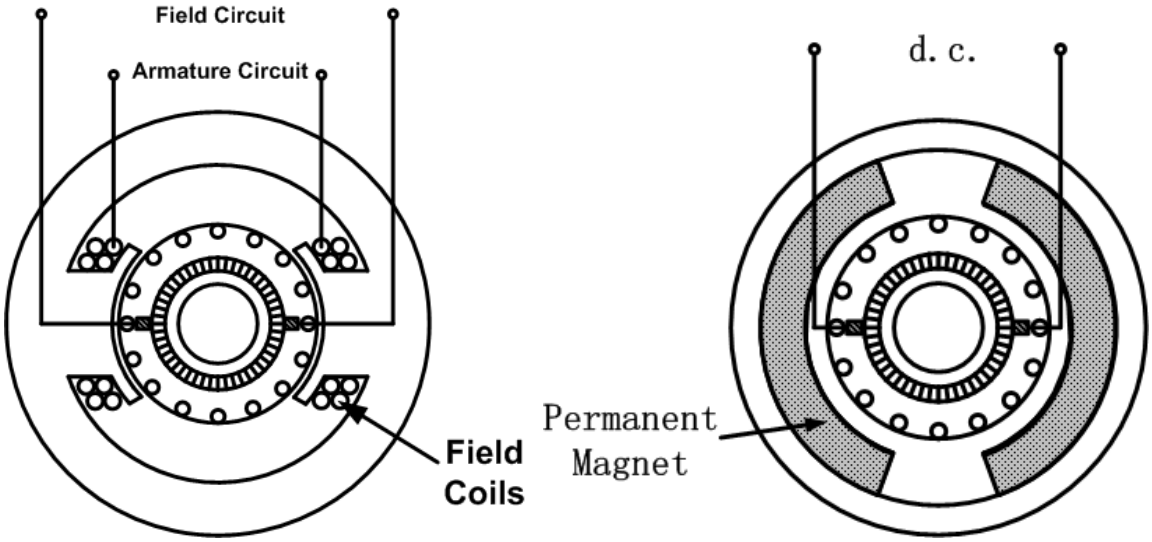

(a) (b)

Figure 1.3: Typical Configurations of (a) A DC Machine (b) A PM DC Machine

1.2 Permanent Magnet Materials

The most distinguishing part of a permanent magnet machine is that the permanent magnet is placed inside to provide the field excitation. The design, performance and application of a permanent magnet machine are closely related to the characteristics of permanent magnet materials. The basic operational characteristic of a magnet material is the portion of its hysteresis loop in the second quadrant. It is also called the demagnetization curve. Fig. 1.4 illustrated the basic magnetic

properties of permanent magnets.

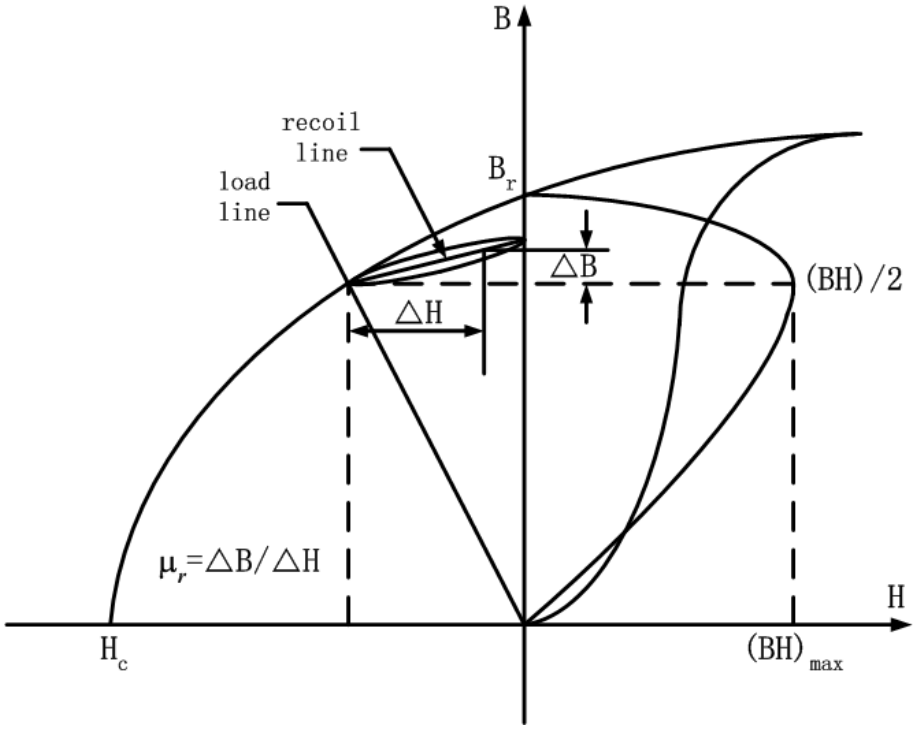

Figure 1.4: Demagnetization curve and energy product of permanent magnets

When a permanent magnet has been magnetized, it remains magnetized even if the applied magnetic field intensity is decreased to zero. The magnetic flux density at this point is called the remanence flux density, B_r. If a reverse magnetic field intensity is applied, the flux density decreases. If the value of the reverse magnetic field is large enough, the flux density eventually becomes zero. The field intensity value at this point is called the magnetic coercive force or coercivity, H_c. When the reverse field intensity is removed, the flux density recovers according to a minor hysteresis loop. Reapplying a reverse field intensity again reduces the flux density to the original value thus completing the hysteresis loop. The hysteresis loop is usually a very narrow loop so that it can be approximated by a straight line called recoil line. The gradient of this line is called recoil permeability, μ_r. It is this permeability that determines the change in flux density if the external field

changes according to $\mu_r = \Delta B/\Delta H$. The operating point of a permanent magnet is the intersection point of a B-H curve of the external magnetic circuit (load line) and the demagnetisation curve of a permanent magnet. The operation point moves along the demagnetisation curve with changes in the outer magnetic circuit. The absolute value of the product of the flux density B and the field intensity H at each point along the demagnetization curve can be represented by the energy product and this quantity is one of the indexes of the strength of the permanent magnet.

The characteristics of permanent magnet materials vary with the structure and processing of the materials. The most common type of magnets used in permanent magnet machines are Alnico, ferrites, samarium-cobalt (SmCo) and neodymium-iron-boron (NdFeB), their typical characteristic demagnetization curves are shown in Fig. 1.5.

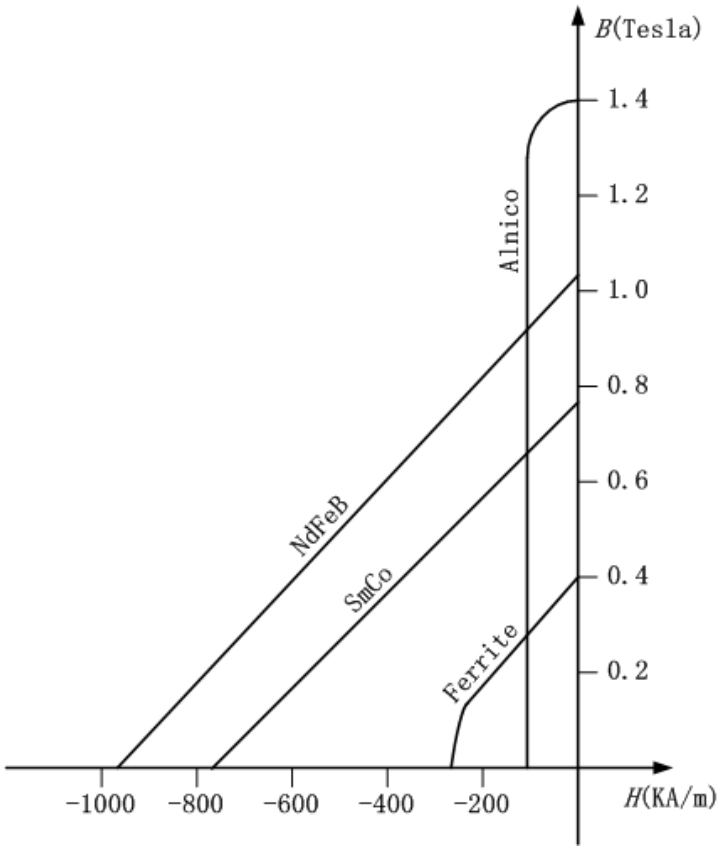

Figure 1.5: Characteristics of Permanent Magnet Materials

Permanent magnets have been used in electric machines almost from the beginning of the development of these machines as replacements for wound field excitation systems. But the low energy densities of permanent magnets prevented the use of permanent magnets in any types of machines other than very low power control machines and signal transducers [3]. Modern permanent magnet machines began with the development of Alnico magnets by Bell Labortories in the 1930's. This kind of magnets have the lowest temperature coefficient of B_r and the highest operating temperature. It has a B_r value of up to 1.4 Tesla but with only a H_c less than 120 kA/m. The applications of Alnico permanent magnet were limited. However, the introduction of Alnico is the very start of widespread use of permanent magnets in various devices.

Ferrite magnets were developed in 1950's and have been used for decades. It promoted the widespread use of permanent magnets in commercial and aerospace applications. This kind of magnets has a B_r value of around 0.3$\sim$0.45 Tesla but with a very high H_c up to 200 KA/m or more. Ferrite magnets have the lowest cost and low core losses. They can be operational up to 100^oC [4].

A revolution in permanent magnets commenced about 1960's with the introduction of samarium-cobalt (Sm-Co) family of hard magnets. It has a high value of B_r which is around 0.8$\sim$1.1 Tesla and a strong H_c about 800 KA/m. However the high cost of both samarium and cobalt makes this magnet one of the most expensive magnetic materials in use today.

The revolution in magnetic materials accelerated with the discovery of another new rare-earth magnet, neodymium-iron-boron (NdFeB) types. This kind of magnets have higher B_r values up to about 1.25 Tesla. The maximum tempera-

ture for NdFeB ranges from 100^o to 180^o depending on the detailed composition [4]. The cost of this magnet is still high but it is more efficient in terms of flux per dollar.

1.3 Line-Start Permanent Magnet Synchronous Machines

A line-start permanent magnet synchronous machine is characterized in structure with squirrel cage bars (or damper windings) in the rotor for asynchronous starting, as shown in Fig. 1.6. It is an induction machine with added permanent magnets in the rotor, but it has a higher efficiency than induction machine and may represent an alternative to the induction machine.

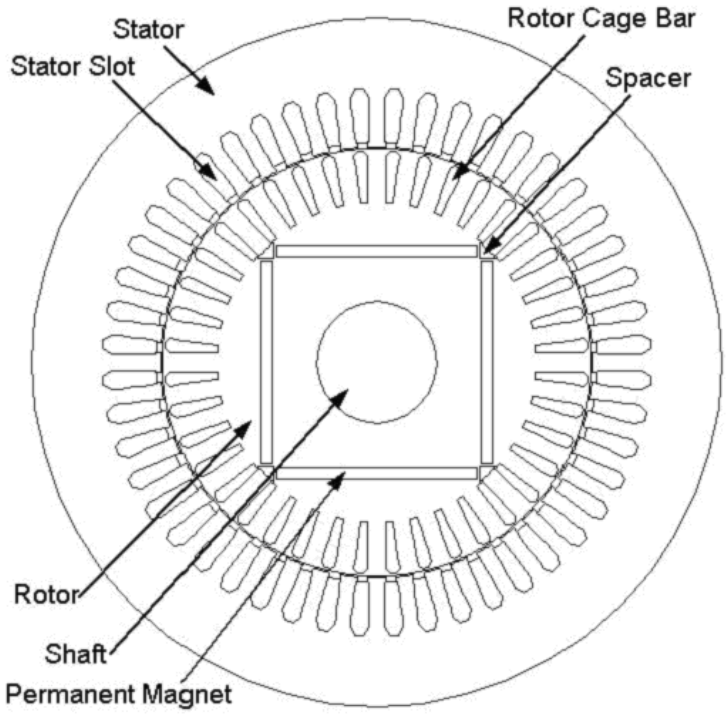

Figure 1.6: Cross Section of a Line-Start Permanent Magnet Synchronous Machine

Line-start permanent magnet synchronous machines have several advantages for industrial applications. The presence of the magnets means that the magnetizing current is unnecessary, which improves the power factor of the machine. The absence of field ohmic losses and the much lower rotor losses once synchronized make the efficiency of the machine high.

When a line-start permanent magnet synchronous machine is run up from zero speed to the rated speed, several factors have to be considered, such as starting current, starting torque, run-up time, etc. The maximum current occurs at run-up as in a normal induction machine. The heavy inrush of current at starting may cause demagnetization of the magnets unless suitable precautions are taken in the design of such machines. Although the squirrel cage bars can protect the magnets from demagnetization during the transients associated with the start-up, the magnet thickness must be designed such that it can withstand the maximum possible demagnetization current. In practice, this high starting current should be prevented from happening often so as to protect the permanent magnet. Therefore frequent self-starting of the machine should be avoided or the machine should be started at low voltage and light loads.

Starting torque is another important issue during the starting of a line-start permanent magnet synchronous machine. Three different torques appear in the process of starting [5]:

- braking torque due to the magnet;
- pulsating torque due to rotor saliency acting as a braking torque;
- accelerating torque due to the rotor bars.

The squirrel cage bars in the rotor can provide the accelerating torque that drive the machine to near synchronous speed. The magnet torque is a braking torque that opposes the cage torque during run-up. The stronger the magnet field, the greater the braking torque. The accelerating torque must overcome, not only the applied load torque, but also the generated magnet braking toques due to the presence of the permanent magnet flux and the rotor saliency. As the motor approaches synchronous speed, the level of accelerating cage torque is lowered and the magnet torque reverses its role and becomes the sole source of accelerating torque. This synchronizing toque from the permanent magnet must be big enough so as to pull the machine into synchronism. For large capacity machines, a stronger magnet field is needed for the synchronism. However, this high magnetic field will result in a big braking torque at low speed and prevent the machine from starting. Therefore for some line-start permanent magnet synchronous machines, especially some large capacity machines, the self-starting is quite difficult or even impossible.

The ability of starting and synchronizing a considerable load and inertia against friction and windage is crucial for self-starting permanent magnet synchronous machine. Bigger load inertia causes larger starting current which may bring demagnetization to the permanent magnet. With bigger load inertia, stronger magnetic field is required to pull the machine into synchronism, which may result in a big braking torque at low speed.

Pulsating torque is caused by the machine saliency during the run-up. It will bring oscillation to the speed and hence mechanical variation to the shaft. This pulsation torque persists right up to the moment of pull-in. Such oscillation may be severe and cause damage to the shaft during the starting process.

Heat is generated in the cage of the line start machines during start-up. This heat is more of a problem in permanent magnet machines because of the proximity of the cages to the magnets. Both the residual flux density and coercivity of some permanent magnets reduce as a function of temperature. Indeed if the temperature excursion is beyond a certain value, permanent demagnetization can happen. Therefore for permanent magnet synchronous machines with very high bar current during the self-starting process, the heat effects brought along by the current may cause the demagnetization of the permanent magnet. For such machines frequent self-starting should not be applied.

The starting performance of a line-start permanent magnet synchronous machine from the moment of switch-on to the onset of stable synchronous running forms an important part of the assessment of such machines for practical applications. The machine can be self-starting when connected to supply mains directly. However, a few aspects as described above during the self-starting process have to be considered, including the starting current, the demagnetization of permanent magnet, the torque, etc. The machine can also be started with supply fed from an inverter, where many starting quantities can be controlled, such as the starting current, torque and frequency.

1.4 Computational Analysis of Permanent Magnet Machines

Permanent magnet machines are widely used in industrial applications for their superior performances. Performance simulation is vital to machine design as it is a fast and low-cost way of predicting machine performances. The act of making and remaking prototypes for actual testing, due to design changes, is both costly and

time consuming. This becomes especially important for large or special-purpose equipment where trial and error methods are impossible or prohibitively expensive. So analysis and simulation of machines are competitive when compared with the experimental methods of development. It is for this reason that the study of permanent magnet machine performance using mathematical methods has received much attention in recent years [6] - [8]. Generally, two methods are used for evaluating the performance of electromagnetic devices: analytical and numerical methods.

1.4.1 Analytical Methods

Traditional analytical methods, such as lumped parameter models and equivalent circuits, are computationally fast and designers can also have a good view of model sensitivities to design parameters. These methods are simple and involved only a few simple circuit equations to be evaluated. The circuit equations can be either algebraic in a steady state condition or in the form of ordinary differential equations in the transient conditions. Simple computer programs can also be easily written for this purpose. Most available type of machines can be analyzed using a circuit model once the machine parameters are known.

The main limitation of this method is that accurate determination of necessary parameters is very difficult for permanent magnet machines. Most of the standard methods used in conventional machines are not suitable for permanent magnet machines because the field excitation cannot be varied or switched off. Moreover, the parameters especially the transient parameters are dependent on current and speed to some extent. So unless a proper method is developed to take these factors into account it is impossible to determine all the machine parameters accurately by experimental methods [9].

Other analytical methods, such as the method of images, can give us the solutions to electromagnetic field problems [10]. These closed form solutions are usually expressed through exact mathematical formulation. However, these methods can only be used to solve the field problem with simple geometries. For example, the method of images can only be applied to a range of problems in electrostatics and magnetostatics when they involve relatively simple sources and possess an easily identifiable symmetry. In reality, almost all the field problems are very complicated. The resultant mathematical expressions may be too complicated for the engineers to gain some intuitive feelings for the field behaviours. Sometimes it is even difficult to obtain a mathematical expression just because of the complexity of the problem [11].

1.4.2 Numerical Analysis

The limitations of the analytical methods require us to surrender the expectations of closed form analytical solutions and to seek rigorous numerical field values directly. Using numerical methods, the solution of the field is not an analytical expression, but the field values at some points in the field domain. If we can obtain more such field points, we can find out more information about the field to be solved. Although numerical methods are approximate by definition, high degrees of accuracy are now possible.

In the analysis of electric machines, it is essential to be able to consider any aspects of the design in great detail. Some critical factors, such as losses, temperature rise and efficiency, are dependent on the distribution of electromagnetic fields. The computation of these fields to the accuracy now desired cannot be achieved by

analytical method. Numerical methods offer a more accurate and powerful design tool. Most important aspects of the field computation, such as material properties, non-linearities and structural details, can be taken into account. It is particularly effective when dealing with such qualitative analysis as the optimization, demagnetization and transient phenomena in the machine. With numerical methods few simplifications are necessary. It is possible to calculate the field in the machine very close to that in an actual operation.

1.5 Analysis of Electric Machines Using Finite Element Method

Numerical methods are more suitable for the electromagnetic field analysis of permanent magnet machines. There are a number of numerical methods available for the analysis of electromagnetic field problems. A few of them are, finite difference method (FDM) [12], boundary element method (BEM) [13] and finite element method (FEM) [8]. These methods have their advantages and disadvantages. However, finite element method incorporates most of the advantages of the other two methods without incurring significant disadvantages; especially for the analysis of electric machines where many factors need to be considered, such as complex geometries, magnetic and electric materials, induced currents, coupling of thermal and mechanical effects, etc.. In such cases, the finite element method is more suitable. For example, the finite difference method is not easily applicable to the field involving rapid changes of the gradient or complex geometries. Nodal distribution can be very inefficient. This is not so with finite elements. Equally, boundary element method is not efficient at handling non-linear materials [14]. Finite element method is well suited for the analysis involved with nonlinearities. It can be used

for solving both linear and non-linear field problems including simple and complex geometries. Thus it is well recognized that finite element method offers considerable advantages in electrical machine analysis [14] - [16].

The finite element method was first introduced for the computation of magnetic field in nonlinear electromagnetic devices by Chari and Silvester in 1970's [17, 18]. It was mainly for solving nonlinear magnetostatic problems. Hannala and MacDonald pioneered the numerical calculation of transient phenomenon during the operation of electric machines [19]. They used time stepping techniques and nodal method to predict the transient behavior of electric machines. The use of time-stepping finite element method for analyzing nonlinear transient electromagnetic field problems in electrical machines was presented by Tandon *et al* in the 1980's [20].

In modern power systems, electric machines are often operated together with the external circuits. The coupling of a comprehensive field analysis and circuit analysis is necessary. Moreover, there are movable mechanical components in the machine, like the rotor. Electromagnetic force determines the movement of these components and the positions of these components in turn affect the electromagnetic field within the machine. Therefore the coupling of mechanical movement with the field and circuit analysis is also important.

Circuit equations are first applied to the steady state performance evaluation of a turbine-generator by Brandl *et al* in 1975 [21]. A method of accounting for the circuits in electric machines in the frequency domain was presented by Williamson and Ralph in 1983 [22]. The direct coupling of fields and circuit equations in time domain was applied by Nakata and Takahosi [23] in 1982. Later similar methods

were also used by many other researchers in the 1980's [24]-[26].

An integrated approach to couple fields, circuits and mechanical motion was first presented by Arkkio [27] and Istfan [28] in 1987. Then a detailed description was given by Salon *et al* [29]. Given the machine geometry, winding connections, material characteristics, applied voltage and the loading conditions, machine currents, fields and the motion can be computed accordingly. Such type of finite element method is often referred to as field-circuit coupled time stepping method. It has been widely used in the analysis of various electric machines [30]-[34].

Currently many commercial softwares, such as Flux2D [35], Maxwell [36] and many others [37]-[40], are available to researchers for analysis of various complex field problems of static and time varying nature.

The field-circuit coupled time stepping finite element method has been applied to the computation of line-start permanent magnet synchronous machine before [31, 41, 42]. Most of the application is for single phase line-start permanent magnet synchronous machine as in [31]. The implementation of this method to the three phase machines are presented in [41, 42]. However, the coupling of electromagnetic field with the external circuit, such as inverter, is not included in these works.

1.6 Parameter Determination of Permanent Magnet Synchronous Machines

Performance simulation is vital to machine analysis as it is a fast and low-cost way of predicting machine performances. Traditional analytical methods, such as lumped parameter models are computationally fast and simple in determining the

machine performances. The designers can also have a good view of model sensitivities to parameters. The analytical analysis requires machine parameters and the accuracy of the analysis is wholly dependent on the accuracy of these parameters. Therefore parameter determination is very important for performance evaluations of electric machines.

Parameter determination is also important for the operations of machines. Many synchronous machine drives are operated under various control schemes. For example the flux weakening control is used in the synchronously rotating reference frame to actively vary the d-axis armature current as a function of loading and speed. Such operation is realized with the knowledge of machine parameters. It is for this reason that the accurate determination of machine parameters is indispensable.

Many methods have been used for the determination of parameters of permanent magnet synchronous machines [43] - [60], mainly focusing on the steady-state synchronous reactances. Generally we can classify these methods as computational methods and experimental methods. Computational methods, such as finite elements [44, 45], allow assessment of parameters which are difficult to determine experimentally and the estimation of various parameters even before the machine prototype is made. But the limitation of computation modelling must be appreciated [46]. The parameters of permanent magnet synchronous machines vary nonlinearly due to the structural speciality of the rotor, the load condition and current phase angle. Therefore the model should account for the parameter variations at different loading conditions and the iron saturation. Different authors have proposed alternative methods to evaluate the variations of parameters with iron saturation [47], [48]-[50]. However some assumptions have been made, such as

the constant permanent magnet flux linkage with load conditions [48, 49] and no mutual coupling between the two axes [48]-[50].

Experimental methods, such as static test (locked rotor test) [51]-[54], no-load tests [53, 55], load tests [43], [56]-[58] and other methods [59, 60] have been applied by many researchers. Most of the methods are based on the steady state two-axis model of permanent magnet synchronous machines and some necessary simplifications. For example, it is assumed in the static test that parameters are constant with one frequency. In no-load tests the variation of permanent magnet flux linkage under different loading conditions is neglected. Some load tests take into account the iron saturation but the issue of variable permanent magnet excitation still cannot be solved.

1.7 Scope of the Thesis

This thesis presents the dynamic analysis of permanent magnet synchronous machines using field-circuit coupled time stepping finite element method. It also deals with the parameter estimation of permanent magnet synchronous machines using both experimental and computational methods.

A line-start interior permanent magnet synchronous machine is used in this work. In modern power system, the line start interior permanent magnet synchronous machine is often operated with external circuits. The coupling of a comprehensive field analysis and circuit analysis is necessary. Moreover, electric machines are electromagnetic devices for electro-mechanical energy conversion. The electromagnetic field inside the motor affects the movement of the rotor and the position of the rotor in turn affects the electromagnetic field. Therefore the coupling

of mechanical movement with the field and circuit analysis is important. To analyze the dynamic performance of line-start permanent magnet synchronous machine comprehensively, the field-circuit coupled time stepping finite element method is implemented. The modelling of line-start permanent magnet synchronous machine system is presented in Chapter 2. The finite element analysis is presented in Chapter 3. As one of the dynamic performances, the starting process is computed and presented in Chapter 5. This starting process includes both the self-starting and the starting processes under different control schemes. The computational results are validated by the experimental results.

Another important aspect in the analysis of permanent magnet synchronous machines is the determination of its parameters, among which the most important ones are the direct axis reactance X_d, the quadrature axis reactance X_q and the permanent magnet excitation voltage E_0. In Chapter 4 both the experimental method and the computational method are discussed in combination to determine these parameters. Two novel methods are proposed through the application of linear regression and Hopfield neural network. Finite element analysis has been used to compute the machine parameters as well.

Chapter 2

Mathematical Modelling of Line-Start Permanent Magnet Synchronous Machines

2.1 Introduction

Line-start permanent magnet synchronous machines have complex geometrical configurations consisting of magnets, conductors, barriers, etc. Precise analysis and simulation of these machines are challenging tasks for those who design and use these machines. The accomplishment of these tasks depends on the accurate computation of electromagnetic fields in the machine using analytical or numerical methods. Essentially the method selected has to be able to analyze the electric machines in considerable detail, so that a near exactness may be obtained. Electric machines are complicated devices, with difficulties such as complex geometries, nonlinearities of materials and eddy currents, which cannot be included in an analytical method. However, the use of numerical analysis can easily overcome these difficulties.

The fundamental basis of applying numerical methods is the modelling of electric machines. Electric machines receive power from external sources through electric circuits. This in turn requires the modelling of electromagnetic fields inside

the machine to be coupled with electric circuit analysis. Moreover electric machines are electro-mechanical conversion devices. It is important to take into account also the interaction of electromagnetic fields, mechanical forces and motions. Therefore a comprehensive modelling of electromagnetic fields, circuits and mechanical motion of an electrical machine system should be considered together.

Line-start permanent magnet synchronous machines have the capabilities of self-starting. However, several factors and problems have to be considered, including the starting current, the demagnetization of permanent magnets, the synchronization, etc. The machine can also be started with supply fed from an inverter, where many starting quantities can be controlled. Fig. 2.1 shows the configuration of a line-start permanent magnet synchronous machine connected with an inverter. The modelling of the whole system will be described in the remaining parts of this chapter.

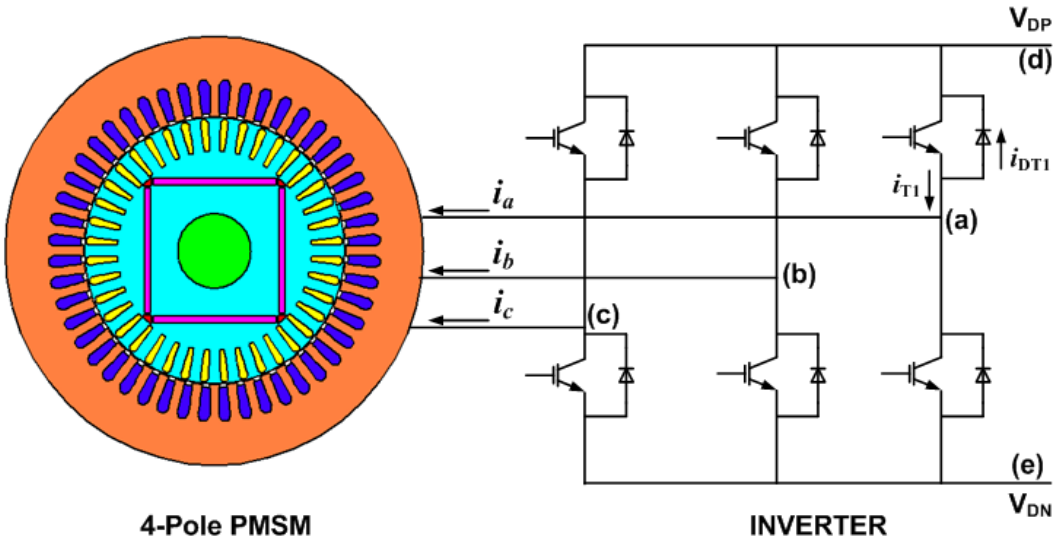

Figure 2.1: A Line-Start PMSM Connected with Inverter

2.2 Representation of Permanent Magnets

The properties and performances of a permanent magnet machine are greatly affected by the characteristics of permanent magnets. Therefore proper representation of permanent magnet is very important in the design and analysis of a permanent magnet machine. Generally there are two models to represent permanent magnets: a magnetization vector model [8] and an equivalent current sheet model [61]. These two methods have different starting points but they result in the same set of equations [8]. In this work the magnetization vector model has been used.

Magnetic behavior of magnet materials is described in terms of three interrelated vectors: $B-$ magnetic induction or flux density, $H-$ magnetic field intensity and $M-$ magnetization. For a magnet material $NdFeB$ operated in the second quadrant of its normal hysteresis loop, it can be represented as a straight line as shown in Fig. 2.2. The relationship of the three vectors B, H and M can be expressed as [62]:

$$B = \mu_0 H + \mu_0 M \tag{2.1}$$

where μ_0 is the permeability of the free space.

While calculating distributed fields, it is usual to describe the vector M in terms of its remanent value M_r (when $H = 0$) and M' which is the function of magnetic susceptibility χ_m and H :

$$\begin{aligned} M &= M' + M_r \\ &= \chi_m H + M_r \end{aligned} \tag{2.2}$$

So equation (2.1) can be written as

$$\begin{aligned} B &= \mu_0[(1+\chi_m)H + \mu_0 M_r] \\ &= \mu_0(\mu_r H + M_r) \\ &= \mu H + \mu_0 M_r \end{aligned} \tag{2.3}$$

where $\mu_r = (1+\chi_m)$ is the relative permeability.

Equation (2.3) represents the relationship of B, H and M_r. It is the representation of permanent magnet in terms of magnetization vector used in this work.

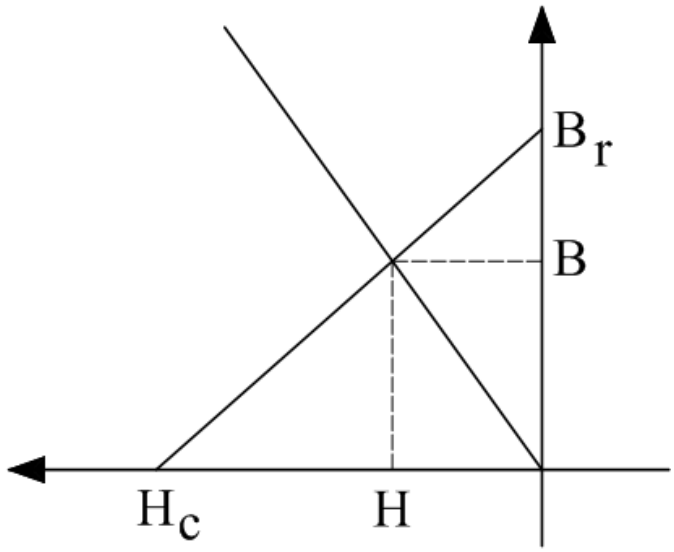

Figure 2.2: Straight Line Approximation of Magnet Characteristics

2.3 Modelling of Electromagnetic Fields

The electromagnetic field in an electric machine is governed by Maxwell's equations:

$$\nabla \times H = J \tag{2.4}$$

$$\nabla \times E = -\frac{\partial B}{\partial t} \tag{2.5}$$

$$\nabla \cdot B = 0 \tag{2.6}$$

with the constitutive relationship:

$$J = \sigma E \tag{2.7}$$

and

$$B = \mu H \tag{2.8}$$

where

$J =$ current density

$E =$ electric field intensity

$\sigma =$ conductivity

Since

$$\nabla \cdot B = 0,$$

we are able to find a vector A whose curl is equal to B and the $\nabla \cdot B$ is assured to be zero through $\nabla \cdot (\nabla \times A) = 0$. Thus

$$B = \nabla \times A \tag{2.9}$$

and A is the magnetic vector potential.

Substituting equation (2.9) into equation (2.5) yields

$$\nabla \times E = -\frac{\partial(\nabla \times A)}{\partial t} = -\nabla \times \frac{\partial A}{\partial t} \tag{2.10}$$

or

$$\nabla \times (E + \frac{\partial A}{\partial t}) = 0. \tag{2.11}$$

Since the curl of a gradient is identically zero, we can write

$$E + \frac{\partial A}{\partial t} = -\nabla\psi \tag{2.12}$$

or

$$E = -\frac{\partial A}{\partial t} - \nabla\psi \tag{2.13}$$

where $\nabla\psi$ is the gradient of a scalar quantity ψ called the scalar potential. Substituting equation (2.13) into equation (2.7), the current density vector becomes

$$J = \sigma E = -\sigma(\frac{\partial A}{\partial t} + \nabla\psi). \tag{2.14}$$

The current density in equation (2.14) includes two parts: one is induced quantity $\frac{\partial A}{\partial t}$ produced by electromagnetic induction and the other one is $\nabla\psi$ caused by the effect of charge build up at the conductor end.

If we consider a current-carrying conductor of length l, its positive terminal is point a and negative terminal is point b. If the difference in electric scalar potential between point a and b is V_{tz} volts, we can write

$$V_{tz} = V_a - V_b = \int_a^b E_{scale} dl = -\int_a^b \nabla\psi dl. \tag{2.15}$$

In two-dimensional field problems $\nabla\psi$ is considered to be constant in $z-$direction, then equation (2.15) becomes

$$V_{tz} = -\nabla\psi \cdot l \tag{2.16}$$

or

$$\nabla\psi = -\frac{V_{tz}}{l} \tag{2.17}$$

Therefore the current density vector for a stationary two-dimensional field is

$$J = -\sigma\frac{\partial A}{\partial t} + \sigma\frac{V_{tz}}{l} \tag{2.18}$$

When the field is moving with a relative velocity v, two reference frames (coordinate systems) have to be defined. One frame $O(x, y, z)$ is stationary and the other frame $O'(x', y', z')$ is moving. Assuming the time t and t' measured in the two frame are same, then following relation exists for vector E [63]:

$$E' = E + v \times B \tag{2.19}$$

Therefore the current density observed from the stationary frame $O(x, y, z)$ is

$$\begin{aligned} J &= \sigma(E + v \times B) \\ &= -\sigma\frac{\partial A}{\partial t} + \sigma\frac{V_{tz}}{l} + \sigma v \times B \end{aligned} \tag{2.20}$$

Combining with equation (2.4) yields

$$\nabla \times H = -\sigma\frac{\partial A}{\partial t} + \sigma\frac{V_{tz}}{l} + \sigma v \times B. \tag{2.21}$$

Recalling equations (2.8) and (2.9),

$$B = \mu H$$

$$\nabla \times A = B$$

then equation (2.21) becomes

$$\nabla \times (\nu\nabla \times A) = -\sigma\frac{\partial A}{\partial t} + \sigma\frac{V_{tz}}{l} + \sigma v \times B \tag{2.22}$$

where $\nu = \frac{1}{\mu}$ is the reluctivity.

For permanent magnets which are represented by

$$B = \mu H + \mu_0 M_r, \tag{2.23}$$

$$\begin{aligned} \nabla \times H &= \nabla \times (\nu B) - \nabla \times (\nu \mu_0 M_r) \\ &= \nabla \times (\nu \nabla \times A) - \nabla \times (\nu \mu_0 M_r). \end{aligned}$$

Since

$$\nabla \times H = J,$$

combining with equation (2.20) yields the governing equation for permanent magnet,

$$\nabla \times (\nu \nabla \times A) = -\sigma \frac{\partial A}{\partial t} + \sigma \frac{V_{tz}}{l} + \sigma v \times B + \nabla \times (\nu \mu_0 M_r). \tag{2.24}$$

For soft magnetic materials, equation (2.24) is reduced to equation (2.22) since no remanent magnetization ($M_r = 0$). Therefore equation (2.24) is taken as the general governing equation for moving time-varying field problems.

Employing the moving frame as reference frame, the relative velocity v becomes zero and equation (2.24) can be simplified as:

$$\nabla \times (\nu \nabla \times A) = -\sigma \frac{\partial A}{\partial t} + \sigma \frac{V_{tz}}{l} + \nabla \times (\nu \mu_0 M_r) \tag{2.25}$$

Equation (2.25) is the fundamental governing equation for the modelling of various field problems. It can be solved for a wide class of field problems, involving relative motion, non-linear material properties and time-variations. In the analysis of electric machines, it is common to evaluate the field solution in two dimensions considering the current density J and magnetic vector potential A having only z-directed invariant components. This analysis is valid for most cases because the air gap between the rotor and stator in an electrical machine is so small that for most of the length of the machine, except the end regions, the machine is practically

two-dimensional in operation. Comparing with three dimensional technique, two-dimensional technique distinctively saves the computational cost and time despite the possible loss in accuracy. Three dimensional effects such as skewing and end winding effect can somehow be compensated by employing correction factors to the field solution or applying some other techniques, like multi-slice [64]. Thus for a given a problem domain or region, equation (2.25) with B and H in $x-y$ plane becomes,

$$\frac{\partial}{\partial x}(\nu\frac{\partial A}{\partial x})+\frac{\partial}{\partial y}(\nu\frac{\partial A}{\partial y})=\sigma\frac{\partial A}{\partial t}-\sigma\frac{V_{tz}}{l}-\nabla\times(\nu\mu_0 M_r) \tag{2.26}$$

2.4 Circuit Equations

The analysis of electric machines depends on the accurate field analysis. The approach to analysis commonly involves two dimensional numerical methods with specified current sources for the conductors. The knowledge of input currents is essential for the successful field analysis of electrical devices. However in practice electric devices are mostly connected to voltage sources instead of the ideal current sources. The problem is further complicated by the connections of the conductors. Therefore analysis of field problems with a voltage source and arbitrary waveforms is preferred. Circuit equations that represent the relations of current and voltages are needed. The coupling of circuit equations to the field analysis is necessary.

Modern electric machines are often operated under some external circuits connected to a known voltage source. The behaviours of such circuits affect the integrity and performance of all the connected devices. Unless the interactions of these external circuits with the electric machines are considered, the analysis of the electric machines cannot assumed to be complete. Thus it is necessary to include the modelling and circuit description of such devices.

2.4.1 Representation of a Conductor

The sources of magnetic fields in machines are currents in the stator windings and the rotor cage bars. These windings and bars can be modelled using individual conductors as circuit components in our modelling. Let us consider a conductor as shown in Fig. 2.3 (a). It has length of l_i and a cross-section area of s_i. The current flowing in the conductor is I_i and the terminal voltage is V_{tz}. From equation (2.20) we can see that the current density in a conductor of length l_i is given by (in moving reference frame):

$$J = -\sigma \frac{\partial A}{\partial t} + \sigma \frac{V_{tz}}{l_i}. \tag{2.27}$$

Integrating equation (2.27) over its corresponding cross-sectional area s_i yields the total current I_i flowing in this conductor, which is:

$$\begin{aligned} I_i &= \int\int_{s_i} J dx dy \\ &= -\sigma \int\int_{s_i} \frac{\partial A}{\partial t} dx dy + \sigma \frac{V_{tz}}{l_i} \int\int_{s_i} dx dy \\ &= -\sigma \int\int_{s_i} \frac{\partial A}{\partial t} dx dy + \sigma \frac{s_i}{l_i} V_{tz} \end{aligned} \tag{2.28}$$

Rearranging equation (2.28) by moving term $-\sigma \int\int_{s_i} \frac{\partial A}{\partial t} dx dy$ to the other side yields

$$\sigma \frac{s_i}{l_i} V_{tz} = I_i + \sigma \int\int_{s_i} \frac{\partial A}{\partial t} dx dy. \tag{2.29}$$

Divided by $\sigma \frac{s_i}{l_i}$ on both sides of equation (2.29), the terminal voltage V_{tz} across a z-directed conductor with length l_i and cross-section area s_i is:

$$\begin{aligned} V_{tz} &= \frac{l_i}{\sigma s_i} I_i + \frac{l_i}{s_i} \int\int_{s_i} \frac{\partial A}{\partial t} dx dy \\ &= R_{dci} I_i + \frac{l_i}{s_i} \int\int_{s_i} \frac{\partial A}{\partial t} dx dy \end{aligned} \tag{2.30}$$

where $R_{dci} = l_i/(\sigma s_i)$ is the dc resistance of the conductor. Thus one conductor can be represented as one resistor together with an induced voltage $\frac{l_i}{s_i} \int\int_{s_i} \frac{\partial A}{\partial t} dx dy$ as shown in Fig. 2.3 (b).

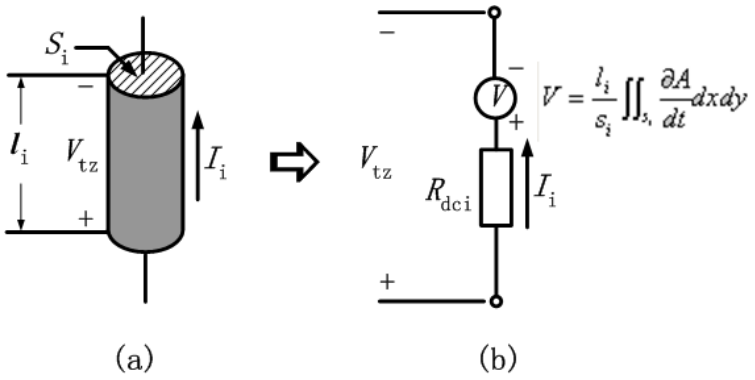

Figure 2.3: Representation of a Conductor

Both stator windings and rotor cage bars are made up of conductors connected in series or in parallel. It is possible to model them using two-dimensional models based on the modelling of one conductor. However some properties and features due to the inherent three dimensional nature of electric machines have to be taken into account. Among these features the most important ones are the stator end-windings and rotor end rings. These end effects lie outside the jurisdiction of two dimensional numerical models, which can only account for the currents flowing in $Z-$direction. Therefore some means must be found to deal with these end effects.

Stator end-winding effects are dealt with simply by adding an appropriate external impedance in the stator circuit equations [23]. For rotor end-ring effects, Strangas [25] neatly combines the end-ring impedance with the field analysis by means of rotor loop equations. These methods are quite effective when including the three-dimensional effects into the two-dimensional field analysis. They have been used frequently in the analysis of electric machines [27, 64].

2.4.2 Equivalent Circuits of Stator Windings

Stator windings are made up by conductors connected in many turns. If we consider a 'go' and 'return' loop of current-carrying conductors (Fig. 2.4) connected to an external input voltage source V_{ext} through an external resistance R_{ext} and inductance L_{ext}, we can get:

$$V_{ext} = V_{tz}^{+} - V_{tz}^{-} + R_{exti}I + L_{exti}\frac{dI}{dt} \tag{2.31}$$

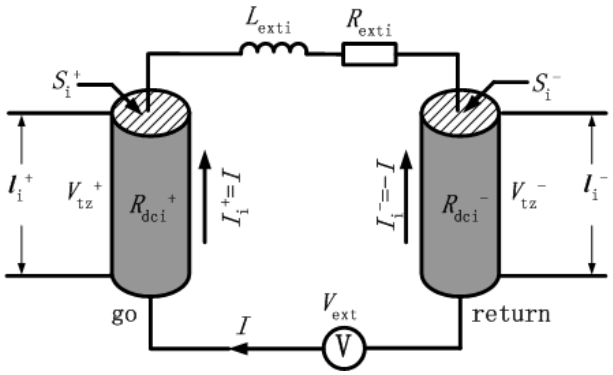

Figure 2.4: One Turn of 'Go' and 'Return' Loop of Conductors

Substituting equation (2.30) into equation (2.31) yields

$$V_{ext} = R_{dci}^{+}I_i^{+} - R_{dci}^{-}I_i^{-} + \frac{l_i^{+}}{s_i^{+}}\int\int_{s_i^{+}}\frac{\partial A}{\partial t}dxdy - \frac{l_i^{-}}{s_i^{-}}\int\int_{s_i^{-}}\frac{\partial A}{\partial t}dxdy + R_{exti}I + L_{exti}\frac{dI}{dt} \tag{2.32}$$

For N conductors connected in series (Fig. 2.5),

$$\begin{aligned} V_{ext} &= \sum_{i=1}^{N} R_{dci}^{+}I_i^{+} - \sum_{i=1}^{N} R_{dci}^{-}I_i^{-} + \sum_{i=1}^{N}\frac{l_i^{+}}{s_i^{+}}\int\int_{s_i^{+}}\frac{\partial A}{\partial t}dxdy - \sum_{i=1}^{N}\frac{l_i^{-}}{s_i^{-}}\int\int_{s_i^{-}}\frac{\partial A}{\partial t}dxdy \\ &+ \sum_{i=1}^{N} R_{exti}I + \sum_{i=1}^{N} L_{ext}\frac{dI}{dt} \end{aligned} \tag{2.33}$$

When N is large, the representation of each conductor as shown above is unrealistic to carry out in calculation. Under this condition a uniform current, length and cross section area for each conductor are assumed:

$$\begin{aligned} I_1^+ &= I_2^+ = \ldots = I_N^+ = I \\ I_1^- &= I_2^- = \ldots = I_N^- = -I \\ l_1^+ &= l_2^+ = \ldots = l_N^+ = l \\ l_1^- &= l_2^- = \ldots = l_N^- = l \\ s_1^+ &= s_2^+ = \ldots = s_N^+ = s = S_{tt}/N \\ s_1^- &= s_2^- = \ldots = s_N^- = s = S_{tt}/N \end{aligned} \tag{2.34}$$

Here

$S_{tt} =$ the total cross section area of the $N-$turn conductors

$s =$ the average cross section area of one turn of conductor and the insulation space between the turns are neglected

$+$ is for the 'go' conductor

$-$ is for the 'return' conductor

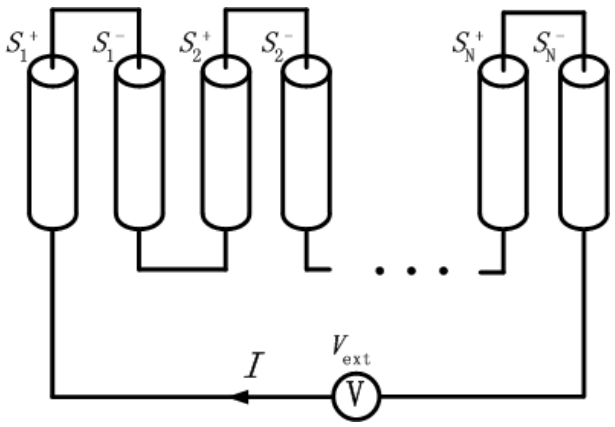

Figure 2.5: N Turns of Conductors Connected in Series

Substituting equation (2.34) to equation (2.33) yields

$$V_{ext} = (R_{dc} + R_{ext})I + L_{ext}\frac{dI}{dt} + \frac{l}{s}(\int\int_{S_{tt}^{+}} \frac{\partial A}{\partial t}dxdy - \int\int_{S_{tt}^{-}} \frac{\partial A}{\partial t}dxdy) \qquad (2.35)$$

where

$R_{dc} = \sum_{i=1}^{N} R_{dci}^{+} + R_{dci}^{-} = \frac{2lN}{\sigma s}$	is the total cross section area of N-turn conductors
$R_{ext} = \sum_{i=1}^{N} R_{exti}$	is the total external resistance
$L_{ext} = \sum_{i=1}^{n} L_{exti}$	is the total external inductance

Equation (2.35) can be extended to get the circuits of stator phase windings in electric machines (Fig. 2.6). The resistance of the windings lying in the body of the stator core is R_{dc}, the resistance of the end windings is represented by R_{ext} and the inductance of the end windings is represented by L_{ext} or L_e. Windings constituted in one phase of the electric machines are not always connected in series. Instead some branches may be connected in parallel as shown in Fig 2.7.

If the phase windings have m branches in parallel, we can get:

$$\begin{aligned}
i_s &= i_{s1} + i_{s2} + \ldots + i_{sm} \\
\Omega^{\pm} &= \Omega_1^{\pm} + \Omega_2^{\pm} + \ldots + \Omega_m^{\pm} \\
\frac{1}{R_{dc}} &= \frac{1}{R_{dc1}} + \frac{1}{R_{dc2}} + \ldots + \frac{1}{R_{dcm}} \\
\frac{1}{R_{ext}} &= \frac{1}{R_{ext1}} + \frac{1}{R_{ext2}} + \ldots + \frac{1}{R_{extm}} \\
\frac{1}{L_e} &= \frac{1}{L_{e1}} + \frac{1}{L_{e2}} + \ldots + \frac{1}{L_{em}}
\end{aligned} \qquad (2.36)$$

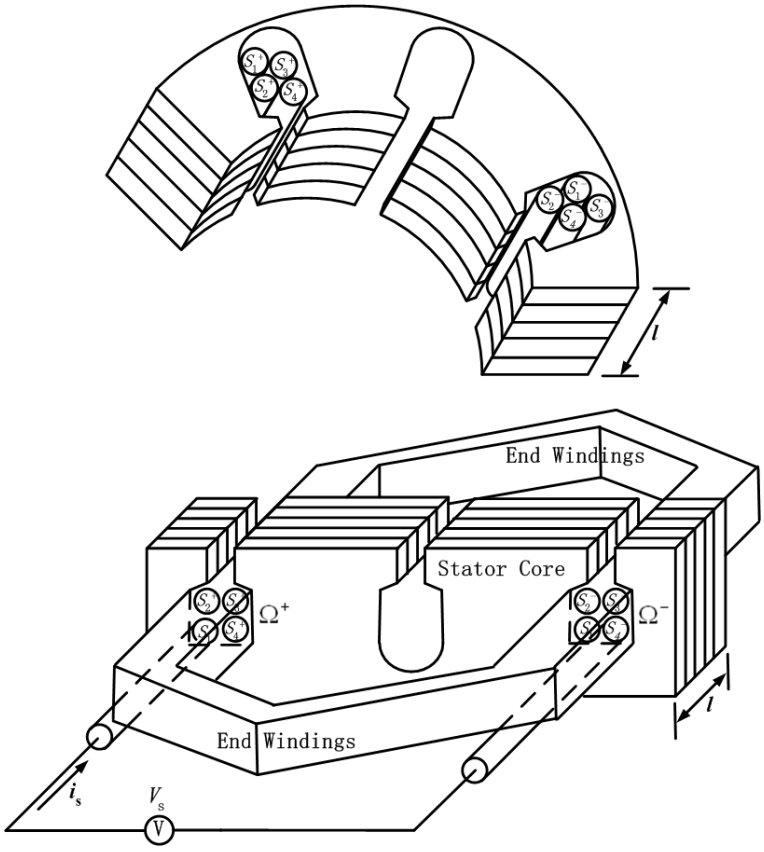

Figure 2.6: Representation of Stator Phase Windings

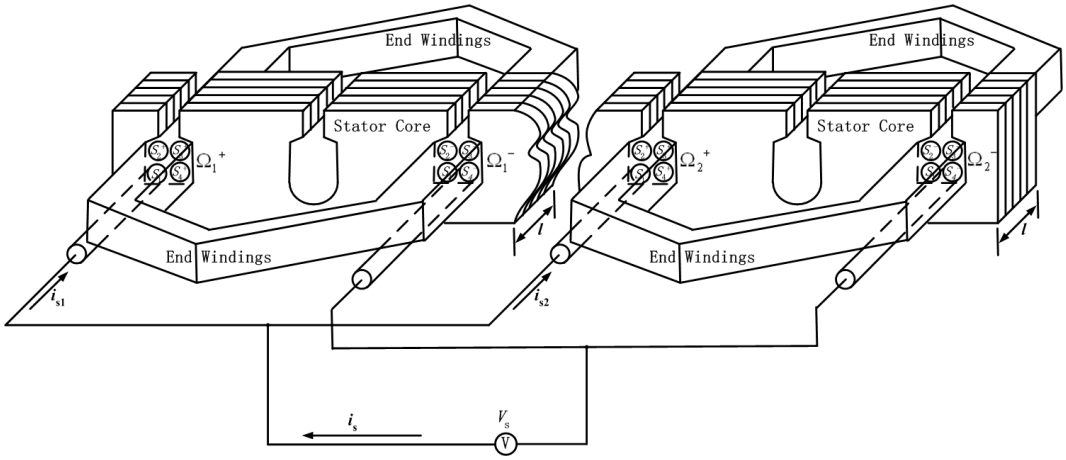

Figure 2.7: Representation of Stator Phase Windings with Branches in Parallel

Therefore the general governing equation for stator phase circuits in electrical machines is:

$$\begin{aligned} V_s &= (R_{dc} + R_{ext})i_s + L_e\frac{di_s}{dt} + \frac{l}{ms}(\int\int_{\Omega^+}\frac{\partial A}{\partial t}dxdy - \int\int_{\Omega^-}\frac{\partial A}{\partial t}dxdy) \\ &= R_s i_s + L_e\frac{di_s}{dt} + \frac{l}{ms}(\int\int_{\Omega^+}\frac{\partial A}{\partial t}dxdy - \int\int_{\Omega^-}\frac{\partial A}{\partial t}dxdy) \\ &= R_s i_s + L_e\frac{di_s}{dt} + V_i \end{aligned} \tag{2.37}$$

where

$V_s =$ applied stator phase voltage

$i_s =$ stator phase current

$R_s =$ total equivalent resistance per phase

$L_e =$ total equivalent inductance of end winding

$l =$ the length of stator windings in $Z-$direction,
usually it uses the same value as the axial length of stator iron core

$m =$ number of stator winding branches in parallel connection

$s =$ equivalent cross section area of one turn of stator windings

$\Omega^+, \Omega^- =$ total cross section area of 'go' and 'return' windings per phase respectively

$V_i =$ induced voltage per phase

Equation (2.37) describes the relationship of external voltage source V_s, corresponding current i_s and vector potential A. Therefore we can calculate the field value A directly from the external voltage source V_s. It is quite effective in the computation of two dimensional electromagnetic fields with coupled external voltage sources.

In three-phase electric machines, usually the stator phases are connected in two different types of connections: a delta ($\triangle$) connection or a star (Y) connection (Fig. 2.8). Representation of sources and circuits in the modelling process can be achieved using common circuit laws such as Kirchoff's voltage rule.

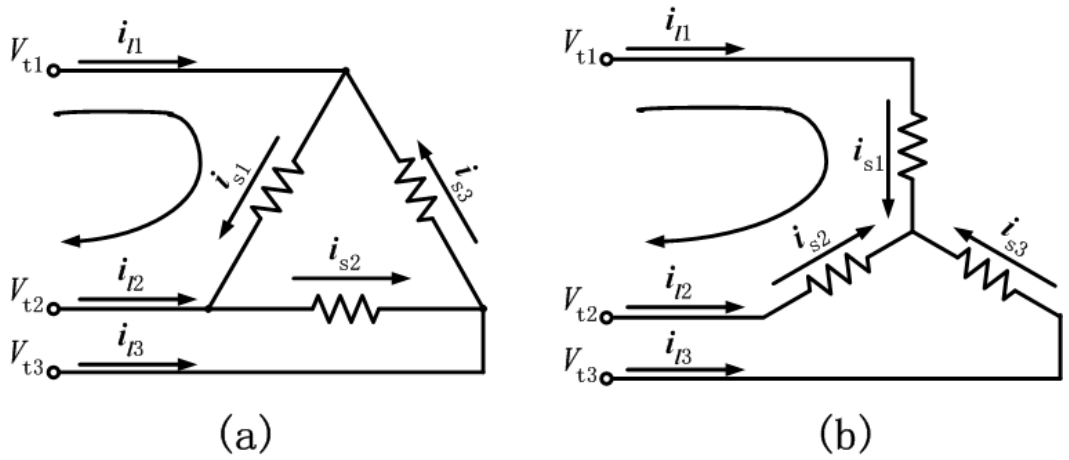

Figure 2.8: Connections of Stator Phase Windings (a) $\triangle$ - Connection (b)Y - Connection

In Fig. 2.8, $V_{tk}|_{k=1,2,3}$ are terminal voltages of the stator phases, i_{lk} are line currents and i_{sk} are phase currents. i_{lk} and V_{tk} are measurable quantities from outside. i_{sk} are the quantities used in the model of stator phases.

Taking loops around every two terminals of $\triangle$ connection yields,

$$\begin{aligned} V_{t1} - V_{t2} &= R_{s1} i_{s1} + L_{e1} \frac{di_{s1}}{dt} + V_{i1} \\ V_{t2} - V_{t3} &= R_{s2} i_{s2} + L_{e2} \frac{di_{s2}}{dt} + V_{i2} \\ V_{t3} - V_{t1} &= R_{s3} i_{s3} + L_{e3} \frac{di_{s3}}{dt} + V_{i3} \end{aligned} \tag{2.38}$$

and

$$\begin{pmatrix} i_{l1} \\ i_{l2} \\ i_{l3} \end{pmatrix} = \begin{pmatrix} 1 & 0 & -1 \\ -1 & 1 & 0 \\ 0 & -1 & 1 \end{pmatrix} \begin{pmatrix} i_{s1} \\ i_{s2} \\ i_{s3} \end{pmatrix} \tag{2.39}$$

Taking loops around every two terminals of Y connection yields,

$$\begin{aligned} V_{t1} - V_{t2} &= R_{s1} i_{s1} + L_{e1} \frac{di_{s1}}{dt} + V_{i1} - (R_{s2} i_{s2} + L_{e2} \frac{di_{s2}}{dt} + V_{i2}) \\ V_{t2} - V_{t3} &= R_{s2} i_{s2} + L_{e2} \frac{di_{s2}}{dt} + V_{i2} - (R_{s3} i_{s3} + L_{e3} \frac{di_{s3}}{dt} + V_{i3}) \\ V_{t3} - V_{t1} &= R_{s3} i_{s3} + L_{e3} \frac{di_{s3}}{dt} + V_{i3} - (R_{s1} i_{s1} + L_{e1} \frac{di_{s1}}{dt} + V_{i1}) \end{aligned} \tag{2.40}$$

and

$$\begin{pmatrix} i_{l1} \\ i_{l2} \\ i_{l3} \end{pmatrix} = \begin{pmatrix} 1 & 0 & 0 \\ 0 & 1 & 0 \\ 0 & 0 & 1 \end{pmatrix} \begin{pmatrix} i_{s1} \\ i_{s2} \\ i_{s3} \end{pmatrix} \tag{2.41}$$

2.4.3 Modelling of Rotor Cage Bars

As illustrated in Fig. 2.9, the cage bars in the rotor of a line-start permanent magnet synchronous machine are usually joined together at their ends by means of conducting end rings. Each cage bar can be modelled using the model of one conductor separately. To include the three-dimensional effects of end rings into the two-dimensional field calculations, a circuit model is used. In this model, the end rings are simplified as impedances. Kirchoff's laws are used to describe the interactions between the cage bars and the end rings.

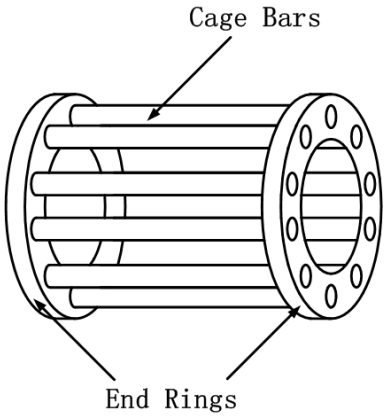

Figure 2.9: Structure of Rotor Cage Bars

Fig. 2.10 shows the equivalent circuit of the rotor cage bars. For each bar, the voltage across its terminals is V_{bk}, where $k = 1, 2, \ldots, n$, and n is the total number of bars. V_k is the induced voltage, i_{bk} is the current flowing in the bar and R_{bk} is the equivalent resistance of the bar. The bars are connected at their ends through end rings, each segments of the end rings possesses both resistance R_{ek} and inductance L_{ek}. The current flowing in the segment of the end rings is i_{ek}.

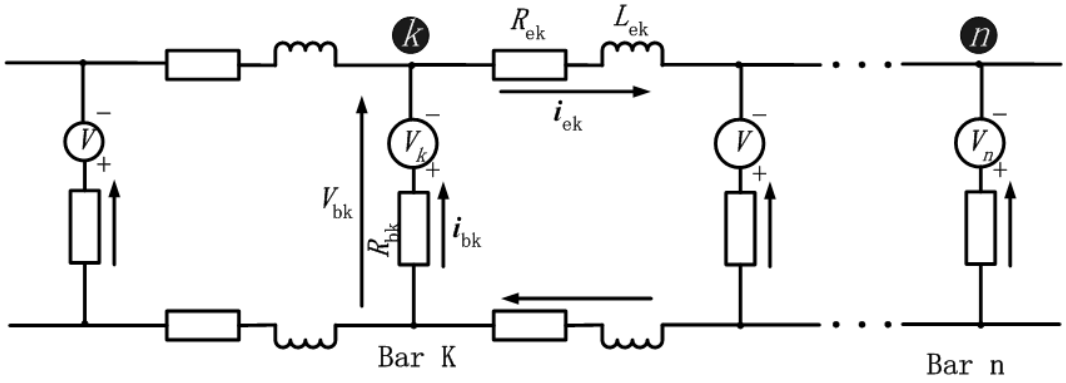

Figure 2.10: Equivalent Circuit of Rotor Cage Bars

Implementing the model of one conductor for each cage bar yields

$$V_{bk} = R_{bk} i_{bk} + \frac{l_{bk}}{s_{bk}} \int \int_{s_{bk}} \frac{\partial A}{\partial t} dx dy \tag{2.42}$$

where l_{bk} is the length of k_{th} bar in $Z-$direction and s_{bk} is the cross section area of the bar.

Applying Kirchoff's current law to each joint $(1, 2, \ldots, k, \ldots, n)$ of cage bars and end rings, we can get:

$$\begin{aligned}
i_{en} \quad &+ \quad i_{b1} - i_{e1} = 0 \\
i_{e1} \quad &+ \quad i_{b2} - i_{e2} = 0 \\
&\vdots \\
i_{e(k-1)} \quad &+ \quad i_{bk} - i_{ek} = 0 \\
&\vdots \\
i_{e(n-1)} \quad &+ \quad i_{bn} - i_{en} = 0
\end{aligned} \tag{2.43}$$

It can also be rewritten as:

$$[i_b] - [C_1][i_e] = 0 \tag{2.44}$$

where

$$[i_b] = \begin{pmatrix} i_{b1} & i_{b2} & \dots & i_{bk} & \dots & i_{bn} \end{pmatrix}^{tr}, \tag{2.45}$$

$$[C_1] = \begin{pmatrix} 1 & \dots & \dots & \dots & \dots & -1 \\ -1 & 1 & \dots & \dots & \dots & \dots \\ \vdots & \vdots & \vdots & \vdots & \vdots & \vdots \\ \dots & \dots & -1 & 1 & \dots & \dots \\ \vdots & \vdots & \vdots & \vdots & \vdots & \vdots \\ \dots & \dots & \dots & \dots & -1 & 1 \end{pmatrix}_{n \times n}, \tag{2.46}$$

$$[i_e] \begin{pmatrix} i_{e1} & i_{e2} & \dots & i_{ek} & \dots & i_{en} \end{pmatrix}^{tr}, \tag{2.47}$$

and '$()^{tr}$' denotes the transpose operation of a matrix.

Applying Kirchoff's voltage law to each loop surrounded by two segments of end rings and two cage bars, we can get:

$$\begin{aligned} V_{b1} &+ 2(R_{e1}i_{e1} + L_{e1}\frac{di_{e1}}{dt}) - V_{b2} = 0 \\ V_{b2} &+ 2(R_{e2}i_{e2} + L_{e2}\frac{di_{e2}}{dt}) - V_{b3} = 0 \\ &\vdots \\ V_{bk} &+ 2(R_{ek}i_{ek} + L_{ek}\frac{di_{ek}}{dt}) - V_{b(k+1)} = 0 \\ &\vdots \\ V_{bn} &+ 2(R_{en}i_{en} + L_{en}\frac{di_{en}}{dt}) - V_{b1} = 0 \end{aligned} \tag{2.48}$$

Putting them in a matrix form yields:

$$[C_2][V_b] + 2\{[R_e] + \frac{d}{dt}[L_e]\}[i_e] = 0 \tag{2.49}$$

where

$$[C_2] = \begin{pmatrix} 1 & -1 & \dots & \dots & \dots & \dots \\ \dots & 1 & -1 & \dots & \dots & \dots \\ \vdots & \vdots & \vdots & \vdots & \vdots & \vdots \\ \dots & \dots & \dots & 1 & -1 & \dots \\ \vdots & \vdots & \vdots & \vdots & \vdots & \vdots \\ -1 & \dots & \dots & \dots & \dots & 1 \end{pmatrix}_{n \times n}, \tag{2.50}$$

$$[V_b] = \begin{pmatrix} V_{b1} & V_{b2} & \dots & V_{bk} & \dots & V_{bn} \end{pmatrix}^{tr}, \tag{2.51}$$

$$[R_e] = \begin{pmatrix} R_{e1} & R_{e2} & \dots & R_{ek} & \dots & R_{en} \end{pmatrix}^{tr}, \tag{2.52}$$

$$[L_e] = \begin{pmatrix} L_{e1} & L_{e2} & \dots & L_{ek} & \dots & L_{en} \end{pmatrix}^{tr}. \tag{2.53}$$

Equations (2.42), (2.44) and (2.49) are three governing equations for the modelling of cage bars. They cover the whole solution domain of the rotor cage bars.

Electric machines are geometrically symmetrical devices. With the intention of saving computational efforts, usually only part of the problem domain is used in the numerical computation. Under this condition, equations (2.44) and (2.49) will have different formats. The main difference lies in the format of matrices $[C_1]$ and $[C_2]$. If there are only $n_p (n_p \leq n)$ bars involved in the computation, the current and voltage of bar n_p and bar n have the following relationships,

$$\begin{aligned} i_{en_p} &= \delta \cdot i_{en} \\ i_{bn_p} &= \delta \cdot i_{bn} \\ V_{bn_p} &= \delta \cdot V_{bn} \end{aligned} \tag{2.54}$$

where $\delta = 1$ or $\delta = -1$. The value of δ depends on how many poles are included in the computation domain. Two cases are illustrated below:

(1) Pairs of poles are included in the computation domain

The cage bars over pairs of poles pitch have identical currents and voltages. Therefore if the domain to be investigated spans over pairs of poles in electric machine, $\delta = 1$. Under this condition, equation (2.43) becomes

$$\begin{aligned} i_{en_p} &+ i_{b1} - i_{e1} = 0 \\ i_{e1} &+ i_{b2} - i_{e2} = 0 \\ &\vdots \\ i_{e(k-1)} &+ i_{bk} - i_{ek} = 0 \\ &\vdots \\ i_{e(n_p-1)} &+ i_{bn_p} - i_{en_p} = 0 \end{aligned} \tag{2.55}$$

or

$$[i_{bp}] - [C_{1p}][i_{e_p}] = 0 \tag{2.56}$$

where

$$[i_{bp}] = \begin{pmatrix} i_{b1} & i_{b2} & \dots & i_{bk} & \dots & i_{bn_p} \end{pmatrix}^{tr}, \tag{2.57}$$

$$[C_{1p}] = \begin{pmatrix} 1 & \dots & \dots & \dots & \dots & -1 \\ -1 & 1 & \dots & \dots & \dots & \dots \\ \vdots & \vdots & \vdots & \vdots & \vdots & \vdots \\ \dots & \dots & -1 & 1 & \dots & \dots \\ \vdots & \vdots & \vdots & \vdots & \vdots & \vdots \\ \dots & \dots & \dots & \dots & -1 & 1 \end{pmatrix}_{n_p \times n_p}, \tag{2.58}$$

$$[i_{ep}] = \begin{pmatrix} i_{e1} & i_{e2} & \dots & i_{ek} & \dots & i_{en_p} \end{pmatrix}^{tr}. \tag{2.59}$$

Similarly substituting equation (2.54) into equation (2.48) when $\delta = 1$ yields,

$$\begin{aligned}
V_{b1} &+ 2(R_{e1}i_{e1} + L_{e1}\frac{di_{e1}}{dt}) - V_{b2} = 0 \\
V_{b2} &+ 2(R_{e2}i_{e2} + L_{e2}\frac{di_{e2}}{dt}) - V_{b3} = 0 \\
&\vdots \\
V_{bk} &+ 2(R_{ek}i_{ek} + L_{ek}\frac{di_{ek}}{dt}) - V_{b(k+1)} = 0 \\
&\vdots \\
V_{bn_p} &+ 2(R_{en_p}i_{en_p} + L_{en_p}\frac{di_{en_p}}{dt}) - V_{b1} = 0
\end{aligned} \tag{2.60}$$

or

$$[C_{2p}][V_{bp}] + 2\{[R_{ep}] + \frac{d}{dt}[L_{ep}]\}[i_{ep}] = 0 \tag{2.61}$$

where

$$[C_{2p}] = \begin{pmatrix} 1 & -1 & \dots & \dots & \dots & \dots \\ \dots & 1 & -1 & \dots & \dots & \dots \\ \vdots & \vdots & \vdots & \vdots & \vdots & \vdots \\ \dots & \dots & \dots & 1 & -1 & \dots \\ \vdots & \vdots & \vdots & \vdots & \vdots & \vdots \\ -1 & \dots & \dots & \dots & \dots & 1 \end{pmatrix}_{n_p \times n_p}, \tag{2.62}$$

$$[V_{bp}] = \begin{pmatrix} V_{b1} & V_{b2} & \dots & V_{bk} & \dots & V_{bn_p} \end{pmatrix}^{tr}, \tag{2.63}$$

$$[R_{ep}] = \begin{pmatrix} R_{e1} & R_{e2} & \dots & R_{ek} & \dots & R_{en_p} \end{pmatrix}^{tr}, \tag{2.64}$$

$$[L_{ep}] = \begin{pmatrix} L_{e1} & L_{e2} & \dots & L_{ek} & \dots & L_{en_p} \end{pmatrix}^{tr}. \tag{2.65}$$

(2) Odd number of poles are included in the computation domain

On the other hand, the cage bars over one-pole pitch have equivalent current and voltage in magnitude but in opposite direction. So if the domain to be investigated spans over one pole in electric machine, $\delta = -1$ for equation (2.54). Equation

(2.43) becomes

$$\begin{aligned} -i_{en_p} &+ i_{b1} - i_{e1} = 0 \\ i_{e1} &+ i_{b2} - i_{e2} = 0 \\ &\vdots \\ i_{e(k-1)} &+ i_{bk} - i_{ek} = 0 \\ &\vdots \\ i_{e(n_p-1)} &+ i_{bn_p} - i_{en_p} = 0 \end{aligned} \tag{2.66}$$

and matrix $[C_{1p}]$ becomes

$$[C_{1p}] = \begin{pmatrix} 1 & \dots & \dots & \dots & \dots & +1 \\ -1 & 1 & \dots & \dots & \dots & \dots \\ \vdots & \vdots & \vdots & \vdots & \vdots & \vdots \\ \dots & \dots & -1 & 1 & \dots & \dots \\ \vdots & \vdots & \vdots & \vdots & \vdots & \vdots \\ \dots & \dots & \dots & \dots & -1 & 1 \end{pmatrix}_{n_p \times n_p} . \tag{2.67}$$

Similarly equation (2.48) becomes

$$\begin{aligned} V_{b1} &+ 2(R_{e1}i_{e1} + L_{e1}\frac{di_{e1}}{dt}) - V_{b2} = 0 \\ V_{b2} &+ 2(R_{e2}i_{e2} + L_{e2}\frac{di_{e2}}{dt}) - V_{b3} = 0 \\ &\vdots \\ V_{bk} &+ 2(R_{ek}i_{ek} + L_{ek}\frac{di_{ek}}{dt}) - V_{b(k+1)} = 0 \\ &\vdots \\ -V_{bn_p} &+ 2(R_{en_p}i_{en_p} + L_{en_p}\frac{di_{en_p}}{dt}) - V_{b1} = 0 \end{aligned} \tag{2.68}$$

and matrix $[C_{2p}]$ becomes

$$[C_{2p}] = \begin{pmatrix} 1 & -1 & \dots & \dots & \dots & \dots \\ \dots & 1 & -1 & \dots & \dots & \dots \\ \vdots & \vdots & \vdots & \vdots & \vdots & \vdots \\ \dots & \dots & \dots & 1 & -1 & \dots \\ \vdots & \vdots & \vdots & \vdots & \vdots & \vdots \\ +1 & \dots & \dots & \dots & \dots & 1 \end{pmatrix}_{n_p \times n_p} . \tag{2.69}$$

In summary, matrices $[C_1]$ and $[C_2]$ are:

$$[C_1] = \begin{pmatrix} 1 & \dots & \dots & \dots & \dots & \mp 1 \\ -1 & 1 & \dots & \dots & \dots & \dots \\ \vdots & \vdots & \vdots & \vdots & \vdots & \vdots \\ \dots & \dots & \dots & -1 & 1 & \dots \\ \vdots & \vdots & \vdots & \vdots & \vdots & \vdots \\ \dots & \dots & \dots & \dots & -1 & 1 \end{pmatrix}_{n_p \times n_p} , \tag{2.70}$$

$$[C_2] = \begin{pmatrix} 1 & -1 & \dots & \dots & \dots & \dots \\ \dots & 1 & -1 & \dots & \dots & \dots \\ \vdots & \vdots & \vdots & \vdots & \vdots & \vdots \\ \dots & \dots & \dots & 1 & -1 & \dots \\ \vdots & \vdots & \vdots & \vdots & \vdots & \vdots \\ \mp 1 & \dots & \dots & \dots & \dots & 1 \end{pmatrix}_{n_p \times n_p} , \tag{2.71}$$

where $n_p (n_p \leq n)$ is the number of cage bars in the computation domain. If the domain to be investigated spans over one pair of poles in electric machine, the signs '$\mp$' in equations (2.70) and (2.71) should be '-'. If the studied domain covers odd number of poles, then the signs should be '+'.

2.4.4 Modelling of External Circuit Components

A suitable simulation of the behavior of the machines and drives should take into account the numerical models of electrical, electronic circuit and electromagnetic fields. In the modelling of electronic circuits, the main difficulties lie in the modelling of transistors, diodes and other active nonlinear semiconductor devices. The method proposed by F. Piriou and A. Razek [65, 66] could be used to get the simultaneous solution of the field equations and equations of the circuits with nonlinear semiconductor elements. This method basically is an application of Newton-Raphson algorithm to both the magnetic core nonlinearity and the nonlinearity of the semiconductor components. A. Demenko [67] simplified the method and approximated the volt-ampere characteristics (the nonlinearity) of semiconductor

components by piecewise linear functions. By using this simplified method, the calculation time can be reduced to some extent, but this method is still not easy to apply in computation because the nonlinearities of the semiconductors are included to some extent. For high voltage machines the semiconductor voltage drops are not very significant compared to line voltages, and as such these components can be simplified as linear elements in modelling.

Generally, the semiconductor components(transistors and diodes) can be simulated in the switching mode as they are operated in the power electronics controllers. The model of a diode is shown in Fig. 2.11.

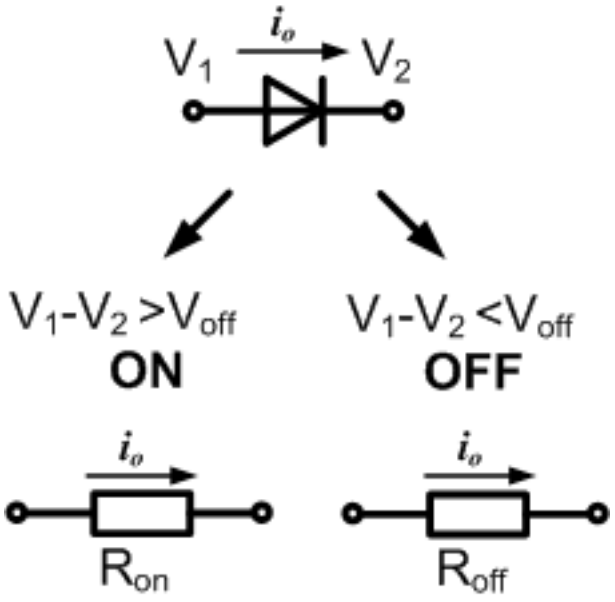

Figure 2.11: Representation of a Diode

The working behaviours of diodes are either forward biased or reverse biased. For an ideal diode we can take the forward bias (diode is 'ON') as a short circuit operation and the reverse bias (diode is 'OFF') as an open circuit operation. In reality the diode has offset voltage and a resistance for forward bias [68]. Therefore the operations of a diode can be modelled in terms of the offset voltage V_{off} and a resistance. As shown in Fig. 2.11, a resistance R_{on} is considered as the resistance

of the diode for forward bias and a resistance R_{off} with sufficient high value to simulate the reverse bias operation. The diode switches into conduction when the applied voltage $(V_1 - V_2)$ exceeds the offset voltage V_{off} otherwise it reverts to the blocking states.

This is a suitable model to simulate the diodes because the instants of commutation are determined by function of the behaviour of the electric circuit. We do not have to impose the instants of commutation.

The model of a transistor is shown in Fig. 2.12. The output performance of a transistor is the relation of i_c with V_{CE} under switching signal V_{GE}. If $V_{GE} > 0$, the transistor is 'ON'; while $V_{GE} < 0$, the transistor is 'OFF'. A low resistance value R_{on} is used to simulate the conduction state and a sufficient high resistance value R_{off} is used when it is blocked. The switching signals V_{GE} is determined by the control strategy.

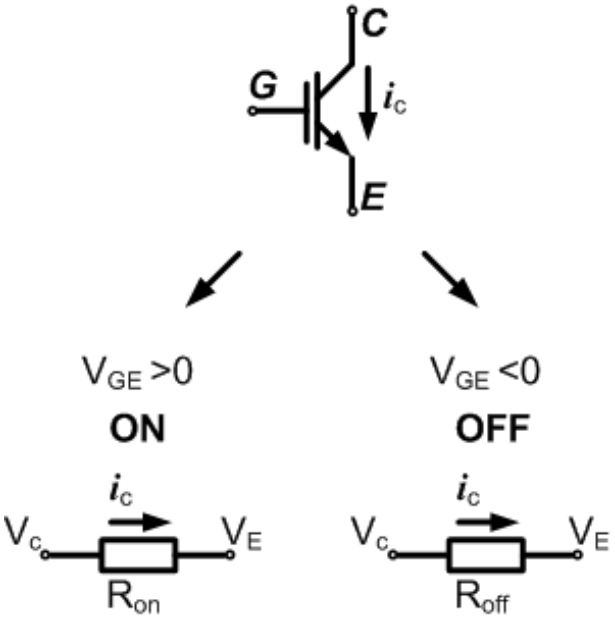

Figure 2.12: Representation of a Transistor

In power application, most of the external circuits connected to electric machines consist of mainly semiconductor components, resistors (R), inductors (L) and capacitors (C). Now with the semiconductor components being modelled as resistors, the external circuits can be simplified as $R-L-C$ circuits only.

As shown in Fig. 2.13, the external circuits can be represented by several branches of circuits made up by resistors, inductors or capacitors. Each branch has terminal voltages V_{in} and V_{out}. A current i_{sb} flows through the branch. In the part of electric machine, the terminal voltages of phases are represented by V_{t1}, V_{t2} and V_{t3}. The line currents are i_{l1}, i_{l2} and i_{l3}. The governing equations for different types of branches are:

- for resistor,

$$R_{sb}i_{sb} = V_{in} - V_{out}; \tag{2.72}$$

- for inductor,

$$L_{sb}\frac{di_{sb}}{dt} = V_{in} - V_{out}; \tag{2.73}$$

- for capacitor,

$$i_{sb} = C_{sb}(\frac{dV_{in}}{dt} - \frac{dV_{out}}{dt}); \tag{2.74}$$

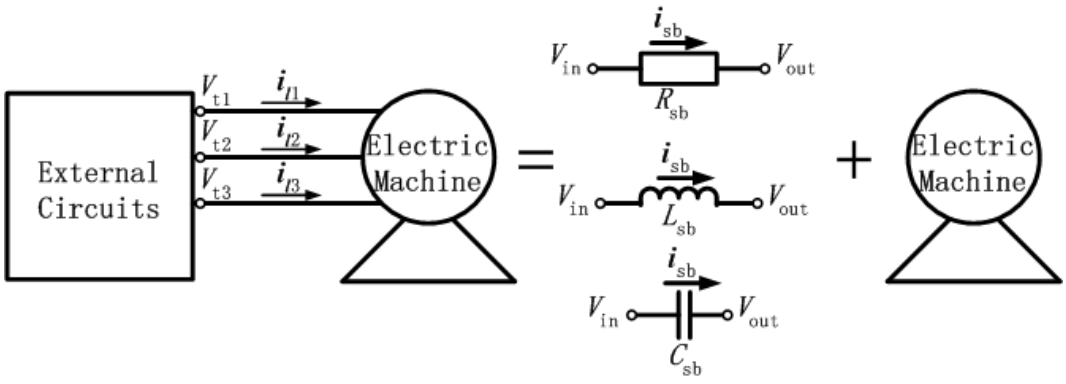

Figure 2.13: Representation of a Machine Connected with External Circuits

In forming the circuits all the branches are connected by joints in series or in parallel, as shown in Fig. 2.14. Therefore the governing equation for external circuits is:

$$\{[R_{sb}] + \frac{d}{dt}[L_{sb}]\}[i_{sb}] + [C_{sb}]\frac{d}{dt}[V_{sb}; V_t] = 0 \tag{2.75}$$

where i_{sb} is the current flowing in all the branches of the external circuits

$$[i_{sb}] = \begin{pmatrix} i_{sb1} & i_{sb2} & \dots & i_{sbk} & \dots & i_{sbM} \end{pmatrix}^{tr}, \tag{2.76}$$

V_{sb} is the terminal voltages of all the joints in the external circuits

$$[V_{sb}] = \begin{pmatrix} V_1 & V_2 & \dots & V_k & \dots & V_M \end{pmatrix}^{tr}, \tag{2.77}$$

V_t is the terminal voltages of the electric machine

$$[V_t] = \begin{pmatrix} V_{t1} & V_{t2} & V_{t3} \end{pmatrix}^{tr} \tag{2.78}$$

and M is the total number of joints in the external circuits.

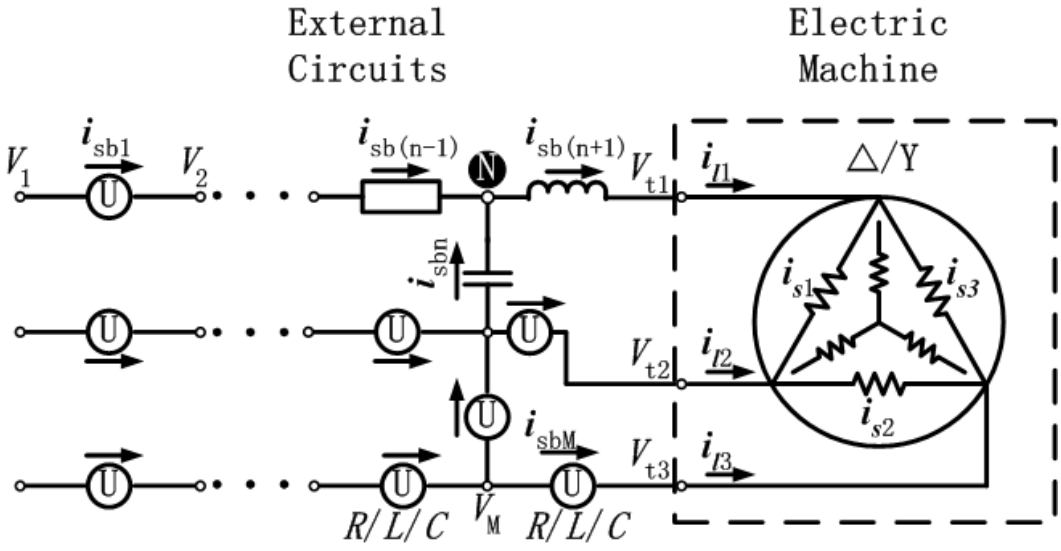

Figure 2.14: Circuits Description of a Machine Connected with External Circuits

For each joint in the circuit, Kirchoff's current law is applied. For example, for joint 'N' in Fig. 2.14, the current equation is:

$$i_{sb(n-1)} + i_{sbn} - i_{sb(n+1)} = 0. \tag{2.79}$$

The current equations for the whole circuit are:

$$[C_3][i_{sb}] + [C_4][i_s] = 0 \tag{2.80}$$

where $[i_s]$ is the stator phase currents

$$[i_s] = \begin{pmatrix} i_{s1} & i_{s2} & i_{s3} \end{pmatrix}^{tr}, \tag{2.81}$$

$[C_3]$ is the coefficient matrix decided by the structure of the external circuits and $[C_4]$ is the coefficient matrix decided by the '$\triangle$' or 'Y' connection of stator phase winding.

2.5 Equation of Motion

Rotating electric machines are one kind of electromagnetic devices for electro-mechanical energy conversion. Normally the electric machines have two fundamental parts: the stator that is fixed and the rotor that is rotating mechanically. The movement of the rotor is determined by the electromagnetic forces originated from the interaction between the electromagnetic field in the air gap and the currents. The positions of rotor is changed continuously with the movement, which in turn affects the electromagnetic field within the machine. Therefore a complete analysis of electric machine should take into account the dynamic mechanical movement of the rotor.

The analysis of electric machines involves the continuous movement of the rotor, which is governed by:

$$J_r \frac{d\omega_m}{dt} = T_{em} - T_L - B_f \omega_m, \tag{2.82}$$

$$\frac{d\theta_m}{dt} = \omega_m \tag{2.83}$$

where

$J_r =$ the moment of inertia of the rotor

$\theta_m =$ the rotor position

$\omega_m =$ the mechanical motor speed

$T_{em} =$ the electromagnetic torque

$T_L =$ the applied load torque

$B_f =$ the coefficient of friction

For a particular machine, J_r and B_f are taken as constants. The value of T_L is decided by the loading conditions of the machine. Equations (2.82) and (2.83) are time-dependent. The values of θ_m, ω_m and T_{em} vary with the instants of time.

2.6 Conclusion

This chapter presented the modelling of electric machines with coupled circuits and motion. The governing equations for the magnetic field, the circuits and the motion are summarized below:

- The field equation,

$$\frac{\partial}{\partial x}(\nu \frac{\partial A}{\partial x}) + \frac{\partial}{\partial y}(\nu \frac{\partial A}{\partial y}) = \sigma \frac{\partial A}{\partial t} - \sigma \frac{V_{tz}}{l} - \nabla \times (\nu \mu_0 M_r)$$

- Stator phase equation,

$$V_s = R_s i_s + L_e \frac{di_s}{dt} + \frac{l}{ms}\left(\int\int_{\Omega^+} \frac{\partial A}{\partial t} dxdy - \int\int_{\Omega^-} \frac{\partial A}{\partial t} dxdy\right)$$

- Equations for cage bars,

$$V_{bk} = R_{bk} i_{bk} + \frac{l_{bk}}{s_{bk}} \int\int_{s_{bk}} \frac{\partial A}{\partial t} dxdy$$

$$[i_b] - [C_1][i_e] = 0$$

$$[C_2][V_b] + 2\{[R_e] + \frac{d}{dt}[L_e]\}[i_e] = 0$$

- Equations for external circuits,

$$\{[R_{sb}] + \frac{d}{dt}[L_{sb}]\}[i_{sb}] + [C_{sb}]\frac{d}{dt}[V_{sb}; V_t] = 0$$

$$[C_3][i_{sb}] + [C_4][i_s] = 0$$

- Equations for mechanical motion,

$$\begin{aligned} J_r \frac{d\omega_m}{dt} &= T_{em} - T_f - B_f \omega_m, \\ \frac{d\theta_m}{dt} &= \omega_m \end{aligned}$$

Formulation of finite element computational procedures is based on the simultaneous solutions of these sets of equations. Detailed account of numerical analysis are presented in the following chapters.

Chapter 3

Finite Element Analysis of Line-Start Permanent Magnet Synchronous Machines With Coupled Circuits and Motion

3.1 Introduction

Finite element method is a numerical tool used in solving partial differential equations in a given domain including the boundary conditions. Variational principle or the method of weighted residuals is used to derive the finite element equations [8]. The fundamental concept of the method is to divide the problem domain into a number of small subregions or elements. The unknown field values are approximated in those elements by simple shape functions, mostly linear or quadratic. After the finite element formulation of governing equation in each element and the assembly of all the elements, a large linear system of equations is generated. The solution to this system of equations gives the field values of the whole problem domain. Compared with other numerical methods, the main advantages of finite element methods are its flexibility for modelling complex geometries, the capability of handling nonlinearities and eddy currents, easy implementation and stable solutions.

In general, the following steps are involved in the finite element method:

- Define the problem of interest by partial differential equations;
- Subdivide the problem field region into many small subregions;
- Choose the interpolation function in terms of the nodal vales of the elements;
- Derive the finite element equations within each element in terms of energy-related functions or weighted residual expressions;
- Assembly of the element equations and the global system of equations is generated;
- Impose boundary conditions;
- Solve the global system of equations with appropriate methods;
- Convert the field solutions to useful design quantities.

When the finite element field analysis is coupled with the circuit analysis and the mechanical motion, the following steps should also be included:

- the discretization of equations in time domain;
- the combination of field equations with the circuit equations;
- the simulation of the rotor motion.

3.2 Summary of the Equations

Finite element analysis of electric machines is based on the proper definition or the modelling of the problem. A complete model of an electric machine should include:
(1) the electromagnetic field,
(2) the circuits that transfer the external power to the field,

(3) the motion of rotor that have interaction with the field.

The governing equations for the field, circuit and motion have been derived in Chapter 2 and they are listed as follows:

- The field equation,

$$\frac{\partial}{\partial x}(\nu\frac{\partial A}{\partial x})+\frac{\partial}{\partial y}(\nu\frac{\partial A}{\partial y})=\sigma\frac{\partial A}{\partial t}-\sigma\frac{V_{tz}}{l}-\nabla\times(\nu\mu_0 M_r) \tag{3.1}$$

- Stator phase equation,

$$V_s=R_s i_s+L_e\frac{di_s}{dt}+\frac{l}{ms}(\int\int_{\Omega^+}\frac{\partial A}{\partial t}dxdy-\int\int_{\Omega^-}\frac{\partial A}{\partial t}dxdy) \tag{3.2}$$

- Equations for cage bars,

$$V_{bk}=R_{bk}i_{bk}+\frac{l_{bk}}{s_{bk}}\int\int_{s_{bk}}\frac{\partial A}{\partial t}dxdy \tag{3.3}$$

$$[i_b]-[C_1][i_e]=0 \tag{3.4}$$

$$[C_2][V_b]+2\{[R_e]+\frac{d}{dt}[L_e]\}[i_e]=0 \tag{3.5}$$

- Equations for external circuits,

$$\{[R_{sb}]+\frac{d}{dt}[L_{sb}]\}[i_{sb}]+[C_{sb}]\frac{d}{dt}[V_{sb};V_t]=0 \tag{3.6}$$

$$[C_3][i_{sb}]+[C_4][i_s]=0 \tag{3.7}$$

- Equations for mechanical motion,

$$J_r\frac{d\omega_m}{dt} = T_{em}-T_f-B_f\omega_m, \tag{3.8}$$

$$\frac{d\theta_m}{dt} = \omega_m \tag{3.9}$$

Equations (3.1)-(3.3) are directly field-dependent. Finite element formulations of these equations are needed. Equations (3.4)-(3.9) are indirectly related to the field values. Therefore they can be taken as constraints and finite element formulations are unnecessary.

3.3 Domain Discretization

To discretize the domain into subregions (finite elements) is the first step in finite element method. The shapes, sizes and the configurations of the elements may vary, but a few important points must be taken into consideration during the mesh generation process:

(a) the nodes should be placed within the region and on the boundary of the field domain;

(b) the density of the nodes should be high in those areas where the field varies rapidly and the elements could be large while the field is uniform;

(c) the elements cannot overlap meanwhile no empty spaces can be left;

(d) for a region composed of different materials, the separating lines should be represented by the boundaries of elements;

(e) in order to reduce the storage and bandwidth of the resultant global matrix, the numbering of the nodes should be optimized [69].

There are many types and shapes of elements that can be used for the discretization of a domain. Fig. 3.1 shows some two and three dimensional finite elements. In the two-dimensional electromagnetic field analysis of electric machines, triangular elements are usually used. The best in triangular elements are the free topology irregular triangular meshes. Any complicated geometry can finally be represented without any undue mathematical complexity [9]. Because of their shapes, triangular elements are one of the most suitable class of elements which can represent accurately a very complicated machine geometry. This type of element has been used extensively in the analysis of electric machine problems [18, 19, 20, 64].

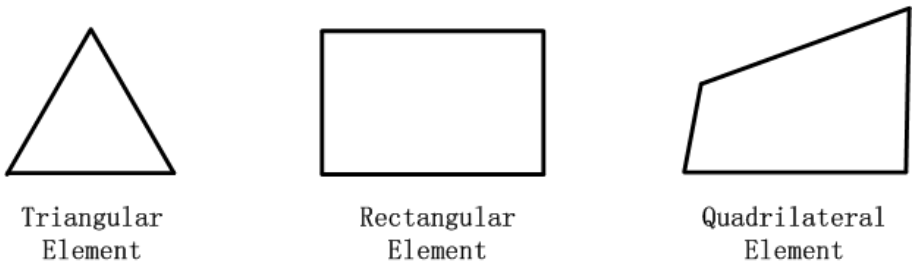

(a) Two-dimensional elements

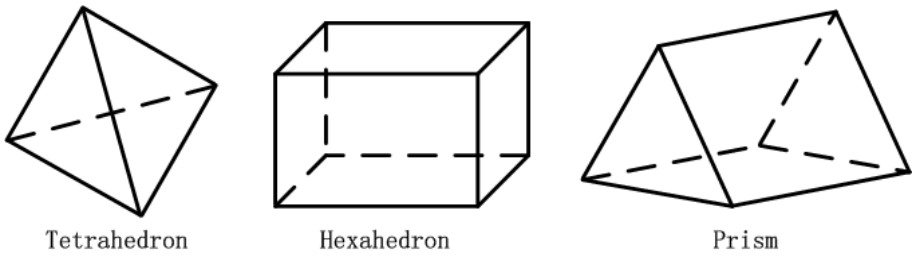

(b) Three-dimensional elements

Figure 3.1: Some of the Widely Used Elements in Domain Discretization

Mesh generation is one of the most time-consuming problems encountered when using finite element method. To overcome this problem, automatic mesh generation has been proposed for producing meshes for any geometry without user intervention [70]. The principal object we use automatic mesh generation is to achieve good-quality meshes which is essential for accurate solutions. In this work the pre-processer of commercial software FLUX2D [35] is used to do the mesh generation.

3.4 The Choice of Shape Functions

Once the problem domain has been discretized into finite elements, a trial function is used to approximate the behaviour of the field quantities within the element. Usually a polynomial function is chosen because it is easy to differentiate and integrate polynomials. For two-dimensional field problems, a complete n^{th} order

polynomial may be written as:

$$f = a_0 + a_1 x + a_2 y + a_3 xy + a_4 x^2 + a_5 y^2 + \ldots + a_m y^n \tag{3.10}$$

where

$$\begin{aligned} n &= && \text{the order of the polynomial} \\ m = \tfrac{(n+1)(n+2)}{2} &= && \text{the total number of coefficients in the expansion} \end{aligned}$$

The terms in a complete two-dimensional polynomial may be conveniently determined by referring to the Pascal triangle [71] which is shown in Fig. 3.2.

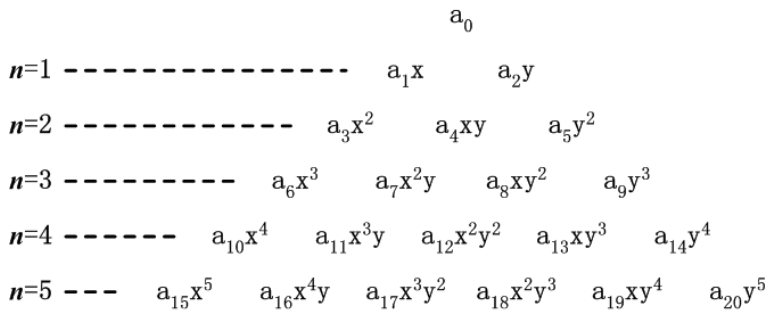

Figure 3.2: Pascal Triangle of Polynomial Expansion

In Fig. 3.2, only the expansion for highest order of $n = 5$ is given. It can be extended to any higher order also. For the same size of mesh, the higher order polynomials are expected to yield better accuracy.

For a first-order triangular element shown in Fig. 3.3, the corresponding linear interpolation function for the magnetic vector potential in the element can be expressed as:

$$\hat{A}(x, y) = k_0 + k_1 x + k_2 y \tag{3.11}$$

where k_0, k_1 and k_2 are constant coefficients to be determined.

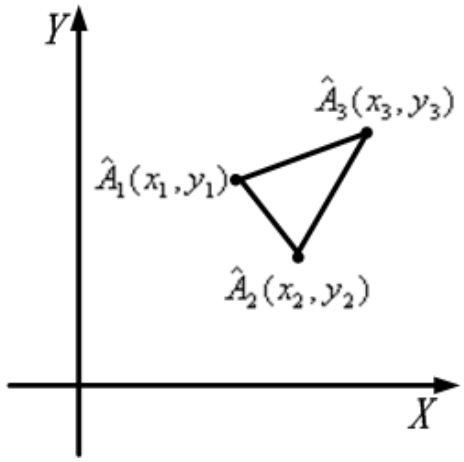

Figure 3.3: A Typical Triangular Element in the $X - Y$ Plane

Relating the coefficients of equation (3.11) to the potentials at the 3 element nodes, we can get:

$$\begin{pmatrix} k_0 \\ k_1 \\ k_2 \end{pmatrix} = \begin{pmatrix} 1 & x_1 & y_1 \\ 1 & x_2 & y_2 \\ 1 & x_3 & y_3 \end{pmatrix}^{-1} \begin{pmatrix} \hat{A}_1 \\ \hat{A}_2 \\ \hat{A}_3 \end{pmatrix}. \tag{3.12}$$

Substituting equation (3.12) into equation (3.11), the interpolating function of $\hat{A}$ in terms of values of $\hat{A}_i (i = 1, 2, 3)$ at the nodes can be obtained as:

$$\hat{A}(x, y) = N_1 \hat{A}_1 + N_2 \hat{A}_2 + N_3 \hat{A}_3 = \sum_{i=1}^{3} N_i \hat{A}_i \tag{3.13}$$

where

$$\begin{aligned} N_1 &= \frac{1}{2\Delta}(a_1 + b_1 x + c_1 y) \\ N_2 &= \frac{1}{2\Delta}(a_2 + b_2 x + c_2 y) \\ N_3 &= \frac{1}{2\Delta}(a_3 + b_3 x + c_3 y) \end{aligned} \tag{3.14}$$

are the shape functions, Δ is the area of the triangular element which is given by

$$\Delta = \frac{1}{2} \begin{vmatrix} 1 & x_1 & y_1 \\ 1 & x_2 & y_2 \\ 1 & x_3 & y_3 \end{vmatrix} \tag{3.15}$$

and

$$a_1 = x_2y_3 - y_2x_3; \quad a_2 = x_3y_1 - y_3x_1; \quad a_3 = x_1y_2 - y_1x_2;$$

$$b_1 = y_2 - y_3; \qquad b_2 = y_3 - y_1; \qquad b_3 = y_1 - y_2;$$

$$c_1 = x_3 - x_2; \qquad c_2 = x_1 - x_3; \qquad c_3 = x_2 - x_1;$$

In the two dimensional finite element analysis, the magnetic vector potential A has only invariant z-directed components in the x, y, z-coordinates. Therefore we can get

$$A = A_z. \tag{3.16}$$

Since the flux density is the derivative of the vector potential

$$B = \nabla \times A = \begin{vmatrix} \hat{x} & \hat{y} & \hat{z} \\ \frac{\partial}{\partial x} & \frac{\partial}{\partial y} & \frac{\partial}{\partial z} \\ 0 & 0 & A_z \end{vmatrix} = \frac{\partial A_z}{\partial y} \cdot \hat{x} - \frac{\partial A_z}{\partial x} \cdot \hat{y}, \tag{3.17}$$

Combination of equations (3.16) and (3.17) yields:

$$B_x = \frac{\partial A}{\partial y} \tag{3.18}$$

$$B_y = -\frac{\partial A}{\partial x}. \tag{3.19}$$

Substituting equation (3.13) into equations (3.18) and (3.19) yields the x and y components of flux density

$$B_x = \frac{1}{2\Delta}(b_1\hat{A}_1 + b_2\hat{A}_2 + b_3\hat{A}_3) \tag{3.20}$$

$$B_y = -\frac{1}{2\Delta}(c_1\hat{A}_1 + c_2\hat{A}_2 + c_3\hat{A}_3) \tag{3.21}$$

From equations (3.20) and (3.21), we can see that the flux density is constant within each element.

3.5 Deriving Finite Element Equations Based on the Method of Weighted Residuals

When the unknown field quantities of equation (3.1)-(3.3) are substituted by the approximate function $\hat{A} = \sum_{i=1}^{3} N_i \hat{A}_i$ in each element, the residual R or an error of approximation is unavoidable. For example, for field equation (3.1), the residual is

$$R = \frac{\partial}{\partial x}(\nu \frac{\partial \hat{A}}{\partial x}) + \frac{\partial}{\partial y}(\nu \frac{\partial \hat{A}}{\partial y}) - \sigma \frac{\partial \hat{A}}{\partial t} + \sigma \frac{V_{tz}}{l} + \nabla \times (\nu \mu_0 M_r) \tag{3.22}$$

If the residual R in the whole domain tends to zero, the $\hat{A}$ can be regarded as an acceptable approximate solution. There are several principle of error minimization, such as principle of weighted residuals [72], orthogonal projection principle [73] and variational principle [72, 74]. In numerical methods the most often used ones are the principle of weighted residuals or the variational principle. The variational method is based on the equivalent functional of the governing equation. The weighted residual approach is based on the operator equation directly. Although these two principles are based on different starting equations, they yield the same set of equations. The principle of weighted residual can be used for all numerical methods. Based on the choice of weighting functions, shape functions and the approach to discretization, different methods are formulated, including sub-domain method, collocation method, Galerkin's method and least-square method [75]. The most often used method for deriving finite element equations is the Galerkin's method.

The method of weighted residual involves finding the unknown parameters contained in the approximate solution such that the residual is as close to zero as possible. This usually means determining the parameters such that some weighted integral of the residual over the whole problem domain is zero. For our problem,

one would require that,

$$\int\int_{\Omega} WRdxdy = 0. \tag{3.23}$$

where

$W =$ the weighting function

$\Omega =$ the area of the whole domain

This surface integral may be broken into summations over small areas. The whole domain is replaced with small sub-domains so called finite elements, and integration can easily be performed over the individual elements. Therefore we can get

$$\int\int_{\Omega} WRdxdy = \sum_{e=1}^{M} \int\int_{\Omega_e} [W^e]R^e dxdy = 0. \tag{3.24}$$

where

$M =$ the number of finite element in the domain

$\Omega_e =$ the area of one individual element

$[W^e] =$ the weighting function of one individual element

$R^e =$ the residual of one one individual element

According to the principle of the Galerkin's method, the weighting functions are chosen to be the same as the shape functions

$$[W^e] = [N_i^e] = \begin{bmatrix} N_1 \\ N_2 \\ N_3 \end{bmatrix}. \tag{3.25}$$

3.5.1 Finite Element Formulation of Field Equations

The residual of field equation given in equation (3.22) and the combination of equations (3.22)-(3.25) leads to the integral equation for individual element

$$\begin{aligned}\int\int_{\Omega_e}[W^e]R^e dxdy &= \int\int_{\Omega_e}[N_i^e][\frac{\partial}{\partial x}(\nu\frac{\partial\hat{A}}{\partial x})+\frac{\partial}{\partial y}(\nu\frac{\partial\hat{A}}{\partial y})-\sigma\frac{\partial\hat{A}}{\partial t}+\sigma\frac{V_{tz}}{l} \\ &\quad +\nabla\times(\nu\mu_0 M_r)]dxdy \\ &= \int\int_{\Omega_e}[N_i^e][\frac{\partial}{\partial x}(\nu\frac{\partial\hat{A}}{\partial x})+\frac{\partial}{\partial y}(\nu\frac{\partial\hat{A}}{\partial y})]dxdy \\ &\quad -\int\int_{\Omega_e}[N_i^e](\sigma\frac{\partial\hat{A}}{\partial t})dxdy \\ &\quad +\int\int_{\Omega_e}[N_i^e](\sigma\frac{V_{tz}}{l})dxdy \\ &\quad +\int\int_{\Omega_e}[N_i^e][\nabla\times(\nu\mu_0 M_r)]dxdy \\ &= 0. \end{aligned} \tag{3.26}$$

Equation (3.26) has four terms. The integration of these four terms gives the element matrix equation for field equation (3.1).

(a) Integration of the first term of equation (3.26) $\int\int_{\Omega_e}[N_i^e][\frac{\partial}{\partial x}(\nu\frac{\partial\hat{A}}{\partial x})+\frac{\partial}{\partial y}(\nu\frac{\partial\hat{A}}{\partial y})]dxdy$

Integrating the first term by parts,

$$\int\int_{\Omega_e}[N_i^e][\frac{\partial}{\partial x}(\nu\frac{\partial\hat{A}}{\partial x})+\frac{\partial}{\partial y}(\nu\frac{\partial\hat{A}}{\partial y})]dxdy = \oint_\Gamma \nu[N_i^e]\frac{\partial\hat{A}}{\partial n}d\Gamma-\int\int_{\Omega_e}\nu(\frac{\partial[N_i^e]}{\partial x}\frac{\partial\hat{A}}{\partial x}+\frac{\partial[N_i^e]}{\partial y}\frac{\partial\hat{A}}{\partial y})dxdy. \tag{3.27}$$

The line integral in equation (3.27) is only employed over elements which have a side common with the boundary Γ. By imposing the natural boundary condition, i.e., $\frac{\partial\hat{A}}{\partial n}=0$, this integral is vanished. Then equation (3.27) becomes

$$\int\int_{\Omega_e}[N_i^e][\frac{\partial}{\partial x}(\nu\frac{\partial\hat{A}}{\partial x})+\frac{\partial}{\partial y}(\nu\frac{\partial\hat{A}}{\partial y})]dxdy = -\int\int_{\Omega_e}\nu(\frac{\partial[N_i^e]}{\partial x}\frac{\partial\hat{A}}{\partial x}+\frac{\partial[N_i^e]}{\partial y}\frac{\partial\hat{A}}{\partial y})dxdy. \tag{3.28}$$

Recalling equations (3.13), (3.14) and (3.25), the partial derivatives of $[N_i^e]$ and $\hat{A}$ with respect to x, y are

$$\frac{\partial[N_i^e]}{\partial x} = \begin{bmatrix} \frac{\partial N_1}{\partial x} \\ \frac{\partial N_2}{\partial x} \\ \frac{\partial N_3}{\partial x} \end{bmatrix} = \frac{1}{2\Delta} \begin{bmatrix} b_1 \\ b_2 \\ b_3 \end{bmatrix}, \tag{3.29}$$

$$\frac{\partial[N_i^e]}{\partial y} = \begin{bmatrix} \frac{\partial N_1}{\partial y} \\ \frac{\partial N_2}{\partial y} \\ \frac{\partial N_3}{\partial y} \end{bmatrix} = \frac{1}{2\Delta} \begin{bmatrix} c_1 \\ c_2 \\ c_3 \end{bmatrix}. \tag{3.30}$$

and

$$\frac{\partial \hat{A}}{\partial x} = \frac{1}{2\Delta}(b_1\hat{A}_1 + b_2\hat{A}_2 + b_3\hat{A}_3) = \frac{1}{2\Delta} \begin{bmatrix} b_1 & b_2 & b_3 \end{bmatrix} \begin{bmatrix} \hat{A}_1 \\ \hat{A}_2 \\ \hat{A}_3 \end{bmatrix}, \tag{3.31}$$

$$\frac{\partial \hat{A}}{\partial y} = \frac{1}{2\Delta}(c_1\hat{A}_1 + c_2\hat{A}_2 + c_3\hat{A}_3) = \frac{1}{2\Delta} \begin{bmatrix} c_1 & c_2 & c_3 \end{bmatrix} \begin{bmatrix} \hat{A}_1 \\ \hat{A}_2 \\ \hat{A}_3 \end{bmatrix}. \tag{3.32}$$

Substituting equations (3.29)-(3.32) into equation (3.28) and considering that

$$\int\int_{\Omega_e} dxdy = \Delta, \tag{3.33}$$

then the first term of equation (3.26) becomes

$$\int\int_{\Omega_e} [N_i^e][\frac{\partial}{\partial x}(\nu\frac{\partial \hat{A}}{\partial x}) + \frac{\partial}{\partial y}(\nu\frac{\partial \hat{A}}{\partial y})]dxdy = -\frac{\nu}{4\Delta} \begin{pmatrix} S_{11} & S_{12} & S_{13} \\ S_{21} & S_{22} & S_{23} \\ S_{31} & S_{32} & S_{33} \end{pmatrix} \begin{pmatrix} \hat{A}_1 \\ \hat{A}_2 \\ \hat{A}_3 \end{pmatrix} \tag{3.34}$$

where

$$S_{11} = b_1^2 + c_1^2; \qquad S_{12} = b_1b_2 + c_1c_2; \quad S_{13} = b_1b_3 + c_1c_3;$$

$$S_{21} = b_2b_1 + c_2c_1; \quad S_{22} = b_2^2 + c_2^2; \qquad S_{23} = b_2b_3 + c_2c_3;$$

$$S_{31} = b_3b_1 + c_3c_1; \quad S_{32} = b_3b_2 + c_3c_2; \quad S_{33} = b_3^2 + c_3^2;$$

(b) Integration of the second term of equation (3.26) $-\int\int_{\Omega_e}[N_i^e](\sigma\frac{\partial\hat{A}}{\partial t})dxdy$

Recalling equation (3.13), the vector potential in a finite element can be represented as

$$\hat{A} = N_1\hat{A}_1 + N_2\hat{A}_2 + N_3\hat{A}_3 = [N_i^e]^{tr}[\hat{A}_i^e] \tag{3.35}$$

where $[\hat{A}_i^e] = \begin{pmatrix} \hat{A}_1 & \hat{A}_2 & \hat{A}_3 \end{pmatrix}^{tr}$ represents the vector potentials of the 3 nodes and superscript '$()^{tr}$' represents the transpose operation of a matrix.

Therefore the second term of equation (3.26) can be rewritten as

$$\begin{aligned} -\int\int_{\Omega_e}[N_i^e](\sigma\frac{\partial\hat{A}}{\partial t})dxdy &= -\int\int_{\Omega_e}[N_i^e](\sigma\frac{\partial([N_i^e]^{tr}[\hat{A}_i^e])}{\partial t})dxdy \\ &= -\sigma\int\int_{\Omega_e}[N_i^e][N_i^e]^{tr}\frac{\partial[\hat{A}_i^e]}{\partial t}dxdy \end{aligned} \tag{3.36}$$

Considering that

$$\begin{aligned} \int\int_{\Delta} N_i^2 dxdy &= \frac{\Delta}{6} \\ \int\int_{\Delta} N_i N_j dxdy &= \frac{\Delta}{12}, (i \neq j) \end{aligned} \tag{3.37}$$

equation (3.36) becomes

$$-\int\int_{\Omega_e}[N_i^e](\sigma\frac{\partial\hat{A}}{\partial t})dxdy = -\frac{\sigma\Delta}{12}\begin{pmatrix} 2 & 1 & 1 \\ 1 & 2 & 1 \\ 1 & 1 & 2 \end{pmatrix}\begin{pmatrix} \partial\hat{A}_1/\partial t \\ \partial\hat{A}_2/\partial t \\ \partial\hat{A}_3/\partial t \end{pmatrix} \tag{3.38}$$

(c) Integration of the third term of equation (3.26) $\int\int_{\Omega_e}[N_i^e](\sigma\frac{V_{tz}}{l})dxdy$

Since the terminal voltage V_{tz} and length l are invariant within one finite element, we can get

$$\int\int_{\Omega_e}[N_i^e](\sigma\frac{V_{tz}}{l})dxdy = (\sigma\frac{V_{tz}}{l})\cdot\int\int_{\Omega_e}[N_i^e]dxdy \tag{3.39}$$

Considering that

$$\int\int_{\Delta} N_i dxdy \;=\; \frac{\Delta}{3}$$

equation (3.39) becomes

$$\int\int_{\Omega_e} [N_i^e](\sigma\frac{V_{tz}}{l})dxdy = \frac{\Delta}{3}\cdot(\sigma\frac{V_{tz}}{l})\begin{pmatrix}1\\1\\1\end{pmatrix} \tag{3.40}$$

(d) Integration of the fourth term of equation (3.26) $\int\int_{\Omega_e}[N_i^e][\nabla\times(\nu\mu_0 M_r)]dxdy$

Considering the triple scalar product

$$\vec{A}\cdot(\vec{B}\times\vec{C}) = (\vec{A}\times\vec{B})\cdot\vec{C} = -(\vec{B}\times\vec{A})\cdot\vec{C},$$

the fourth term becomes

$$\int\int_{\Omega_e}[N_i^e][\nabla\times(\nu\mu_0 M_r)]dxdy = -\int\int_{\Omega_e}\nu\mu_0(\nabla\times[N_i^e])\cdot M_r dxdy. \tag{3.41}$$

For the two-dimensional case, M_r has only x and y components,

$$M_r = M_{rx}\cdot\vec{x} + M_{ry}\cdot\vec{y}, \tag{3.42}$$

and

$$\nabla\times[N_i^e] = -\frac{\partial[N_i^e]}{\partial y}\cdot\vec{x} + \frac{\partial[N_i^e]}{\partial x}\cdot\vec{y}. \tag{3.43}$$

Combination of equations (3.41)-(3.43) yields

$$\int\int_{\Omega_e}[N_i^e][\nabla\times(\nu\mu_0 M_r)]dxdy = \int\int_{\Omega_e}\nu\mu_0(M_{rx}\frac{\partial[N_i^e]}{\partial y} - M_{ry}\frac{\partial[N_i^e]}{\partial x})dxdy \tag{3.44}$$

Substitute equations (3.29), (3.30) and (3.33) into equation (3.44), the fourth term of equation (3.26) becomes

$$\int\int_{\Omega_e}[N_i^e][\nabla\times(\nu\mu_0 M_r)]dxdy = \frac{\nu\mu_0}{2}\left[M_{rx}\begin{pmatrix}c_1\\c_2\\c_3\end{pmatrix} - M_{ry}\begin{pmatrix}b_1\\b_2\\b_3\end{pmatrix}\right] \tag{3.45}$$

Finally, substituting equations (3.34), (3.38), (3.40) and (3.45) into equation (3.26) yields the element matrix equation for field equation (3.1):

$$\frac{\nu}{4\Delta}[SS][\hat{A}_i^e] + \frac{\sigma\Delta}{12}[TT]\frac{\partial[\hat{A}_i^e]}{\partial t} = \frac{\Delta}{3}\cdot(\sigma\frac{V_{tz}}{l})[O_i] + \frac{\nu\mu_0}{2}\{M_{rx}[c_i] - M_{ry}[b_i]\} \quad (3.46)$$

where

$$[SS] = \begin{pmatrix} S_{11} & S_{12} & S_{13} \\ S_{21} & S_{22} & S_{23} \\ S_{31} & S_{32} & S_{33} \end{pmatrix}; [TT] = \begin{pmatrix} 2 & 1 & 1 \\ 1 & 2 & 1 \\ 1 & 1 & 2 \end{pmatrix};$$

$$\begin{bmatrix} \hat{A}_i^e \end{bmatrix} = \begin{pmatrix} \hat{A}_1 \\ \hat{A}_2 \\ \hat{A}_3 \end{pmatrix}; [O_i] = \begin{pmatrix} 1 \\ 1 \\ 1 \end{pmatrix}; [c_i] = \begin{pmatrix} c_1 \\ c_2 \\ c_3 \end{pmatrix}; [b_i] = \begin{pmatrix} b_1 \\ b_2 \\ b_3 \end{pmatrix}.$$

To simplify the computation, the reluctivity ν, the x and y components of magnetization vector, M_{rx} and M_{ry} are all taken as scalers.

3.5.2 Finite Element Formulation of Stator Phase Circuit Equation

Recalling equation (3.2), we can get

$$V_s = R_s i_s + L_e\frac{di_s}{dt} + \frac{l}{ms}(\int\int_{\Omega^+}\frac{\partial\hat{A}}{\partial t}dxdy - \int\int_{\Omega^-}\frac{\partial\hat{A}}{\partial t}dxdy) \quad (3.47)$$

Breaking the surface integral into summations over small sub-domains called finite elements, equation (3.47) can be rewritten as

$$V_s = R_s i_s + L_e\frac{di_s}{dt} + \frac{l}{ms}(\sum_{e=1}^{M^+}\int\int_{\Omega_e}\frac{\partial\hat{A}}{\partial t}dxdy - \sum_{e=1}^{M^-}\int\int_{\Omega_e}\frac{\partial\hat{A}}{\partial t}dxdy). \quad (3.48)$$

where M^+ denotes the number of finite elements in the domain of positively oriented coils side, M^- denotes the number of finite elements in the domain of negatively oriented coils side and Ω_e is the surface area of one element.

Since

$$\hat{A} = [N_i^e]^{tr}[\hat{A}_i^e],$$

equation (3.48) becomes

$$\begin{aligned} V_s &= R_s i_s + L_e \frac{di_s}{dt} \\ &\quad + \frac{l}{ms}\left(\sum_{e=1}^{M^+}\int\int_{\Omega_e}\frac{\partial([N_i^e]^{tr}[\hat{A}_i^e])}{\partial t}dxdy - \sum_{e=1}^{M^-}\int\int_{\Omega_e}\frac{\partial([N_i^e]^{tr}[\hat{A}_i^e])}{\partial t}dxdy\right) \\ &= R_s i_s + L_e \frac{di_s}{dt} \\ &\quad + \frac{l}{ms}\left(\sum_{e=1}^{M^+}\int\int_{\Omega_e}[N_i^e]^{tr}\frac{\partial[\hat{A}_i^e]}{\partial t}dxdy - \sum_{e=1}^{M^-}\int\int_{\Omega_e}[N_i^e]^{tr}\frac{\partial[\hat{A}_i^e]}{\partial t}dxdy\right). \end{aligned} \quad (3.49)$$

As

$$\int\int_{\Delta} N_i dxdy = \frac{\Delta}{3}$$

equation (3.49) becomes

$$V_s = R_s i_s + L_e \frac{di_s}{dt} + \frac{l}{ms}\left(\sum_{e=1}^{M^+}\frac{\Delta}{3}\frac{\partial[\hat{A}_i^e]}{\partial t} - \sum_{e=1}^{M^-}\frac{\Delta}{3}\frac{\partial[\hat{A}_i^e]}{\partial t}\right), \quad (3.50)$$

or

$$R_s i_s + L_e \frac{di_s}{dt} + \frac{l}{ms}[KK]_{sp}\frac{\partial[\hat{A}]_{sp}}{\partial t} - V_s = 0 \quad (3.51)$$

where

$$\begin{aligned} [KK]_{sp} &= \left(\ldots \quad \pm\tfrac{\Delta}{3} \quad \pm\tfrac{\Delta}{3} \quad \pm\tfrac{\Delta}{3} \quad \ldots \right), \\ \left[\hat{A} \right]_{sp} &= \left(\ldots \quad \hat{A}_1 \quad \hat{A}_2 \quad \hat{A}_3 \quad \ldots \right)^{tr}. \end{aligned}$$

The sign '$\pm$' is '+' when the triangle element is in the domain of positively oriented coils side, and it is '$-$' when the element is in the domain of negatively oriented coils side. Matrices $[KK]_{sp}$ and $[\hat{A}]_{sp}$ are only used for those elements that locate in the region of stator phase windings.

3.5.3 Finite Element Formulation of Cage Bar Equation

Recalling equation (3.3), we can get

$$V_{bk} = R_{bk} i_{bk} + \frac{l_{bk}}{s_{bk}} \int \int_{s_{bk}} \frac{\partial \hat{A}}{\partial t} dxdy \tag{3.52}$$

Breaking the surface integral into summations over the finite elements, equation (3.52) can be rewritten as

$$V_{bk} = R_{bk} i_{bk} + \frac{l_{bk}}{s_{bk}} \sum_{e=1}^{M_{cb}} \int \int_{\Omega_e} \frac{\partial \hat{A}}{\partial t} dxdy \tag{3.53}$$

Since

$$\hat{A} = [N_i^e]^{tr} [\hat{A}_i^e],$$

equation (3.53) becomes

$$\begin{aligned} V_{bk} &= R_{bk} i_{bk} + \frac{l_{bk}}{s_{bk}} \sum_{e=1}^{M_{cb}} \int \int_{\Omega_e} \frac{\partial ([N_i^e][\hat{A}_i^e])}{\partial t} dxdy \\ &= R_{bk} i_{bk} + \frac{l_{bk}}{s_{bk}} \sum_{e=1}^{M_{cb}} \int \int_{\Omega_e} [N_i^e] \frac{\partial [\hat{A}_i^e]}{\partial t} dxdy \end{aligned} \tag{3.54}$$

where M_{cb} is the number of finite elements in this cage bar.

As

$$\int \int_{\Delta} N_i dxdy = \frac{\Delta}{3}$$

equation (3.54) becomes

$$V_{bk} = R_{bk} i_{bk} + \frac{l_{bk}}{s_{bk}} \sum_{e=1}^{M_{cb}} \frac{\Delta}{3} \frac{\partial [\hat{A}_i^e]}{\partial t}, \tag{3.55}$$

or

$$R_{bk} i_{bk} + \frac{l_{bk}}{s_{bk}} [KK]_{cb} \frac{\partial [\hat{A}]_{cb}}{\partial t} - V_{bk} = 0 \tag{3.56}$$

where

$$[KK]_{cb} = \left(\ldots \ \tfrac{\Delta}{3} \ \tfrac{\Delta}{3} \ \tfrac{\Delta}{3} \ \ldots \right),$$
$$\left[\ \hat{A} \ \right]_{cb} = \left(\ldots \ \hat{A}_1 \ \ \hat{A}_2 \ \ \hat{A}_3 \ \ \ldots \right)^{tr}.$$

Matrices $[KK]_{cb}$ and $[\hat{A}]_{cb}$ are only used for those elements that locate in the region of cage bars.

Other equations (3.4)$\sim$(3.9), describe the cage bar circuits, external circuit and mechanical motions. They are not field-dependent directly. Therefore the finite element formulation of these equations are not necessary.

3.6 Discretization of Governing Equations in Time Domain

As shown in equations (3.1)-(3.9), electric machines are often modelled in terms of a complete set of partial differential equations or linear algebraic equations with solution functions expressed in the space and time domains. The space solution is determined by the finite element technique while the time solution is evaluated by time-stepping methods that consist of implicit or explicit time-integration procedures [76]-[78]. The time-stepping method is the method that solves a time-dependent quantity by discretizing the time at short time intervals Δt and evaluating the quantitiy at times t_1, t_2, t_3, ..., $(t_{k+1} = t_k + \Delta t)$. The accuracy of the solution depends on the particular time-stepping algorithm applied, as well as the size of the time step used. The most often used time-stepping algorithms are:

- Explicit algorithm (Forward Euler's method)

$$\frac{\partial A^t}{\partial t} = \frac{A^{(t+\Delta t)} - A^t}{\Delta t} \tag{3.57}$$

If the value of A and its time derivative at t are known, its value at $(t + \Delta t)$ is obtainable using equations (3.57).

- Implicit algorithm

  - Crank-Nicholson Algorithm

$$\frac{1}{2}\left(\frac{\partial A^{(t+\Delta t)}}{\partial t} + \frac{\partial A^t}{\partial t}\right) = \frac{A^{(t+\Delta t)} - A^t}{\Delta t} \tag{3.58}$$

The time derivatives at t and $(t + \Delta t)$ are used to find the value of A at $(t + \Delta t)$, $A^{(t+\Delta t)}$.

  - Backward difference scheme (Backward Euler's method)

$$\frac{\partial A^{(t+\Delta t)}}{\partial t} = \frac{A^{(t+\Delta t)} - A^t}{\Delta t} \tag{3.59}$$

If the value of A and its time derivative at $(t + \Delta t)$ are known, its value at $(t + \Delta t)$ is obtainable using equations (3.59).

It has been shown that implicit algorithms have distinct advantages over the explicit ones, due to higher degree of numerical stability and larger time step possibility [76]-[80]. Inside the group of implicit algorithm, Tsukerman [80, 81] examined the stabilities of Crank-Nicholson algorithm and Backward Euler's algorithm in coupled field-circuit problems. It was shown that Backward Euler's method is stable while the Crank-Nicholson scheme generates undamped or in some cases even divergent oscillations. Therefore, in this work the Backward Euler's method is chosen in the time discretization of the governing equations.

3.6.1 Discretization of Field Equation

Recalling the element matrix equation for field (3.46),

$$\frac{\nu}{4\Delta}[SS][\hat{A}_i^e]^{t+\Delta t}+\frac{\sigma\Delta}{12}[TT]\frac{\partial[\hat{A}_i^e]^{t+\Delta t}}{\partial t}=\frac{\Delta}{3}\cdot(\sigma\frac{V_{tz}^{(t+\Delta t)}}{l})[O_i]+\frac{\nu\mu_0}{2}\left\{M_{rx}[c_i]-M_{ry}[b_i]\right\} \tag{3.60}$$

According to equation (3.59),

$$\frac{\partial[\hat{A}_i^e]^{(t+\Delta t)}}{\partial t}=\frac{[\hat{A}_i^e]^{(t+\Delta t)}-[\hat{A}_i^e]^t}{\Delta t}, \tag{3.61}$$

the element matrix equation for field becomes,

$$\begin{aligned}&\left(\frac{\nu}{4\Delta}[SS]+\frac{\sigma\Delta}{12}[TT]\right)\cdot\frac{[\hat{A}_i^e]^{t+\Delta t}-[\hat{A}_i^e]^t}{\Delta t}-\frac{\Delta}{3}\cdot(\sigma\frac{V_{tz}^{(t+\Delta t)}}{l})[O_i]\\ =\;&\frac{\nu\mu_0}{2}\left\{M_{rx}[c_i]-M_{ry}[b_i]\right\}.\end{aligned} \tag{3.62}$$

Rearranging terms to isolate the $(t+\Delta t)$ term yields,

$$\begin{aligned}&\left\{\frac{\nu}{4\Delta}[SS]+\frac{\sigma\Delta}{12\Delta t}[TT]\right\}[\hat{A}_i^e]^{t+\Delta t}-\frac{\Delta}{3}\cdot(\sigma\frac{V_{tz}^{(t+\Delta t)}}{l})[O_i]\\ =\;&\frac{\sigma\Delta}{12\Delta t}[TT][\hat{A}_i^e]^t+\frac{\nu\mu_0}{2}\left\{M_{rx}[c_i]-M_{ry}[b_i]\right\}.\end{aligned} \tag{3.63}$$

Equation (3.63) shows that as long as the values at t are known, the values at $(t+\Delta t)$ can be calculated readily by solving this equation. In other words, a dynamic process can be evaluated in steps or the dynamic behaviours of a device can be analyzed using time-stepping method.

3.6.2 Discretization of Equation for Stator Phase Circuit

Recalling equation (3.51) and considering that,

$$\frac{di_s^{(t+\Delta t)}}{dt} = \frac{i_s^{(t+\Delta t)} - i_s^t}{\Delta t}$$

$$\frac{\partial \left[\hat{A}\right]_{sp}^{t+\Delta t}}{\partial t} = \frac{\left[\hat{A}\right]_{sp}^{t+\Delta t} - \left[\hat{A}\right]_{sp}^{t}}{\Delta t}$$

the equation for stator phase circuit becomes,

$$(R_s + \frac{L_e}{\Delta t})i_s^{(t+\Delta t)} + \frac{l}{ms}\frac{[KK]_{sp}}{\Delta t}[\hat{A}]_{sp}^{t+\Delta t} - V_s^{(t+\Delta t)} = \frac{L_e}{\Delta t}i_s^t + \frac{l}{ms}\frac{[KK]_{sp}}{\Delta t}[\hat{A}]_{sp}^{t} \quad (3.64)$$

3.6.3 Discretization of Governing Equations for Cage Bars

Equation (3.56) can be discretized as:

$$R_{bk}[i_{bk}]^{t+\Delta t} + \frac{l_{bk}}{s_{bk}}\frac{[KK]_{cb}}{\Delta t}[\hat{A}]_{cb}^{t+\Delta t} - [V_{bk}]^{t+\Delta t} = \frac{l_{bk}}{s_{bk}}\frac{[KK]_{cb}}{\Delta t}[\hat{A}]_{cb}^{t} \quad (3.65)$$

Recalling equation (3.4) and considering that it is not time-dependent, it is kept unchanged in time domain:

$$[i_b]^{t+\Delta t} - [C_1][i_e]^{t+\Delta t} = 0 \quad (3.66)$$

Equation (3.5) can be discretized as:

$$[C_2][V_b]^{t+\Delta t} + 2\{[R_e] + \frac{[L_e]}{\Delta t}\}[i_e]^{t+\Delta t} = 2\frac{[L_e]}{\Delta t}[i_e]^t \quad (3.67)$$

3.6.4 Discretization of Equations for External Circuits

Equation (3.6) can be discretized as:

$$\{[R_{sb}] + \frac{[L_{sb}]}{\Delta t}\}[i_{sb}]^{t+\Delta t} + \frac{[C_{sb}]}{\Delta t}[V_{sb}; V_t]^{t+\Delta t} = \frac{[L_{sb}]}{\Delta t}[i_{sb}]^t + \frac{[C_{sb}]}{\Delta t}[V_{sb}; V_t]^t \quad (3.68)$$

Recalling equation (3.7) and considering that it is not time-dependent, it is kept unchanged in time domain:

$$[C_3][i_{sb}]^{t+\Delta t} + [C_4][i_s]^{t+\Delta t} = 0 \quad (3.69)$$

3.6.5 Discretization of Equations for Mechanical Motion

Equation (3.8) can be discretized as:

$$(\frac{J_r}{\Delta t} + B_f)\omega_m^{t+\Delta t} = \frac{J_r}{\Delta t} \cdot \omega_m^t + T_{em} - T_f \quad (3.70)$$

and equation (3.9) can be discretized as:

$$\frac{1}{\Delta t}\theta_m^{t+\Delta t} - \omega_m^{t+\Delta t} = \frac{1}{\Delta t}\theta_m^t \quad (3.71)$$

3.7 Solving the Nonlinear Equations

In the analysis of electric machines the problems are almost always nonlinear due to the presence of ferromagnetic materials in the rotor and stator iron cores. Generally the iron material is characterized by a nonlinear curve relating the magnetic field intensity H to the magnetic flux density B. Mathematically it is represented by the permeability parameter μ at each point of the iron domain,

$$\mu = \frac{B}{H} \tag{3.72}$$

If the distribution of B is known, the value of H can be found according to the nonlinear $B - H$ curve; then μ can be calculated using equation (3.72). Thus the value of magnetic permeability μ is field-dependent, which is characterized as $\nu = \frac{1}{\mu} = f(B)$. To treat the nonlinearities of the materials, two methods are usually used [8, 14, 28]:

1. **The simple iteration method**

   A set of permeability values μ is assumed firstly. In the light of the field solution values obtained, adjust the μ with the following equation

   $$\mu^{n+1} = \mu^{n-1} + k(\mu^n - \mu^{n-1}) \tag{3.73}$$

   where k $(0 < k < 1)$ is a real number and n is the iteration step number. The above solve-adjust cycle is continued until satisfactory convergence is obtained.

   This method is very simple in implementation. However the method converges rather slowly and may need considerable computation time. In addition, no known estimate of k may guarantee stability without slowing the iterative process [28].

2. **The Newton-Raphson method**

The method utilizes the rate of change of error with potential to obtain new estimates of potential. For a set of equations

$$[f]_{k\times 1} = [K]_{k\times k}[X]_{k\times 1} = [Q]_{k\times 1},$$

an initial value $[X]^{(0)}$ is assumed as the estimate of solution. The solution is updated iteratively with equation

$$[X]^{(n+1)} = [X]^{(n)} + \{[J]^{(n)}\}^{-1}\{[Q] - [f]^{(n)}\} \tag{3.74}$$

where $[J] = \frac{\partial f_i}{\partial X_j}, (i, j = 1, 2, \ldots, k)$ is the Jacobian matrix and n is the iteration step number. The iteration is continued until satisfactory convergence is obtained. The detailed algorithm of the Newton-Raphson method and the description of Jacobian matrix $[J]$ are presented in Appendix A.

Particularly when $[Q] = 0$, the Newton-Raphson algorithm is:

$$\frac{\partial f_i^{(n)}}{\partial X_1^{(n)}}\Delta X_1^{(n+1)} + \frac{\partial f_i^{(n)}}{\partial X_2^{(n)}}\Delta X_2^{(n+1)} + \ldots + \frac{\partial f_i^{(n)}}{\partial X_k^{(n)}}\Delta X_k^{(n+1)} = -f_i^{(n)} \tag{3.75}$$

The Newton-Raphson method gives more certain and quicker convergence. It is particularly suitable for a nonlinear system of equations.

The application of the Newton-Raphson method to the solution of the nonlinear finite element equations requires extension to matrix equations and was first demonstrated by Chari and Silvester [17]. Then it has been extensively used in the solution of finite element problems by many others [18]-[20],[22]-[30].

3.7.1 Linearization of Field Equation

Recalling equation (3.63) and let

$$[PP] = \begin{pmatrix} P_1 \\ P_2 \\ P_3 \end{pmatrix} = \frac{\sigma\Delta}{12\Delta t}[TT][\hat{A}_i^e]^t + \frac{\nu\mu_0}{2}\left\{M_{rx}[c_i] - M_{ry}[b_i]\right\}, \tag{3.76}$$

then equation (3.63) becomes

$$\left\{\frac{\nu}{4\Delta}[SS] + \frac{\sigma\Delta}{12\Delta t}[TT]\right\}[\hat{A}_i^e]^{t+\Delta t} - \frac{\Delta}{3}\cdot(\sigma\frac{V_{tz}^{(t+\Delta t)}}{l})[O_i] = [PP]. \tag{3.77}$$

or

$$\left\{\frac{\nu}{4\Delta}\begin{pmatrix} S_{11} & S_{12} & S_{13} \\ S_{21} & S_{22} & S_{23} \\ S_{31} & S_{32} & S_{33} \end{pmatrix} + \frac{\sigma\Delta}{12\Delta t}\begin{pmatrix} 2 & 1 & 1 \\ 1 & 2 & 1 \\ 1 & 1 & 2 \end{pmatrix}\right\}\begin{pmatrix} \hat{A}_1 \\ \hat{A}_2 \\ \hat{A}_3 \end{pmatrix}^{t+\Delta t}$$
$$-\frac{\Delta}{3}\frac{\sigma}{l}V_{tz}^{(t+\Delta t)}\begin{pmatrix} 1 \\ 1 \\ 1 \end{pmatrix} = \begin{pmatrix} P_1 \\ P_2 \\ P_3 \end{pmatrix} \tag{3.78}$$

Let

$$\begin{cases} f_1 = \frac{\nu}{4\Delta}(S_{11}\hat{A}_1^{t+\Delta t} + S_{12}\hat{A}_2^{t+\Delta t} + S_{13}\hat{A}_3^{t+\Delta t}) \\ f_2 = \frac{\nu}{4\Delta}(S_{21}\hat{A}_1^{t+\Delta t} + S_{22}\hat{A}_2^{t+\Delta t} + S_{23}\hat{A}_3^{t+\Delta t}) \\ f_3 = \frac{\nu}{4\Delta}(S_{31}\hat{A}_1^{t+\Delta t} + S_{32}\hat{A}_2^{t+\Delta t} + S_{33}\hat{A}_3^{t+\Delta t}) \end{cases} \tag{3.79}$$

or

$$\begin{pmatrix} f_1 \\ f_2 \\ f_3 \end{pmatrix} = \frac{\nu}{4\Delta}\begin{pmatrix} S_{11} & S_{12} & S_{13} \\ S_{21} & S_{22} & S_{23} \\ S_{31} & S_{32} & S_{33} \end{pmatrix}\begin{pmatrix} \hat{A}_1 \\ \hat{A}_2 \\ \hat{A}_3 \end{pmatrix}^{t+\Delta t}, \tag{3.80}$$

then equation (3.78) can be rewritten into 3 equations

$$F_1 = f_1 + \frac{\sigma\Delta}{12\Delta t}\begin{pmatrix} 2 & 1 & 1 \end{pmatrix}\begin{pmatrix} \hat{A}_1 \\ \hat{A}_2 \\ \hat{A}_3 \end{pmatrix}^{t+\Delta t} - \frac{\Delta}{3}\frac{\sigma}{l}V_{tz}^{(t+\Delta t)} - P_1 = 0 \tag{3.81}$$

$$F_2 = f_2 + \frac{\sigma\Delta}{12\Delta t}\begin{pmatrix} 1 & 2 & 1 \end{pmatrix}\begin{pmatrix} \hat{A}_1 \\ \hat{A}_2 \\ \hat{A}_3 \end{pmatrix}^{t+\Delta t} - \frac{\Delta}{3}\frac{\sigma}{l}V_{tz}^{(t+\Delta t)} - P_2 = 0 \tag{3.82}$$

$$F_3 = f_3 + \frac{\sigma\Delta}{12\Delta t}\begin{pmatrix} 1 & 1 & 2 \end{pmatrix}\begin{pmatrix} \hat{A}_1 \\ \hat{A}_2 \\ \hat{A}_3 \end{pmatrix}^{t+\Delta t} - \frac{\Delta}{3}\frac{\sigma}{l}V_{tz}^{(t+\Delta t)} - P_3 = 0 \tag{3.83}$$

To find the derivatives necessary for the Newton-Raphson method, equations (3.81)-(3.83) need to be differentiated with respect to the variables. The differentiation of equation (3.81) gives

$$\frac{\partial F_1}{\partial \hat{A}_1^{(t+\Delta t)}} = \frac{\nu}{4\Delta}S_{11} + \frac{f_1}{\nu}\cdot\frac{\partial \nu}{\partial B}\cdot\frac{\partial B}{\partial \hat{A}_1^{(t+\Delta t)}} + \frac{\sigma\Delta}{12\Delta t}\cdot 2 \tag{3.84}$$

$$\frac{\partial F_1}{\partial \hat{A}_2^{(t+\Delta t)}} = \frac{\nu}{4\Delta}S_{12} + \frac{f_1}{\nu}\cdot\frac{\partial \nu}{\partial B}\cdot\frac{\partial B}{\partial \hat{A}_2^{(t+\Delta t)}} + \frac{\sigma\Delta}{12\Delta t}\cdot 1 \tag{3.85}$$

$$\frac{\partial F_1}{\partial \hat{A}_3^{(t+\Delta t)}} = \frac{\nu}{4\Delta}S_{13} + \frac{f_1}{\nu}\cdot\frac{\partial \nu}{\partial B}\cdot\frac{\partial B}{\partial \hat{A}_3^{(t+\Delta t)}} + \frac{\sigma\Delta}{12\Delta t}\cdot 1 \tag{3.86}$$

$$\frac{\partial F_1}{\partial V_{tz}^{(t+\Delta t)}} = -\frac{\Delta}{3}\frac{\sigma}{l} \tag{3.87}$$

Since (see Appendix B)

$$\frac{\partial B}{\partial \hat{A}_1^{(t+\Delta t)}} = \frac{f_1}{B\nu\Delta}$$

$$\frac{\partial B}{\partial \hat{A}_2^{(t+\Delta t)}} = \frac{f_2}{B\nu\Delta}$$

$$\frac{\partial B}{\partial \hat{A}_3^{(t+\Delta t)}} = \frac{f_3}{B\nu\Delta}$$

equations (3.84)-(3.86) become

$$\frac{\partial F_1}{\partial \hat{A}_1^{(t+\Delta t)}} = \frac{\nu}{4\Delta}S_{11} + \frac{f_1 f_1}{\nu^2 B\Delta}\cdot\frac{\partial \nu}{\partial B} + \frac{\sigma\Delta}{12\Delta t}\cdot 2 \tag{3.88}$$

$$\frac{\partial F_1}{\partial \hat{A}_2^{(t+\Delta t)}} = \frac{\nu}{4\Delta} S_{12} + \frac{f_1 f_2}{\nu^2 B \Delta} \cdot \frac{\partial \nu}{\partial B} + \frac{\sigma \Delta}{12 \Delta t} \cdot 1 \tag{3.89}$$

$$\frac{\partial F_1}{\partial \hat{A}_3^{(t+\Delta t)}} = \frac{\nu}{4\Delta} S_{13} + \frac{f_1 f_3}{\nu^2 B \Delta} \cdot \frac{\partial \nu}{\partial B} + \frac{\sigma \Delta}{12 \Delta t} \cdot 1 \tag{3.90}$$

Applying equation (3.75), the Newton-Raphson equation is

$$\frac{\partial F_1}{\partial \hat{A}_1^{(t+\Delta t)}} \cdot [\Delta \hat{A}_1]_{(n+1)}^{(t+\Delta t)} + \frac{\partial F_1}{\partial \hat{A}_2^{(t+\Delta t)}} \cdot [\Delta \hat{A}_2]_{(n+1)}^{(t+\Delta t)}$$

$$+ \frac{\partial F_1}{\partial \hat{A}_3^{(t+\Delta t)}} \cdot [\Delta \hat{A}_3]_{(n+1)}^{(t+\Delta t)} + \frac{\partial F_1}{\partial V_{tz}^{(t+\Delta t)}} \cdot [\Delta V_{tz}]_{(n+1)}^{(t+\Delta t)} = -F_1. \tag{3.91}$$

Substituting equations (3.87)-(3.90) into equation (3.91) yields the linearization of equation F_1

$$\begin{aligned}
& \frac{\nu}{4\Delta} \begin{pmatrix} S_{11} & S_{12} & S_{13} \end{pmatrix} \begin{pmatrix} \Delta \hat{A}_1 \\ \Delta \hat{A}_2 \\ \Delta \hat{A}_3 \end{pmatrix}_{(n+1)}^{t+\Delta t} + \frac{\sigma \Delta}{12 \Delta t} \begin{pmatrix} 2 & 1 & 1 \end{pmatrix} \begin{pmatrix} \Delta \hat{A}_1 \\ \Delta \hat{A}_2 \\ \Delta \hat{A}_3 \end{pmatrix}_{(n+1)}^{t+\Delta t} \\
& + \frac{1}{\nu^2 B \Delta} \cdot \frac{\partial \nu}{\partial B} \begin{pmatrix} f_1 f_1 & f_1 f_2 & f_1 f_3 \end{pmatrix} \begin{pmatrix} \Delta \hat{A}_1 \\ \Delta \hat{A}_2 \\ \Delta \hat{A}_3 \end{pmatrix}_{(n+1)}^{t+\Delta t} - \frac{\Delta}{3} \frac{\sigma}{l} [\Delta V_{tz}]_{(n+1)}^{(t+\Delta t)} \\
= \; & -\frac{\nu}{4\Delta} \begin{pmatrix} S_{11} & S_{12} & S_{13} \end{pmatrix} \begin{pmatrix} \hat{A}_1 \\ \hat{A}_2 \\ \hat{A}_3 \end{pmatrix}_{(n)}^{t+\Delta t} - \frac{\sigma \Delta}{12 \Delta t} \begin{pmatrix} 2 & 1 & 1 \end{pmatrix} \begin{pmatrix} \hat{A}_1 \\ \hat{A}_2 \\ \hat{A}_3 \end{pmatrix}_{(n)}^{t+\Delta t} \\
& + \frac{\Delta}{3} \frac{\sigma}{l} [V_{tz}]_{(n)}^{(t+\Delta t)} + P_1
\end{aligned} \tag{3.92}$$

Repeating the similar processes for F_2 and F_3, we can get

$$\begin{aligned}
&\frac{\nu}{4\Delta}\begin{pmatrix} S_{21} & S_{22} & S_{23}\end{pmatrix}\begin{pmatrix}\Delta\hat{A}_1\\ \Delta\hat{A}_2\\ \Delta\hat{A}_3\end{pmatrix}_{(n+1)}^{t+\Delta t}+\frac{\sigma\Delta}{12\Delta t}\begin{pmatrix}1 & 2 & 1\end{pmatrix}\begin{pmatrix}\Delta\hat{A}_1\\ \Delta\hat{A}_2\\ \Delta\hat{A}_3\end{pmatrix}_{(n+1)}^{t+\Delta t}\\
&+\frac{1}{\nu^2 B\Delta}\cdot\frac{\partial\nu}{\partial B}\begin{pmatrix} f_2f_1 & f_2f_2 & f_2f_3\end{pmatrix}\begin{pmatrix}\Delta\hat{A}_1\\ \Delta\hat{A}_2\\ \Delta\hat{A}_3\end{pmatrix}_{(n+1)}^{t+\Delta t}-\frac{\Delta}{3}\frac{\sigma}{l}[\Delta V_{tz}]_{(n+1)}^{(t+\Delta t)}\\
=\;&-\frac{\nu}{4\Delta}\begin{pmatrix} S_{21} & S_{22} & S_{23}\end{pmatrix}\begin{pmatrix}\hat{A}_1\\ \hat{A}_2\\ \hat{A}_3\end{pmatrix}_{(n)}^{t+\Delta t}-\frac{\sigma\Delta}{12\Delta t}\begin{pmatrix}1 & 2 & 1\end{pmatrix}\begin{pmatrix}\hat{A}_1\\ \hat{A}_2\\ \hat{A}_3\end{pmatrix}_{(n)}^{t+\Delta t}\\
&+\frac{\Delta}{3}\frac{\sigma}{l}[V_{tz}]_{(n)}^{(t+\Delta t)}+P_2
\end{aligned}\tag{3.93}$$

$$\begin{aligned}
&\frac{\nu}{4\Delta}\begin{pmatrix} S_{31} & S_{32} & S_{33}\end{pmatrix}\begin{pmatrix}\Delta\hat{A}_1\\ \Delta\hat{A}_2\\ \Delta\hat{A}_3\end{pmatrix}_{(n+1)}^{t+\Delta t}+\frac{\sigma\Delta}{12\Delta t}\begin{pmatrix}1 & 1 & 2\end{pmatrix}\begin{pmatrix}\Delta\hat{A}_1\\ \Delta\hat{A}_2\\ \Delta\hat{A}_3\end{pmatrix}_{(n+1)}^{t+\Delta t}\\
&+\frac{1}{\nu^2 B\Delta}\cdot\frac{\partial\nu}{\partial B}\begin{pmatrix} f_3f_1 & f_3f_2 & f_3f_3\end{pmatrix}\begin{pmatrix}\Delta\hat{A}_1\\ \Delta\hat{A}_2\\ \Delta\hat{A}_3\end{pmatrix}_{(n+1)}^{t+\Delta t}-\frac{\Delta}{3}\frac{\sigma}{l}[\Delta V_{tz}]_{(n+1)}^{(t+\Delta t)}\\
=\;&-\frac{\nu}{4\Delta}\begin{pmatrix} S_{31} & S_{32} & S_{33}\end{pmatrix}\begin{pmatrix}\hat{A}_1\\ \hat{A}_2\\ \hat{A}_3\end{pmatrix}_{(n)}^{t+\Delta t}-\frac{\sigma\Delta}{12\Delta t}\begin{pmatrix}1 & 1 & 2\end{pmatrix}\begin{pmatrix}\hat{A}_1\\ \hat{A}_2\\ \hat{A}_3\end{pmatrix}_{(n)}^{t+\Delta t}\\
&+\frac{\Delta}{3}\frac{\sigma}{l}[V_{tz}]_{(n)}^{(t+\Delta t)}+P_3
\end{aligned}\tag{3.94}$$

Writing equations (3.92)-(3.94) in matrix format,

$$\left\{\frac{\nu}{4\Delta}[SS]+\frac{1}{\nu^2 B\Delta}\cdot\frac{\partial\nu}{\partial B}[ff]+\frac{\sigma\Delta}{12\Delta t}[TT]\right\}[\Delta\hat{A}]_{(n+1)}^{t+\Delta t}-\frac{\Delta}{3}\frac{\sigma}{l}[O_i][\Delta V_{tz}]_{(n+1)}^{(t+\Delta t)}$$

$$=\ -\left\{\frac{\nu}{4\Delta}[SS]+\frac{\sigma\Delta}{12\Delta t}[TT]\right\}[\hat{A}]_{(n)}^{t+\Delta t}+\frac{\Delta}{3}\frac{\sigma}{l}[O_i][V_{tz}]_{(n)}^{(t+\Delta t)}+[PP] \tag{3.95}$$

where

$$[\Delta\hat{A}] = \begin{pmatrix} \Delta\hat{A}_1 & \Delta\hat{A}_2 & \Delta\hat{A}_3 \end{pmatrix}^{tr},$$

$$[ff] = \begin{pmatrix} f_1f_1 & f_1f_2 & f_1f_3 \\ f_2f_1 & f_2f_2 & f_2f_3 \\ f_3f_1 & f_3f_2 & f_3f_3 \end{pmatrix}.$$

Substituting $[PP]$ or equation (3.76) into equation (3.95) yields the linearized field equation

$$\left\{\frac{\nu}{4\Delta}[SS]+\frac{1}{\nu^2 B\Delta}\cdot\frac{\partial\nu}{\partial B}[ff]+\frac{\sigma\Delta}{12\Delta t}[TT]\right\}[\Delta\hat{A}]_{(n+1)}^{t+\Delta t}-\frac{\Delta}{3}\frac{\sigma}{l}[O_i][\Delta V_{tz}]_{(n+1)}^{(t+\Delta t)}$$

$$=\ -\ \left\{\frac{\nu}{4\Delta}[SS]+\frac{\sigma\Delta}{12\Delta t}[TT]\right\}[\hat{A}]_{(n)}^{t+\Delta t}+\frac{\Delta}{3}\frac{\sigma}{l}[O_i][V_{tz}]_{n}^{(t+\Delta t)}+\frac{\sigma\Delta}{12\Delta t}[TT][\hat{A}]^{t}$$

$$+\ \frac{\nu\mu_0}{2}\{M_{rx}[c_i]-M_{ry}[b_i]\} \tag{3.96}$$

From equation (3.96), we can see that the term $\frac{\partial\nu}{\partial B}$ is necessary for the coefficient matrix. $\nu = H/B$ and $B-H$ curves are generally established by giving tabulated sets of $B-H$ values. For computer implementation, it is desirable to model the $B-H$ curve by an appropriate mathematical expression or by a suitable numerical method. Chari and Silvester [17, 18] have used piecewise linear approximations to represent nonlinear iron characteristics. However quadratic convergence may not be guaranteed unless the curves were at least continuously differentiable. Such a $B-H$

curve is not smooth at the joints of segments. Hence the accuracy of piecewise linear representation is limited by the number of the straight-line segments. Silvester [82] used cubic splines to model the reluctivity characteristic. This method uses splines constructed of piecewise third-order polynomials which pass through a set of data points. It results in a smooth curve with continuous first and second derivatives over the range of the data sets. Thus the nonlinear iron can be characterized by a single very smooth curve, from which both the reluctivity and its derivative can be obtained simultaneously. The method of cubic splines is quite effective in representing the nonlinear $B-H$ curve and has been used widely in numerical computation of electromagnetic fields [8, 28]. The implementation of this method in the representation of $B-H$ curve and the calculation of $\frac{\partial \nu}{\partial B}$ are introduced in Appendix C in detail.

3.7.2 Linearization of Stator Phase Equation

Recalling equation (3.64) and moving all the terms to the left hand side, we can get

$$\begin{aligned}&(R_s+\frac{L_e}{\Delta t})i_s^{(t+\Delta t)}+\frac{l}{ms}\frac{[KK]_{sp}}{\Delta t}[\hat{A}]_{sp}^{t+\Delta t}-V_s^{(t+\Delta t)}\\&-\left\{\frac{L_e}{\Delta t}i_s^t+\frac{l}{ms}\frac{[KK]_{sp}}{\Delta t}[\hat{A}]_{sp}^{t}\right\}=0\end{aligned}\tag{3.97}$$

Let

$$\begin{aligned}F &= (R_s+\frac{L_e}{\Delta t})i_s^{(t+\Delta t)}+\frac{l}{ms}\frac{[KK]_{sp}}{\Delta t}[\hat{A}]_{sp}^{t+\Delta t}-V_s^{(t+\Delta t)}\\&- \left\{\frac{L_e}{\Delta t}i_s^t+\frac{l}{ms}\frac{[KK]_{sp}}{\Delta t}[\hat{A}]_{sp}^{t}\right\},\end{aligned}\tag{3.98}$$

then the differentiation of F gives

$$\begin{aligned}
\frac{\partial F}{\partial i_s^{(t+\Delta t)}} &= R_s + \frac{L_e}{\Delta t}, \\
\frac{\partial F}{\partial [\hat{A}]_{sp}^{t+\Delta t}} &= \frac{l}{ms}\frac{[KK]_{sp}}{\Delta t}, \\
\frac{\partial F}{\partial V_s^{(t+\Delta t)}} &= -1
\end{aligned}$$

According to equation (3.75), the Newton-Raphson equation is

$$\frac{\partial F}{\partial i_s^{(t+\Delta t)}} \cdot [\Delta i_s]_{(n+1)}^{(t+\Delta t)} + \frac{\partial F}{\partial [\hat{A}]_{sp}^{t+\Delta t}} \cdot \{[\Delta \hat{A}]_{sp}\}_{(n+1)}^{t+\Delta t} + \frac{\partial F}{\partial V_s^{(t+\Delta t)}} \cdot [\Delta V_s]_{(n+1)}^{(t+\Delta t)} = -F. \quad (3.99)$$

Thus the linearization of equation for stator phase circuit is

$$\begin{aligned}
& (R_s + \frac{L_e}{\Delta t})[\Delta i_s]_{(n+1)}^{(t+\Delta t)} + \frac{l}{ms}\frac{[KK]_{sp}}{\Delta t}\{[\Delta \hat{A}]_{sp}\}_{(n+1)}^{t+\Delta t} - [\Delta V_s]_{(n+1)}^{(t+\Delta t)} \\
= \; & - \; (R_s + \frac{L_e}{\Delta t})[i_s]_{(n)}^{(t+\Delta t)} - \frac{l}{ms}\frac{[KK]_{sp}}{\Delta t}\{[\hat{A}]_{sp}\}_{(n)}^{t+\Delta t} + [V_s]_{(n)}^{(t+\Delta t)} \\
& + \; \left\{ \frac{L_e}{\Delta t}[i_s]^t + \frac{l}{ms}\frac{[KK]_{sp}}{\Delta t}[\hat{A}]_{sp}^t \right\}. \quad (3.100)
\end{aligned}$$

3.7.3 Linearization of Equations for Cage Bars

Repeating the similar linearization process for equation (3.65) yields

$$R_{bk}[\Delta i_{bk}]_{(n+1)}^{t+\Delta t} + \frac{l_{bk}}{s_{bk}}\frac{[KK]_{cb}}{\Delta t}\{[\Delta \hat{A}]_{cb}\}_{(n+1)}^{t+\Delta t} - [\Delta V_{bk}]_{(n+1)}^{t+\Delta t}$$

$$= - R_{bk}[i_{bk}]_{(n)}^{t+\Delta t} - \frac{l_{bk}}{s_{bk}}\frac{[KK]_{cb}}{\Delta t}\{[\hat{A}]_{cb}\}_{(n)}^{t+\Delta t} + [V_{bk}]_{(n)}^{t+\Delta t}$$

$$+ \frac{l_{bk}}{s_{bk}}\frac{[KK]_{cb}}{\Delta t}\{[\hat{A}]_{cb}\}^{t}. \tag{3.101}$$

The linearization of equation (3.66) is

$$[\Delta i_b]_{(n+1)}^{t+\Delta t} - [C_1][\Delta i_e]_{(n+1)}^{t+\Delta t} = -[i_b]_{(n)}^{t+\Delta t} + [C_1][i_e]_{(n)}^{t+\Delta t} \tag{3.102}$$

The linearization of equation (3.67) is

$$[C_2][\Delta V_b]_{(n+1)}^{t+\Delta t} + 2\{[R_e] + \frac{[L_e]}{\Delta t}\}[\Delta i_e]_{(n+1)}^{t+\Delta t}$$

$$= -[C_2][V_b]_{(n)}^{t+\Delta t} - 2\{[R_e] + \frac{[L_e]}{\Delta t}\}[i_e]_{(n)}^{t+\Delta t} + 2\frac{[L_e]}{\Delta t}[i_e]^{t} \tag{3.103}$$

3.7.4 Linearization of Equations for External Circuits

The linearization of equation (3.68) is

$$\begin{aligned} & \{[R_{sb}] + \frac{[L_{sb}]}{\Delta t}\}[\Delta i_{sb}]_{(n+1)}^{t+\Delta t} + \frac{[C_{sb}]}{\Delta t}[\Delta V_{sb}; \Delta V_t]_{(n+1)}^{t+\Delta t} \\ = \; - \; & \{[R_{sb}] + \frac{[L_{sb}]}{\Delta t}\}[i_{sb}]_{(n)}^{t+\Delta t} - \frac{[C_{sb}]}{\Delta t}[V_{sb}; V_t]_{(n)}^{t+\Delta t} \\ + \; & \frac{[L_{sb}]}{\Delta t}[i_{sb}]^t + \frac{[C_{sb}]}{\Delta t}[V_{sb}; V_t]^t \end{aligned} \tag{3.104}$$

The linearization of equation (3.69) is

$$[C_3][\Delta i_{sb}]_{(n+1)}^{t+\Delta t} + [C_4][\Delta i_s]_{(n+1)}^{t+\Delta t} = -[C_3][i_{sb}]_{(n)}^{t+\Delta t} - [C_4][i_s]_{(n)}^{t+\Delta t} \tag{3.105}$$

3.8 Assembly of All the Equations

3.8.1 Assembly of the Element Equations

Every triangle element in the solution domain has an element matrix. To build up the contributions of all the triangle element, we need to combine all the element matrices into one global matrix, this process is often referred to as the assembling process. Details of this process are illustrated below.

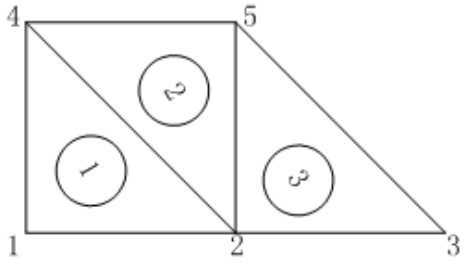

Figure 3.4: Sample Field Domain in Assembling Process (5 Nodes, 3 Elements)

As shown in Fig. 3.4, it is assumed that the field domain is divided into 3 triangle elements with 5 nodes. The element matrices of the three elements are:

- element 1, nodes $(1, 2, 4)$

$$\begin{pmatrix} S_{11} & S_{12} & S_{14} \\ S_{21} & S_{22} & S_{24} \\ S_{41} & S_{42} & S_{44} \end{pmatrix} \begin{pmatrix} \hat{A}_1 \\ \hat{A}_2 \\ \hat{A}_4 \end{pmatrix} = \begin{pmatrix} p_1 \\ p_2 \\ p_4 \end{pmatrix} \tag{3.106}$$

- element 2, nodes $(2, 5, 4)$

$$\begin{pmatrix} S_{22} & S_{25} & S_{24} \\ S_{52} & S_{55} & S_{54} \\ S_{42} & S_{45} & S_{44} \end{pmatrix} \begin{pmatrix} \hat{A}_2 \\ \hat{A}_5 \\ \hat{A}_4 \end{pmatrix} = \begin{pmatrix} p_2 \\ p_5 \\ p_4 \end{pmatrix} \tag{3.107}$$

- element 3, nodes $(2, 3, 5)$

$$\begin{pmatrix} S_{22} & S_{23} & S_{25} \\ S_{32} & S_{33} & S_{35} \\ S_{52} & S_{53} & S_{55} \end{pmatrix} \begin{pmatrix} \hat{A}_2 \\ \hat{A}_3 \\ \hat{A}_5 \end{pmatrix} = \begin{pmatrix} p_2 \\ p_3 \\ p_5 \end{pmatrix}. \tag{3.108}$$

Since there are 5 nodes totally, the size of the global coefficient matrix $[S]$ is 5×5 and the size of force matrix $[p]$ is 5×1. The initial value of $[S]$ and $[p]$ are set to be 0,

$$[S] = \begin{pmatrix} 0 & 0 & 0 & 0 & 0 \\ 0 & 0 & 0 & 0 & 0 \\ 0 & 0 & 0 & 0 & 0 \\ 0 & 0 & 0 & 0 & 0 \\ 0 & 0 & 0 & 0 & 0 \end{pmatrix} \tag{3.109}$$

$$[p] = \begin{pmatrix} 0 & 0 & 0 & 0 & 0 \end{pmatrix}^{tr} \tag{3.110}$$

Since element 1 is made up by nodes $(1, 2, 4)$, the coefficients of its element matrix will be added up to column $1, 2, 4$ and row $1, 2, 4$ of the global matrix. Equations (3.111) and (3.112) show the updated matrices $[S]$ and $[p]$ after element 1 is assembled,

$$[S] = \begin{pmatrix} S_{11}^{(1)} & S_{12}^{(1)} & 0 & S_{14}^{(1)} & 0 \\ S_{21}^{(1)} & S_{22}^{(1)} & 0 & S_{24}^{(1)} & 0 \\ 0 & 0 & 0 & 0 & 0 \\ S_{41}^{(1)} & S_{42}^{(1)} & 0 & S_{44}^{(1)} & 0 \\ 0 & 0 & 0 & 0 & 0 \end{pmatrix} \tag{3.111}$$

$$[p] = \begin{pmatrix} p_1^{(1)} & p_2^{(1)} & 0 & p_4^{(1)} & 0 \end{pmatrix}^{tr} \tag{3.112}$$

where the superscripts $^{(1)}$ denote the index number of the triangular elements, the subscripts $_{11,12}, \ldots$ denote the index number of the nodes and $(\ldots)^{tr}$ denotes the transpose operation of a matrix.

Repeating the similar process for element 2 and 3, the final global matrix after assembly process is

$$[S][\hat{A}] = [p] \tag{3.113}$$

where

$$[S] = \begin{pmatrix} S_{11}^{(1)} & S_{12}^{(1)} & 0 & S_{14}^{(1)} & 0 \\ S_{21}^{(1)} & S_{22}^{(1)+(2)+(3)} & S_{23}^{(3)} & S_{24}^{(1)+(2)} & S_{25}^{(2)+(3)} \\ 0 & S_{32}^{(3)} & S_{33}^{(3)} & 0 & S_{35}^{(3)} \\ S_{41}^{(1)} & S_{42}^{(1)+(2)} & 0 & S_{44}^{(1)+(2)} & S_{45}^{(2)} \\ 0 & S_{52}^{(2)+(3)} & S_{53}^{(3)} & S_{54}^{(2)} & S_{55}^{(2)+(3)} \end{pmatrix},$$

$$[\hat{A}] = \begin{pmatrix} \hat{A}_1 & \hat{A}_2 & \hat{A}_3 & \hat{A}_4 & \hat{A}_5 \end{pmatrix}^{tr},$$

$$[p] = \begin{pmatrix} p_1^{(1)} & p_2^{(1)+(2)+(3)} & p_3^{(3)} & p_4^{(1)+(2)} & p_5^{(2)+(3)} \end{pmatrix}^{tr},$$

3.8.2 Global System of Equations

Applying the above assembly process for all the elemental equations (equation (3.96) and combining with the other circuit equations (equations (3.100)-(3.103)) yields a linear set of algebraic equations. In combination with the equations for mechanical motion (equations (3.70) and (3.71)), we can get a global system of equations

$$[GML][\Delta X]_{(n+1)}^{t+\Delta t} = [GMR1][X]_{(n)}^{t+\Delta t} + [GMR2][X]^t + [SOURCE], \tag{3.114}$$

and

$$(\frac{J_r}{\Delta t} + B_f)\omega_m^{t+\Delta t} = \frac{J_r}{\Delta t} \cdot \omega_m^t + T_{em} - T_f \tag{3.115}$$

$$\frac{1}{\Delta t}\theta_m^{t+\Delta t} - \omega_m^{t+\Delta t} = \frac{1}{\Delta t}\theta_m^t \tag{3.116}$$

where

$$[GML] = \begin{bmatrix} \{\frac{\nu}{4\Delta}[SS]+ \frac{1}{\nu^2 B\Delta}\frac{\partial\nu}{\partial B}[ff] +\frac{\sigma\Delta}{12\Delta t}[TT]\} & 0 & -\frac{\Delta}{3}\frac{\sigma}{l}[O_i] & 0 & 0 & 0 & 0 \\ \frac{l}{ms}\frac{[KK]_{sp}}{\Delta t} & \{R_s +\frac{L_e}{\Delta t}\} & 0 & 0 & 0 & -1 & 0 \\ \frac{l_{bk}}{s_{bk}}\frac{[KK]_{cb}}{\Delta t} & 0 & -1 & R_{bk} & 0 & 0 & 0 \\ 0 & 0 & 0 & 1 & -[C_1] & 0 & 0 \\ 0 & 0 & [C_2] & 0 & 2\{[R_e] +\frac{[L_e]}{\Delta t}\} & 0 & 0 \\ 0 & 0 & 0 & 0 & 0 & \frac{[C_{sb}]}{\Delta t} & \{[R_{sb}] +\frac{[L_{sb}]}{\Delta t}\} \\ 0 & [C_4] & 0 & 0 & 0 & 0 & [C_3] \end{bmatrix}$$

$$[GMR1] = \begin{bmatrix} -\{\frac{\nu}{4\Delta}[SS]+ \frac{\sigma\Delta}{12\Delta t}[TT]\} & 0 & \frac{\Delta}{3}\frac{\sigma}{l}[O_i] & 0 & 0 & 0 & 0 \\ -\frac{l}{ms}\frac{[KK]_{sp}}{\Delta t} & -\{R_s +\frac{L_e}{\Delta t}\} & 0 & 0 & 0 & 1 & 0 \\ -\frac{l_{bk}}{s_{bk}}\frac{[KK]_{cb}}{\Delta t} & 0 & 1 & -R_{bk} & 0 & 0 & 0 \\ 0 & 0 & 0 & -1 & [C_1] & 0 & 0 \\ 0 & 0 & -[C_2] & 0 & -2\{[R_e] +\frac{[L_e]}{\Delta t}\} & 0 & 0 \\ 0 & 0 & 0 & 0 & 0 & -\frac{[C_{sb}]}{\Delta t} & -\{[R_{sb}] +\frac{[L_{sb}]}{\Delta t}\} \\ 0 & -[C_4] & 0 & 0 & 0 & 0 & -[C_3] \end{bmatrix}$$

$$[GMR2] = \begin{bmatrix} \frac{\sigma\Delta}{12\Delta t}[TT] & 0 & 0 & 0 & 0 & 0 & 0 \\ \frac{l}{ms}\frac{[KK]_{sp}}{\Delta t} & \frac{L_e}{\Delta t} & 0 & 0 & 0 & 0 & 0 \\ \frac{l_{bk}}{s_{bk}}\frac{[KK]_{cb}}{\Delta t} & 0 & 0 & 0 & 0 & 0 & 0 \\ 0 & 0 & 0 & 0 & 0 & 0 & 0 \\ 0 & 0 & 0 & 0 & 2\frac{[L_e]}{\Delta t} & 0 & 0 \\ 0 & 0 & 0 & 0 & 0 & \frac{[C_{sb}]}{\Delta t} & \frac{[L_{sb}]}{\Delta t} \\ 0 & 0 & 0 & 0 & 0 & 0 & 0 \end{bmatrix}$$

$$[SOURCE] = \begin{bmatrix} \frac{\nu\mu_0}{2}\{M_{rx}[c_i] - M_{ry}[b_i]\} & 0 & 0 & 0 & 0 & 0 & 0 \end{bmatrix}^{tr}$$

$$[X] = \begin{bmatrix} [A] & [i_s] & [V_{bk}] & [i_{bk}] & [i_{ek}] & [V_{sb}; V_t] & [i_{sb}] \end{bmatrix}^{tr}$$

$$[\Delta X] = \left[\begin{array}{ccccccc} [\Delta A] & [\Delta i_s] & [\Delta V_{bk}] & [\Delta i_{bk}] & [\Delta i_{ek}] & [\Delta V_{sb}; \Delta V_t] & [\Delta i_{sb}] \end{array} \right]^{tr}$$

The first line of equation (3.114) represents all the field equations. The second line represent the equations for stator phase circuits. The third, fourth and fifth lines represent all the equations for cage bars. The sixth and seventh lines represent all the equations for external circuits. In the resultant matrix equation, $[GML]$ is the coefficient matrix. It is non-symmetrical due to the coupling of circuits equations and mechanical motion equations. $[\Delta X]$ is the solution vector where

n	denotes the n^{th} Newton-Raphson iteration
$[\Delta A]$	denotes the incremental nodal vector potential solution
$[\Delta i_s]$	denotes the incremental stator phase currents
$[\Delta V_{bk}]$	denotes the incremental cage bar voltages
$[\Delta i_{bk}]$	denotes the incremental cage bar currents
$[\Delta i_{ek}]$	denotes the incremental currents of the end rings
$[\Delta V_{sb}; \Delta V_t]$	denotes the incremental terminal voltages of the external circuits and the electric machines
$[\Delta i_{sb}]$	denotes the incremental currents of the external circuits

The solution vector $[\Delta X]$ is updated at each Newton-Raphson iteration until the incremental solution vector becomes within a prescribed tolerance. The known input sources are the permanent magnet excitation $\frac{\nu\mu_0}{2}\{M_{rx}[c_i] - M_{ry}[b_i]\}$ and some terminal voltages applied to the external circuits.

3.9 Application of Boundary Conditions

Before the global system of equations can be solved for the unknown vector $[\Delta X]$, boundary conditions need to be imposed on the solution domain. The two most important boundary conditions in finite element analysis are the Dirichlet and periodical boundary conditions.

3.9.1 Dirichlet Boundary Condition

In most practical problems one or more of the unknown vector values will be specified as fixed. Such cases most commonly arise where a flux-line boundary is specified at a machine surface or where for some reason the vector value is known to have certain values. In Fig. 3.5, the Dirichlet boundary conditions are imposed on the surfaces of the stator and the shaft, which is

$$A|_{\widehat{AEC}} = A|_{\widehat{BFD}} = 0. \tag{3.117}$$

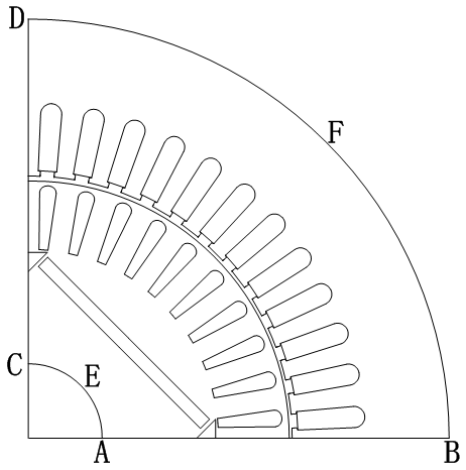

Figure 3.5: Boundaries of a Quarter of Machine

This boundary condition is imposed by assigning the specified values to the vectors on the boundary. In the assembly process, some rows and columns have to be modified.

Let the set of all the unknown vectors $[X]$ be divided into two parts: the free vectors $[X_{fr}]$ and the vectors with fixed values $[X_{fi}]$. Recalling equation (3.74), we can get the iterative process for the set of equations $[f]_{k\times 1} = [K]_{k\times k}[X]_{k\times 1} = [Q]_{k\times 1}$ is:

$$[X]^{(n+1)} = [X]^{(n)} + \{[J]^{(n)}\}^{-1}\{[Q] - [f]^{(n)}\} \tag{3.118}$$

where $[J] = \frac{\partial f_i}{\partial X_j}, (i, j = 1, 2, \ldots, k)$ is the Jacobian matrix and n is the iteration step number.

To include the vectors with fixed values into the iteration process, equation (3.118) can be modified as

$$\begin{pmatrix} X_f r \\ X_f i \end{pmatrix}^{(n+1)} = \begin{pmatrix} X_f r \\ X_f i \end{pmatrix}^{n} + \begin{pmatrix} [J^{(n)}] & 0 \\ 0 & [I] \end{pmatrix}^{-1} \begin{pmatrix} [Q] - [f]^{(n)} \\ 0 \end{pmatrix} \tag{3.119}$$

where $[I]$ is the identity matrix.

The inclusion of the segment of identity matrix with $[J]$ is necessary to guarantee that the modified Jacobian matrix is nonsingular and equation (3.119) is solvable. From equation (3.119) we can see that the fixed vector values $[X_{fi}]$ are not altered by the iteration. In other words, the Dirichlet boundary condition is satisfied using equation (3.119). In practice, if the row number of the global matrix corresponds to a vector with a fixed value (or the vector meets the Dirichlet boundary condition), the fixed value is assigned to this vector. In the iterative process, row of the identity matrix is substituted in the Jacobian matrix and zero entry is substituted in the right-hand vector.

3.9.2 Periodical Boundary Condition

In electric machine problems, there arise boundary conditions which do not correspond to explicit knowledge of unknown vectors or derivatives, but merely state that the vector value at one point is linearly related to the value at another point. The most common occurrence of this kind of conditions arise in connection with the analysis of loaded machines. When an electric machine operates under load and at a power factor different from zero, the pole axis is no longer an axis of symmetry and is not a flux line boundary. However the stator conductors in one pole pitch carrying currents in one direction have their equivalent and identical conductors in the next pole-pitch but carrying current in the opposite direction. As a result, the vector potentials one pole pitch apart have equal magnitude but opposite sign. In Fig. 3.5, the relationship between the potential values at different positions are:

$$A|_{AB} = -A|_{CD}. \tag{3.120}$$

Similarly there occur other cases, in which the potentials of any two points are identical both in magnitude and sign. All these purely periodic cases can be represented by the constraint

$$A_{p1} = \pm A_{p2} \tag{3.121}$$

where A_{p1} and A_{p2} are the potential values on the anti-periodical boundaries.

When imposing periodical boundary conditions one always deals with only two triangles at a time. Hence it is only necessary to derive the matrix operation involved in imposing such periodical condition on a pair of triangles only. Fig. 3.6 shows two triangles $(1, 2, 3)$ and $(4, 5, 6)$ having two nodes of each triangle on the pole axis. Therefore,

$$\begin{aligned} A_1 &= \pm A_5, \\ A_3 &= \pm A_6. \end{aligned} \tag{3.122}$$

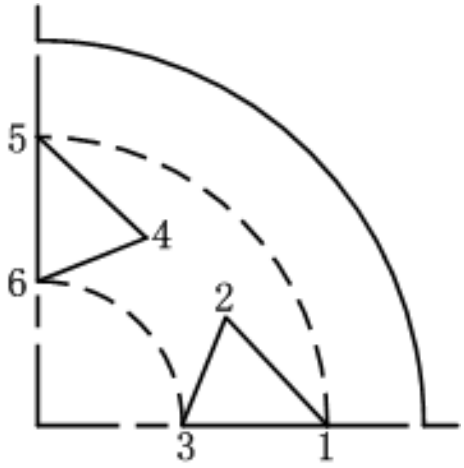

Figure 3.6: Application of the Periodical Boundary Condition

Recalling equation (3.118), the iterative process for these two triangles is

$$[A]^{(n+1)} = [A]^{(n)} + [J]^{-1}[P_R] \tag{3.123}$$

where

$$[A] = \begin{pmatrix} A_1 & A_2 & A_3 & A_4 & A_5 & A_6 \end{pmatrix}^{tr}, \tag{3.124}$$

$$[J] = \begin{pmatrix} J_{11} & J_{12} & J_{13} & 0 & 0 & 0 \\ J_{21} & J_{22} & J_{23} & 0 & 0 & 0 \\ J_{31} & J_{32} & J_{33} & 0 & 0 & 0 \\ 0 & 0 & 0 & J_{44} & J_{45} & J_{46} \\ 0 & 0 & 0 & J_{54} & J_{55} & J_{56} \\ 0 & 0 & 0 & J_{64} & J_{65} & J_{66} \end{pmatrix}, \tag{3.125}$$

and

$$[P_R] = [Q] - [f]^{(n)} = \begin{pmatrix} P_{R1} & P_{R2} & P_{R3} & P_{R4} & P_{R5} & P_{R6} \end{pmatrix}^{tr}. \tag{3.126}$$

Rewriting equation (3.123) in terms of potential changes during the n_{th} step, one has

$$[J][\Delta A]^{(n+1)} = [P_R] \tag{3.127}$$

If it is assumed that $[\Delta A']$ represents the total incremental vector potential for the connected triangles and the sum of the individual incremental potential vectors for the unconnected triangle is represented by $[\Delta A]$, then these can be related by a connection matrix $[C]$ in the following manner

$$[\Delta A] = [C] \cdot [\Delta A'] \tag{3.128}$$

where

$$[\Delta A'] = \begin{pmatrix} \Delta A_1 \\ \Delta A_2 \\ \Delta A_3 \\ \Delta A_4 \end{pmatrix}, [C] = \begin{pmatrix} 1 & 0 & 0 & 0 \\ 0 & 1 & 0 & 0 \\ 0 & 0 & 1 & 0 \\ 0 & 0 & 0 & 1 \\ \pm 1 & 0 & 0 & 0 \\ 0 & 0 & \pm 1 & 0 \end{pmatrix}, [\Delta A] = \begin{pmatrix} \Delta A_1 \\ \Delta A_2 \\ \Delta A_3 \\ \Delta A_4 \\ \Delta A_5 \\ \Delta A_6 \end{pmatrix}.$$

The similar operations can be applied on the right hand side matrix $[P_R]$ and $[P'_R]$ can be used to represent the total connected vectors, thus

$$[P'_R] = [C_t] \cdot [P_R] \tag{3.129}$$

where

$$[P'_R] = \begin{pmatrix} P'_{R1} \\ P'_{R2} \\ P'_{R3} \\ P'_{R4} \end{pmatrix} = \begin{pmatrix} P_{R1} \pm P_{R5} \\ P_{R2} \\ P_{R3} \pm P_{R6} \\ P_{R4} \end{pmatrix}, [C_t] = \begin{pmatrix} 1 & 0 & 0 & 0 & \pm 1 & 0 \\ 0 & 1 & 0 & 0 & 0 & 0 \\ 0 & 0 & 1 & 0 & 0 & \pm 1 \\ 0 & 0 & 0 & 1 & 0 & 0 \end{pmatrix}.$$

Substituting equation (3.128) into equation (3.127) yields

$$[P_R] = [J][\Delta A] = [J][C][\Delta A'] \tag{3.130}$$

Combining equation (3.130) and (3.129) yields

$$[P'_R] = [C_t][P_R] = [C_t][J][C][\Delta A']. \tag{3.131}$$

Since

$$[P'_R] = [J'] \cdot [\Delta A'] \tag{3.132}$$

where $[J']$ is the Jacobian matrix after applying periodical boundary conditions, then comparing equation (3.132) and (3.131) yields

$$[J'] = [C_t][J][C] = \begin{pmatrix} J_{11} + J_{55} & J_{12} & J_{13} + J_{56} & \pm J_{54} \\ J_{21} & J_{22} & J_{23} & 0 \\ J_{31} + J_{65} & J_{32} & J_{33} + J_{66} & \pm J_{64} \\ \pm J_{45} & 0 & \pm J_{46} & J_{44} \end{pmatrix} \tag{3.133}$$

or

$$[J'] = \begin{pmatrix} J_{11} & J_{12} & J_{13} & 0 \\ J_{21} & J_{22} & J_{23} & 0 \\ J_{31} & J_{32} & J_{33} & 0 \\ 0 & 0 & 0 & 0 \end{pmatrix} + \begin{pmatrix} J_{55} & 0 & J_{56} & \pm J_{54} \\ 0 & 0 & 0 & 0 \\ J_{65} & 0 & J_{66} & \pm J_{64} \\ \pm J_{45} & 0 & \pm J_{46} & J_{44} \end{pmatrix} \tag{3.134}$$

Therefore the iterative process after imposing periodical boundary condition is

$$[A']^{(n+1)} = [A']^{(n)} + [J']^{-1}[P'_R] \tag{3.135}$$

It can be seen that the inclusion of the periodical boundary conditions merely requires that certain matrix segments be assembled with altered signs. The rows and columns of these segments correspond to the nodes where periodical boundary conditions are applied.

3.10 The Storage and the Solution of the System of Equations

3.10.1 The Storage of the Coefficient Matrix

The resultant coefficient matrix of the system equations is a large sparse matrix. According to the methods used to solve the matrix equation, usually two strategies are employed to store the coefficient matrix: skyline storage and non-zero elements storage [83].

When the coefficient matrix is symmetric, banded and non-zero terms are clustered around the main diagonal, only the terms within the bandwidth of upper or lower triangle matrix need to be stored (Fig. 3.7). In this case, the skyline method can be used to store the terms between the first non-zero element and the diagonal element of each row. In this model, certain zero terms are still contained which occupy space in the computer memory. This storage is needed when using the Gaussian elimination method to solve the system of equations.

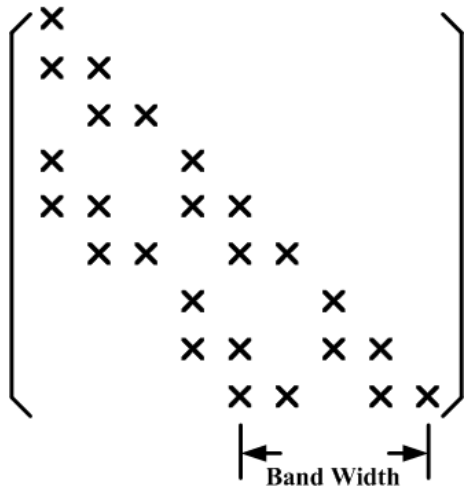

Figure 3.7: Skyline Storage of the System Matrix

When the iterative method is used to solve the system of equations, all the zero elements have no relation to the calculation of iteration, hence no zero elements need to be stored. Non-zero storage schemes (sparse storage schemes) allocate contiguous storage in memory for the nonzero elements of the matrix. These storage schemes include coordinate storage, compressed row storage, compressed column storage, etc [84]-[86]. To illustrate various storage formats, we use the nonsymmetric sparse matrix A as an example

$$A = \begin{pmatrix} 9 & -2 & 0 & 0 & 3 \\ 10 & 8 & 7 & 0 & 0 \\ 0 & 6 & 5 & 0 & 21 \\ 0 & 0 & 0 & 14 & 0 \\ 11 & 0 & 0 & 0 & -1 \end{pmatrix} \tag{3.136}$$

Coordinate storage is the most straightforward scheme to denote a sparse matrix by simply recording each nonzero entry together with its row and column index. For the nonsymmetric sparse matrix A, we create three vectors: one for floating point numbers $'val'$ and the other two for integers $'row-ind', 'col-ind'$. The $'val'$ vector stores the values of the nonzero elements of the matrix. The $'row-ind'$ and $'col-ind'$ vectors store the row indexes and column indexes of the elements in the $'val'$ vector respectively. Thus the matrix A in (3.136) can be stored as Table 3.1.

Table 3.1: Coordinate Storage of the Coefficient Matrix

val	9	-2	3	10	8	7	6	5	21	14	11	-1
row-ind	1	1	1	2	2	2	3	3	3	4	5	5
col-ind	1	2	5	1	2	3	2	3	5	4	1	5

The compressed row storage scheme views non-zero elements in each row as a sparse vector. The non-zero element values and their column indexes are stored in vectors $'val'$ and $'col-ind'$ respectively. The locations of the non-zero elements in vector $'val'$ that start a row are stored in vector $'row-ptr'$. An additional element

is appended to the $row - ptr$ array specifying the number of nonzero elements. Thus the matrix A in (3.136) can be stored as Table 3.2.

Table 3.2: Compressed Row Storage of the Coefficient Matrix

row-ptr	1	4	7	10	11	12						
val	9	-2	3	10	8	7	6	5	21	14	11	-1
col-ind	1	2	5	1	2	3	2	3	5	4	1	5

Analogous to compressed row storage, there is compressed column storage, which is also called the Harwell-Boeing sparse matrix format [87]. The compressed column storage format parallels compressed row storage, but with the roles of rows and columns reversed. With the compressed column storage scheme, the matrix A in (3.136) can be stored as Table 3.3.

Table 3.3: Compressed Column Storage of the Coefficient Matrix

col-ptr	1	4	7	10	11	12						
val	9	10	11	-2	8	6	7	5	14	3	21	-1
row-ind	1	2	5	1	2	3	2	3	4	1	3	5

The non-zero storage formats are the most general: they make absolutely no assumptions about the sparsity structure of the matrix, and they do not store any unnecessary elements. Comparing with the skyline storage, the non-zero elements storage is much more economical for saving the computer memory. But the disadvantage is that more complex programming is needed to keep track of the terms stored.

Some of the popular sparse matrix formats have been used in numerical software packages such as ITPACK [88], NSPCG [89], SPARSPAK [90] and MATLAB [91]. In Matlab, the compressed column storage scheme is adopted. In this work the program is written in Matlab and the Matlab function of 'sparse' is used directly to convert a full matrix to sparse form by squeezing out any zero elements. Therefore the compressed column storage is used automatically.

3.10.2 Solving the Global System of Equations

The system of equations is non-symmetric linear. The solution algorithm of such matrix equations can generally be classified as direct methods and iterative methods [83].

The most commonly used direct method for non-symmetric linear system of equations is Gaussian elimination. Direct methods are characterized by always requiring a constant amount of work. Another class of methods, iterative methods, require a variable amount of work that depends on the problem being solved. The appeal of iterative methods is that they may require less work than a direct method for many problems. In particular, they are effective on large sparse linear systems.

Iterative methods are generally used to solve system of equations which is too large to be handled by direct methods. Iterative methods do not guarantee a solution for every system of equations. However, when they do yield a solution, they are usually less expensive than direct methods. Iterative methods can be expressed in the simple form

$$X^{(n+1)} = T \cdot X^{(n)} + C. \tag{3.137}$$

Depending on the nature of T and C, iterative methods can be classified into two main categories, stationary iterative methods and non-stationary iterative methods. In stationary method, the iterative matrix T and vector C stays the same throughout the iteration, while a new iterative matrix T or vector C is generated in every step of the non-stationary iterative methods. Conjugate gradient methods for symmetric positive definite problems and conjugate gradient look-alike methods for nonsymmetric problems are examples of nonstationary iterative methods [92].

Several conjugate gradient-like iterative solvers, such as bi-conjugate gradient iteration (BiCG), bi-conjugate iteration stabilized (BiCGSTAB), conjugate gradient squared iteration (CGS) and quasi minimal residual iteration (QMR), are available for solving general non-symmetric system of linear equations. They are particularly attractive to solve sparse matrices which are normally direct results of spatial discretization of differential equations [92, 93]. In this work, method of BiCG is used. The details of the method is shown in Appendix D.

3.11 The Calculation of Electromagnetic Torque

3.11.1 Introduction

Electromagnetic torque, T_{em}, is the motive that drive the rotor of a electric machine. The knowledge of the electromagnetic torque in terms of the rotation angle is very important for the designer to evaluate the performances and operating qualities of the machine. Electromagnetic forces and torques can be computed in a variety of methods. The three basic methods often employed with finite element analysis are Lorentz method [94], Energy methods [95, 96] and Maxwell's stress tensor method [8, 97].

Lorentz method is used to calculate electromagnetic forces acting on current carrying structures only. Although it is easy to cooperate with the finite element field solutions, it cannot be applied to determine forces acting on ferromagnetic structures, except where the reaction force of a single coil appears on the iron. Due to the limitation of the Lorentz method, it is ignored in our computation.

Electromagnetic torque can also be calculated by energy methods based on the principle of conservation of energy. The force acting on a movable part of a

device may be derived from the variation of the stored magnetic energy, W, or co-energy, W' of the entire device against small space displacement $\Delta\theta$ [8, 95]. The flux linkage λ and current I are kept constant while derived from energy and co-energy respectively. Although the method is quite straightforward and easy to implement, it suffers from two major shortcomings. First, important numerical errors may be introduced as a consequence of a small incremental choice of $\Delta\theta$. Second, the field computation has to be performed twice for one torque value, causing the computation time doubled.

The Coulomb virtual work method overcomes these shortcomings by taking direct, closed form differentiation of magnetic energy or co-energy of the free space region between the moveable and the fixed parts of the system under consideration. By this way, only one finite element solution is necessary.

Forces and torques can also be integrated using Maxwell stress tensor over any closed surface surrounding the moving body [8, 97]. Both the Coulomb's virtual work method and the Maxwell stress tensor method can be used to calculate the electromagnetic torque. These two methods have the following advantages [28, 96]:
(1) Both methods are applicable to any rigid body in the finite element problems.
(2) Both methods need only one field computation.
(3) Both methods require a single integration involving only air gap elements .
(4) Both methods can give similar results if a good surface is chosen for the Maxwell stress tensor method [98, 96].

In this work the Maxwell stress tensor method is used to calculated the electromagnetic torque.

3.11.2 Calculation of Torque with Maxwell Stress Tensor Method

The Maxwell stress tensor method is commonly used in the calculation of forces and torques in the finite element analysis of electrical devices. The Maxwell tensor can be expressed as

$$\sigma = \frac{1}{\mu_0}(B \cdot \vec{n})B - \frac{1}{2\mu_0}(B^2\vec{n}). \tag{3.138}$$

where σ is the Maxwell's stress tensor, B is the flux density and $\vec{n}$ is the unit normal vector

The torque applied to one part of the magnetic circuit can be obtained by integrating the Maxwell stress tensor along a path Γ placed in the air and enclosing this part. In the case of electric machines, this integration path is normally placed in the air gap and the torque can be calculated by

$$T = L \int_{\Gamma} (r \times \sigma) d\Gamma \tag{3.139}$$

where L is the axial length and r is the lever arm.

Since

$$B = B_n\vec{n} + B_t\vec{t} \tag{3.140}$$

and

$$B^2 = B_n^2 + B_t^2, \tag{3.141}$$

substituting equations (3.140) and (3.141) into equation (3.138) yields

$$\sigma = \frac{1}{2\mu_0}(B_n^2 - B_t^2)\vec{n} + \frac{1}{\mu_0}(B_n B_t)\vec{t} \tag{3.142}$$

where B_n and B_t are the normal and tangential components of flux density respectively, $\vec{t}$ is the unit tangential vector.

A closed integration path C with radius of r that surrounds the rotor in free space along the air-gap is chosen (Fig. 3.8). The force in the tangential component is

$$F_t = \frac{l}{\mu_0} \int_\Gamma (B_n B_t) d\Gamma \tag{3.143}$$

where l is the axial length of the electric machine.

In two-dimensional cases, since

$$B_r = B_n, \tag{3.144}$$

$$B_\theta = B_t, \tag{3.145}$$

$$d\Gamma = r \cdot d\theta$$

equation (3.143) can be rewritten as

$$F_t = \frac{l}{\mu_0} \oint_C B_r B_\theta r d\theta \tag{3.146}$$

where B_r and B_θ are the radial and tangential components of flux density.

In the two-dimensional electromagnetic field, the electromagnetic torque for the rotation of rotor is generated by the tangential component of force. Substituting equation (3.146) into equation (3.139) yields

$$T = r \times F_t = \frac{L}{\mu_0} \oint_C r^2 B_r B_\theta d\theta \tag{3.147}$$

If the solution were exact, the value of the torque calculated from equation (3.147) would be independent of the radius of r when r varies between the inner and outer radius of the air gap. However, in an approximate solution the integration path has an effect on the result [96, 27]. When first order triangular finite elements are used for the field computation, the best results are obtained when the integration

path crosses triangles at the middle of the edges [96, 99].

As shown in Fig. 3.8, the integration path is drawn in dash circular and it connected the middle points of two sides of the triangular element k. If only one pole of the electric machine is taken as the solution domain and the solution domain starts from θ_1 and ends at θ_2, the total electromagnetic torque is

$$T_{em} = \frac{2pl}{\mu_0} \int_{\theta_1}^{\theta_2} r^2 B_r B_\theta d\theta. \tag{3.148}$$

where p is the number of pole pairs.

Assume that in the air gap, there are N_e triangular elements on the integration path, then we can have

$$T_{em} = \frac{2plr^2}{\mu_0} \sum_{k=1}^{N_e} \int_{\theta_k}^{\theta_{k+1}} B_{kr} B_{k\theta} d\theta, \tag{3.149}$$

where B_k is the flux density of triangle element k.

Since

$$\begin{aligned} B_{kr} &= B_{kx} \cos\theta + B_{ky} \sin\theta \\ B_{k\theta} &= B_{ky} \cos\theta - B_{kx} \sin\theta \end{aligned}$$

finally the electromagnetic torque in discrete format is

$$\begin{aligned} T_{em} = \frac{2plr^2}{\mu_0} \sum_{k=1}^{N_e} [\quad & \frac{1}{2}(B_{ky}^2 - B_{kx}^2) \sin(\theta_{k+1} + \theta_k) \sin(\theta_{k+1} - \theta_k) \\ & + B_{kx} B_{ky} \cos(\theta_{k+1} + \theta_k) \sin(\theta_{k+1} - \theta_k)]. \end{aligned} \tag{3.150}$$

3.12 The Simulation of Rotor Motion

The rotor of an electric machine moves relative to the stator when the dynamic case is considered. To guarantee the continuity of the nodal unknowns in the

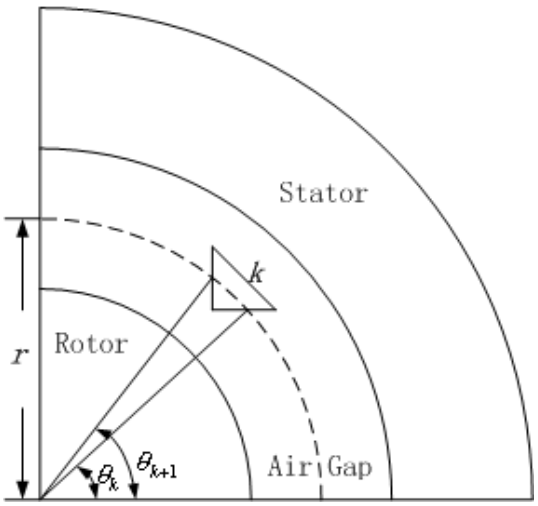

Figure 3.8: Integration Path of the Electromagnetic Torque

finite element analysis, the two different finite element meshes in the rotor and the stator have to be matched at the boundary between two regions. Several methods have been described in the literature to take into account the rotor movement. The known approaches can be broadly divided into two categories: (1) method of meshless air gap, (2) method of meshed airgap.

3.12.1 Meshless Air Gap

The air gap is not discretized, as shown in Fig. 3.9. In this case, Abdel-Razek [100, 101] presented the principle of air gap macro-element which is based on the Fourier analysis solution of the field in the air gap combined with a finite element analysis of the field in the rotor and the stator. The torque computed using this method is relatively more accurate, therefore it is adopted when high accuracy is required [102]. Another method of meshless air gap is the hybrid finite element-boundary element method in two dimensions [103, 104]. The boundary element method is applied to the region of air gap while the finite element method is applied to the regions of the stator and the rotor.

Both the macro-element and hybrid finite element-boundary element method

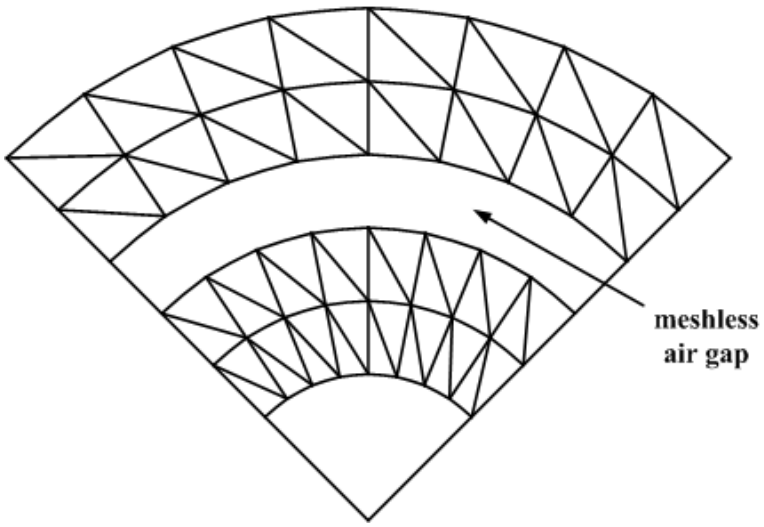

Figure 3.9: The Meshless Air Gap in Simulation of Rotor Motion

may reduce the number of unknowns and avoid the handling of triangular elements in the air gap region. However the sparsity of the stiffness matrix is lost because of the full matrix part contributed by the boundary element method and the analytical method. Due to the long time spent on assembly process, the efficiency of these methods are not guaranteed. This may be a disadvantage for dynamic problems, thus these two methods are not considered in our computation.

3.12.2 Meshed Air Gap

The air gap is discretised, as shown in Fig. 3.10. In this case, the air gap is subdivided into meshes and the rotation can take place by means of a layer of finite element placed in the air gap. This layer can occupy all the air gap region or just a part of it. Since the rotor is moving and the stator is fixed, this layer of meshes will distort as time going on (Fig. 3.11).

To avoid the need of remeshing the distorted elements, the Lagrange multipliers techniques [105] is used which allows a finite element mesh to move with respect to an adjacent mesh freely. At different positions, only the terms which

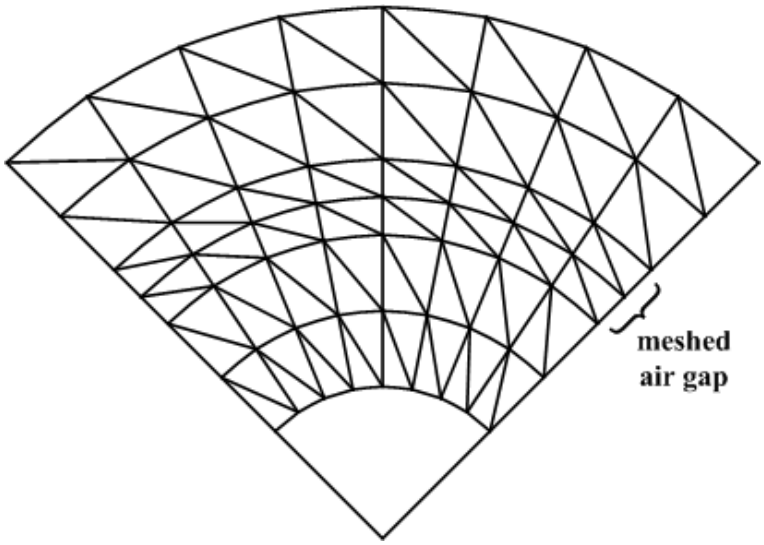

Figure 3.10: Triangular Element Subdivision of the Air Gap

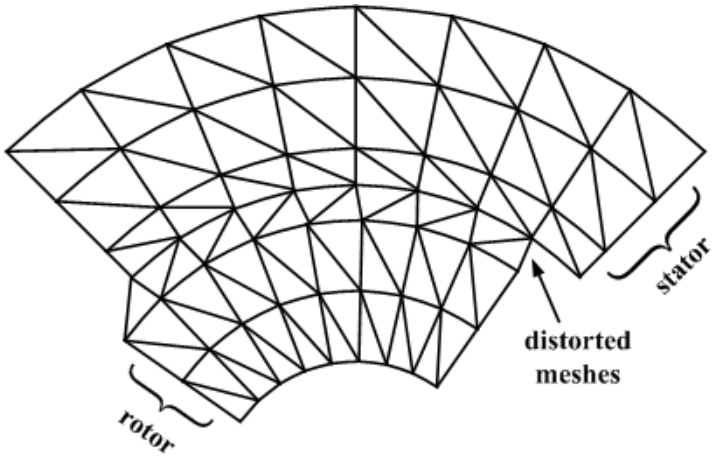

Figure 3.11: Triangular Element Subdivision of the Air Gap

couple the meshes together at the interface are altered. However the resultant matrix is weakly conditioned and new formulations are necessary for each problem [106]. The nodal interpolation method [107]-[109] avoids the remeshing also. However the continuity of the vector potential in [107] may not be guaranteed and the stiffness matrix in [108] may be singular [110]. Their efficiencies have not been tested on the electromagnetic force calculation yet. Therefore these two methods are not considered in our computation also.

Another technique of handling the distorted air gap elements is the method of moving band [111]. This method is based on the rotational moving band and successfully used to model the motion of rotating electric machine [98, 106, 112, 113]. In this method, the air gap is meshed and the translation displacement is taken into account by means of a layer of finite elements placed in the air gap (Fig. 3.12). The displacement is a function of the time step and the speed. At each step, the moving part is displaced (Fig. 3.13), so the elements of the moving band are distorted. When the distortion is large enough, the air gap is remeshed. Periodical or anti-periodical boundary condition(boundaries $\widehat{AB}$ and $\widehat{A'B'}$) are used to perform a dynamic allocation of domain nodes (Fig. 3.14). Thus the size of the corresponding matrices is not increased [98].

3.12.3 Simulation of Rotor Motion with Method of Moving Band

In this work, the method of moving band is used. The air gap is divided into three layers (Fig. 3.15). The inner layer is assigned to the rotor and it rotates together with the rotor, while the other two layers are assigned to the stator and are kept fixed. The second layer is the moving band.

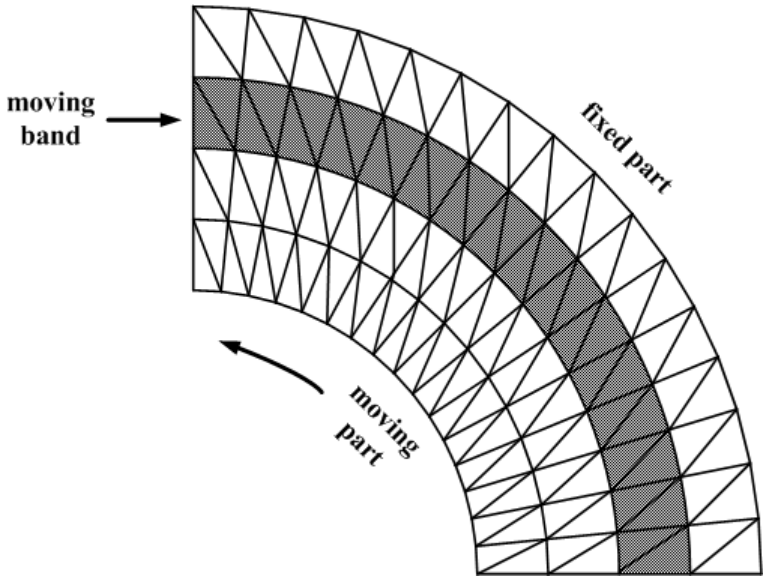

Figure 3.12: Moving Band in the Air Gap

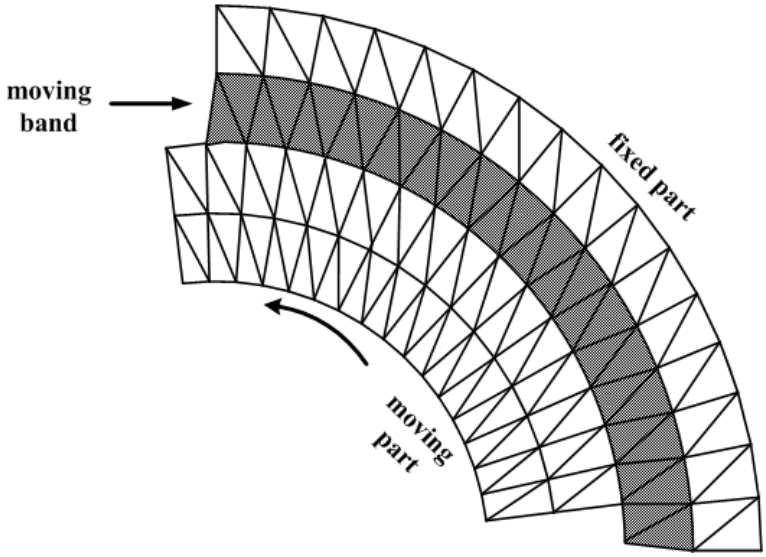

Figure 3.13: Moving Band With Rotor Displacement

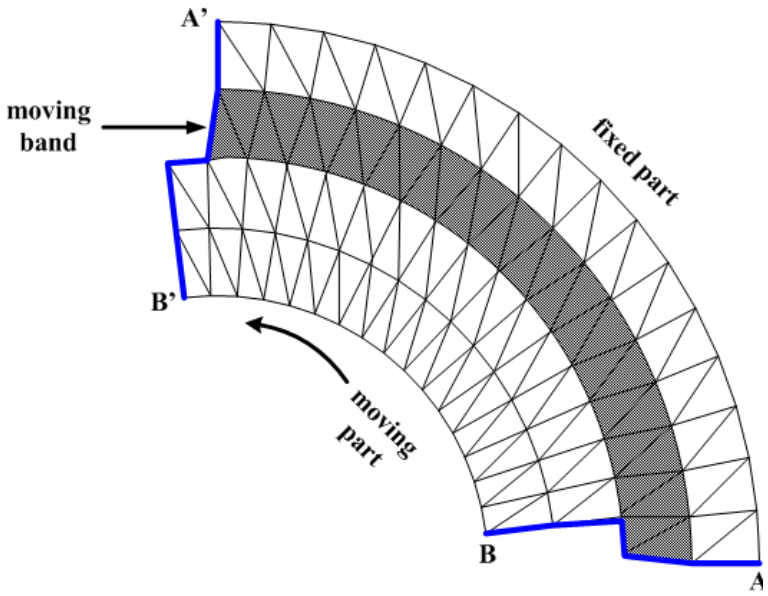

Figure 3.14: Boundary Conditions in Method of Moving Band

In order to avoid the generation of new nodes during the rotor movement [106, 112], The nodes on the interface boundary between the rotor and the stator are numbered twice (Fig. 3.15). One set of numbers $(1, 2, 3, \ldots, N_{bc})$ are assigned to the stationary region and the other set $(1', 2', 3', \ldots, N'_{bc})$ are assigned to the moving region, where N_{bc} is the number of nodes on the interface.

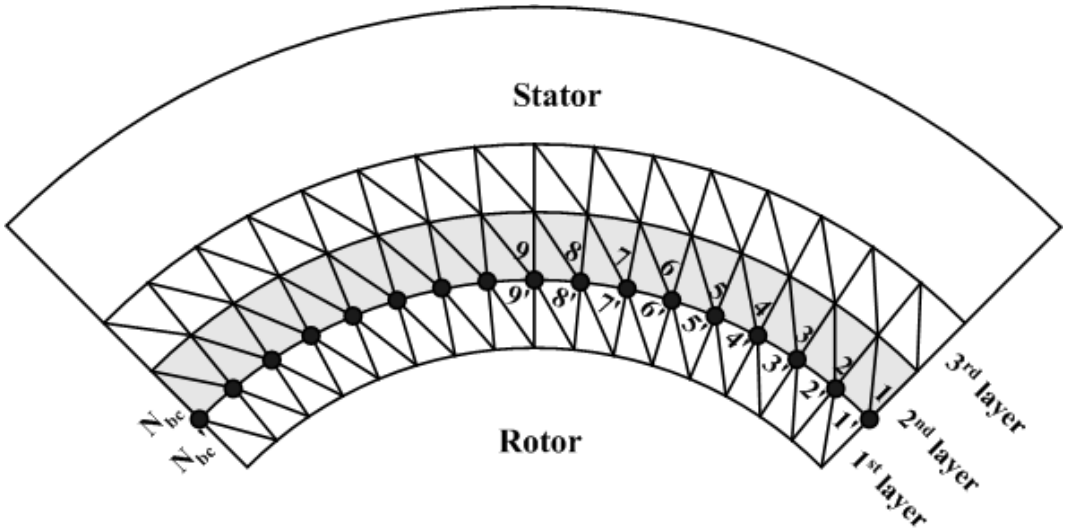

Figure 3.15: Three Layers in the Air Gap and the Numbering of Interface

At every time step of the movement, the coordinates of the nodes on the rotor side are changed while those on the stator side are fixed. If the displacement of this step is equal to the distance between two consecutive nodes, then there is no distortion in the moving band and a lot of effort can be saved (Fig. 3.16). This condition is easy to achieve by imposing some restrictions on the time step length or the meshes [114, 115]. For example, the interface between rotor and surface has to be subdivided into a number of equal intervals whose length must always be less than the movement associated with the smallest time-step. With the motor operating at any speed, the time-step length can be controlled to ensure that as the rotor moves, nodes on the interface always coincide peripherally. However, when coupled field and circuit or a dynamic case considered, the time step is variable. With electronic circuits, the length of the time-step is decided by the controller and the characteristics of the semiconductor components. Thus the rotor movement cannot always be coincident with the distance of consecutive nodes on the interface, thus the distortion in the air gap occurs or the continuity of the vector potential is broken (Fig. 3.17).

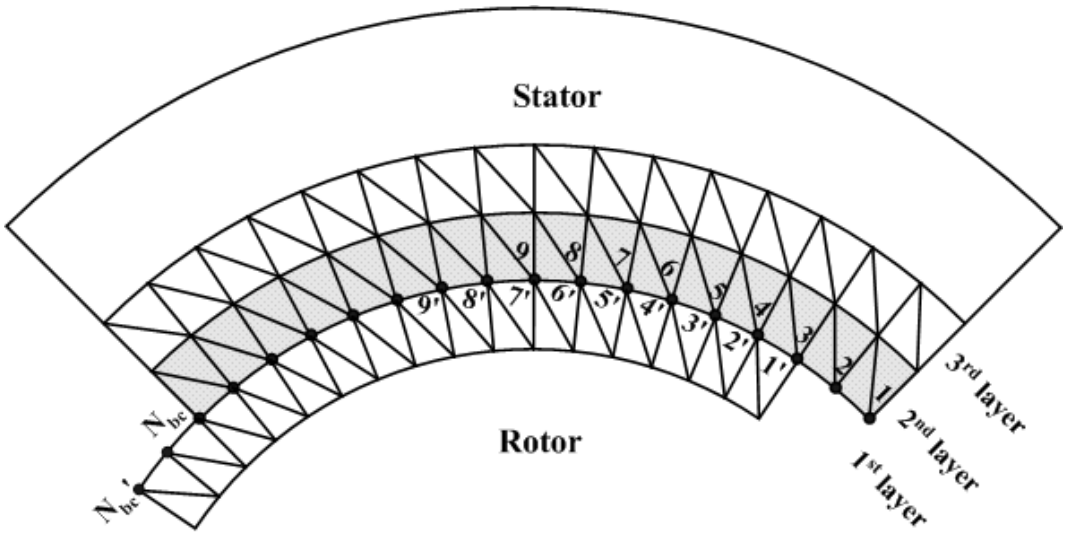

Figure 3.16: Movement of Rotor Without Distortion in the Air Gap

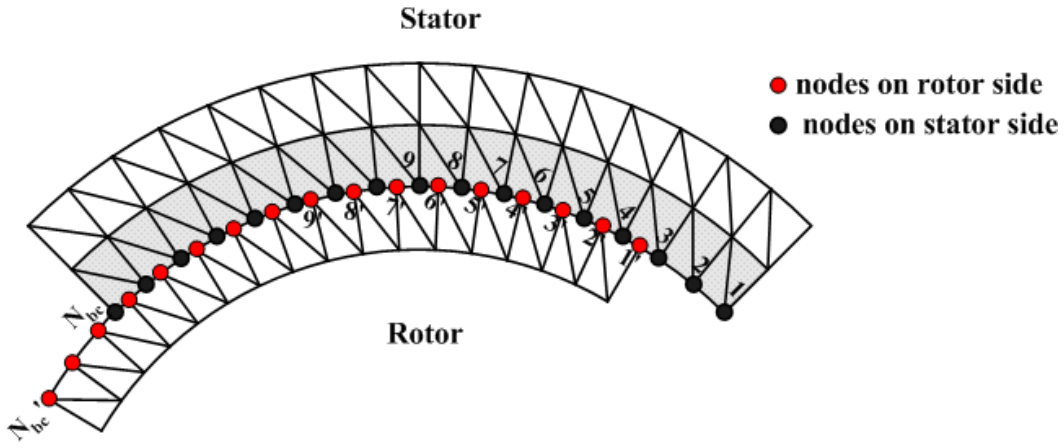

Figure 3.17: Movement of Rotor With Distortion in the Air Gap

When the rotor movement is not coincident with the distance of consecutive nodes on the interface, the finite elements in the moving band have to be remeshed. As shown in Fig. 3.18, the nodes of the moving band on the interface are relocated according to the rotor position. With the new node coordinates, the finite elements in the moving band are remeshed. The nodes on the interface of the rotor and stator are connected by the periodical or anti-periodical boundary conditions. As shown in Fig. 3.19, the boundary condition at this moment are

$$A|_{\Gamma_1} = -A|_{\Gamma_2}$$

$$A|_{\Gamma_3} = A|_{\Gamma_4}$$

Since only the nodes on the interface and the meshes in the moving band are handled every time, much computation time can be saved. and the effects of time step size on the meshes can also be eliminated.

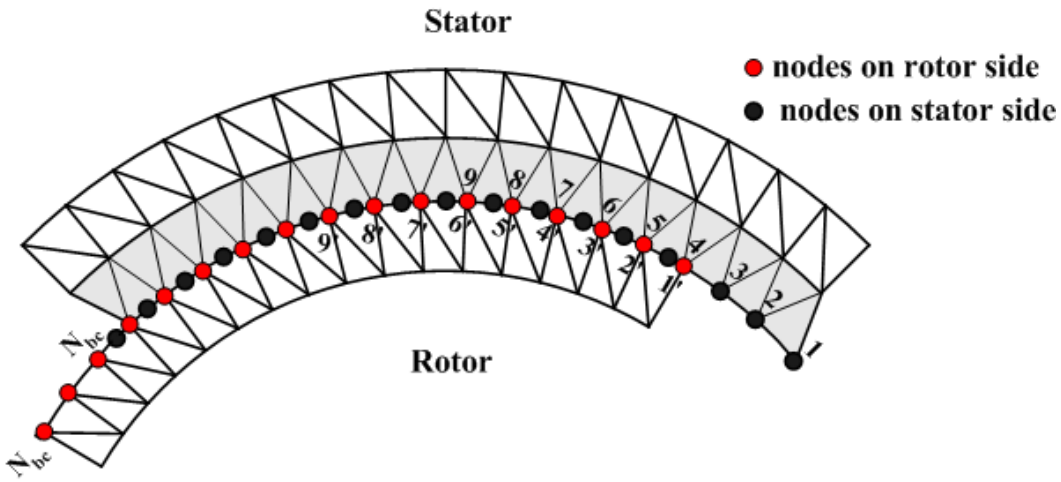

Figure 3.18: Relocation of the Moving Band Nodes on the Interface

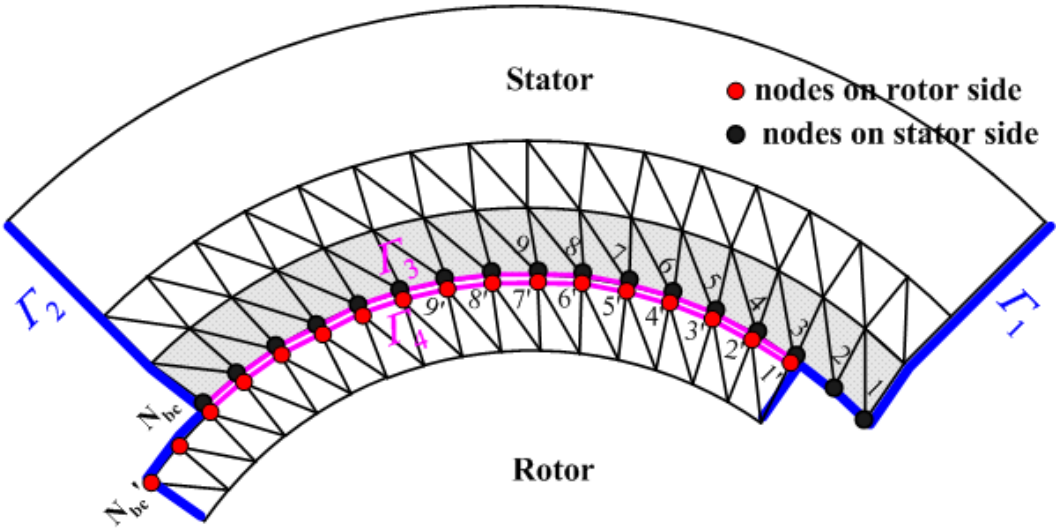

Figure 3.19: Connection of Interface Nodes Using Boundary Conditions

3.13 Conclusion

This chapter presented the complete process of field-circuit coupled time stepping finite element computation of line-start permanent magnet synchronous machine.

Most of the governing equations are space dependent or time dependent. The space dependent quantities can be formulated by the method of weighted residual. The time dependent quantities are evaluated by the time-stepping method and the backward Euler's method is recognized as one of the most stable ones. Since nonlinear materials are used for the iron cores of the stator and the rotor, the resultant global system of equations is nonlinear. Newton-Raphson iterative method can be chosen to solve these nonlinear equations and the cubic splines are used to represent the characteristics of the nonlinear materials. Because of the coupling of circuit equations, the resultant global coefficient matrix is non-symmetric also. To get the solution of this set of non-symmetrical linear equations, bi-conjugate gradient method can be used in each Newton-Raphson iteration. With the electromagnetic field solution, the motor torque can be calculated using Maxwell stress tensor method. Once the motor torque is available, the rotor speed and rotor position are obtainable with the mechanical motion equations. If we continue the computation with the new time and new position, the dynamic performance of the machine can be calculated step by step. The flow chart for this computation process is shown in Appendix E.

In general, this field-circuit coupled time stepping finite element computation process can be used to calculate the dynamics of any electric machine. It will be used to calculate the dynamics of a line-start permanent magnet synchronous machine in Chapter 5.

Chapter 4

Parameter Estimation of the Line-Start Permanent Magnet Synchronous Machines

4.1 Introduction

Permanent magnet synchronous machines are receiving much attention due to their high speed, power density and efficiency characteristics. New rotor configurations and the commercial availability of high field strength permanent magnets have reduced the cost of these machines. Permanent magnet synchronous machines now can provide a significant and affordable performance improvement in many applications. However, manufactures of such commercially available machines provide very little information about the parameters which are very important for implementing various types of controllers. Thus parameter estimation is extremely important for the operators of modern drives to implement high performance control. It is also invaluable for the machine designer and manufacturers wishing to do various simulation and analysis before the prototypes are made.

The testing and analysis of permanent magnet synchronous machines are based on the recognized equivalent circuit modelling. This equivalent circuit is based on the classical two-axis model and the parameters of this two-axis model

are the ones of interest in this work. These machine parameters usually consist of the synchronous reactance of direct axis X_d, the synchronous reactance of the quadrant axis X_q and the magnet induced voltage E_0.

The parameter determination of the permanent magnet synchronous machines are in principle similar to the procedures applied to conventional synchronous motors with wound rotors and slip rings. However, because of the permanent magnet excitation, classical methods applied to conventional synchronous machines are no longer appropriate. For example, without the ability to remove field excitation of the permanent magnet from the permanent magnet synchronous machine, the conventional methods of electrical parameter identification using the open circuit saturation curve, the short circuit current curve, the zero power factor curve or the slip test cannot be utilized [56].

To tackle the problems of parameter determination of permanent magnet synchronous machines, various techniques and methods have been used by many researchers [43] - [60]. In this work, the methods that were mostly used before by other researchers are reviewed first. Then two new methods are proposed by the implementation of linear regression and Hopfield neural network. Parameters calculated by finite element method are also presented.

4.2 Lumped Parameter Model of Permanent Magnet Synchronous Machines

The lumped parameter model of a permanent magnet synchronous machine is derived from generalized electrical machine theory. The standard two-axis theory with fixed rotor reference frame is used. A transformation that transforms the three-phase model to such and equivalent two-phase description is needed. It is desirable to utilize a particular transformation such that the representation of electrical power in the machine is preserved. As a result, the developed torques are invariant over the transformation. The Park's transformation is used to transform the variables from the stator reference frame *abc* to the rotor reference frame *dq*0 [116]. To keep the power invariant, the transformation is given by [117]:

$$\begin{bmatrix} f_{ds} \\ f_{qs} \\ f_{0s} \end{bmatrix} = \sqrt{\frac{2}{3}} \begin{bmatrix} \sin\theta_e & \sin(\theta_e - 2\pi/3) & \sin(\theta_e + 2\pi/3) \\ \cos\theta_e & \cos(\theta_e - 2\pi/3) & \cos(\theta_e + 2\pi/3) \\ \sqrt{1/2} & \sqrt{1/2} & \sqrt{1/2} \end{bmatrix} \begin{bmatrix} f_{as} \\ f_{bs} \\ f_{cs} \end{bmatrix}, \tag{4.1}$$

where f_{ds}, f_{qs} and f_{0s} are the direct, quadrature and zero-sequence quantities, respectively.

Fig. 4.1 shows the trigonometric interpretation of the change of stator variables using Park's transformation. In Fig. 4.1, θ_m is the rotor angle, θ_e is the rotor electrical angle, which equals to the number of pole pairs times θ_m. ω_m denotes the mechanical speed of the rotor and its positive direction is assumed to be counterclockwise. The rotor position is decided by

$$\theta_m = \theta_0 + \int_0^t \omega_m dt \tag{4.2}$$

where θ_0 is the initial rotor position.

Equation (4.1) can be written in a more compact form of:

$$\boldsymbol{f}_{dq0s} = \boldsymbol{K}\boldsymbol{f}_{abcs}, \tag{4.3}$$

where $\boldsymbol{f}$ represents any of the stator voltage, current or flux-linkage vector and $\boldsymbol{K}$ is Park's transformation matrix. The directions of f_{as}, f_{bs} and f_{cs} shown in Fig. 4.1 are the positive direction of the magnetic axes of the stator windings of phases a, b and c, respectively. The direction of f_{ds} is designated to be the positive direction of the rotor permanent magnet flux, while f_{qs} leads f_{ds} by 90 electrical degrees. The zero-sequence variable, f_{0s}, is zero for balanced condition and will be neglected in the following analysis.

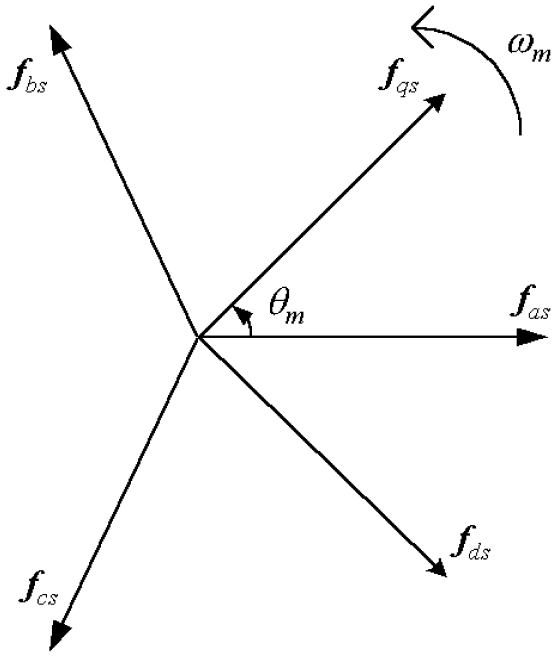

Figure 4.1: Trigonometric Interpretation of the Change of Stator Variables

Applying such a transformation to the variables of a three-phase interior permanent magnet synchronous machine, the three-phase symmetrical windings A, B and C can be replaced by equivalent two-phase windings d and q as shown in

Fig. 4.2, in which the magnets are identified by i_f and the rotor cage is represented by equivalent shorted D and Q windings [50].

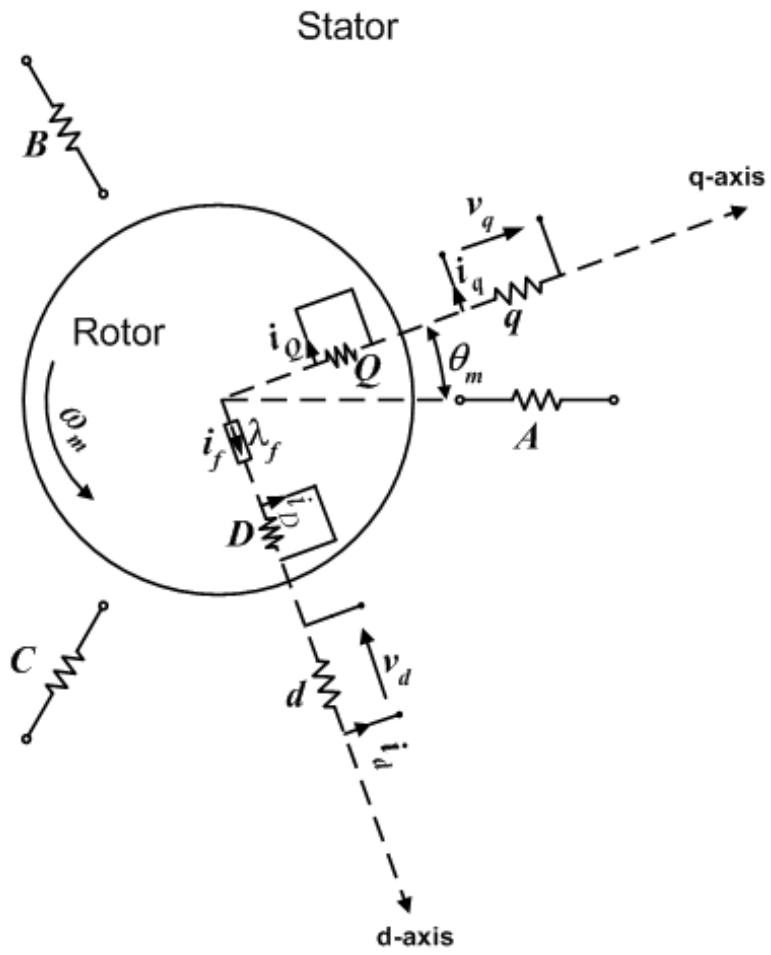

Figure 4.2: Physical Model of Interior Permanent Magnet Synchronous Machine

If the three-phase terminal voltages and currents are

$$\begin{bmatrix} v_a \\ v_b \\ v_c \end{bmatrix} = \begin{bmatrix} \sqrt{2}V\cos\omega t \\ \sqrt{2}V\cos(\omega t - \frac{2\pi}{3}) \\ \sqrt{2}V\cos(\omega t - \frac{4\pi}{3}) \end{bmatrix} \tag{4.4}$$

and

$$\begin{bmatrix} i_a \\ i_b \\ i_c \end{bmatrix} = \begin{bmatrix} \sqrt{2}I\cos(\omega t - \psi) \\ \sqrt{2}I\cos(\omega t - \frac{2\pi}{3} - \psi) \\ \sqrt{2}I\cos(\omega t - \frac{4\pi}{3} - \psi) \end{bmatrix} \tag{4.5}$$

then through the commutator transformation described in equation (4.1), the cor-

responding voltages and currents in $dq0$ system are

$$\begin{bmatrix} v_d \\ v_q \\ v_0 \end{bmatrix} = \sqrt{3}V \begin{bmatrix} -\sin(\omega t - \theta_e) \\ \cos(\omega t - \theta_e) \\ 0 \end{bmatrix} = \sqrt{3}V \begin{bmatrix} -\sin\delta \\ \cos\delta \\ 0 \end{bmatrix} \tag{4.6}$$

and

$$\begin{aligned} \begin{bmatrix} i_d \\ i_q \\ i_0 \end{bmatrix} &= \sqrt{3}I \begin{bmatrix} -\sin(\omega t - \theta_e - \psi) \\ \cos(\omega t - \theta_e - \psi) \\ 0 \end{bmatrix} = \sqrt{3}I \begin{bmatrix} -\sin(\delta - \psi) \\ \cos(\delta - \psi) \\ 0 \end{bmatrix} \\ &= \sqrt{3}I \begin{bmatrix} \cos(\frac{\pi}{2} + \delta - \psi) \\ \sin(\frac{\pi}{2} + \delta - \psi) \\ 0 \end{bmatrix} \end{aligned} \tag{4.7}$$

where ω is the stator angular velocity, $\delta = \omega t - \theta_e$ is the torque angle and ψ is power factor angle.

Let

$$\beta = \frac{\pi}{2} + \delta - \psi \tag{4.8}$$

then equation (4.7) is rewritten as

$$\begin{bmatrix} i_d \\ i_q \\ i_0 \end{bmatrix} = \sqrt{3}I \begin{bmatrix} \cos\beta \\ \sin\beta \\ 0 \end{bmatrix} \tag{4.9}$$

Assuming balanced operating conditions, with the model shown in Fig. 4.2, the voltage equations are written as:

$$\begin{cases} v_d = \frac{d\lambda_d}{dt} - \omega_e\lambda_q + R_s i_d \\ v_q = \frac{d\lambda_q}{dt} + \omega_e\lambda_d + R_s i_q \\ 0 = \frac{d\lambda_D}{dt} + R_D i_D \\ 0 = \frac{d\lambda_Q}{dt} + R_Q i_Q \end{cases} \tag{4.10}$$

where λ is the flux linkage, ω_e is the rotor angular velocity, suffixes d and q denote the $d-$axis and $q-$axis quantities of the stator, suffixes D and Q denote the $d-$axis

and $q-$axis quantities of the rotor.

With the permanent magnet being represented by equivalent current i_f, the flux linkages can be written as:

$$\begin{cases} \lambda_d &= L_d i_d &+ L_{md} i_D &+ L_{md} i_f \\ \lambda_q &= L_q i_q &+ L_{mq} i_Q & \\ \lambda_D &= L_D i_D &+ L_{md} i_d &+ L_{md} i_f \\ \lambda_Q &= L_Q i_Q &+ L_{mq} i_q & \end{cases} \tag{4.11}$$

where L denotes the inductances and suffix m denotes the mutual quantities.

Substituting equation (4.11) into equation (4.10) yields

$$[v] = [R][i] + [L]\frac{d[i]}{dt} + \omega_e[G][i] + \omega_e[C]\lambda_f \tag{4.12}$$

where

$$\lambda_f = L_{md} i_f$$

$$[v] = \begin{bmatrix} v_d & v_q & 0 & 0 \end{bmatrix}^{tr}$$

$$[i] = \begin{bmatrix} i_d & i_q & i_D & i_Q \end{bmatrix}^{tr}$$

$$[R] = diag(R_s, R_s, R_D, R_Q)$$

$$[L] = \begin{bmatrix} L_d & 0 & L_{md} & 0 \\ 0 & L_q & 0 & L_{mq} \\ L_{md} & 0 & L_D & 0 \\ 0 & L_{mq} & 0 & L_Q \end{bmatrix}$$

$$[G] = \begin{bmatrix} 0 & -L_q & 0 & -L_{mq} \\ L_d & 0 & L_{md} & 0 \\ 0 & 0 & 0 & 0 \\ 0 & 0 & 0 & 0 \end{bmatrix}$$

$$[C] = \begin{bmatrix} 0 & 1 & 0 & 0 \end{bmatrix}^{tr}$$

and 'diag' means the diagonals of the matrix.

When the permanent magnet synchronous machine is running in steady state or under synchronous operation, the rotor is synchronized with the stator, $\omega_e = \omega$. Therefore no current is induced in the rotor or $i_D = i_Q = 0$. Thus equation (4.12) can be simplified as

$$\begin{cases} v_d = -\sqrt{3}V\sin\delta = -\omega L_q i_q + R_s i_d \\ v_q = \sqrt{3}V\cos\delta = \omega L_d i_d + \omega\lambda_f + R_s i_q \end{cases} \tag{4.13}$$

If E_0 represents the induced phase voltage in *abc* system by the permanent magnet under synchronous speed, then

$$\sqrt{3}E_0 = \omega\lambda_f \tag{4.14}$$

Since the reactance of d and q axis under synchronous operation are

$$\begin{cases} X_d = \omega L_d \\ X_q = \omega L_q \end{cases} \tag{4.15}$$

substituting equations (4.9), (4.14) and (4.15) into equation (4.13) yields

$$\begin{cases} -\sqrt{3}V\sin\delta = -X_q\sqrt{3}I\sin\beta + R_s\sqrt{3}I\cos\beta \\ \sqrt{3}V\cos\delta = X_d\sqrt{3}I\cos\beta + R_s\sqrt{3}I\sin\beta + \sqrt{3}E_0 \end{cases} \tag{4.16}$$

or

$$\begin{cases} V\sin\delta = X_q I\sin\beta - R_s I\cos\beta \\ V\cos\delta = X_d I\cos\beta + R_s I\sin\beta + E_0 \end{cases} \tag{4.17}$$

With reference to the standard phasor diagram of permanent magnet synchronous machine during synchronous motor operation shown in Fig. 4.3, the two-axis model of permanent magnet synchronous machine can be elaborated by equations (4.18)-(4.20).

$$\begin{cases} V\cos\delta &= E_0 &+ X_d I_d &+ R_s I_q \\ V\sin\delta &= X_q I_q &- R_s I_d & \end{cases} \tag{4.18}$$

$$I_d = I\cos\beta; I_q = I\sin\beta \tag{4.19}$$

$$\beta = \frac{\pi}{2} + \delta - \psi. \tag{4.20}$$

where X is the reactance, δ is the load angle, ψ is the power factor angle and β is the angle between the stator flux linkage and the permanent magnet flux linkage.

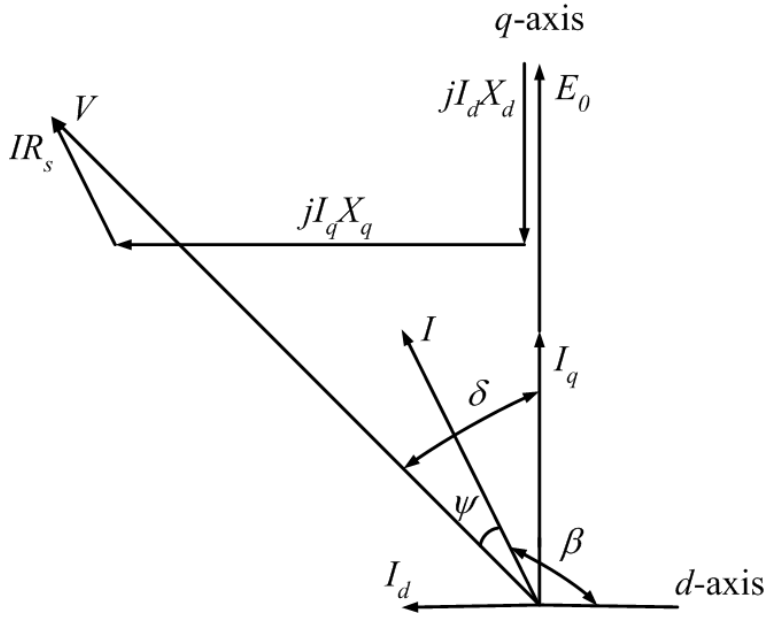

Figure 4.3: The Phasor Diagram of a Permanent Magnet Synchronous Machine

4.3 Parameter Estimation of Line-Start Permanent Magnet Synchronous Machine

The presence of permanent magnets in the permanent magnet synchronous machine prevents the use of the most conventional parameter measurement methods, which are applicable to the wound field synchronous machines. To tackle this problem, various techniques and methods have been used by many researchers for the determination of machine parameters. The experimental methods that were used often are static test (locked rotor), sensorless no-load test and load test, while one of the most popular computational methods is the finite element method.

The static tests are carried out with some assumptions, such as the constant parameters with different frequencies or constant parameters with different load conditions. These assumptions result in simple measurement procedure, but not enough parameter information for machine dynamic operations. The conventional sensorless no-load test and load test methods are based on the two-axis model of permanent magnet synchronous machines. They have an important limit that a constant value, E_0, is assumed for the induced EMF due to permanent magnets. Although the load test methods are modified later by taking into account of the variation of E_0, the results are still irregular. In this work, the experimental methods that were used before by other researchers were reviewed. Based on the modified load test method, two novel techniques through the implementation of linear regression and Hopfield neural network are presented.

In the finite element analysis, the machine parameters can be calculated from the stored magnetic energy or flux linkage. Different authors have proposed alternative methods to evaluate the machine parameters and their variations with

iron saturation. However assumption of constant permanent magnet flux linkage is made also. To overcome this drawback, a method based on the variation of current angle is used in this work, which allows the two-axis parameters to be evaluated with the variation of load condition.

4.3.1 Working Model in This Work

The parameters of a 3-phase, 4-pole, 2.2 kW line-start permanent magnet synchronous machine is determined using various methods. The cross section of the machine is shown in Fig. 4.4. The specifications and dimensions of the machine are shown in Appendix F.

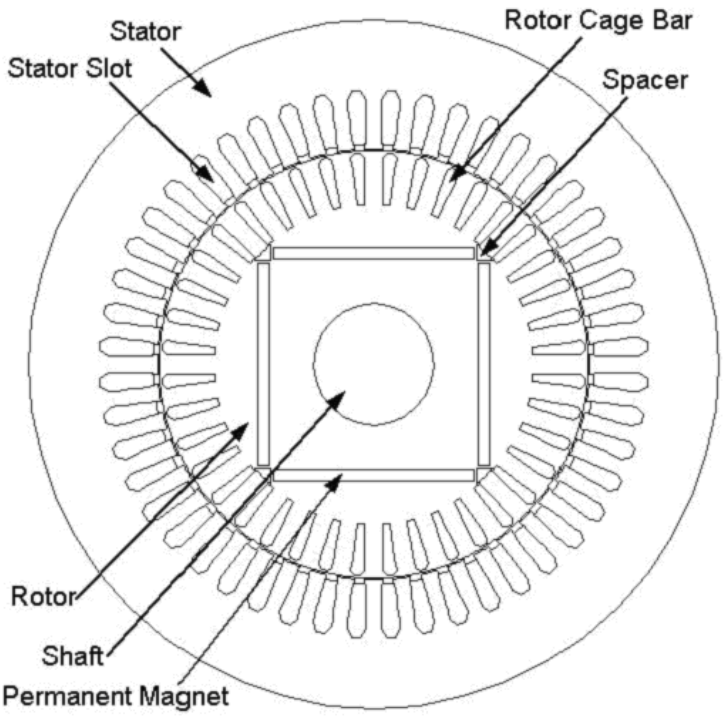

Figure 4.4: Cross Section of Line-Start Permanent Magnet Synchronous Machine

4.3.2 BH Characteristic of Lamination Material

The material property of motor core is necessary for the finite element analysis. A section of stator is taken out and wound with two windings similar to transformer windings as shown in Fig. 4.5.

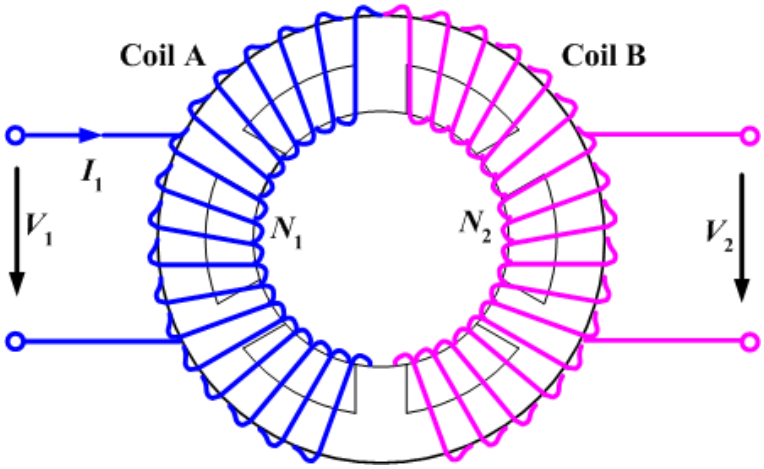

Figure 4.5: Wound Motor Core for Testing of BH Characteristics

Two coils, coil A and coil B are wound on the motor core similar to a toroidal transformer. Coil A is taken as the primary winding and coil B is taken as the secondary winding. Coil A is connected to a $50Hz$ line supply through a variac; while coil B remains as open circuit. The variac is used to control the voltage across coil A, V_1. For every V_1, the current flowing in coil A, I_1, and the voltage across coil B, V_2, are measured. The magnetic flux density, B, and magnetic field intensity, H, can be calculated as

$$H = \frac{N_1 I_1}{l_{mag}} \tag{4.21}$$

and

$$B = \frac{V_2}{\sqrt{2}\pi f N_2 S_{eff}} \tag{4.22}$$

where N_1 and N_2 represent the number of turns of primary winding and secondary winding respectively. l_{mag} is the length of magnetic path and S_{eff} is the effective

cross section area of magnetic flux.

The dimensional specifications of the motor core used for the testing of BH are shown in Appendix G. The experimental data of I_1 and V_2 are shown in Appendix G, Table G.1, the computational BH data are shown in Table G.2. The resultant BH curve is plotted in Fig. 4.6.

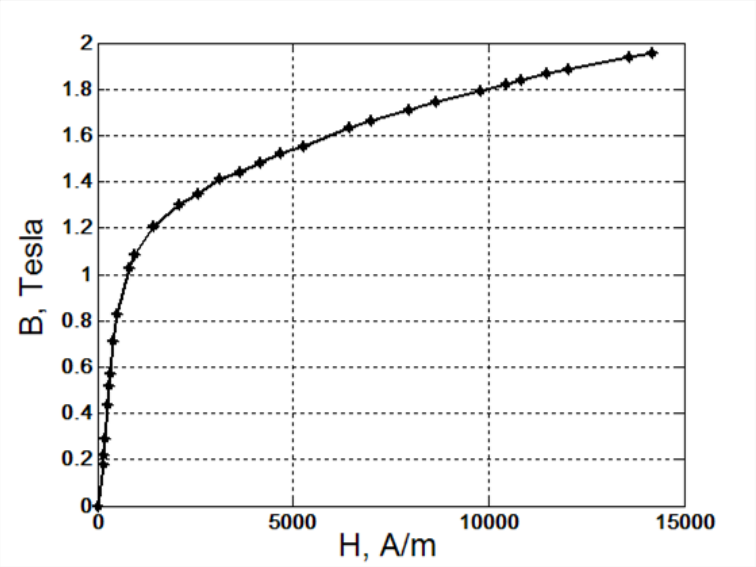

Figure 4.6: BH Characteristics of the Motor Core

4.3.3 Review of Previous Experimental Methods for Parameter Estimation

4.3.3.1 DC Current Decay Measurement Method

The synchronous reactances of permanent magnet synchronous machine can be measured from a static test provided that the rotor is locked to prevent any induced voltage from movement of the magnetic field. There are two approaches taken, direct flux integration [59, 53] and current integration with computation [54]. The first method requires direct computation of flux within the circuit as well as balancing the inductance bridge to eliminate the effect of rotor cage bars

(damper windings) on the AC measurements. The requirements include balancing the inductance bridge and integrating the flux. The uses of flux integrator and the L-R circuits for flux integration make the method complicated somehow.

The second method requires a simple setup and a small-capacity dc power supply. The direct- and quadrature-axes operational impedences are obtained from the voltage and current measured when the two armature winding terminals are short circuited while a dc current flows between these terminals. It was proposed by Yamamoto and others [54] to predict the starting parameters of permanent magnet machines and was named as DC current decay method.

The first method can include the variation of parameters with different currents, and the assumption of constant parameters with all frequencies is made. The second method can get parameters for different frequencies, but the variation of parameters with currents is not considered. Since the experimental setup and measurement procedure are relatively simple, the second method is selected in this work.

Fig. 4.7 shows the circuit configuration of the power supply and measurement setup used for the DC decay testing method. First the $d-$axis rotor position is determined. A dc voltage V_{DC} is applied so that a current I_{DC} which is lower than the rated current flows between the two armature winding terminals, as shown in Fig. 4.8(a). The stator and rotor interact by magnetic force, as a result, the rotor is held in a certain position, which is the $d-$axis position. The rotor is locked along the direct-axis and the two terminals are short circuited by opening the switch S_1. The current waveforms $i(t)$ are captured by oscilloscope upon opening the switch. Since the two terminals are short circuited, the current flowing in the windings

decays with time, as shown in Fig. 4.9(a).

A similar process is applied for the measurement of $q-$axis parameters. Without changing the rotor position, a different stator terminal voltage configuration is applied to the machine, as shown in Fig. 4.8(b). Upon opening the switch, the decay current waveform is captured as shown in Fig. 4.9(b).

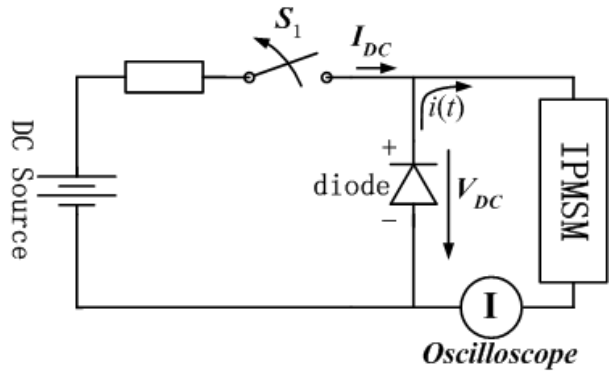

Figure 4.7: DC Current Decay Experimental Setup

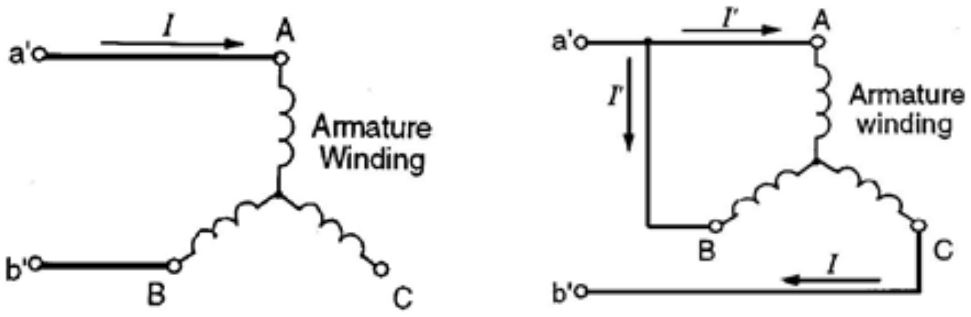

(a) (b)

Figure 4.8: Terminal Configuration for (a) $d-$axis and (b) $q-$axis

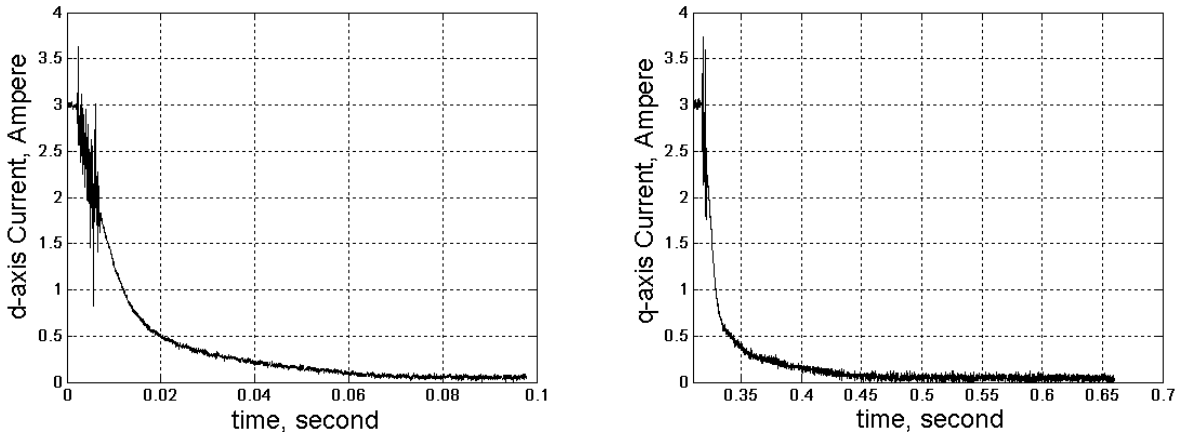

(a) (b)

Figure 4.9: Measured DC Decay Current (a) $d-$axis and (b) $q-$axis

The voltage and current waveforms before and after short-circuiting are illustrated in Fig. 4.10. The current waveform is represented by solid line and the voltage waveform is represented by broken line.

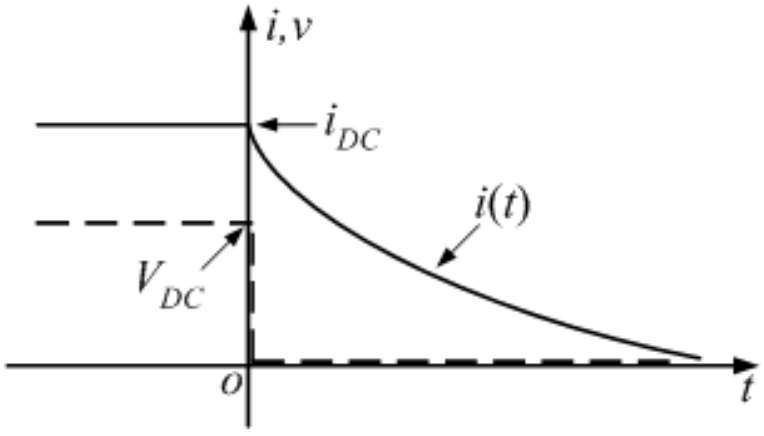

Figure 4.10: Voltage and Current Waveforms before and after Short-Circuited

The voltage waveform is processed first by Fourier transform and then by the inverse transform to obtain [118]

$$v(t) = \int_{-\infty}^{+\infty} j\frac{V_{DC}}{2\pi\omega_e} e^{j\omega_e t} d\omega_e + \frac{V_{DC}}{2} \tag{4.23}$$

where t is time, $j = \sqrt{-1}$ and ω_e is the angular frequency.

Similarly the current waveform is also processed by Fourier transform and inverse transform to obtain

$$i(t) = \int_{-\infty}^{+\infty} \frac{1}{2\pi} \left[\int_{0}^{+\infty} i(t) e^{-j\omega_e t} dt + j \frac{I_{DC}}{\omega_e} \right] e^{j\omega_e t} d\omega + \frac{I_{DC}}{2} \tag{4.24}$$

Comparing the frequency components of the integrand in the first term on the right hand sides of equations (4.23) and (4.24), the corresponded AC voltage and AC current are

$$v_{ac} = j \frac{V_{DC}}{2\pi\omega_e} e^{j\omega_e t} \tag{4.25}$$

and

$$i_{ac} = \frac{1}{2\pi} \left[\int_{0}^{+\infty} i(t) e^{-j\omega_e t} dt + j \frac{I_{DC}}{\omega_e} \right] e^{j\omega_e t} \tag{4.26}$$

Therefore the impedence $Z(\omega_e)$ at each frequency is given by

$$\frac{1}{Z(\omega_e)} = \frac{i_{ac}}{v_{ac}} = (\frac{\omega_e}{jV_{DC}}) \int_{0}^{+\infty} i(t) e^{-j\omega_e t} dt + \frac{I_{DC}}{V_{DC}} \tag{4.27}$$

The d and $q-$axis (per phase) can be calculated as:

$$\begin{cases} X_d(\omega_e) &= [Z_d(\omega_e) - 2R_s]/[2(\omega_e/\omega_0)j] \\ X_q(\omega_e) &= 2[Z_q(\omega_e) - 3R_s/2]/(3(\omega_e/\omega_0)j) \end{cases} \tag{4.28}$$

where ω_0 is the base frequency of the power supply. Applying equation (4.28) to the captured $d-$ and $q-$axis current waveforms, the reactances values of different frequencies can be calculated, and the synchronous reactances X_d and X_q are those when ω_e/ω_0 is equal to zero [54]. The reactances values obtained using this method are listed in Table 4.1.

Table 4.1: Results of DC Current Decay Method

	V_{DC}/Volt	I_{DC}/Ampere	X/Ohm
$d-$axis	4.95	3.00	3.913
$q-$axis	3.59	3.00	11.026

Compared with the conventional standstill tests, this method has the merit that the reactances, including those for the low frequency range are obtainable using simple and low cost equipment. However, this method gives single values for X_d and X_q for one frequency. The measurement of parameter E_0 is not realized and the variation of parameters with load conditions is not included. Hence the parameters measured using this method cannot provide enough information for some dynamic operations when these variations are needed.

4.3.3.2 Sensorless No-Load Test

Mellor *et al* [53] and Nee *et al* [55] used a no-load test method with variable stator voltage to determine the motor parameters. It is based on the machine phasor diagram during motoring operation as shown in Fig. 4.11 and the two-axis model represented by equations (4.29)-(4.32).

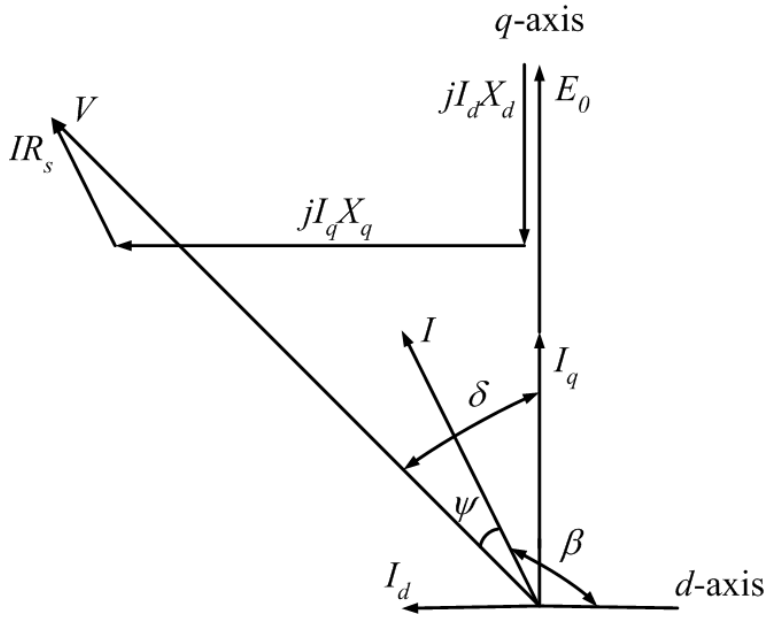

Figure 4.11: The Phasor Diagram of a Permanent Magnet Synchronous Machine

$$V\cos\delta = E_0 + X_dI_d + R_sI_q \tag{4.29}$$

$$V\sin\delta = X_qI_q - R_sI_d \tag{4.30}$$

$$I_d = I\cos\beta; I_q = I\sin\beta \tag{4.31}$$

$$\beta = \frac{\pi}{2} + \delta - \psi. \tag{4.32}$$

In this method, it is assumed that at no load the angle δ is zero and $I_q = 0$ (no torque current). As stator voltage V varies, stator current varies also. Taking the value of V at the point of minimum I as E_0, from equation (4.29), the reactance

of $d-$axis can be calculated as:

$$X_d = \frac{|V - E_0|}{I}. \tag{4.33}$$

In the experiment, the machine is run at rated speed of $1500rpm$ without load. The terminal voltage was varied from 200 volt to 100 volt and at the same time various voltages and currents are measured. The pairs of measured V and I values are listed in Appendix H, Table H.1, and the result of X_d (reactance of $d-$axis) is shown in Fig. 4.12.

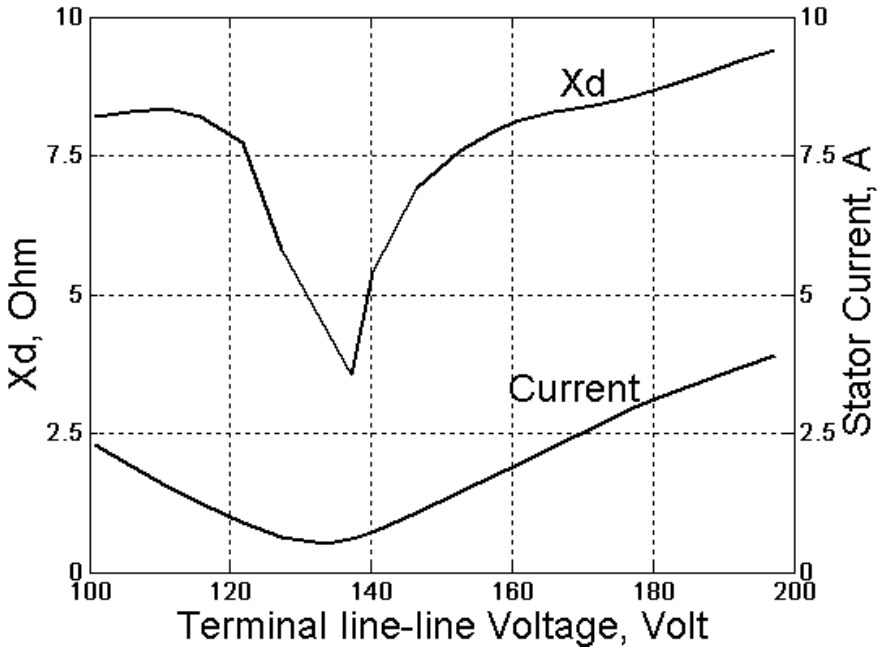

Figure 4.12: Results of X_d Using No-Load Test Method

The value of E_0 obtained here is 77.1 (line-line 133.54) volt. As stated in [55], from Fig. 4.12, we can see that this method is not valid in the vicinity of the point $V = E_0$. The reason is that at this point the current is at a minimum value, and any error in the measurement of a small current will be amplified to get erratic X_d values. At a certain distance away from this point, this method is a good approximation. However, using this method, we can only obtain a set of values of X_d and the variation of E_0 with current is not considered.

4.3.3.3 Load Test Method

The load test method for PMSM was first proposed by Miller [59]. It is also based on the two-axis model represented by equations (4.34)-(4.37).

$$V\cos\delta = E_0 + X_d I_d + R_s I_q \tag{4.34}$$

$$V\sin\delta = X_q I_q - R_s I_d \tag{4.35}$$

$$I_d = I\cos\beta; I_q = I\sin\beta \tag{4.36}$$

$$\beta = \frac{\pi}{2} + \delta - \psi. \tag{4.37}$$

The method is used to determine the X_d from the stator $d-$axis voltage component and X_q from the $q-$axis component respectively. Once the data of applied voltage V, current I, input power P and torque angle δ are known from the load test, power factor angle can be easily obtained as

$$\psi = arccos(\frac{P}{3IV}) \tag{4.38}$$

Thereafter other quantities, β, I_d and I_q, can be calculated using equations (4.36)-(4.37). From equation (4.35), the value of X_q can be easily obtained. However, from equation (4.34), it is inadequate to evaluate the two unknown quantities E_0 and X_d. To this end, E_0 is assumed to be constant by Miller [59] and it is equal to the open-circuit value. This assumption leads to the irregularity of X_d over a load range where the armature reaction in direct axis is changing from magnetizing to demagnetizing regions [59].

This load test was modified by Rahman and Zhou [57] by not making the simplifying assumption that the permanent magnet excitation voltage E_0 is constant. Instead, an attempt was made to solve for X_d and E_0 simultaneously by getting two sets of readings while making a change of $\Delta\beta$ in angle β. With the

new $\beta' = \beta + \Delta\beta$, another set of test data are obtained and one more equation is written

$$V' \cos \delta' = E_0 + X_d I'_d + R_s I'_q \tag{4.39}$$

Now with the three algebraic equations (4.34), (4.35) and (4.39), the values of X_d, X_q and E_0 are obtainable simultaneously.

In practice, the test procedure is to produce two sets of data for one load condition. The typical setup for a load test is used in this experiment, as shown in Fig. 4.13. The test machine is coupled to a DC machine and an incremental encoder is mounted on the shaft of the test machine so as to detect the rotor position θ_m. Two watt meters are used to measure the input power of the system.

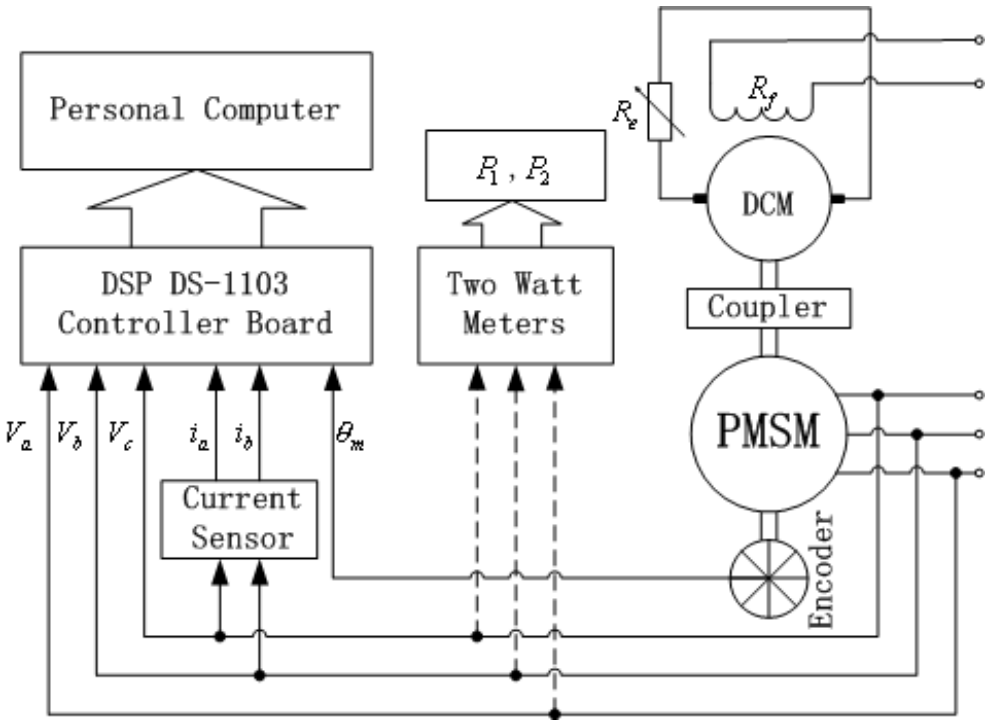

Figure 4.13: Experiment Setup for Load Test Method

In this experiment, the test machine is run as a generator first, and the back EMF v_{ab0}, v_{bc0}, v_{ca0} are recorded as reference waveforms, as the waveform V_0 in Fig. 4.14. Then the test machine is run as a motor at different loads. As shown

in Fig. 4.15, by varying the external resistance R_e, the armature current I_a of DC machine will be changed accordingly. Since the generating torque of DC machine is proportional to I_a [119], the DC machine torque varies with R_e. Therefore, the load of the test machine is varied with R_e also.

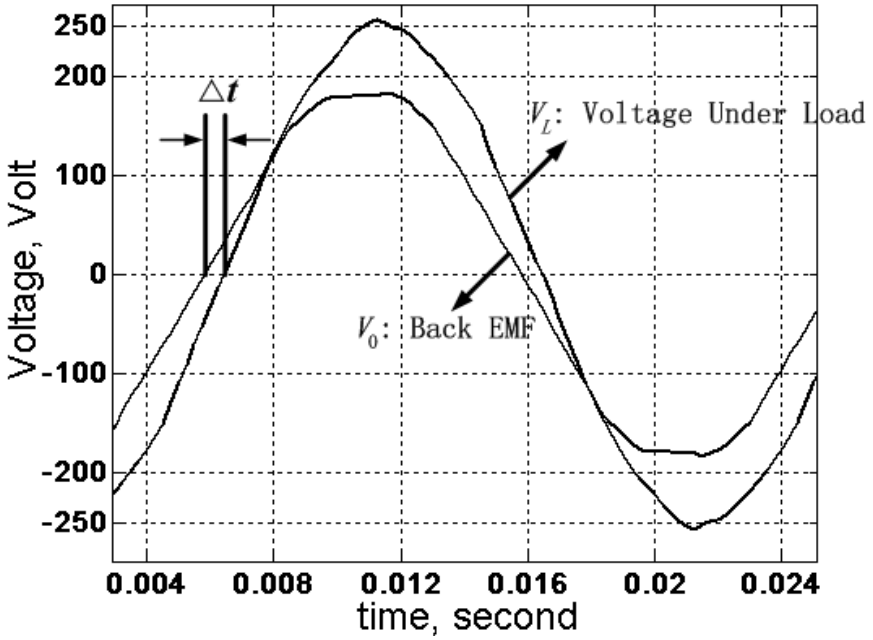

Figure 4.14: Measurement of Torque Angle δ

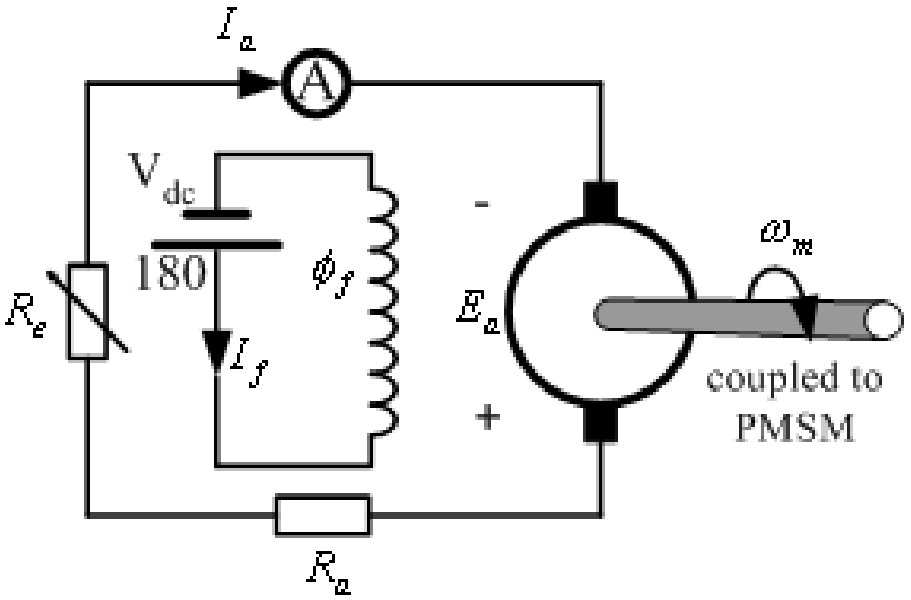

Figure 4.15: Configuration of the PMSM Loading System

When the test machine is run under different loads, the voltage (v_{ab},v_{bc},v_{ca}, waveform V_L in Fig. 4.14), current (i_a, i_b, i_c) waveforms and input power (P_1, P_2) are recorded for every load (see Appendix H, Tables H.2 and H.3). The phase angle difference between the $V_{ab,bc,ca}$ and the $V_{ab0,bc0,ca0}$ was taken as the torque angle δ, as shown in Fig. 4.14, $\delta = \Delta t \cdot \omega_e$. With the measured input power $P = P_1 + P_2$, phase voltage V and phase current I, the power factor angle ψ can be calculated as

$$\psi = \arccos(\frac{P}{3IV})$$

With the values of angles δ and ψ, β can be calculated using $\beta = \frac{\pi}{2} + \delta - \psi$, hence the values of I_d and I_q can be determined by $I_d = I\cos\beta$ and $I_q = I\sin\beta$ respectively. Therefore, a set of values of V, δ,I_d and I_q can be determined.

To create the other set of data, a small change of $\Delta\beta$ in β is needed. The new $\beta' = \beta + \Delta\beta$ should not be too far from β as they are taken as the operation points for the same load condition. Therefore, $\Delta\beta$ should be small enough and in this work a suggested value of 0.1^0 is selected [58]. In order to achieve such a small change in angle β, we make a small change to the DC armature current through the slight downward adjustment of the DC field excitation voltage, i.e. from 180 to 175 volt. By doing so, the load angle changes slightly (no more than 0.10^0), and with that we get a new set of voltage, current and real power values. Therefore with these two set of experiment data, the X_d, X_q and E_0 can be calculated by solving the following set of equations:

$$\begin{cases} V\cos\delta &= E_0 &+ X_d I_d &+ R_s I_q \\ V\sin\delta &= X_q I_q &- R_s I_d & \\ V'\cos\delta' &= E_0 &+ X_d I'_d &+ R_s I'_q \end{cases}$$

The experiment data of the load test are listed in Appendix H Tables H.2 and H.3. The results of parameters are listed in Appendix G Table H.4 and plotted in Fig. 4.16.

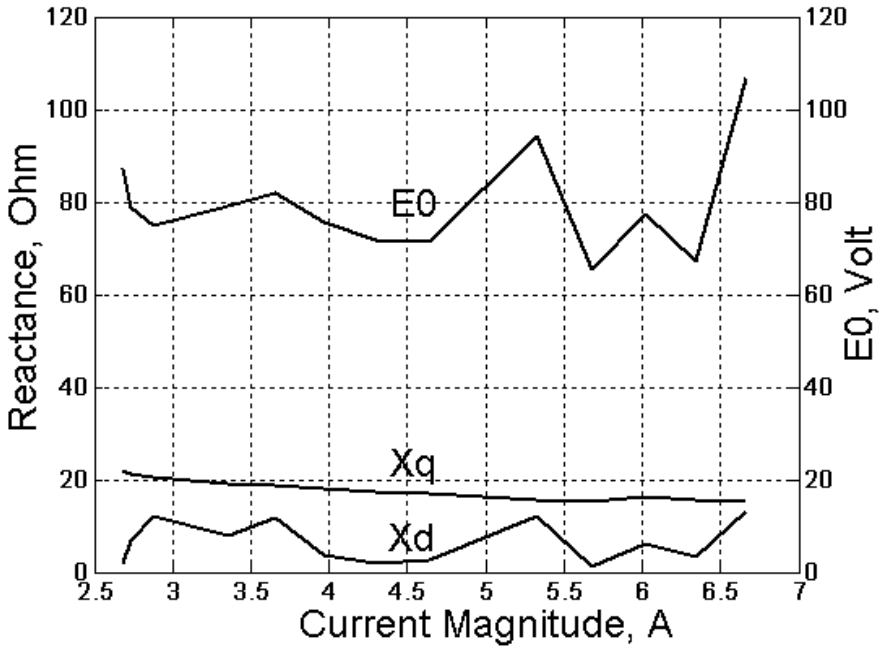

Figure 4.16: Results of Load Test Method

We can see that the values of X_d and E_0 are fluctuating, while that of X_q shows a more consistent trend. The main reason for this inconsistency could be due to the very small change in the angle β, which can make the equations ill-conditioned and hence cannot be solved accurately. In the experiment, the achievement of the small change in β is possible but very difficult and uncertain. This uncertainty may bring inaccuracies to the recorded data, thereafter affect the accuracies of the result parameters. Especially when the accuracies of X_d and E_0 are completely determined by the measurement of a few angles, including δ, β, δ' and β', a small uncertainty in one of these angles may cause big error in the result.

4.3.4 New Methods for Parameter Determination

The DC current decay method is easy to carry out, but only single values of X_d and X_q are obtained. The sensorless no-load test is also easy in implementation, but only a group of X_d values are obtained. The load test suffers from the shortcoming of the fact that we need a very small change of angle β. The change of such a small margin in experiment is very difficult to achieve, and it could also lead to the inconsistency of experimental results.

In order to overcome these drawbacks and difficulties, the load test is applied in combination with a linear regression model and a Hopfield neural network model respectively. By using the combined methods, one would avoid the measurement of the load angle δ, and the power factor angle ψ, but the rotor position would be required. Thus the load test processes become much simpler with the combination techniques.

4.3.4.1 Combination of Load Test and Linear Regression

The main concept of linear regression model is to adapt parameters from input and output data by searching for the minimum of the mean square error (MSE) [120]. For example, suppose d is the desired output of n inputs $x_1, x_2, \ldots, x_n$, the error between the estimated output and the desired output is:

$$\varepsilon = d - \sum_{k=0}^{n} h_k x_k$$

where $h_k (k = 0, 1, \ldots, n)$ are the weights, h_0 is the bias and x_0 is 1. Hence the MSE of m sample is:

$$J = \frac{1}{2m} \sum_{i=1}^{m} (d_i - \sum_{k=0}^{n} h_k x_{ik})^2$$

The differential of J with respect to the unknowns (h_k) is:

$$\nabla = [\frac{\partial J}{\partial h_0}, \frac{\partial J}{\partial h_1}, \ldots, \frac{\partial J}{\partial h_n}] = CH - D$$

where

$$\begin{aligned} \frac{\partial J}{\partial h_k}|_{(k=0,1,\ldots,n)} &= \frac{1}{m}[\sum_{j=0}^{n}(h_j \sum_{i=1}^{m} x_{ij}x_{ik}) - \sum_{i=1}^{m} d_i x_{ik}] \\ H &= [h_0, h_1, \ldots, h_n]^{tr} \end{aligned}$$

The optimal $H^\star$ is obtained by setting $\nabla = 0$. Therefore,

$$H^\star = C^{-1}D. \tag{4.40}$$

To apply this method for the processing of load test data, the oscillations of stator currents in the steady state are taken into account. As the governing equations of permanent magnet synchronous machine in the steady state are:

$$v_d = R_s i_d - \omega_e L_q i_q + L_d \frac{di_d}{dt} \tag{4.41}$$

$$v_q = R_s i_q + \omega_e L_d i_d + L_q \frac{di_q}{dt} + \sqrt{3}E_0 \tag{4.42}$$

By applying the sum (4.42)+(4.41) and the difference (4.42)−(4.41) of these two equations, we can get

$$\begin{cases} Y_1 = L_d X_{11} + L_q X_{12} + b_0 \\ Y_2 = L_d X_{21} + L_q X_{22} + b_0 \end{cases}$$

where

$$\begin{cases} Y_1 = (v_d - R_s i_d) + (v_q - R_s i_q); \quad X_{11} = \omega_e i_d + \frac{di_d}{dt}; \quad X_{12} = \frac{di_q}{dt} - \omega_e i_q; \\ Y_2 = (v_q - R_s i_q) - (v_d - R_s i_d); \quad X_{21} = \omega_e i_d - \frac{di_d}{dt}; \quad X_{22} = \frac{di_q}{dt} + \omega_e i_q; \\ b_0 = \sqrt{3}E_0; \end{cases}$$

Taking X_{11}, X_{12}, X_{21} and X_{22} as the inputs, Y_1 and Y_2 as the desired outputs and L_d, L_q and b_0 as the weights, we try to find the best linear regression on all the inputs using equation (4.40) so that we can determine the values of L_d, L_q and E_0.

In the experiment, the conventional load test is taken. For each load condition, a large amount (more than 2000) of samples is recorded. With these samples values of $i_a(t)$, $i_b(t)$, $i_c(t)$, $v_a(t)$, $v_b(t)$ and $v_c(t)$, the values of $i_d(t)$, $i_q(t)$, $v_d(t)$ and $v_q(t)$ can be calculated using Park's transformation. Hence $di_d(t)/dt$ and $di_q(t)/dt$ can be determined by

$$\begin{aligned} \frac{di_d}{dt}|_{(t=t_0)} &= \frac{i_d|_{t=t_0} - i_d|_{t=(t_0-\Delta t)}}{\Delta t}; \\ \frac{di_q}{dt}|_{(t=t_0)} &= \frac{i_q|_{t=t_0} - i_q|_{t=(t_0-\Delta t)}}{\Delta t} \end{aligned}$$

where t is time, t_0 is one point of time and Δt is the incremental time step from the previous point of time.

The terminal voltage values we measure from the load test are line-line voltages. Since phase voltages are needed in the Park's transformation, following equation is used to change the line-line voltages to phase voltages:

$$\begin{pmatrix} v_a \\ v_b \\ v_c \end{pmatrix} = \frac{1}{3} \begin{pmatrix} -1 & 0 & -1 \\ -1 & 1 & 0 \\ 0 & -1 & 1 \end{pmatrix} \begin{pmatrix} v_{ab} \\ v_{bc} \\ v_{ca} \end{pmatrix} = \frac{1}{3} \begin{pmatrix} v_{ab} - v_{ca} \\ v_{bc} - v_{ab} \\ v_{ca} - v_{bc} \end{pmatrix}. \tag{4.43}$$

Another necessary condition for Park's transformation is to locate the $d, q-$axes with reference to the encoder position system; in other words, we have to decide the initial position of $d-$axis. The phase difference between the rising zero crossing of the back EMF waveform (phase) and the zero index signal of the incremental encoder was the position of $d-$axis. As shown in Fig. 4.17, the initial position of $d-$axis is $\theta_0 = \Delta t \cdot \omega_e$.

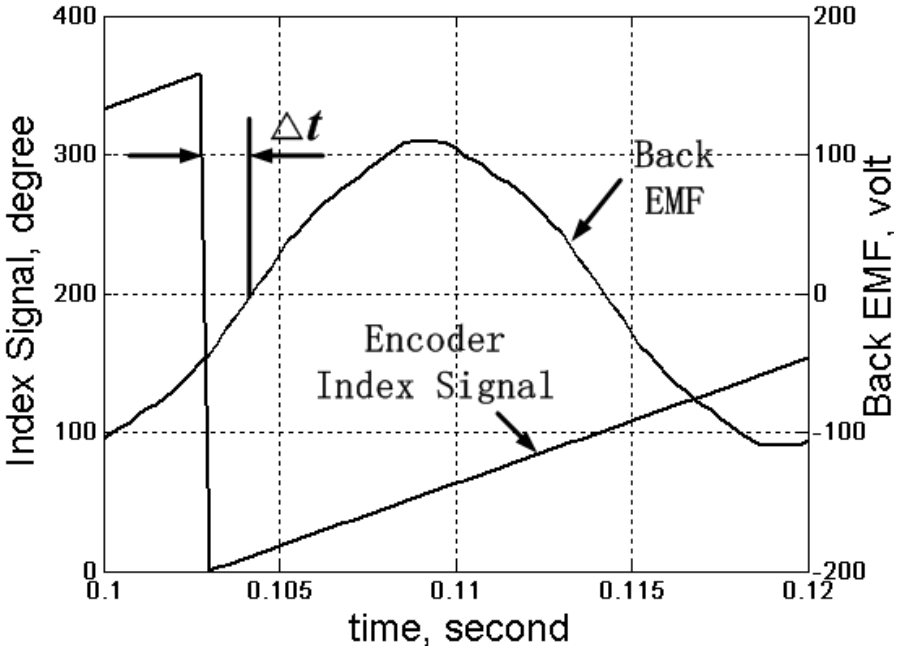

Figure 4.17: Determination of Initial Position of $d-$axis

After the data sets of $i_d, i_q, v_d, v_q, di_d/dt$ and di_q/dt are ready, we use a regression model. The results obtained by using this technique are listed in Appendix H Table H.5 and plotted in Fig. 4.18.

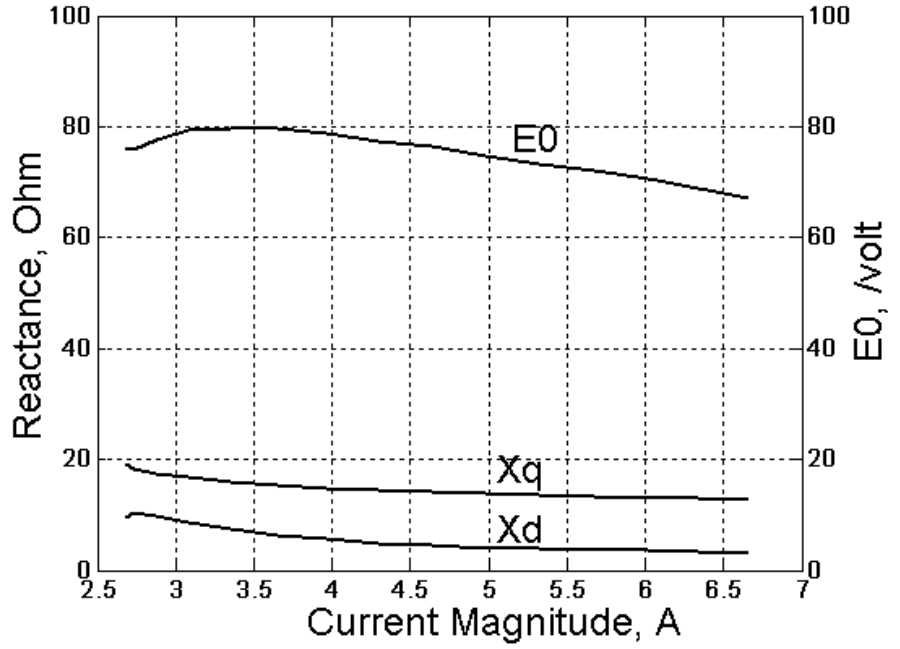

Figure 4.18: Results of Regression Model

Comparing with the Miller's load test method, this combined technique has the merit that the variation of E_0 with load condition is taken into account. Comparing with the Zhou's modified load test method, this technique overcomes the difficulty of achieving a very small change in angle β during the experiment. The uncertainties in angle measurements are lessened and the experiment procedure is simplified.

Comparing Fig. 4.18 with Fig. 4.16, we can see that the zigzags in the results of load test method are removed by the new combination technique. All the parameters obtained by the combination technique vary smoothly with the current and the trends shown in the variations of waveforms are more obvious. The reason is that Miller's method and Zhou's method are based on the solution of two or three equations, the accuracies of the solved parameters are totally dependent on a few data. A small mistake in one of these few data may lead to big unexpected error in the resultant parameters. Especially in Zhou's method, when the X_d and E_0 are determined by two sets of data (v, i, δ, β) and $(v', i', \delta', \beta')$ which are very close to each other, the small uncertainties may cause the equations ill-conditioned and produce inaccuracies in the results. The combination technique used in this work overcomes this drawback by getting a optimal solution based on the linear regression of thousands of samples. Therefore accuracies of the solved parameters are improved greatly. This improvement can be very significant in the analysis for dynamics and transients where accurate parameters are needed.

4.3.4.2 Combination of Load Test and Hopfield Neural Network

Hopfield neural network model was proposed by Hopfield [121] and was further explored to solve some classes of optimization problems by Hopfield and Tank [122] - [124]. In 1990, S. R. Chu *et al* [125] modified this network and applied it successfully for identification of linear time invariant or time varying systems by measuring the inputs, states and derivations of the states. In the following years, this method was used by many researchers for system identification, state estimation and control in various areas [126] - [130]. As for the application of Hopfield neural network in the parameter estimation of electric machines, some work has been done in induction machines and DC machines [127, 130, 131]. In order to get more accurate machine parameters and also to overcome the difficulties of using only load test, we have applied the Hopfield neural network in combination with the load test.

Artificial neural networks (ANN) can be considered as highly interconnected dynamical systems consisting of simple processing elements called neurons. Feedforward and recurrent type artificial neural network architectures are the two major type of ANNs being investigated. The distinction between feedforward and recurrent type networks is that the former learns the function mapping by updating its connection weights while the latter seeks to retain its minimum computational energy as its neurons evolve in time [132]. Hopfield neural network is just one kind of recurrent network.

The Hopfield neural network was proposed by John Hopfield of the California Institute of Technology in 1982 . He devised an array of neurons that were fully interconnected, with each neuron feeding its output to all others. The concept was that all the neurons would transimit signals back and forth to each other in a

closed feedback loop until their states became stable. It is one type of single-layer iterative (or recurrent) network. There are two types of Hopfield neural networks: discrete type and continuous type. The main difference of these two versions lies in the format of neuron active function. For discrete type Hopfield neural network, usually a discrete time function, i.e. Sign() function, is selected. For continuous type Hopfield neural network, usually a continuous time function, i.e. Sigmoid or hyperbolic tangent function, is used. The continuous Hopfield model is a generalization of the discrete case. So in this work the continuous type Hopfield neural network is used.

The structure of continuous Hopfield neural network is shown in Fig. 4.19. The network is made up by n neurons. Each neuron is realized by analog circuits (including resistor, capacitor and amplifier) and the structure of one neuron is shown in Fig. 4.20.

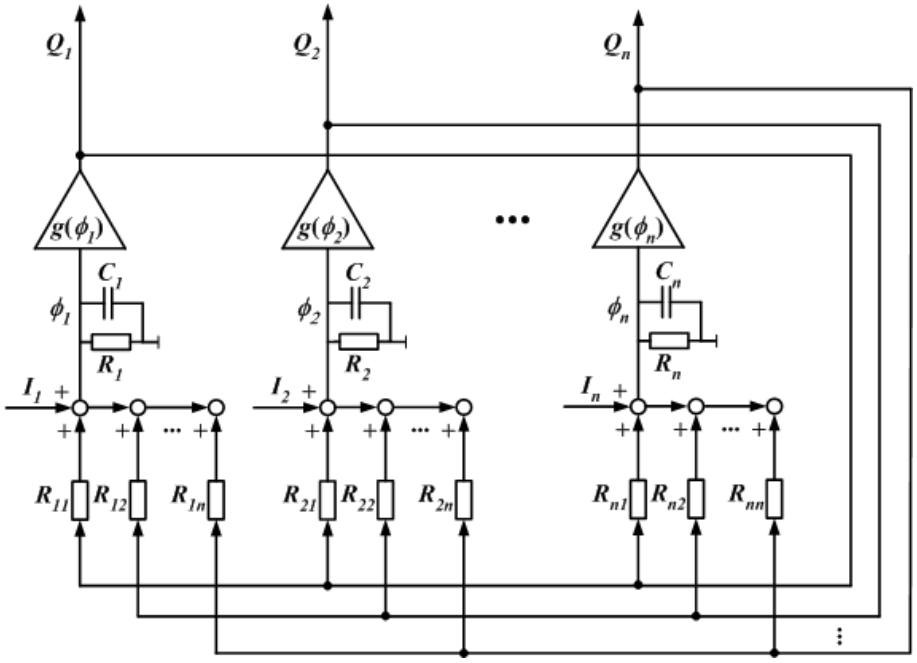

Figure 4.19: Structure of Hopfield Neural Network

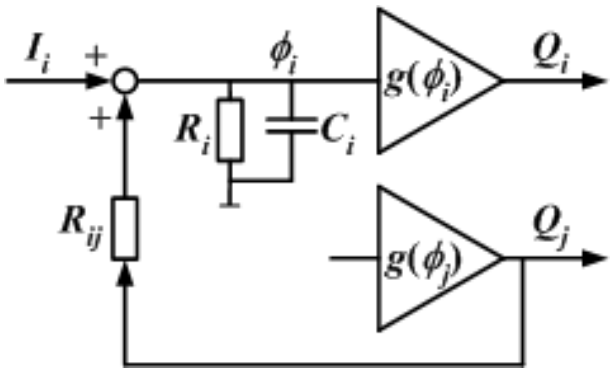

Figure 4.20: Structure of One Neuron

From Fig. 4.20, we can see that the governing equations for i_{th} neuron is:

$$C_i \frac{d\phi_i}{dt} = \sum_{j=1}^{n} \frac{Q_j - \phi_i}{R_{ij}} - \frac{\phi_i}{R_i} + I_i \tag{4.44}$$

$$Q_i = g(\phi_i) \tag{4.45}$$

where

$n =$ the number of neurons in the network

$C_i =$ the neuron capacitance

$R_i =$ the neuron resistance

$I_i =$ the bias input of neuron

$Q_i =$ the output of neuron

$\phi_i =$ the state of neuron

$g(x) =$ nonlinear sigmoidal function

Let

$$\frac{1}{R_i'} = \frac{1}{R_i} + \sum_{j=1}^{n} \frac{1}{R_{ij}} \tag{4.46}$$

and

$$T_{ij} = \frac{1}{R_{ij}} \tag{4.47}$$

then we can get

$$C_i \frac{d\phi_i}{dt} = -\frac{1}{R_i'}\phi_i + \sum_{j=1}^{n} T_{ij} Q_j + I_i \tag{4.48}$$

Considering the quantity

$$E = -\frac{1}{2}\sum_{i=1}^{n}\sum_{j=1}^{n} T_{ij} Q_i Q_j - \sum_{i=1}^{n} Q_i I_i + \sum_{i=1}^{n} \frac{1}{R_i'} \int_0^Q g^{-1}(Q) dQ \tag{4.49}$$

where $g^{-1}(Q)$ is the inverse function of $Q = g(\phi)$.

Its differential with time is

$$\frac{\partial E}{\partial t} = \sum_{i=1}^{n} \frac{\partial E}{\partial Q_i} \frac{\partial Q_i}{\partial t} \tag{4.50}$$

where

$$\frac{\partial E}{\partial Q_i} = -\frac{1}{2}\sum_{j=1}^{n} T_{ij} Q_j - \frac{1}{2}\sum_{j=1}^{n} T_{ij} Q_j - I_i + \frac{1}{R_i'}\phi_i \tag{4.51}$$

If

$$T_{ij} = T_{ji} \tag{4.52}$$

then equation (4.51) can be written as

$$\frac{\partial E}{\partial Q_i} = -\sum_{j=1}^{n} T_{ij} Q_j - I_i + \frac{1}{R_i'}\phi_i \tag{4.53}$$

Comparing equation (4.53) with equation (4.44), we can get

$$\frac{\partial E}{\partial Q_i} = -C_i \frac{d\phi_i}{dt} = -C_i \frac{d\phi_i}{dQ_i}\frac{dQ_i}{dt} = -C_i \left(\frac{dQ_t}{dt}\right) \frac{d}{dQ_i} g^{-1}(Q_i) \tag{4.54}$$

Substituting equation (4.54) into equation (4.50) yields

$$\frac{\partial E}{\partial t} = -\sum_{i=1}^{n} C_i \left(\frac{dQ_i}{dt}\right)^2 \frac{d}{dQ_i} g^{-1}(Q_i) \tag{4.55}$$

If function $g(Q_i)$ is mono-increasing, its inverse function $g^{-1}(Q_i)$ is mono-increasing also. In other words,

$$\frac{d}{dQ_i} g^{-1}(Q_i) > 0 \tag{4.56}$$

Therefore equation (4.50) becomes

$$\frac{\partial E}{\partial t} \leq 0 \tag{4.57}$$

Equation (4.57) shows that the time evolution of the system is a motion in state space that seeks out minima in E and comes to a stop at such point. E is a Lyapunov function for the system and is taken as the computational energy of the network.

For simplicity, we can always choose $R_i' = R$ and $C_i = C$, independent of i. Dividing by C and redefining T_{ij}/C and I_i/C as T_{ij} and I_i, equations (4.48), (4.45) and (4.49) become

$$\frac{d\phi_i}{dt} = \sum_{j=1}^{n} T_{ij} Q_j + I_i - \frac{\phi_i}{RC} \tag{4.58}$$

$$Q_i = g(\phi_i) \tag{4.59}$$

and

$$E = -\frac{1}{2} \sum_{i=1}^{n} \sum_{j=1}^{n} T_{ij} Q_i Q_j - \sum_{i=1}^{n} Q_i I_i + \sum_{i=1}^{n} \frac{1}{R} \int_0^Q g^{-1}(Q) dQ \tag{4.60}$$

Equations (4.58)-(4.60) are the Hopfield neural network model and energy function that are used often in various applications.

While the input resistance of each neuron $R \to \infty$, the network dynamic model and energy function can be further simplified as:

$$\frac{d\phi_j}{dt} = \sum_{i=1}^{n} T_{ij} Q_j + I_j \tag{4.61}$$

$$Q_j = g(\phi_j), j = 1, \ldots, n \tag{4.62}$$

$$E = -\frac{1}{2}\sum_{i=1}^{n}\sum_{j=1}^{n} T_{ij}Q_iQ_j - \sum_{i=1}^{n} Q_iI_i \tag{4.63}$$

It has been shown in equations (4.52) and (4.56) that we can get the minima of the energy function if $T_{ij} = T_{ji}$ and function $Q_j = g(\phi_j)$ is mono-increasing as well. Generally, function $g(\phi_j)$ is selected as:

$$Q_j = g(\phi_j) = \rho\frac{1 - e^{-k\phi_j}}{1 + e^{-k\phi_j}} \tag{4.64}$$

Here k is the slope of the sigmoid nonlinearity, the ρ is such that when ϕ_j tends to $\pm\infty$, the function $Q_j = g(\phi_j)$ tends to $\pm\rho$.

Consider a dynamical system in state space as:

$$[\dot{x}] = [A_t][x] + [B_t][u] \tag{4.65}$$

The definition of $[A_t]$, $[B_t]$, $[x]$ and $[u]$ are list in equation 4.66, where $[A_t]$ and $[B_t]$ are the system matrices, $[x]$ is the state vector and $[u]$ is the input.

$$\begin{aligned}
[A_t]_{n\times n} &= \begin{bmatrix} a_{11} & a_{12} & \dots & a_{1n} \\ a_{21} & a_{22} & \dots & a_{2n} \\ \vdots & & & \\ a_{n1} & a_{n2} & \dots & a_{nn} \end{bmatrix}, \quad [x]_{n\times 1} = \begin{bmatrix} x_1 \\ x_2 \\ \vdots \\ x_n \end{bmatrix} \\
[B_t]_{n\times m} &= \begin{bmatrix} b_{11} & b_{12} & \dots & b_{1m} \\ b_{21} & b_{22} & \dots & b_{2m} \\ \vdots & & & \\ b_{n1} & b_{n2} & \dots & b_{nm} \end{bmatrix}, \quad [u]_{n\times 1} = \begin{bmatrix} u_1 \\ u_2 \\ \vdots \\ u_m \end{bmatrix}
\end{aligned} \tag{4.66}$$

The aim of system identification is to get $[A_t]$ and $[B_t]$ with known values of $[x]$,$[\dot{x}]$ and $[u]$. Suppose $[A_s]$ and $[B_s]$ are estimated parameter values of $[A_t]$ and $[B_t]$, then the error between the real system and the estimated system is:

$$[\dot{e}] = [\dot{x}] - [A_s]x - [B_s]u$$

and the identification energy function is defined as

$$\begin{aligned} E &= \frac{1}{2t}\int_0^t [\dot{e}]^{tr}[\dot{e}]dt \\ &= \frac{1}{2t}\int_0^t ([\dot{x}] - [A_s]x - [B_s]u)^{tr}([\dot{x}] - [A_s]x - [B_s]u)dt \end{aligned}$$

When we compare this energy function with the standard energy function of Hopfield neural network in equation 4.63, we can get the weight matrix $[T_{ij}]$ and the bias matrix $[I_j]$, which are crucial for the training of the neural network.

Defining $[Q]$ as

$$[Q] = [a_{11}, \ldots, a_{1n}, \ldots, a_{n1}, \ldots, a_{nn}, b_{11}, \ldots, b_{1m}, \ldots, b_{n1}, \ldots, b_{nm}]^{tr},$$

the weight matrix $[T_{ij}]$ and bias matrix $[I_j]$ can be computed using equation 4.67, and the definition of the matrix elements in $[PT]$ is shown in equation 4.68. In equation 4.68, $'diag'$ means diagonals of the matrix. The other elements of matrices $[PT_{11}]$,$[PT_{12}]$,$[PT_{21}]$ and $[PT_{22}]$ are all zeros except the diagonals.

$$\begin{cases} [T_{ij}] &= -\frac{1}{t}\int_0^t [PT]\,dt = -\frac{1}{t}\int_0^t \begin{bmatrix} PT_{11} & PT_{12} \\ PT_{21} & PT_{22} \end{bmatrix} dt \\ [I_i] &= \frac{1}{t}\int_0^t \begin{bmatrix} \dot{x}_1[x], & \ldots, & \dot{x}_n[x], & \dot{x}_1[u], & \ldots, & \dot{x}_n[u] \end{bmatrix}^{tr} dt \end{cases} \tag{4.67}$$

$$\begin{aligned} [PT_{11}]_{n^2\times n^2} &= diag\begin{pmatrix} [x][x]^{tr} & [x][x]^{tr} & \ldots & [x][x]^{tr} \end{pmatrix} \\ [PT_{12}]_{n^2\times nm} &= diag\begin{pmatrix} [x][u]^{tr} & [x][u]^{tr} & \ldots & [x][u]^{tr} \end{pmatrix} \\ [PT_{21}]_{nm\times n^2} &= diag\begin{pmatrix} [u][x]^{tr} & [u][x]^{tr} & \ldots & [u][x]^{tr} \end{pmatrix} \\ [PT_{22}]_{nm\times nm} &= diag\begin{pmatrix} [u][u]^{tr} & [u][u]^{tr} & \ldots & [u][u]^{tr} \end{pmatrix} \end{aligned} \tag{4.68}$$

Therefore, for the sigmoid function shown in equation 4.64, the expression for the evolution of $[Q]$ can be obtained as

$$\frac{dQ_i}{dt}|_{(i=1,\ldots,n^2+nm)} = \frac{dQ_i}{d\phi_i}\frac{d\phi_i}{dt} = \frac{k(\rho^2 - Q_i^2)}{2\rho}\left[\sum_{j=1}^{n^2+nm} T_{ij}Q_j + I_i\right]. \tag{4.69}$$

Integration of the above equation gives the solution to the parameter estimation problem.

To apply this method in combination with the load test for the determination of machine parameter, the oscillations of stator currents in the steady state are taken into account. The governing equations of permanent magnet synchronous machine in the steady state are:

$$v_d = R_s i_d - \omega_e L_q i_q + L_d \frac{di_d}{dt} \tag{4.70}$$

$$v_q = R_s i_q + \omega_e L_d i_d + L_q \frac{di_q}{dt} + \sqrt{3} E_0 \tag{4.71}$$

Rewriting equations (4.70) and (4.71) into state space model, we can get

$$[\dot{X}] = [A_d][X] + [B_d][U]. \tag{4.72}$$

where

$$[A_d] = \begin{bmatrix} -\frac{R_s}{L_d} & \omega_e \frac{L_q}{L_d} \\ -\omega_e \frac{L_d}{L_q} & -\frac{R_s}{L_q} \end{bmatrix}, \quad [X] = \begin{bmatrix} i_d \\ i_q \end{bmatrix}, \quad [B_d] = \begin{bmatrix} \frac{1}{L_d} & 0 & 0 \\ 0 & \frac{1}{L_q} & -\frac{\sqrt{3}E_0}{L_q} \end{bmatrix}, \quad [U] = \begin{bmatrix} v_d \\ v_q \\ 1 \end{bmatrix} \tag{4.73}$$

Comparing with the standard model in equations 4.65 and 4.66, we can get $n = 2$ and $m = 3$; and the number of unknown values is 10. The matrix $[Q]$ is given by:

$$\begin{aligned} [Q] &= [Q_1, Q_2, Q_3, Q_4, Q_5, Q_6, Q_7, Q_8, Q_9, Q_{10}] \\ &= [-\frac{R_s}{L_d}, \omega_e \frac{L_q}{L_d}, -\omega_e \frac{L_d}{L_q}, 0, 0, 0, \frac{1}{L_q}, -\frac{\sqrt{3}E_0}{L_q}]. \end{aligned}$$

Form the expression of $[Q]$, we can see that the values of $[Q]$ are not all free unknowns, it also includes some constraints. Taking R_s (see Appendix H) and ω_e (rated value of 314.16 rad/s) as known values, the constraints are:

$$\begin{cases} Q_6 = Q_7 = Q_8 = 0; \\ Q_1 = -R_s Q_5; & Q_4 = -R_s Q_9 \\ Q_2 Q_3 = -\omega_e^2; & Q_9 = \omega_e (Q_5/Q_2) \end{cases} \tag{4.74}$$

Using equation 4.69 together with the constraints in equation 4.74, matrix $[Q]$ can be computed; and hence the values of L_d, L_q and E_0 can be determined. To illustrate this process, the revolutions of Q_1 and Q_5 are shown in Figs. 4.21(a) and 4.21(b) respectively.

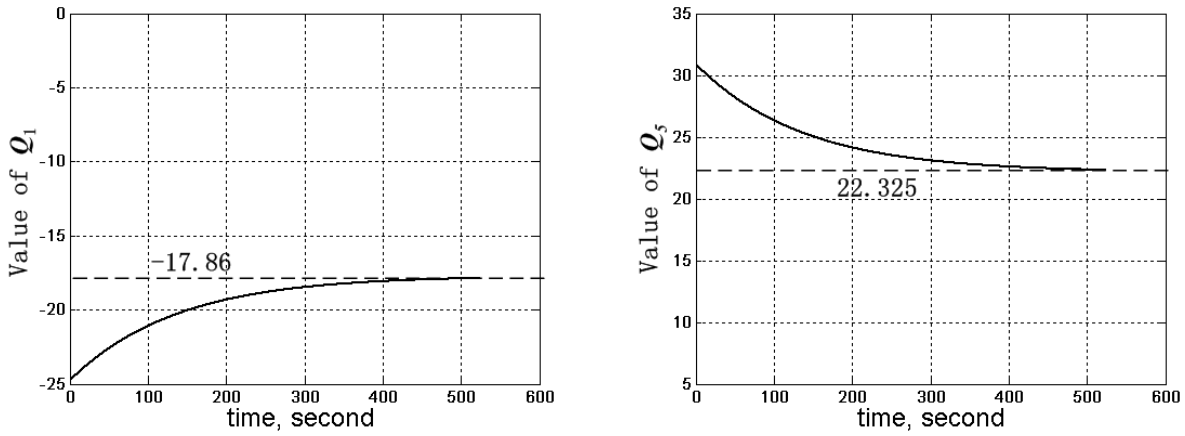

(a) (b)

Figure 4.21: Revolution of matrix $[Q]$, (a) Q_1 (b) Q_5

It is clear in Fig. 4.21 that with time, Q_1 and Q_5 approach some constant values gradually. Q_1 is very close to -17.86 and Q_5 approaches 22.325. These final constant values are the ones we desire, from which we can calculate $L_d = 1/Q_5 = 0.044974H$ and the constraint, $Q_1 = -R_s Q_5$ is met as well.

Following the above procedure, other values of $[Q]$ can be obtained as well. The results obtained using the combined Hopfield neural network and the load test methods are list in Appendix H Table H.6 and plotted in Fig. 4.22.

The results obtained using this method are very close to those obtained by the regression model. Like the combination technique of regression model, the small change in angle β is also avoided in this method. Therefore the experiment

procedure is simplified as well. Compared with the results obtained by Zhou's load test method, we can see that the zigzags of the results in load test method are removed. The variations of all the parameters are very smooth and the variation trends are more obvious. These improvements lie in the fact that the result parameters are identified on the basis of large amount of samples by minimizing the estimation error. In comparison with method of load test only, the combination technique is more optimized. The good results from this method also indicated that the Hopfield neural network is a useful tool in the parameter estimation of machine. Since this method can also be used for the identification of time-varying systems [125], it may be explored for the online parameter estimation of machine and drive systems as well.

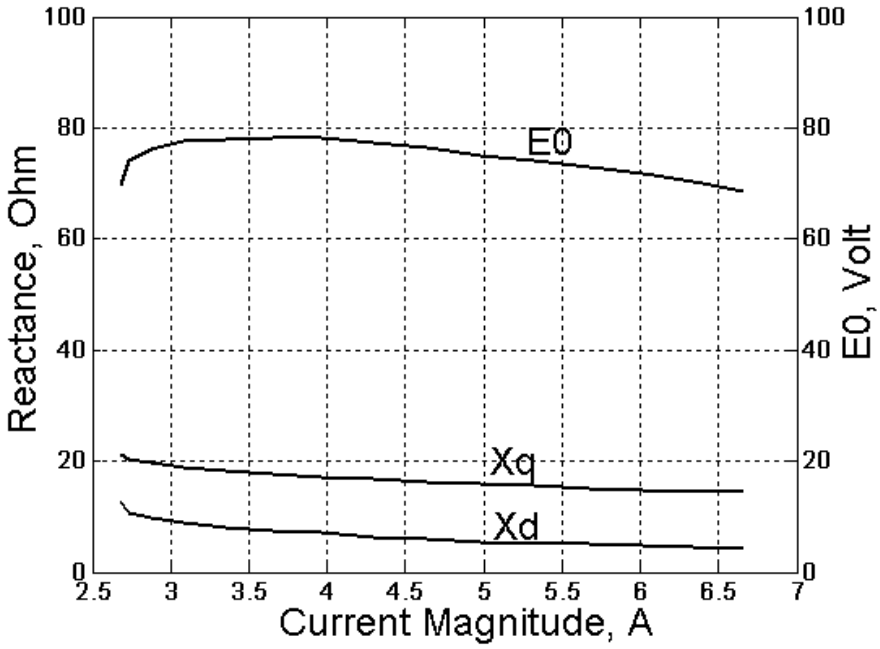

Figure 4.22: Results of Hopfield Neural Network

4.3.5 Parameter Determination Using Finite Element Method

Finite element computation is expensive but provides an easy means of computing machine parameters. Normally, this method can be used for benchmarking all other experimental methods. However, the main limitation of finite element method is in getting a correct and accurate model of the machine. Since finite element method provides an extensive set of values for flux distributions all around, it is much more transparent and can be used to compute machine parameters although many aspects, like eddy losses and hysteresis, are very difficult to represent in finite element models.

4.3.5.1 Inductance Calculation Using Finite Element Method

The evaluation of reactances are realized through the calculation of inductances. Usually, the finite element computation of the steady-state inductances are based on the following two concepts:

- The number of flux linkages of the winding, divided by the current in the winding.
- The energy stored in the inductor, divided by one-half the current squared.

Both concepts give identical results for linear inductances but not the same for nonlinear inductances [45].

Demerdash *et al* and Zhu [133] - [136] have used current and energy perturbation method to calculate the machine parameters. This method is based on the calculation of the total energy stored in the magnetic field of a given device comprising a few windings. On the other hand, many other researchers [49, 137, 138, 139] have calculated the machine parameters on the basis of flux linkages. This method

is realized by applying the Stokes' theorem in the processing of the magnetic field solutions in terms of magnetic vector potentials. The inductance calculation in this work is based on the calculation of flux linkage, current source is used and variation of parameters with load conditions is taken into account as well.

The flux linked by a single turn of coil is

$$\lambda = \int_{\Omega} B \cdot d\Omega. \tag{4.75}$$

where λ is flux linkage, B is flux density and Ω is the area.

Substituting $\nabla \times A = B$ into the above equation and applying the Stokes' theorem, we can get

$$\lambda = \oint A \cdot dl, \tag{4.76}$$

where the integration is around the closed contour formed by the coil and A represents the magnetic vector potential. For the phases windings in machine, neglecting the length at the end of the coil, the flux linkage of one turn of coil is

$$\lambda = l(A^{+} - A^{-}), \tag{4.77}$$

where the superscripts signs $'+'$ and $'-'$ stand for the $'$go$'$ and $'$return$'$ sides of the coils, and l is the axil length of the machine. Therefore, for one phase with N_s equivalent turns of coils, the flux linkages with phases are

$$\lambda_i|_{(i=a,b,c)} = N_s l(\frac{\int\int_{\Omega^+} A^{+} d\Omega}{\Omega^{+}} - \frac{\int\int_{\Omega^-} A^{-} d\Omega}{\Omega^{-}}). \tag{4.78}$$

where Ω^{+} and Ω^{-} are the total cross areas of the positively and negatively oriented coil sides of the phase conductors.

4.3.5.2 Evaluation of Machine Parameters by Applying a Small Change in Current Angle

The method of calculating the machine parameters by varying the current angle is based on the modified load test method used by Zhou [50, 57]. Zhou *et al* and Chang [138] have used the method to estimate the machine parameters using two finite element solutions for each point of operation.

When the permanent magnet synchronous machine is run in steady state, the flux linkages in the d and $q-$axis can be represented by

$$\lambda_d = L_d I_d + \lambda_f \tag{4.79}$$

$$\lambda_q = L_q I_q \tag{4.80}$$

where

$$I_d = I\cos\beta$$

$$I_q = I\sin\beta$$

$$\beta = \frac{\pi}{2} + \delta - \psi$$

δ is the torque angle and ψ is the power factor angle.

Since the variation of parameters with load condition is taken into account in the calculation, L_d, L_q and λ_f are unknowns. As equations (4.79) and (4.80) are inadequate for 3 unknowns, a small change in angle β is exerted and a new β' is obtained. Therefore we can have another set of equations as:

$$\lambda'_d = L_d I'_d + \lambda_f \tag{4.81}$$

$$\lambda'_q = L_q I'_q \tag{4.82}$$

where

$$I'_d = I\cos\beta'$$

$$I'_q = I\sin\beta'$$

With the calculated d and q-axis flux linkage values and the injected current values, L_d, L_q and E_0 can be obtained by solving equations (4.79)-(4.82)

$$\begin{bmatrix} L_d \\ \lambda_f \end{bmatrix} = \begin{bmatrix} I_d & 1 \\ I'_q & 1 \end{bmatrix}^{-1} \begin{bmatrix} \lambda_d \\ \lambda'_d \end{bmatrix}, L_q = \frac{\lambda_q + \lambda'_q}{I_q + I'_q}, E_0 = \omega_e \lambda_f \tag{4.83}$$

When a current is applied, the flux linkages of $a, b, c-$axis can be calculated using equation (4.78), then Park's transformation is used to change the flux linkages from $a, b, c-$axis to $d, q-$axis. The results obtained using this method are shown in Fig. 4.23.

The results obtained by FEM are comparable with the experimental results, but the values of X_d, X_q are higher and the value of E_0 decreases faster than the experimental values. This may be caused by the model that does not take into account the various losses, such as hysteresis losses and eddy current losses. But the results of FEM agree with the experimental results to some extent, which indicated that FEM is applicable and useful in predicating the parameters of PMSM.

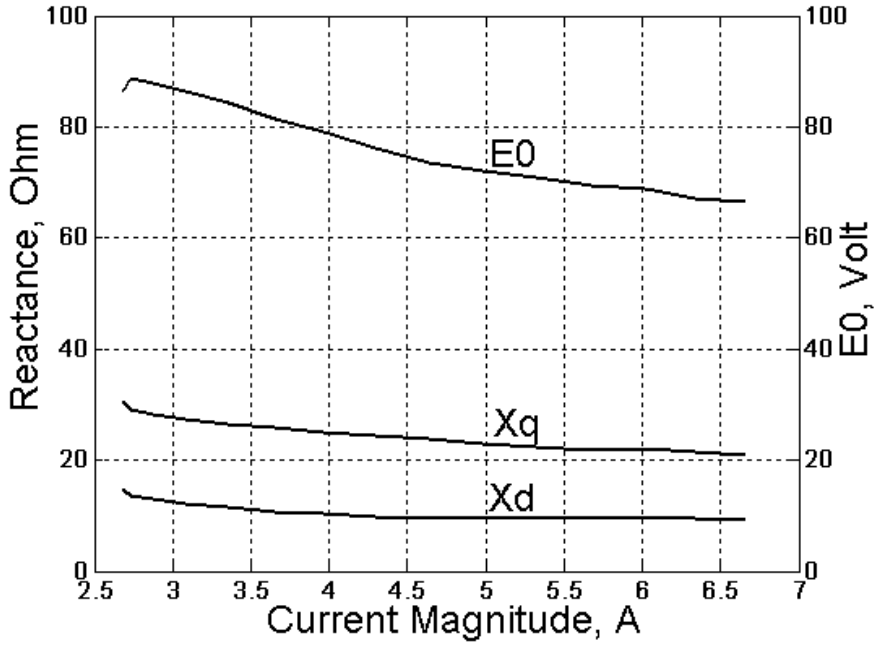

Figure 4.23: Results of FEM Using Current Angle Method

4.4 Conclusion

The lumped parameter model of the line-start permanent magnet synchronous machine is introduced and various techniques for determining machine parameters are discussed in this chapter.

Several experimental methods have been used by other researchers to determine the machine parameters. The DC current decay method can obtain the reactances of various frequencies with simple and low-cost equipment. However, the method can only get single set of reactance values for one frequency and the value of phase voltage due to permanent magnet excitation, E_0, is not obtainable. The parameters obtained from this method is incomplete.

Sensorless no-load test is based on the phasor diagram and two-axis model of permanent magnet machine in steady state. It is assumed that the torque angle is 0 under no-load operation. The stator current varies with the applied voltage.

Phase voltage corresponding to the minimum stator current is E_0. This method is also easy in experimental implementation, and the variation of X_d with saturation is considered. However only a set of X_d can be obtained and the variation of E_0 is neglected. The parameters obtained from this method is still incomplete.

The load test method makes improvement compared with DC current decay method and no-load test method, because both the X_d and X_q can be obtained simultaneously and their variations with loads are considered as well. However, the conventional load test method cannot evaluate the variation of E_0 with the the two equations in two-axis model. The modified load test method overcomes this drawback by imposing a small displacement to the angle β. With one extra equation from the new β, sets of parameters X_d, X_q and E_0 under different load conditions are obtainable. One of the shortcoming of the modified load test method is that the achievement of a small change of β in experiment is very difficult. Another critical shortcoming is that accuracies of the parameters in this method are totally dependent on the measurement of a few experimental data. A small inaccuracy in one data may bring along big mistake to the resultant parameters. Therefore the parameters of X_d and E_0 obtained from this method are fluctuating, which are more likely to be caused by the inaccuracy of the small change in β.

To overcome the shortcomings of the modified load test method, two new methods are proposed. One method is based on the combination of load test and the technique of linear regression, the other is based on the combination of load test and the Hopfield neural network.

The combination of load test and linear regression technique is quite effective in parameter estimation. The difficulty of achieving the small change in β is avoided

so that the experiment procedure is simplified. Moreover, since the parameters are evaluated on the basis of thousands of experimental samples, the accuracies of the results are improved greatly. The fluctuation in load test is removed and the variation trend of parameters with load conditions becomes more obvious.

The combination of load test and Hopfield neural network also shows great improvement compared with the load test only. The results obtained by this method are very close to those obtained by the technique of linear regression. One of the main advantages of this method is the change of β is avoided as well. Since the parameters are identified based on large amount of samples by minimizing the estimation error, good accuracies are achieved. In addition, the Hopfield neural network is applicable for both time-varying and time-invariant system, therefore the method may be applied for the online parameter estimation of machines.

Finite element method (FEM) is used to compute the machine parameters also. Finite element calculation fed with current source is implemented and the variations of parameters with different load conditions are taken into account. The results of FEM are comparable with the experimental results, which suggested that the FEM is a useful means of predicting machine parameters.

Chapter 5

Dynamic Analysis of a Line-Start Permanent Magnet Synchronous Machines with Coupled Circuits

5.1 Introduction

A line-start permanent magnet synchronous machine has squirrel cage bars (or damper windings) in the rotor for asynchronous starting. It is a very high efficiency synchronous machine designed for fixed and variable frequency operations. The excitation is provided partly by the magnets, which are mounted on the rotor, and partly by the line current. The motor is initially started by the the accelerating torque generated in the cages, and finally sustained by the synchronous torque which is due to the magnets and the saliency of the rotor.

When connected to a fixed frequency AC voltage supply, the line-start permanent magnet synchronous machines run up to the synchronous speed. However, several factors have to be considered in the starting process, such as starting current, accelerating toque, heating, synchronization, stability, etc. Some line-start permanent magnet synchronous machines have high starting current and pulsating torque during the self starting process. Frequent self-starting may cause damage to the permanent magnets as well as to the mechanical parts. Synchronization

is another important issue that has to be tackled. The increase of the magnet strength may lead to an increase in the synchronization process. However a strong excitation magnetic field can result in a big braking torque and prevent the machine from starting. Particularly, for large capacity machines, the self-starting is quite difficult or even impossible.

To avoid the problems and difficulties occuring during the self-starting process, a line-start permanent magnet synchronous machine is usually used in applications where frequent self-starting are not common. To ensure the proper operation of the machine, usually external drive circuits become necessary; particulary when adjustable frequency operations are required. Therefore a complete numerical analysis of the machine should include not only the machine itself, but also the peripheral drive circuits.

The methodology of field-circuit coupled time-stepping finite element has been presented in Chapter 3. The method is used here to analyze the dynamics of a line-start permanent magnet synchronous machine. As one of the important performances, the starting process is computed. Two kinds of starting processes are implemented: a self starting process and starting under two different control schemes.

5.2 Experimental Setup of the PMSM Drive

An experimental setup for implementing the test of PMSM drive system has been built. The complete configuration of the whole experimental setup is shown in Fig. 5.1.

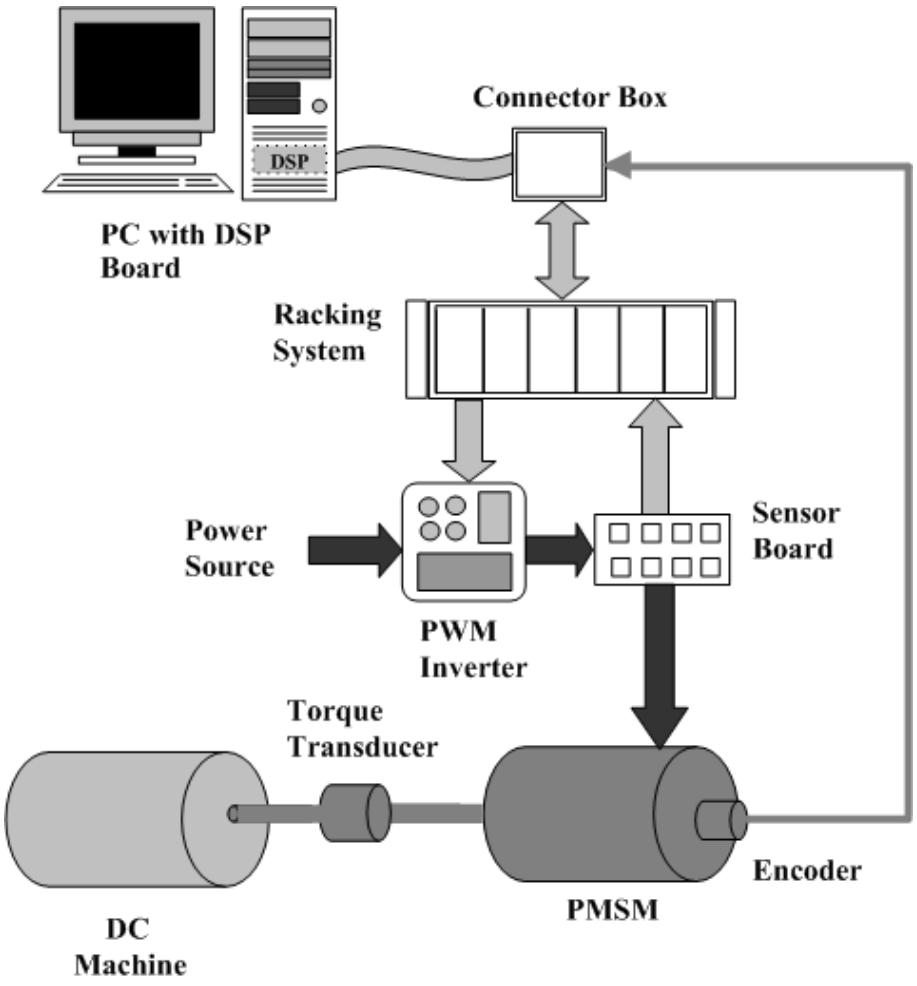

Figure 5.1: Configuration of PMSM Drive Experimental Setup

The test platform consists of a line-start PMSM, a torque transducer, a DC machine and an incremental encoder mounted at the end of the PMSM shaft (Fig. 5.2). The control and measurements are realized by a system based on the dSPACE DS-1102 controller board. This system includes a personal computer, a dSPACE DS-1102 controller board, an inverter, a racking system and a sensor box (Fig. 5.3).

A brief account of the system is given below:

1. DS-1102 Controller Board

   The board consists of a floating-point DSP TMS320C31, a micro-controller TMS320P14 acting as the slave-DSP for the digital I/O subsystem, A/D and D/A converters, and encoder interfaces [140]. The main DSP processes numerically intensive algorithms at a frequency of 60 MHz. The slave-DSP performs digital I/O and PWM generation. The A/D converters convert the analog feedback signals of ± 10 V into digital format so that the DSP can read the measured quantity. Such conversions are used for the measured stator currents feedback signal. The D/A converters convert the digital signals in the DSP into analog signals of ± 10 V so that they can be displayed on the oscilloscope. The encoder interface provides the interfacing of the DSP with the incremental encoder so that the output of the incremental encoder, which is in discrete pulses, can be quantized into digital form.

2. PWM Inverter

   The inverter consists of an IGBT module (MUBW 10-12A7) [141], DC-link capacitors, a transformer board and a driver board. The IGBT module used in the PWM inverter is IXYS model (MUBW 10-12A7). Details of the inverter are given in Appendix H.

3. Racking System

   In the implementation of the experimental PMSM drive setup, it is necessary to provide a hardware interface between the motor drive and the DSP-DS1102. A racking system has been constructed as an integrated interface platform . The platform comprises five cards (or modules), namely the Inverter Control Card, Encoder Interface Card, Digital I/O Card, Current Feedback Card and Torque/Analog Feedback Card [142].

4. Sensor Box

   Accurate measurements of the motor phase currents are essential to ensure high-performance in the PMSM drive system. In the experimental setup described above, two current sensors are utilized to measure the phase currents. The measured currents are converted into voltage signals scaled to a range of ± 10 V using resistors of appropriate values. These voltage signals are then fed into the A/D converters of the DS1102. The LEM module LA 25-NP current sensors are used. The current sensors, resistors and the power supply for the current sensor are included on the current sensor board [142].

5. Software Implementation

   The control schemes used in the starting process of the PMSM drive are implemented using the TMS320C31 DSP [143]. The TMS320C31 has a high speed CPU and adequate memory for software implementation. It has a 60 MHz instruction frequency enabling a high sampling rate in the drive system.

   The entire control program for the starting of the PMSM is written in C language. Programming in C offers greater flexibility in the control program and the user has the freedom to optimize the source code so that it results

in the lowest execution time and hence achieving a fastest sampling time.

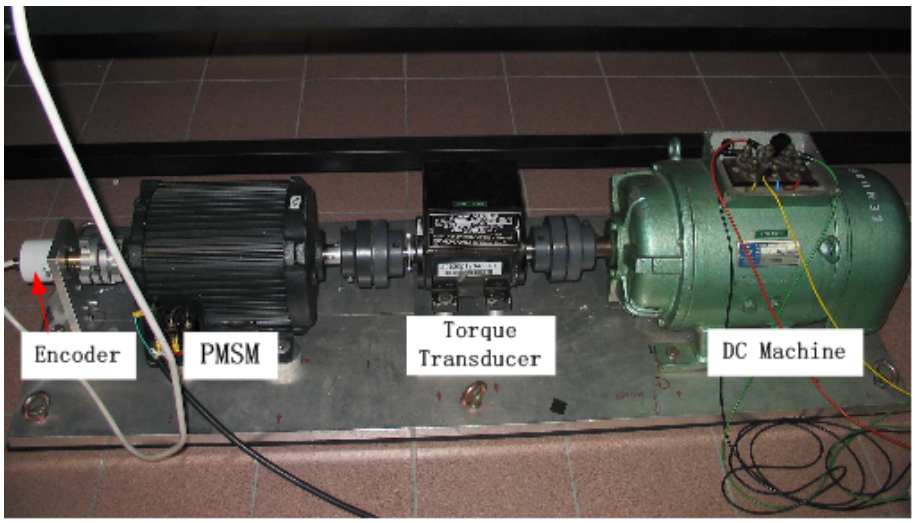

Figure 5.2: PMSM Coupled with DC Machine

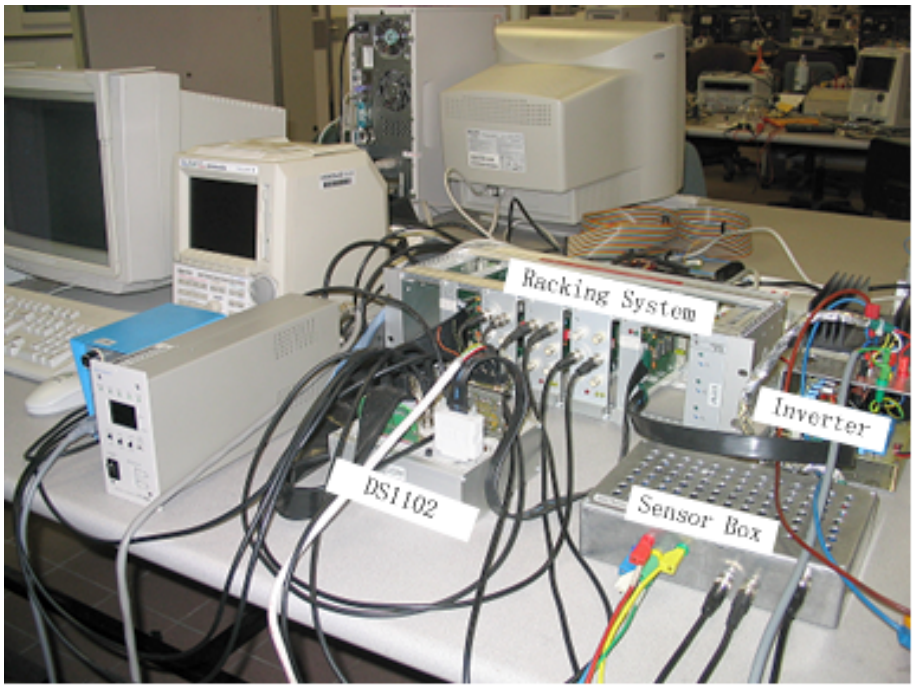

Figure 5.3: Controller Board Based Experimental Platform of PMSM Drive System

5.3 Methodology and Modelling for Analysis

A two-dimensional finite element method is used for modelling the motor performance. Maxwell's equations, applied to the domains, give rise to the diffusion equations. The non-linear field equations are solved simultaneously with the rotor, stator and external circuit equations, allowing current distribution in the rotor bars to be properly accounted for.

5.3.1 Modelling of the Fields

Recalling equation (2.26), the fundamental equations for the magnetic field are represented in the two-dimensional rectangular coordinates as

$$\frac{\partial}{\partial x}(\nu\frac{\partial A}{\partial x}) + \frac{\partial}{\partial y}(\nu\frac{\partial A}{\partial y}) = \sigma\frac{\partial A}{\partial t} - \sigma\frac{V_{tz}}{l} - \nabla \times (\nu\mu_0 M_r) \tag{5.1}$$

For each domain in the machine, the field equation can be represented as:

- In the laminated iron where eddy current is neglected because of the lamination and in the air gap

$$\frac{\partial}{\partial x}(\nu\frac{\partial A}{\partial x}) + \frac{\partial}{\partial y}(\nu\frac{\partial A}{\partial y}) = 0 \tag{5.2}$$

- In the armature windings

$$\frac{\partial}{\partial x}(\nu\frac{\partial A}{\partial x}) + \frac{\partial}{\partial y}(\nu\frac{\partial A}{\partial y}) = -\frac{i_s}{s} \tag{5.3}$$

- In the rotor cage bars where the bars are solid conductors and the eddy current is taken into account in the modelling.

$$\frac{\partial}{\partial x}(\nu\frac{\partial A}{\partial x}) + \frac{\partial}{\partial y}(\nu\frac{\partial A}{\partial y}) = \sigma\frac{\partial A}{\partial t} - \sigma\frac{V_{bk}}{l_b} \tag{5.4}$$

- In the permanent magnets

$$\frac{\partial}{\partial x}(\nu\frac{\partial A}{\partial x})+\frac{\partial}{\partial y}(\nu\frac{\partial A}{\partial y})=-\nabla\times(\nu\mu_0 M_r) \tag{5.5}$$

where

$A =$ magnetic vector potential (having the component of axial direction only)

$i_s =$ armature phase current (i_a, i_b, i_c)

$s =$ the average cross sectional area of one turn of the winding

$\nu =$ reluctivity of the material

$V_{bk} =$ the voltage difference across a cage bar between the far and near ends

$l_b =$ the length of a cage bar in $Z-$direction

$M_r =$ remanent magnetization of permanent magnet

5.3.2 Modelling of the Stator Phase Circuits

Fig. 5.4 shows the circuit of stator windings for the experimental machine. It has three stator phase windings, which are star connected with a neutral.

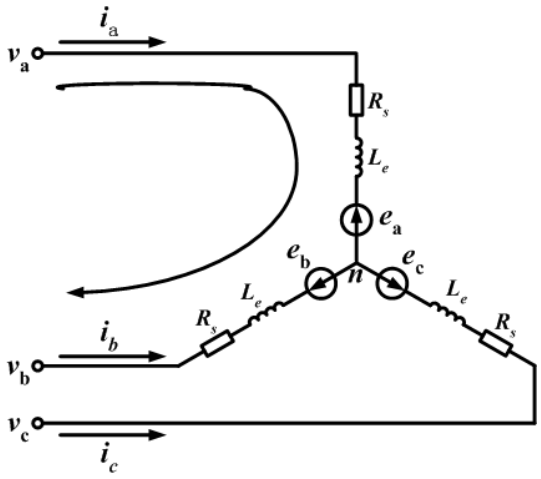

Figure 5.4: Circuit of Stator Windings for the Experimental Machine

The voltage and current equations of the permanent magnet synchronous machine are given as

$$e_a + R_s i_a + L_e \frac{di_a}{dt} = v_a - v_n \tag{5.6}$$

$$e_b + R_s i_b + L_e \frac{di_b}{dt} = v_b - v_n \tag{5.7}$$

$$e_c + R_s i_c + L_e \frac{di_c}{dt} = v_c - v_n \tag{5.8}$$

$$i_a + i_b + i_c = 0 \tag{5.9}$$

where , v_a, v_b and v_c are the phase voltages, subscripts a, b and c represent stator quantities in lines a, b and c respectively. v_n is the potential of the neutral. R_s and L_e are the total resistance and end-winding inductance of the stator winding per phase respectively (methods of computation are given in Appendix J). e_a, e_b and e_c are the induced phase voltages. Recalling equation (2.37), the induced phase voltages are given by the line integral of the vector potential along the stator windings of phase a, b and c respectively

$$e_a = \frac{l}{s}\left(\int\int_{\Omega^+} \frac{\partial A}{\partial t} dxdy - \int\int_{\Omega^-} \frac{\partial A}{\partial t} dxdy\right) \tag{5.10}$$

where l is the length of stator windings in $Z-$direction, Ω^+ and Ω^- are the total cross section area of 'go' and 'return' windings per phase respectively. e_b and e_c can be obtained similarly as in equation (5.10).

5.3.3 Modelling of the Rotor Bars

Fig. 5.5 shows the equivalent circuit of the rotor cage bars for the experimental machine. Only one pole of the machine is involved in the calculation.

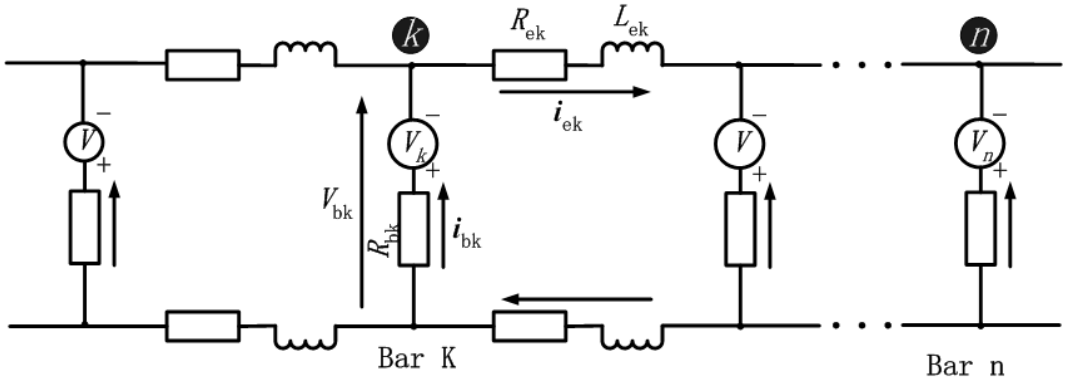

Figure 5.5: Equivalent Circuit of Rotor Cage Bars

Recalling equation (2.42), the governing equation for each bar is

$$V_{bk} = R_{bk} i_{bk} + \frac{l_{bk}}{s_{bk}} \int\int_{s_{bk}} \frac{\partial A}{\partial t} dxdy \tag{5.11}$$

where l_{bk} is the length of k_{th} bar in $Z-$direction and s_{bk} is the cross section area of the bar.

Recalling equations (2.44) and (2.49), the circuit equations for the cage bars are

$$[i_{bk}] - [C_1][i_{ek}] = 0 \tag{5.12}$$

and

$$[C_2][V_{bk}] + 2\{[R_{ek}] + \frac{d}{dt}[L_{ek}]\}[i_{ek}] = 0 \tag{5.13}$$

where

$$[C_1] = \begin{pmatrix} 1 & \dots & \dots & \dots & \dots & \mp 1 \\ -1 & 1 & \dots & \dots & \dots & \dots \\ \vdots & \vdots & \vdots & \vdots & \vdots & \vdots \\ \dots & \dots & -1 & 1 & \dots & \dots \\ \vdots & \vdots & \vdots & \vdots & \vdots & \vdots \\ \dots & \dots & \dots & \dots & -1 & 1 \end{pmatrix}_{n_p \times n_p}, \tag{5.14}$$

$$[C_2] = \begin{pmatrix} 1 & -1 & \dots & \dots & \dots & \dots \\ \dots & 1 & -1 & \dots & \dots & \dots \\ \vdots & \vdots & \vdots & \vdots & \vdots & \vdots \\ \dots & \dots & \dots & 1 & -1 & \dots \\ \vdots & \vdots & \vdots & \vdots & \vdots & \vdots \\ \mp 1 & \dots & \dots & \dots & \dots & 1 \end{pmatrix}_{n_p \times n_p}, \tag{5.15}$$

and n_p is the number of cage bars in the computation domain.

From equation (5.12), we can get

$$[i_{ek}] = [C_1]^{-1}[i_{bk}] \tag{5.16}$$

where $()^{-1}$ represents the inverse operation of a matrix.

Substituting equation (5.16) into equation (5.13) yields

$$[C_2][V_{bk}] + 2\{[R_{ek}] + \frac{d}{dt}[L_{ek}]\}[C_1]^{-1}[i_{bk}] = 0 \tag{5.17}$$

or

$$[C_1][C_2][V_{bk}] + 2\{[R_{ek}] + \frac{d}{dt}[L_{ek}]\}[i_{bk}] = 0 \tag{5.18}$$

Since

$$[C_2] = [C_1]^{tr} \tag{5.19}$$

equation (5.18) becomes

$$2\{[R_{ek}] + \frac{d}{dt}[L_{ek}]\}[i_{bk}] = -[C_1][C_1]^{tr}[V_{bk}] \tag{5.20}$$

where $()^{tr}$ represents the transpose operation of a matrix. R_{ek} represents the end ring resistance and L_{ek} represents the end ring inductance. V_{bk} and i_{bk} represent the bar voltage and bar current respectively. It is assumed that all the segments of end rings have the same values of R_{ek} and L_{ek}. Their values are given in Appendix J. Only one pole of the machine is involved in this work, therefore matrix $[C_1]$ is

given by

$$[C_1] = \begin{pmatrix} 1 & 0 & 0 & \dots & 0 & 1 \\ -1 & 1 & 0 & \dots & 0 & 0 \\ 0 & -1 & 1 & \dots & 0 & 0 \\ \vdots & \vdots & \vdots & & \vdots & \vdots \\ 0 & 0 & 0 & \dots & -1 & 1 \end{pmatrix} \tag{5.21}$$

5.3.4 Modelling of the External Circuits

The connection of the machine with the external circuits is illustrated in Fig. 5.6. Recalling equations (2.75) and (2.80), the governing equations for external circuits are

$$\{[R_{sb}] + \frac{d}{dt}[L_{sb}]\}[i_{sb}] + [C_{sb}]\frac{d}{dt}[V_{sb}; V_s] = 0 \tag{5.22}$$

$$[C_3][i_{sb}] + [C_4][i_s] = 0 \tag{5.23}$$

where $[R_{sb}]$,$[L_{sb}]$ and $[C_{sb}]$ represent the resistance, inductance and capacitance of the external circuits respectively. V_{sb} is terminal voltage of all the joints. V_s represents the three phase voltages of experimental machine, v_a, v_b and v_c. C_3 and $[C_4]$ represent the connection matrix for current flowing in external circuit and the phase current of the machine.

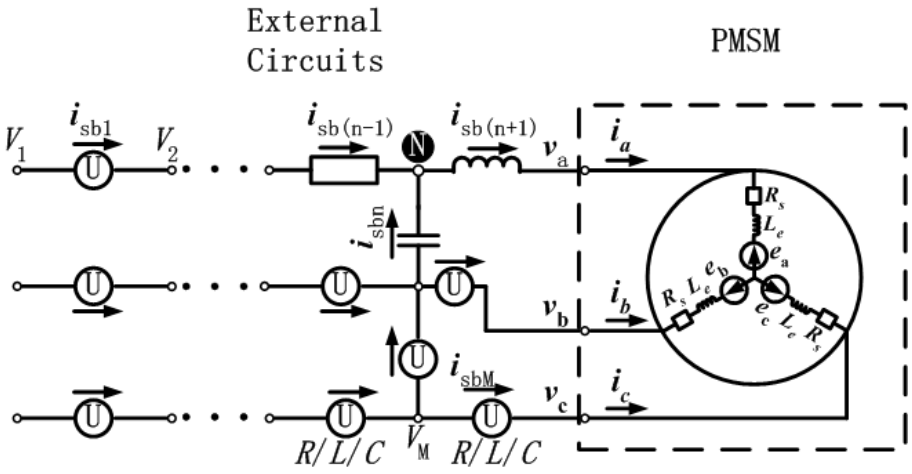

Figure 5.6: Illustration of Line-Start PMSM Connected with External Circuit

5.3.5 Modelling of the Rotor Motion

The mechanical motion of the rotor is governed by

$$J_r \frac{d\omega_m}{dt} = T_{em} - T_L - B_f \omega_m, \tag{5.24}$$

$$\frac{d\theta_m}{dt} = \omega_m \tag{5.25}$$

where ω_m is the rotor speed and θ_m is the rotor position. The parameter values of rotor inertia J_r and friction coefficient B_f is given in Appendix K. The electromagnetic torque is calculated by the method of Maxwell stress tensor.

After the finite element formulation and assembly of equations (5.2)-(5.25), a global matrix equation is be generated. The solution of this matrix provides the information of the drive system for one instant of time or one time step. Continuous computation of the system step by step is required in order to realize the dynamic evaluation of the drive system.

5.4 Evaluating the EMF due to the Permanent Magnets

The line-start permanent magnet synchronous machine is driven by an external machine and run at a speed of $1500rpm$. The terminal voltages of the stator phases are generated by the permanent magnets. In the FEM computation, the machine is run at a constant speed of $1500rpm$ and permanent magnets are taken as the only sources. The induced EMF of stator phases are calculated using equation (5.10). Fig. 5.7 shows the computational and experimental values of this voltage, from which we can see their agreements are quite good.

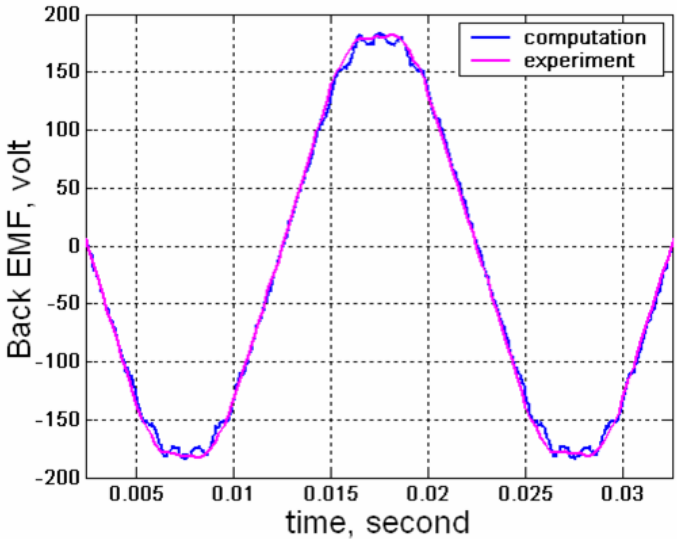

Figure 5.7: Computational and Experimental EMF due to PMs

5.5 The Self-Starting Process of the PMSM

5.5.1 Procedure of Computation

The machine used in this work has cage bars in the rotor, so it has the capability of self-starting. To compute the starting process of the machine, a few steps are involved in finite element analysis:

1. First, the terminal voltage V_l, its initial phase angle ϕ_0 and time step Δt are set. The voltages for the three stator phase windings can be represented by

$$v_a(t) = \sqrt{\frac{2}{3}} V_l \cos(\omega t + \phi_0) \tag{5.26}$$

$$v_b(t) = \sqrt{\frac{2}{3}} V_l \cos(\omega t + \phi_0 - \frac{2\pi}{3}) \tag{5.27}$$

$$v_c(t) = \sqrt{\frac{2}{3}} V_l \cos(\omega t + \phi_0 - \frac{4\pi}{3}) \tag{5.28}$$

2. The vector potential, A, at $t = 0$ is set, where the static field caused by only permanent magnets is given as the initial value.

3. At $t = t + \Delta t$, the value of θ_m^t is set.

4. At $t = t + \Delta t$, each voltage of v_a, v_b and v_c is set.

5. The initial values for A^t, i_a^t, i_b^t and i_c^t are set.

6. The matrix equation constructed by the field-circuit coupled time-stepping finite element techniques is solved.

7. The convergence of solution is tested. Unless solution converges, the process returns to step 6.

8. After the convergence of solution, T_{em} can be calculated. Then a new ω_m and θ_m can be determined by equations (5.24) and (5.25).

9. The calculation process from step 3 to step 8 continues until the steady state is reached.

5.5.2 Results of Self-Starting at No-Load ($T_L = 0N \cdot m$)

Applying the steps listed above, the self-starting process of the machine can be calculated. The rated line-line voltage is applied to the machine. Figs. 5.8 and 5.9 show the computational and experimental results of starting current at no-load. The computed current for the starting is nearly sinusoidal, while that of the experimental one is more like a square wave. The main reason for the disparity is that the maximum values of the experimental starting current were limited by the current limit of the probe [144], so the experimental waveforms were chopped at the peak. It is noted that the computed values are higher than the experimental values at the beginning. This may be caused by the analytical calculation of rotor bar parameters and stator end windings. Because the end rings and the stator end windings are represented by resistors and inductors; the $3D$ electromagnetic fields in the end rings and end windings are simplified using circuit models, some

inaccuracies may be brought in. These inaccuracies can affect the bar current, the electromagnetic field and hence the stator current in the starting process. After the motor is fully run, the rotor is synchronized with the stator; then the effects brought in by the inaccuracy of rotor bar parameters are removed. However, due to the effects of the inaccuracies in analytical stator windings parameters, there are still slight differences between the computational and experimental phase currents as shown in Fig. 5.10.

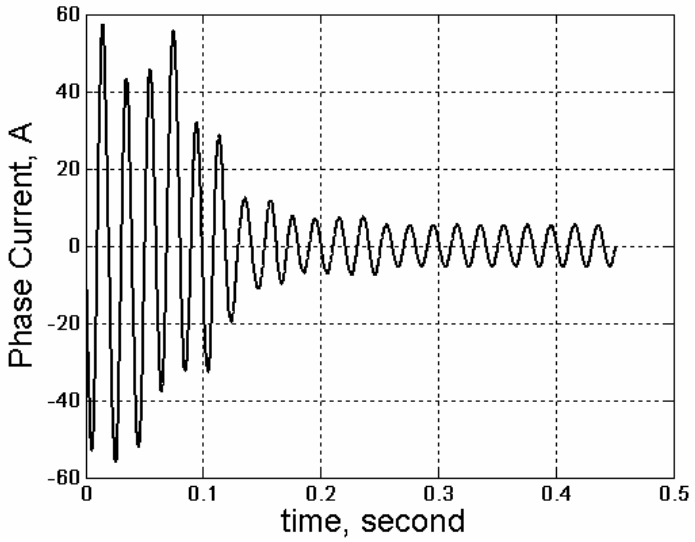

Figure 5.8: Computational Phase Current in Self-Staring Process

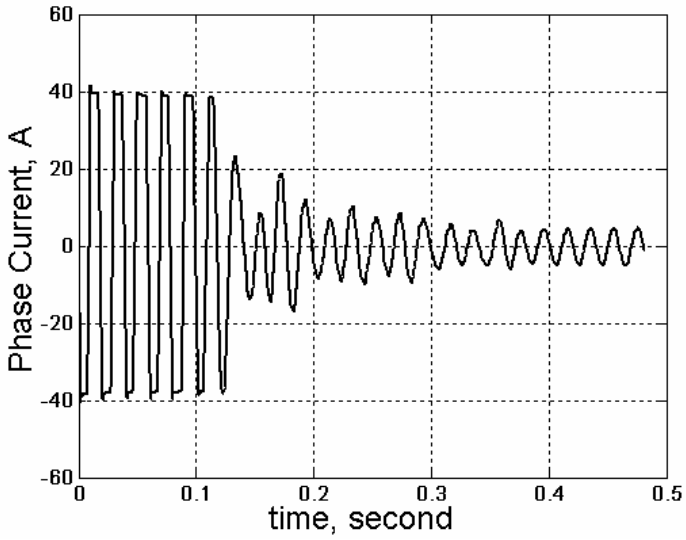

Figure 5.9: Experimental Phase Current in Self-Staring Process

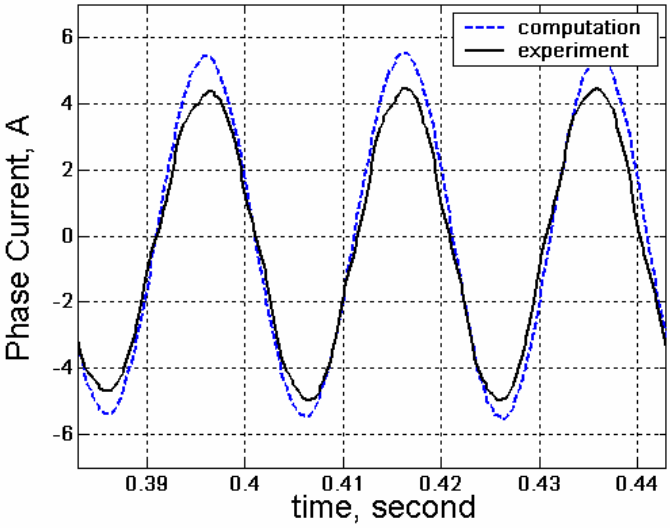

Figure 5.10: Computational and Experimental Phase Current in Steady State

Figs. 5.11 and 5.12 show the computational and experimental speed in the self-starting process. It takes about $0.15s$ for the machine to run up to steady state in both the computational and experimental cases. The computational and the experimental speed agree very well at the beginning when both of them are lower than $200rpm$. Then the computational speed becomes lower than the experimental speed within the time of $0.1s$, although their waveforms are similar in patterns. When the speed is fairly high (above $1000rpm$), the computational speed agrees well with the experimental one. The differences in computational and experimental speed come from the differences in torque. The differences in torque pulsations during the run-up are difficult to explain. Possible causes are cogging torque due to permanent magnet excitation, induction motor cogging torque due to slot effect and of course inaccuracies involved in the modelling of resistances and leakage inductances. $3D$ effects have not been taken into account in this $2D$ modelling. The combined effects of these factors may cause the differences in computational and experimental results. The time step used in this work is $250\mu s$. Computation of cogging torque pulsation is a function of time step, and hence the speed is also related to the time step. The choice of time step may also cause computational result to be damped, resulting into lower peaks in pulsation than the experimental one.

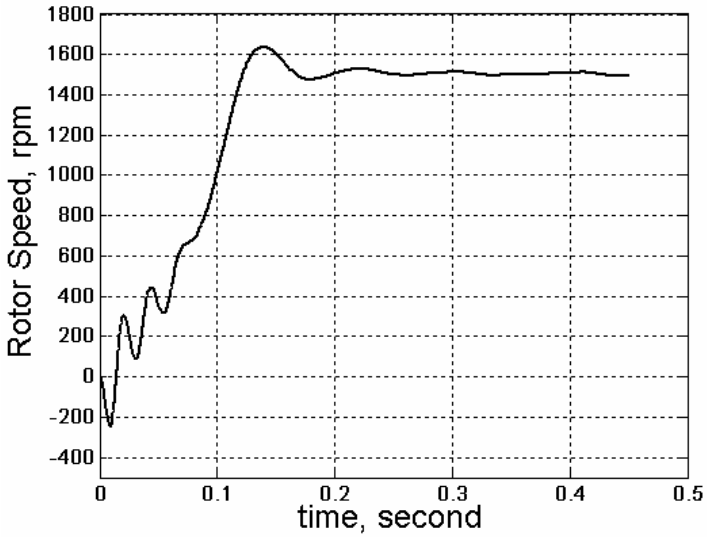

Figure 5.11: Computational Rotor Speed in Self-Starting Process

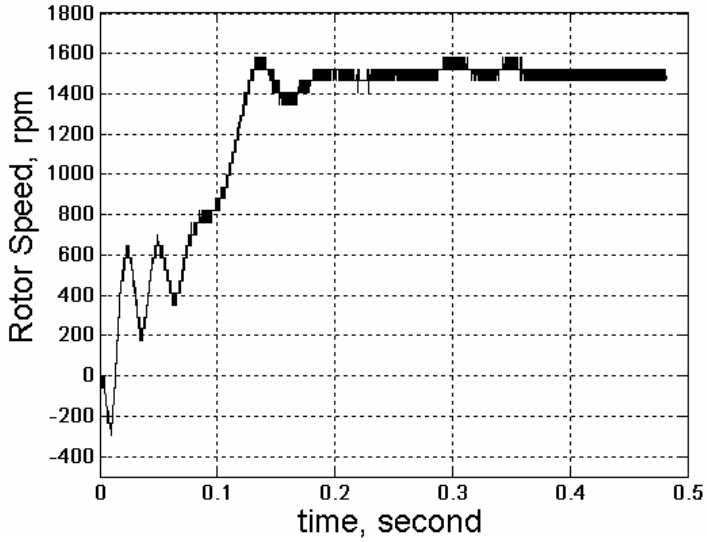

Figure 5.12: Experimental Rotor Speed in Self-Starting Process

Fig. 5.13 shows the motor torque in the self-starting process. Because of the limitation of experimental equipment [145], the experimental result of motor torque is not available. Fig. 5.14 shows the characteristic of motor torque versus rotor speed.

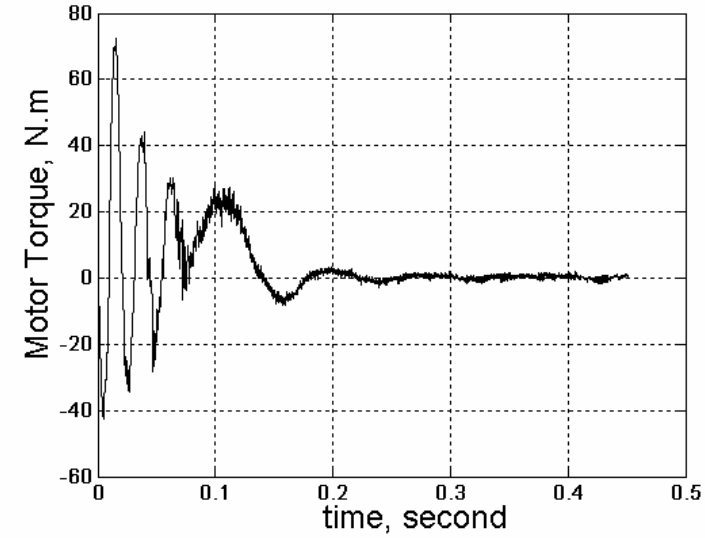

Figure 5.13: Computational Motor Torque in Self-Starting Process

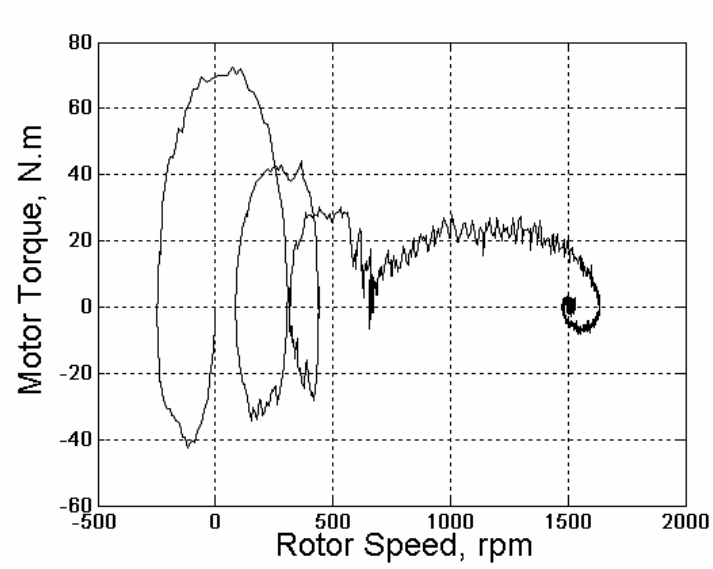

Figure 5.14: Computational Motor Torque versus Rotor Speed in Self-Starting

The maximum current limit information is important for the rating demand of inverters and avoid demagnetization of permanent magnets. The time of run-up to stable synchronization needs to be specified for some applications involving high coupled inertia. The torque level throughout the run-up can be a deciding factor in the suitability of a motor for a particular application. All these engineering information can be found from the results presented in Figs. 5.8 - 5.14.

5.5.3 Results of Self-Starting With Load ($T_L = 8N \cdot m$)

In practice, electric machines are often started with loads.The evaluation of self-starting process with loads are very important for machine designers to predict the machine performances. A load torque of $T_L = 8N \cdot m$ is selected and the self-starting process under this load is calculated.

Figs. 5.15-5.18 show the computational current, speed, motor torque and the characteristic of motor torque versus rotor speed in the self-starting with load.

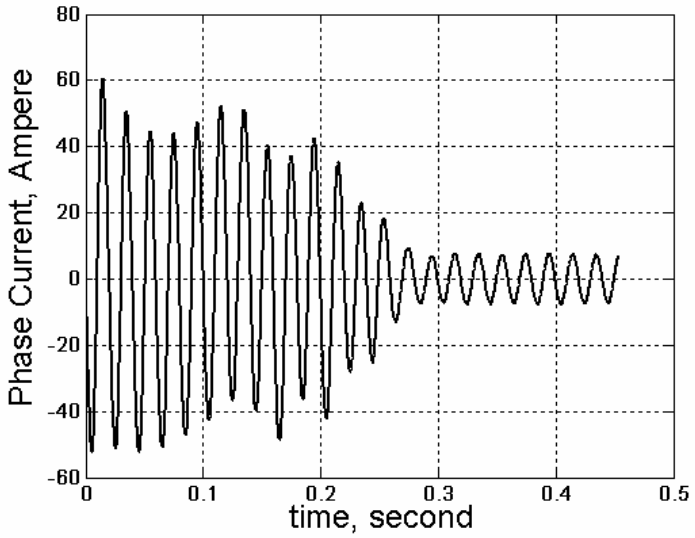

Figure 5.15: Computational Phase Current in Self-Starting With Load

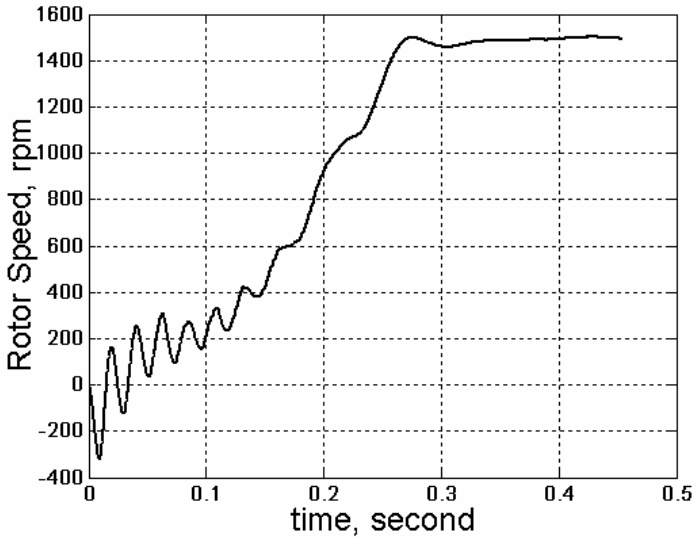

Figure 5.16: Computational Rotor Speed in Self-Starting With Load

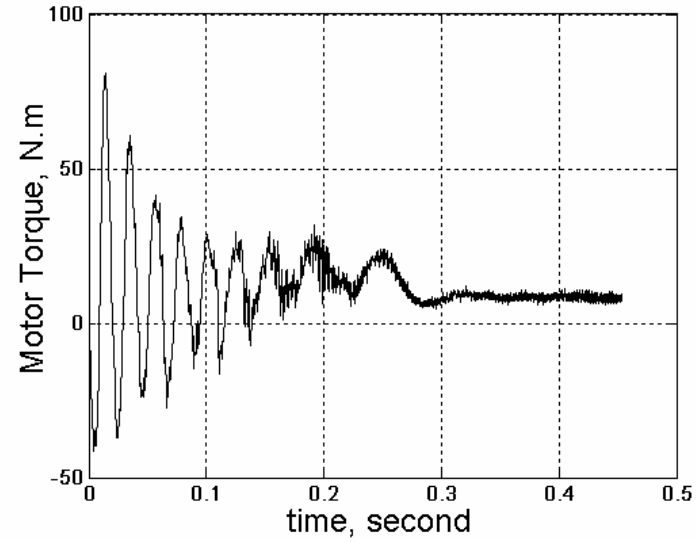

Figure 5.17: Computational Motor Torque in Self-Starting With Load

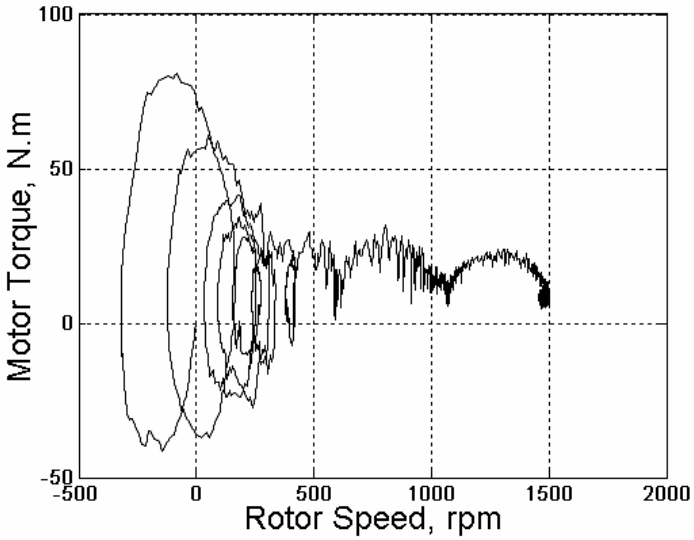

Figure 5.18: Computational Motor Torque versus Rotor Speed in Self-Starting With Load

Comparing with the current and speed at no load, as shown in Figs. 5.19 and 5.20, we can see that it takes longer time for the machine to reach the rated speed with load. The phase current at load is bigger than the one at no-load. Because of the load, there is a phase difference between these two current waveforms.

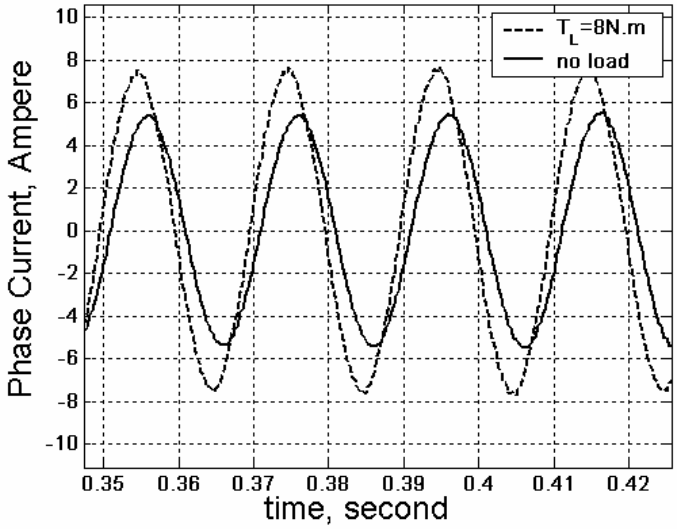

Figure 5.19: Computational Phase Currents at No-Load and Load of 8 N.m

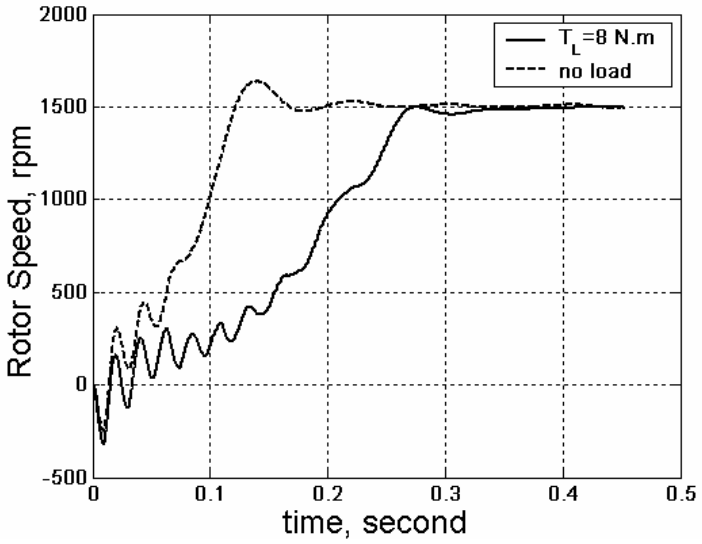

Figure 5.20: Computational Rotor Speed at No-Load and Load of 8 N.m

5.5.4 Results of Self-Starting With Various Loads

The self-starting process of the machine with various loads are computed. The comparisons of phase current and rotor speed are shown in Figs. 5.21 and 5.22 respectively.

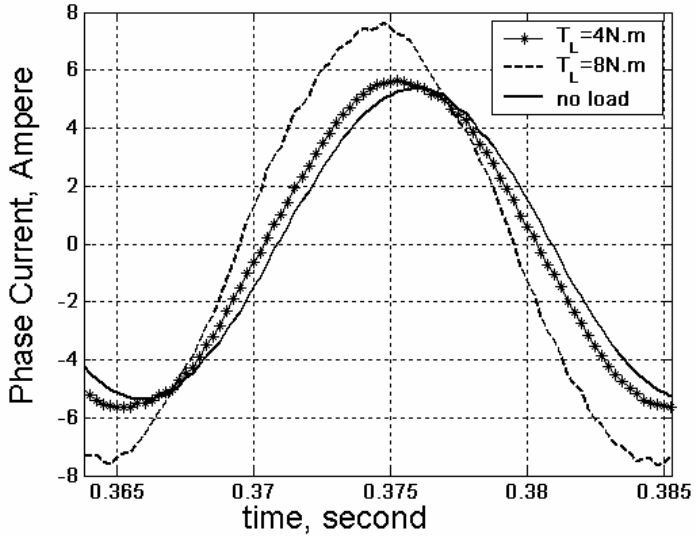

Figure 5.21: Computational Phase Currents Under Various Loads

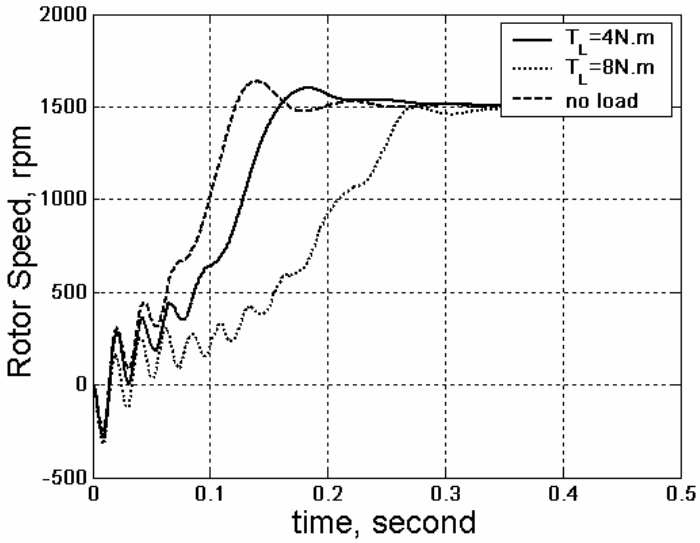

Figure 5.22: Computational Rotor Speed Under Various Loads

5.6 The Starting Process Under V/f Control

5.6.1 The Control Scheme

The constant volts per hertz (V/f) control method has been used for many decades, and its principle is well understood [146]. The most basic V/f control scheme is implemented in this work as shown in Fig. 5.23.

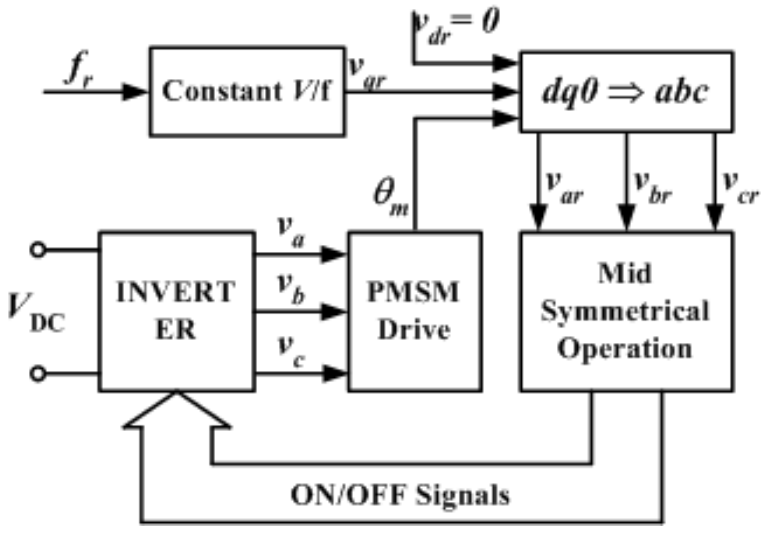

Figure 5.23: Scheme of V/f Control Method

The speed reference was input in terms of frequency reference value f_r. Since (V/f) is a constant and the $d-$axis reference voltage v_{dr} is set to be zero, the $q-$axis reference voltage can be calculated as $v_{qs} = (V/f) \times f_r$. With the known v_{dr}, v_{qr} and the measured rotor position θ_m, the $abc-$axis voltages v_{ar}, v_{br} and v_{cr} can be calculated using inverse Park's transformation. According to this three phase reference voltage, the duty cycles are calculated by the mid-symmetrical operation (See Appendix L) and the $'$ON/OFF$'$ signals for inverter switches are obtained. Therefore, the machine receives its power supply v_a, v_b and v_c from the inverter.

5.6.2 Computational and Experimental Results

The process described above is implemented in the experiment, and several values are set as shown in Table 5.1.

Table 5.1: Constants and Settings in V/f Control

Reference Frequency (f_r:Hz)	9
V/f Constant (c_s)	5.4
Sampling Period (s)	1×10^{-3}
PWM Switching Period (s)	2.5×10^{-4}
Input DC Voltage (V_{DC}:volt)	± 90

The same process as implemented in the experiment is computed by the finite element method. The experimental machine is connected to an inverter circuit as shown in Fig. 5.24. The main circuit components used are diodes and IGBTs. The choice of their equivalent $'ON'$ resistance values are based on the experimental values and values provided in manual [141]. When the status of the circuit component is $'OFF'$, we think that the circuit is open. Therefore a very large equivalent resistance value is set, which is: $R_{OFF} = 10^9$ ohm. In the figure, components $\langle 1 \rangle$-$\langle 6 \rangle$ are IGBTs. The equivalent resistance value for status $'ON'$ is 0.23 ohm, and the value for status $'OFF'$ is 10^9 ohm. For diodes $\langle 7 \rangle$-$\langle 12 \rangle$, the equivalent resistance

values for forward and reverse biasing are 0.056 ohm and 10^9 ohm respectively. V_{DP} and V_{DN} are the input DC voltages from the converter, which are 90V and -90V respectively; they are set as boundary conditions in the finite element computation. For simplification, the values for capacitors $[C_{sb}]$ and inductors $[L_{sb}]$ in equation (5.22) are neglected. The three-phase voltage inputs of the PMSM come from the voltage values of joint (a), (b) and (c) and they are calculated simultaneously by using the coupled circuit analysis in the finite element computation.

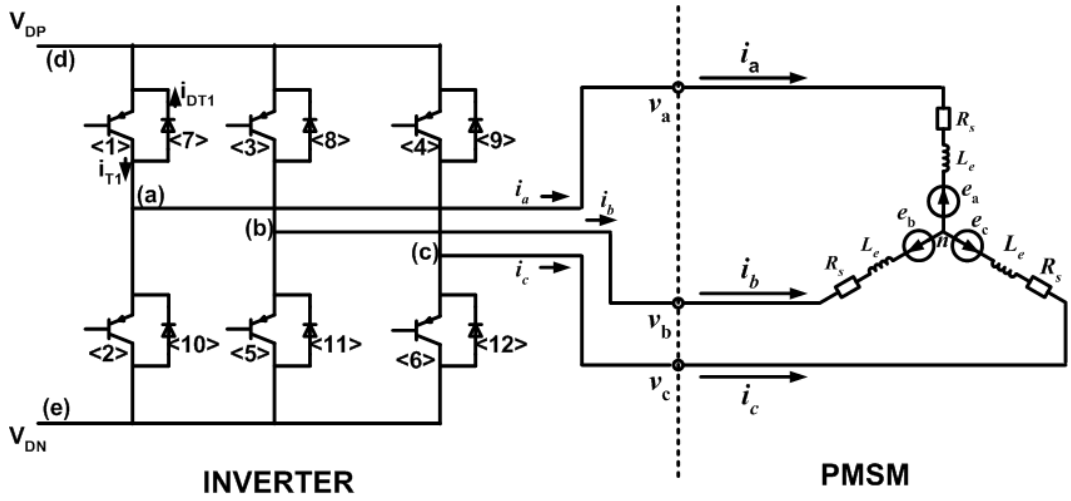

Figure 5.24: Representative Circuit of PMSM Connected with Inverter

The six duty time for six IGBTs in the inverter circuit are calculated from the mid-symmetric operation, so the time step size of the FEM computation is varied from time to time. Since the PWM switch period is $250\mu s$, the time step size of the FEM computation is even smaller than this value. Therefore, for a high reference frequency, it will take a long time to do the computation, though it is only a few seconds in the real experiment. This also explains why in this work the rated frequency 50Hz is not selected, instead $f_r = 9$Hz is set for both experiment and computation. The computational and experimental results are compared in Figs. 5.25 - 5.27.

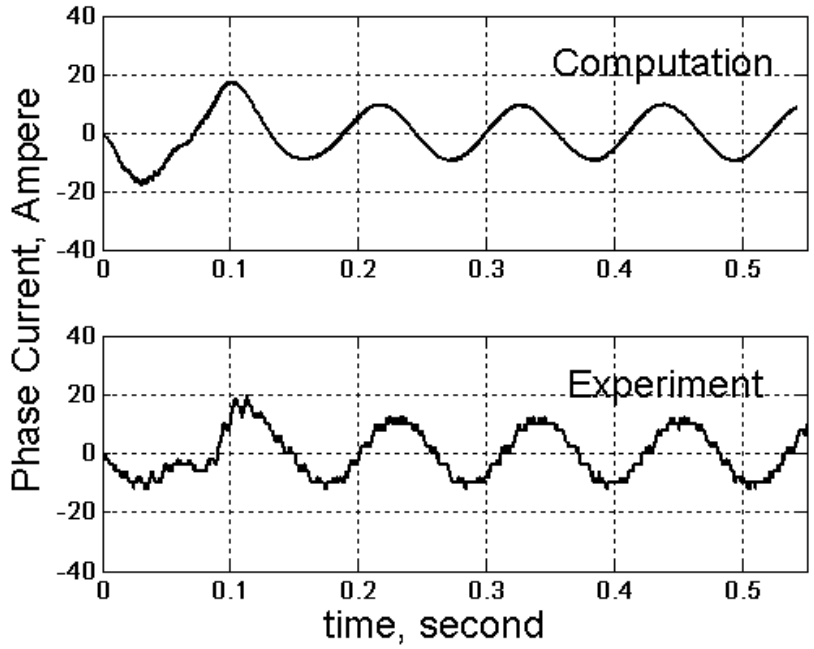

Figure 5.25: Computational and Experimental Phase Current in V/f Control

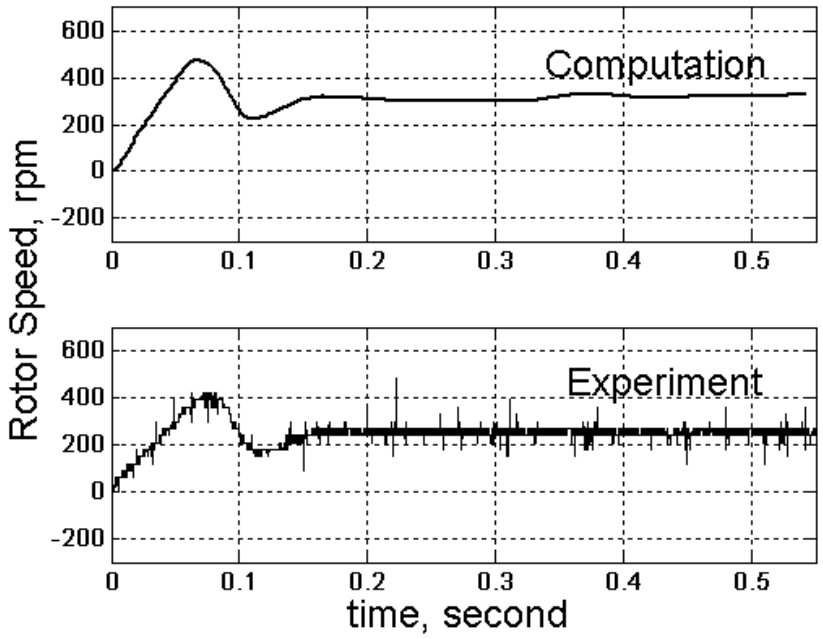

Figure 5.26: Computational and Experimental Rotor Speed in V/f Control

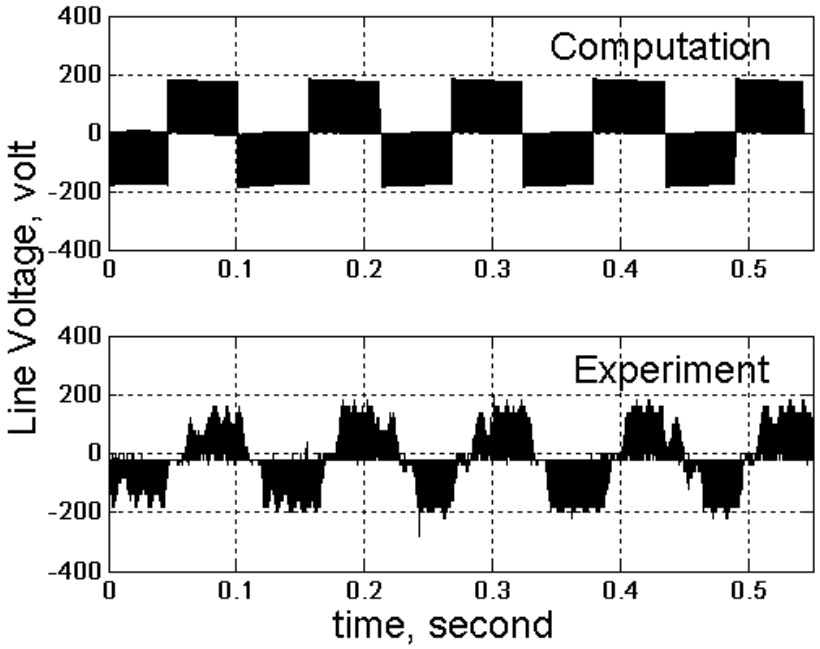

Figure 5.27: Computational and Experimental Line Voltage in V/f Control

The computational and experimental results match well in terms of rotor speed and line voltage as shown in Fig. 5.26 and 5.27. The computational current is a little higher than the experimental one as shown in the first $0.05s$. The rest of the computational and experimental results agree very well. The probable reason is that the starting process under V/f control is very similar to the self-starting process; it can be taken as a kind of low frequency self-starting. The inaccuracies in the computation as explained in relation to self-starting may lead to the difference of computational current and the real current.

5.7 The Starting Process Under Vector Control

5.7.1 The Control Scheme

Vector control method can be realized through the control of stator current. A simple $i_d = 0$ control method is used in this work. The control scheme is shown in Fig. 5.28.

The rotor speed ω_m is derived from the rotor position θ_m which is detected by the incremental encoder. The three stator phase currents i_a, i_b and i_c are transformed to the $d-$ and $q-$axis current i_d and i_q by Park's transformation. The real rotor speed ω_m is compared with the reference speed ω_{mr} and the error value $\omega_{err} = (\omega_{mr} - \omega_m)$ is calculated. Once $\omega_{err} \leq 0$, in other words, once ω_m reaches the reference value ω_{mr}, the $q-$axis reference current i_{qr} will be determined by the PI speed controller. Otherwise, $i_{qr} = 7$A is set. The $d-$axis reference current is always set as $i_{dr} = 0$. With the values of i_{dr}, i_{qr}, i_d and i_q, the PI current controllers are used to determine the primary reference voltages v_{dr}^0 and v_{qr}^0. Using the following equations

$$\begin{aligned} v_{dr} &= v_{dr}^0 - \omega_e L_q i_q, \\ v_{qr} &= v_{qr}^0 + \omega_e (L_d i_d + \lambda_f), \end{aligned}$$

the $d-$ and $q-$axis reference voltages V_{dr} and V_{qr} can be calculated; hence the values of V_{ar}, V_{br} and V_{cr} can be determined by the application of inverse Park's transformation. With these three phase reference voltages, the duty times of IGBTs in the inverter circuit can be decided by the mid-symmetrical operation (See Appendix L).

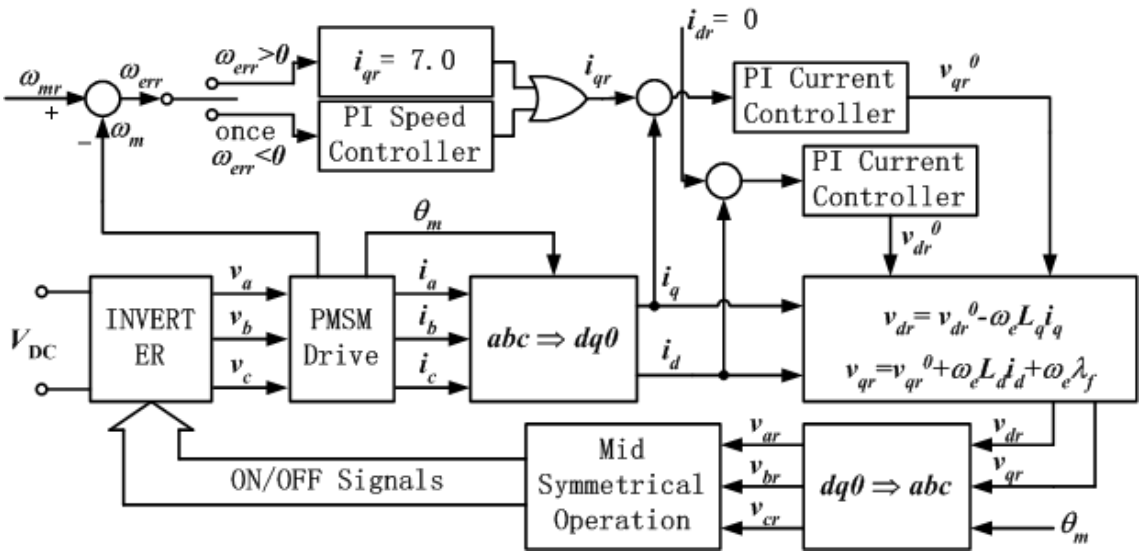

Figure 5.28: Scheme of Vector Control Method

5.7.2 Computational and Experimental Results

The scheme described above is implemented in the experiment and the parameters are set as shown in Table 5.2. Among them, the values of L_d, L_q and λ_f are considered as constants throughout the control process and for the same stator current magnitude, the effect of angle β on the parameters are neglected too. Since $i_{qr} = 7A$, the rms value in $abc-$axis is $7/\sqrt{3} = 4.04A$. Referring to Appendix H, Table H.6, the value of $I_s = 3.986A$ is taken, therefore, we can get

$$\begin{aligned} L_d &= \frac{X_d}{\omega_{rat}} = \frac{7.180}{314.160} = 22.855mH \\ L_q &= \frac{X_q}{\omega_{rat}} = \frac{17.214}{314.160} = 54.795mH \\ \lambda_f &= \frac{\sqrt{3}E_0}{\omega_{rat}} = \frac{\sqrt{3} \times 78.127}{314.160} = 0.431wb \end{aligned}$$

where $\omega_{rat} = 2 \times 1500 \times 2 \times \pi/60 = 314.160\ rad/s$ is the rated angular synchronous speed of the machine.

Table 5.2: Constants and Settings in Vector Control

Reference Speed (ω_{mr}:rpm)		200
Sampling Period (s)		5×10^{-4}
PWM Switching Period (s)		5×10^{-4}
Input DC Voltage (V_{DC}:volt)		± 60
$d-$axis Inductance (L_d:mH)		22.855
$q-$axis Inductance (L_q:mH)		54.795
Flux Linkage of PM (λ_f:wb)		0.431
PI Speed Controller	P Gain	0.012
	I Gain	0.036
PI Current Controller	P Gain	12.5
	I Gain	800

The same process is computed by the field-circuit coupled time stepping FEM. The experimental setup are the same as the one used in V/f control, which is shown in Fig. 5.24. The computational and experimental results in terms of phase current, $q-$axis current and rotor speed are compared in Figs. 5.29, 5.30 and 5.31.

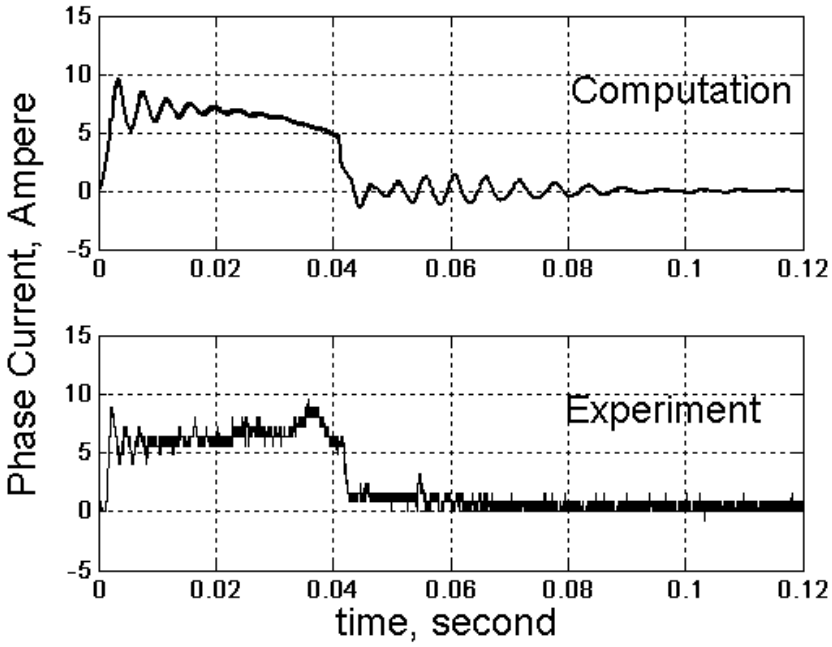

Figure 5.29: Computational and Experimental Phase Current in Vector Control

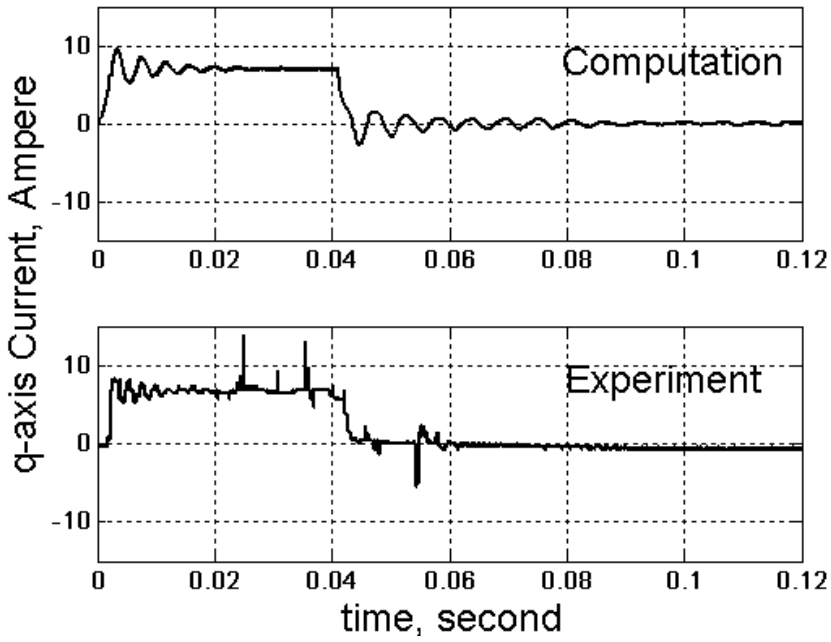

Figure 5.30: Computational and Experimental $q-$axis Current in Vector Control

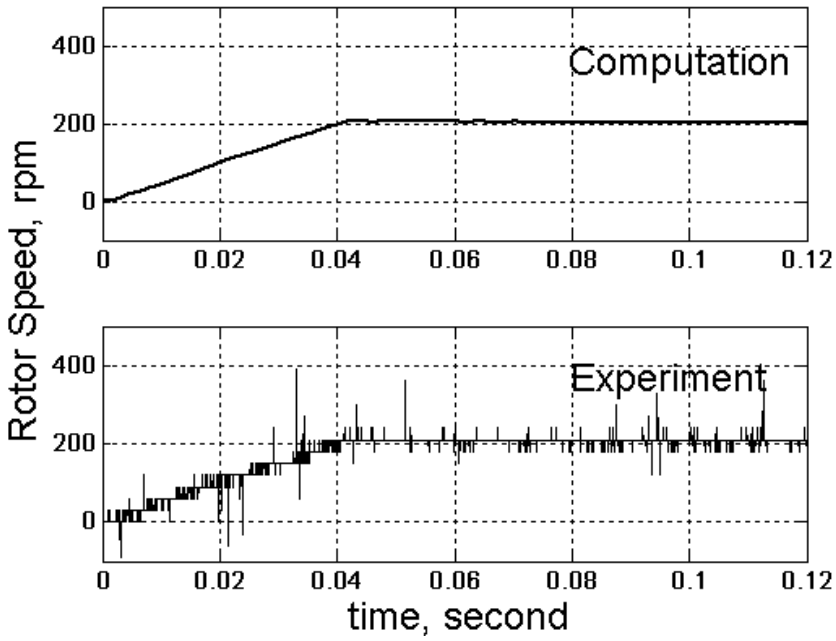

Figure 5.31: Computational and Experimental Rotor Speed in Vector Control

Both the experimental and computational results agree well in terms of speed. However, in the phase current shown in Fig. 5.29, there exists a difference between them around the point of $0.04s$. At this point, the computational one does not have salient variation, while the experimental one has a small surge. The disparity may be due to the uncertain noise in the experiment. These uncertain noises are very obvious in Fig. 5.30 where two spikes appear in the period of $0.02 \sim 0.04s$. Excepting isolated periods, the overall performance of computational and experimental currents match well with each other. The good agreement between the computational and the experimental results indicates that the field-circuit coupled time stepping FEM is a feasible and applicable method for the computation of PMSM dynamic performances.

5.8 Conclusion

The field-circuit time stepping finite element method is used to compute the dynamics of a line-start permanent magnet synchronous machine in this chapter. As one of the important dynamic performances, the starting process is evaluated. Both the self-starting process and the starting under controls are computed.

In the computation of self-starting process, the rotor end rings and stator end windings are represented by resistors and inductors. The $3D$ electromagnetic fields are simplified as circuit models. These simplifications may bring inaccuracies to the computation. Possibly due to these inaccuracies, the computational phase current is higher than the experimental one. Even after the machine is run up and the effects of cage bars are reduced, there are still slight differences between the computational and experimental results.

The pattern of computational speed is the result of computational torque. In the computation of self-starting process, the computational speed is lower than the experimental speed at the beginning, although they are similar in patterns. The differences may be caused by the combined inaccuracies in the computation of cogging torque due to permanent magnet excitation, computation of cogging torque due to slot effect, simplification of $3D$ effects and the choice of time step.

The starting process of machine under V/f control is very similar to the self-starting process, which can be taken as a kind of low frequency self-starting. The inaccuracies in the computation as explained in relation to self-starting may lead to the difference of computational current and the real current in the starting process under V/f control.

When the machine is started under current vector control, both the computational current and speed agree well with the experimental ones. The reason is the frequency of supplies is always in synchronism with the rotor frequency, the effects of cage bars are reduced greatly. Therefore good agreement can be achieved.

From the computation of the various starting processes, we can see that the field-circuit time-stepping finite element method is applicable in evaluating the dynamics of line-start permanent magnet synchronous machine. Most of the important factors in the starting process can be computed, including the starting current, motor torque, rotor speed and starting time. However, possibly due to the limitation of $2D$ modelling, differences still exists between the computational and experimental results in some areas.

Chapter 6

Conclusions and Discussions

This thesis deals with the dynamic analysis of a line start permanent magnet synchronous machines (PMSM) using field-circuit coupled time stepping finite element method (FEM). This method has been widely used based on the $2D$ modelling of machines. The $3D$ effects of the machine like the stator end windings and rotor end rings are represented by resistors and inductors. The $3D$ electromagnetic field is simplified using circuit models. $2D$ modelling is advantageous in simplifying the formulation and saving computation time; particularly for the computation of dynamic process. However, because of the inaccuracies brought along by the simplifications in $2D$ modelling, some differences exist between the computational results and the experimental results. In Chapter 5, we have shown that the transient computational current was higher than the experimental current. Even after the machine was fully run, there were still slight difference in the computational and experimental current due to the inaccuracies involved in the $2D$ modelling of stator end windings. Fortunately the differences between them are not big, and most of the important information for dynamic analysis can be achieved as well.

Electric machines are often operated with external drive circuits, therefore the modelling of these circuits are necessary. The semiconductor components, such as IGBTs and diodes, are simplified as resistors in this work. These resistors have different values depending on their operation status. In other words, these com-

ponents are modelled as linear components and their transient characteristics are neglected. This modelling is quite effective when coupling the effects of external circuits into the electromagnetic fields computation. Accuracies are guaranteed as shown in Chapter 5 where the starting processes under V/f control and vector control were validated. Since the nonlinearities of the component characteristics are neglected, much computation time are saved as well. It should also be noted that for small capacity machine with quite low terminal voltages, the effects of the semiconductor components in external circuits may be significant. Thus the simplification of neglecting their transient characteristics should be carefully considered.

In modelling the geometry by finite elements, triangular element is a widely-recognized choice for electric machine problem. First order element is simple to evaluate. However, if it is possible, higher order elements can be used since higher order elements give a better representation of the field and more accurate results.

The number of nodes used in finite element computation is also very important. Not only the accuracies of the solution but also the time needed to get the solution are dependent on the number of nodes. Larger number of nodes can provide more detailed information about the field. Particularly in the region of air gap, a large number of nodes are usually needed for good-quality meshes and accurate motor torque calculation. However more nodes leads to bigger global matrix, hence longer computation may be required. For dynamic analysis using time-stepping method, time is a big issue. Therefore the good compromise between computation accuracy and computation time should be achieved. In the absence of available methods to determine the optimal number of nodes, we can start the field computation with reasonable number of nodes. Then this number may be increased until satisfactory field representation is achieved.

The choice of time step also affects the computation process of time-stepping finite element method. A bigger time step means shorter computation time, but some details of the dynamic process may be overlooked. As shown in Chapter 5, time step may be one of the causes in the differences of computational and experimental speed in self-starting process. A smaller time step may make the computation more close to the real dynamics, however excessive computation time may be needed. In the author's view, a time step of hundreds of micro-seconds may be reasonable [151].

The resultant global matrix equation after the assembly process is non-symmetric, biconjugate gradient (BICG) method is used in this work to get the solution. Incomplete Choleski conjugate method (ICCG), which is widely used in solving the symmetrical linear system of equations, can also be applied. However, some modifications must be made so as to change the non-symmetric matrix to a symmetrical one. The comparisons between the efficiencies of the BICG and ICCG methods need to be further explored.

The first application of the time-stepping finite element method in this work has been the computation of the self-starting process of the machine. Possibly due to the inaccuracies brought along by the simplified $2D$ model, the computational current is higher than the experimental one when the slip frequency is high. After the machine is run up, the computational current is very close to the experimental one. However, due to the simplifications in modelling the effects of the stator end windings, slight differences still exist between the computational and experimental currents. Therefore, from the aspect of accuracy, $3D$ modelling is preferred. However, due to the excessive demand on computing time and storage requirement that

may be brought along by the $3D$ computation, the application of $3D$ modelling to the time-stepping computation is not practical. The multi-slice model [64] may be a compromise alternative, but so far the method is used mainly for the skew effects and inter-bar current, instead of the $3D$ end effects. Therefore, $2D$ time-stepping finite element method may still be the best choice for dynamic computation so far. With the development of computing capacity of computer and the development of advanced computing structure, i.e. parallel computing, the $3D$ model is more promising for the dynamic computation.

The computational speed in self-starting process is lower than the experimental speed in some areas, although they are similar in pattern. The differences in speed are the reflections of differences in torque. The causes of differences in computational and experimental torque are difficult to explain. The proper reason is the inaccuracies of cogging due to permanent magnets and slot effects. The simplified $2D$ model and the choice of time step may contribute to the differences as well.

The $2D$ time-stepping finite element model is also applied to compute the starting process under V/f control. Due to the similar factors related to the inaccuracies in self-starting process, the computational current in V/f control is also higher than the experimental current. The effect of the $2D$ modelling of stator end windings on stator current in steady state is not obvious.

The method is quite successful in evaluating the starting process under current vector control. Because the rotor is always synchronized with the stator, both the computational current and speed agree well with the experimental results.

This thesis also deals with the parameter determination of line-start perma-

nent magnet synchronous machine. Both computational and experimental methods are used. The experimental methods include DC current decay method, sensorless no-load test method and load test method, while the computational method is referred to as finite element method. Based on the load test method, two new methods are also proposed in this work.

The DC current decay method is realized with simple experimental procedure and low-cost experiment equipment. The direct- and quadrature-axis parameters are obtained from the voltage and current measured when the two armature winding terminals are short circuited while a dc current flows between these terminals. The parameters of various frequencies can be computed by Fourier transform. However only a single set of reactance values can be obtained for one frequency. The saturation effect is neglected and the parameter of E_0 is not obtainable.

Sensorless no-load test is based on the two-axis model of machine. It is assumed that the torque angle under no load condition is zero. The stator current varies with the variation of stator terminal voltage, and the phase voltage corresponding to the minimum stator current is taken as the excitation voltage due to permanent magnet, E_0. The test can be implemented easily and a good approximation of parameter X_d can be obtained when the operation point is away from the point of minimum current. However, the limitation is that only a set of values for X_d is achieved and the variation of E_0 with loads is not considered.

The effects of saturation in permanent magnet machine are profound. Saturation causes X_d and X_q to vary with load, it leads to the variation of E_0 with load as well. To model and control the machine accurately, the variation of all the parameters, X_d, X_q and E_0, should be considered in the parameter determination.

The conventional load test method used by Miller can get a set of X_d and X_q simultaneously. However, it is still based on the assumption of constant E_0 over all the loads. Zhou modified this method by imposing a small change in angle β, the variation of X_d, X_q and E_0 with loads can be achieved simultaneously. Unfortunately, this modified method suffered from the uncertainties brought by the small change of angle β and the complexity of the experimental procedures. The values of X_d and E_0 are fluctuating.

To overcome the drawbacks of the old methods, two new methods were introduced in this work based on the load test method. Linear regression model and Hopfield neural network are used in combination with the load test to determine the machine parameter. Since these two methods are implemented on the basis of large number of experimental samples, the accuracy of results are improved greatly. The fluctuations of the load test are removed and variation trends of the parameters are more obvious. Moveover, since the small change in angle β and the measurement of load angle are avoided, the experimental procedure is simplified. These two new methods are quite effective in the parameter determination of machines; particulary the Hopfield neural network, which is applicable for both the time-invariant and time varying systems.

Finite element method is also applied to calculate the machine parameters. Current source is used and the variation of parameters with loads are considered as well. The results obtained by finite element method are comparable with those experimental results. However, the computational values for X_d and X_q are generally higher than the experimental results, and E_0 decreases faster. The reason for such differences are not known, but a number of factors may contribute to this, such as the modelling inaccuracies, $3D$ effects, etc.

References

[1] Jack F. Giers and Mitchell Wing, "Permanent magnet motor technology: design and applications (2nd edition)," Marcel Dekker, Inc. New York, 2002.

[2] T. M. Jahns, "Motion control with permanent magnet AC machines (Invited Paper)," *Proc. of the IEEE*, vol. 82, no. 8, pp.1241-1251, Aug. 1994. .

[3] S. A. Nasar, I. Boldea and L. E. Unnewehr,"Permanent magnet, reluctance, and self-synchronous motors," Boca Raton, CRC Press, 1993.

[4] Iqbal Husain, "Electric and hybrid vechicles: design fundamentals," Boca Raton, FL: CRC Press, 2003.

[5] V. B. Honsinger, "Permanent magnet machines: asynchronous operation," *IEEE Trans. on Power Apparatus and Systems*, vol. PAS-99, no. 4, pp. 1503-1509, July 1980.

[6] Thomas M. Jahns, Gerald B. Kliman and Thomas W. Neuman, "Interior permanent magnet synchronous motors for adjustable speed drives," *IEEE Trans. on Industry Applications*, vol. IA-22, no. 4, pp. 738-747, July/August 1986.

[7] Pillay Pragasen, "Modelling simulation and analysis of permanent magnet synchronous and burshless DC motor drives ," Ph. D dissertation, Dept. Elec. Eng., Virginia Polytechnic Institute and State University, USA, 1987.

[8] S. J. Salon, "Finite element analysis of electrical machines," Kluwer Academic Publishers, 1995.

[9] M. A. Jabbar, "Analysis of the performance of a permanent magnet A. C. machine ," Ph. D dissertation, Dept. Elec. Eng., University of Southhampton, U.K., June 1977.

[10] Tapeng Tsao, "A concise course in electromagnetism for electrical engineering," World Scientific Publishing, 1994.

[11] S. Ratnajeevan H. Hoole, "Finite elements, electromagnetics and design," Amsterdam; New York: Elsevier, 1995.

[12] K. J. Binns and P. J. Lawrenson, "Analysis and computation of electric and magnetic field problems," 2nd Edition, Oxford, New York, Pergamon Press, 1973.

[13] C. A. Brebbia and J. Dominguez, "Boundary elements: an introductory course," 2nd Edition, Southhampton, Boston: Computational Mechanics Publications; New York: Copublished with McGraw-Hill, 1992.

[14] A. B. J. Reece and T. W. Preston, "Finite element methods in electrical power engineering," Oxford University Press Inc., New York, 2000.

[15] S. Williamson, L. H. Lim and M. J. Robinson, "Finite-element models for cage induction motor analysis," *Conference Record of the IEEE Industry Application Society Annual Meeting*, vol. 1, pp. 23-30, 1-5 Oct. 1989.

[16] Edward P. Furlani, "Permanent magnet and electromechanical devices - materials,analysis and applications," Academic Press, 2001.

[17] M. V. K. Chari and P. Silvester, "Analysis of turbo-alternator magnetic fields by finite elements," *IEEE Transactions on Power Apparatus and Systems*, vol. PAS-90, no. 2, pp. 454-464,1971.

[18] M. V. K. Chari and P. Silvester, "Finite-element analysis of magnetically saturated DC machines," *IEEE Transactions on Power Apparatus and Systems*, vol. PAS-90, pp. 2362-2372,1971.

[19] A. Y. Hannalla and D. C. MacDonald, "Numerical analysis of transient field problems in electric machines," *IEE Proceedings*, vol. 123, no. 9, pp. 893-898, Sept. 1976.

[20] S. C. Tandon, A. f. Armor and M. V. K. Chari, "Nonlinear transient finite element field computation for electrical machines and devices," *IEEE Trans. on Power Apparatus and Systems*, vol. PAS-102, no. 5, pp. 1089-1095, May 1983.

[21] P. Brandl, K. Reichert and W. Vogt, "Simulation of turbogenerators on steady state load,", *Brown Bovery Review*, vol. 9, pp. 444-449, 1975.

[22] S. Williamson and J. W. Ralph, "Finite-element analysis of an induction motor fed from a constant-voltage source,", *IEE Proceedings (Pt. B)*, vol. 130, no. 1, pp. 18-24, Jan. 1983.

[23] T. Nakata and N. Takahashi, "Direct finite element analysis of flux and current distributions under specific conditions," *IEEE Trans. On Magnetics*, vol. MAG-18, no. 2, pp. 325-330, March 1982.

[24] Philip G. Potter and Gregory K. Cambrell, "A combined finite element and loop analysis for nonlinearly interacting fields and circuits," *IEEE Trans. On Magnetics*, vol. MAG-18, no. 6, pp. 2352-2355, Nov. 1983.

[25] Elias G. Strangas and Kenneth R. Theis, "Shaded pole motor design and evaluation using coupled field and circuit equations," *IEEE Trans. On Magnetics*, vol. MAG-21, no. 5, pp. 1880-1882, Sept. 1985.

[26] Elias G. Strangas, "Coupling the circuit equations to the non-linear time dependent field solution in inverter driven induction motors," *IEEE Trans. On Magnetics*, vol. MAG-21, no. 6, pp. 2408-2411, Nov. 1985.

[27] A. Arkkio, "Analysis of induction motor based on the numerical solution of the magnetic field and circuit eqution," Helsinki Acta Polytechnica Scandinavica, Electrical Engineering Series, no. 59, 1987.

[28] Basim F. Istfan, "Extensions to the finite element method for nonlinear magnetic field problems," Ph. D thesis, Rensselaer Polytechnic Institute, Troy, New York, 1987.

[29] S. J. Salon, M. J. Debortoli and R. Palma, "Coupling of transient fields, circuits, and motion using finite element analysis ," *Journal of Electromagnetic Waves and Applications*, vol. 4, no. 11, pp. 1077-1106, 1990.

[30] S. L. Ho, W. N. Fu and H. C. Wong, "Estimation of stray losses of skewed induction motors using coupled 2-D and 3-D time stepping finite element models," *IEEE Trans. on Magnetics*, vol. 34, no. 5, pp.3102-3105, Sept. 1998.

[31] Andrew M. Knight and Catherine I. McClay, "Design of high-efficiency line-start motors," *IEEE Trans. on Industry Applications*, vol. 36, no. 6, pp. 1555-1562, Nov./Dec. 2000.

[32] W. N. Fu, Z. J. Liu and C. Bi, "Dynamic model of the disk drive spindle motor and its applications ," *IEEE Trans. on Magnetics*, vol. 38, no. 2, pp. 973-976, March 2002.

[33] H. C. Karmaker, "Time-stepping finite element analysis of starting performance of large salient-pole synchronous machines," *IEEE International Conference on Electric Machines and Drives (IEMDC'03)*, vol. 3, pp. 1565-1570, 1-4 June 2003.

[34] Wei Wu, Bruce A. Kalan and Howard C. Lovatt, "Time-stepping analysis of a switched reluctance motor by coupling electrical circuit and electromagnetic finite element methods," *Sixth International Conference on Electrical Machines and Systems (ICEMS 2003)*, vol. 2, pp.728-731, 9-11 Nov. 2003.

[35] Magsoft Corporation, "Finite Element Analysis Software Reference Manuals-FLUX2D Version 7.40," 2000. http://www.magsoft-flux.com

[36] Ansoft Corporation, "Maxwell 2D V10," 2003. http://www.ansoft.com

[37] ANSYS, Inc., "ANSYS 8.1," 2004. http://www.ansys.com

[38] David Meeker, "Finite Element Method Magnetics, Freeware Software for 2D FEA," http://femm.foster-miller.net

[39] Magneforce Software Systems, Inc., "MagneForce, FEA for rotating electric machines ," http://www.magneforcess.com

[40] Motorsoft Inc., "SPEEDCAD, Motor Design Software," http://www.motorsoft.net

[41] L. Lefevre and J. Soulard, "Finite element transient start of a line-start permanent magnet synchronous motor," *Proceedings of the International Conference on Electrical Machines (ICEM 2000)*, Helsinki, Finland, August 2000.

[42] Kazumi Kurihara and M. Azizur Rahman, "High-Efficiency Line-Start Interior Permanent-Magnet Synchronous Motors," *IEEE Trans. on Magnetics*, Vol. 40, no. 3, pp. 789-796, MAY/JUNE 2004.

[43] Uwe Schaible and Barna Szabados, "Dynamic motor parameter identification for high speed flux weakening operation of brushless permanent magnet synchronous machines," *IEEE Trans. on Energy Conversion*, vol. 14, no. 3, pp. 486-492, Sept. 1999.

[44] B. Stumberger and b. Hribernik, "Calculation of two-axis parameters of synchronous motor with permanent magnet using finite elements," *Proceedings of IEEE International Conference on Electric Machines and Drives (IEMD'99)* , pp. 98-100, May. 1999.

[45] D. A. Lowther and P. P. Silvester, "Computer-aided design in magnetics," Berlin; New York : Springer-Verlag, 1986.

[46] D. W. Shimmin, J. Wang, N. Bennett and K. J. Binns, "Modelling and stability analysis of a permanent-magnet synchronous machine taking into account the effect of cage bars," *IEE Proc. Electr. Power Appl.*, vol. 142, no. 2, pp. 137-144, March 1995.

[47] Nicola Bianchi and Silverio Bolognani, "Magnetic models of saturated interior permanent magnet motors based on finite element analysis," *The 33rd IEEE Industry Application Conference*, vol. 1, pp. 27-34, 12-15 Oct. 1998.

[48] Liuchen Chang, "Modeling, desing and control of a 30 HP permanent magnet synchronous motor ," Ph. D dissertation, Dept. Electrical Engineering, Queen's University, Kingston, Ontario, Canada, 1991.

[49] Gyu-Hong Kang, Jung-Pyo Hong, Gyu-Tak Kim and Jung-Woo Park, "Improved parameter modeling of interior permanent magnet synchronous mtor based on finite element analysis," *IEEE Trans. on Magnetics*, vol. 36, no. 4, pp. 1867-870, July 2000.

[50] Ping Zhou, "Field and circuit combined analysis of permanent magnet synchronous motors," Ph. D dissertation, Faculty of Engineering and Applied Science, Memorial University of Newfoundland, St. John's, Newfoundland, Canada, 1994.

[51] E. Eitelberg and R. G. Harley, "Estimating synchronous machine electrical parameters from frequency response tests ," *IEEE Trans. on Energy Conversion* , vol. 2, no. 1, pp. 132-138, March 1987.

[52] IEEE Standard Procedures for Obtaining Synchronous Machine Parameters by Standstill Frequency Response Testing, IEEE Std. 115A, 1987.

[53] P. H. Mellor, F. B. Chaaban and K. J. Binns,"Estimation of parameters and performance of rare-earth permanent-magnet motors avoiding measurement of load angle," *IEE Proceedings-B*, vol. 138, no. 6, pp. 322-330, Nov. 1991.

[54] Shu Yamamoto, Takahiro Ara, Shoichi Oda and Kouki Matsuse, "Prediction of starting performance of PM motors by DC decay testing method," *IEEE Trans. on Industry Applications*, vol. 36, no. 4, pp. 1053-1060, July/August 2000.

[55] Hans-Peter Nee, Louis Lefevre, Peter Thelin and Juliette Soulard, "Determination of d and q reactances of permanent-magnet synchronous motors without measurements of the rotor position," *IEEE Trans. on Industry Applications*, vol. 36, no. 5, pp. 1330-1335, Sept./Oct. 2000.

[56] S. F. Gorman, C. Chen and J. J. Cathey, "Determination of permanent magnet synchronous motor parameters for use in brushless dc motor drive analysis ," *IEEE Trans. on Energy Conversion*, vol. 3, no. 3, pp. 674-681, Sept. 1988.

[57] M. A. Rahman and Ping Zhou, "Accurate determination of PM motor parameters by digital torque angle measurement ," *Journal of Applied Physics* , vol. 76, no. 10, pp. 6868-6870, Nov. 1994.

[58] B. Stumberger, B. Kreca and B. Hribernik,"Determination of parameters of synchronous motor with permanent magnets from measurement of load conditions," *IEEE Trans. on Energy Conversion*, vol. 14, no. 4, pp. 1413-1416, Dec. 1999.

[59] T. J. E. Miller, "Methods for testing permanent magnet polyphase AC motors," *IEEE IAS Conf. Rec.*, 23D, pp. 494-499, 1981.

[60] B. J. Chalmers, S. A. Hamed and G. D. Baines,"Parameters and performance of a high field permanent magnet synchronous motor for variable frequency operation ," *IEE Proc. B*, vol. 132, no. 3, pp. 117-124, 1985.

[61] F. A. Fouad, T. W. Nehl and N. A. Demerdash, "Permanenet mmagnet modeling for use in vector potential finite element analysis in electrical machinery," *IEEE Trans. on Magnetics*, vol. MAG-17, no. 6, pp. 3002-3004, Nov. 1981.

[62] Peter Campbell, "Permanent magnet materials and their application," Cambridge University Press, Cambridge, 1994.

[63] Herbert H. Woodson and James R. Melcher, "Electromechanical dynamics, Part I: discrete systems," New York , Wiley, 1968.

[64] W. N. Fu, S. L. Ho, L. Li and H. C. Wong, "A multislice coupled finite element method with uneven slice length division for the simulation study of electric machines," *IEEE Trans. on Magnetics*, vol. 39, no. 3, pp. 1566-1569, May 2003.

[65] F. Piriou and A. Razek, "Coupling of saturated electromagnetic system to nonlinear power electronic devices ," *IEEE Trans. on Magnetics*, vol. 24, no. 1, pp. 274-277, Jan. 1988.

[66] F. Piriou and A. Razek, "Numerical simulation of non-conventional alternator connected to a rectifier," *IEEE Trans. on Energy Conversion*, vol. 5, no. 3, pp. 512-518, Sept. 1990.

[67] A. Demenko, "Time-stepping FE analysis of electric motor drives with semiconductor converters," *IEEE Trans. on Magnetics*, vol. 30, no. 5, pp. 3264-3267, Sept. 1994.

[68] Paul B. Zbar, Albert P. Malvino and Michael A. Miller, "Basic electronics: a text-lab manual," New York, NY: Glencoe, 1994.

[69] P. P. Silvester and R. L. Ferrari, "Finite elements for electrical engineers (2nd ed.)," Cambridge University Press, 1990.

[70] Knneth Baldwin (ed.), "Modern methods for automating finite element mesh generation," *Proceedings of a session sponsored by Engineering Mechanics Divison of the American Society of Civil Engineers in conjuction with the ASCE National Convention*, Boston, Massachusetts, Oct. 1986.

[71] Richard H. Gallagher, "Finite element analysis: fundamentals," Englewood Cliffs, New Jersey, Prentice-Hall, 1975.

[72] Bruce A. Finlayson, "The method of weighted residuals and the variational principles, with application in fluid mechanics, heat and mass transfer," New York, Academic Press, 1972.

[73] Charles W. Steele, "Numerical computation of electric and magnetic fields," New York : Chapman & Hall : International Thomson Pub., 1997.

[74] Laurent Cairo and Theo Kahan (Trans. from French to English by G. D. Sims), "Variational techniques in electromagnetism," New York , Gordon and Breach, 1965.

[75] Antonius Otto, "Methods in numerical simulation," Physics Department, University of Alaska, 2003. http://what.gi.alaska.edu/ao/sim/

[76] C. William Gear, "Numerical initial value problems in ordinary differential equations," Englewood Cliffs, N. J., Prentice-Hall, 1971.

[77] J. D. Lambert, "Computational methods in ordinary differential equations," London, New York, Wiley, 1973.

[78] T. J. R. Hughes and W. K. Liu, "Implicit-explicit finite elements in transient analysis: stability theory," *Journal of Applied Mechanics*, vol. 45, pp. 371-374, 1978.

[79] W. H. Press, B. P. Flannery, S. A. Teukolsky and W. T. Vetterling ,"Numerical recipes in FORTRAN: the art of scientific computing (2nd Edition) ," Cambridge, England, Cambridge University Press, p. 710, 1992.

[80] I. A. Tsukerman, A. Konrad, G. Bedrosian and M. V. K. Chari, "A survey of numberical methods for transient eddy current problems," *IEEE Trans. on Magnetics*, vol. 29, no. 2, pp. 1711-1716, March 1993.

[81] Igor Tsukerman, "A stability paradox for time-stepping schemes in coupled field-circuit problems," *IEEE Trans. on Magnetics*, vol. 31, no. 3, pp. 1857-1860, May 1995.

[82] P. Silvester, H. S. Cabayan and B. T. Browne, "Efficient techniques for finite element analysis of electric machines," *IEEE Trans. on Power Apparatus and Systems*, vol. PAS-92, no. 4, pp. 1274-1281, July/August 1973.

[83] Pei-bai Zhou, "Numerical analysis of electromagnetic fields," Berlin ; New York : Springer-Verlag , c1993.

[84] Yousef Saad, "SPARSKIT, a basic tool-kit for sparse matrix computations (Version 2)," University of Minnesota. http://www-users.cs.umn.edu/ saad/software/SPARSKIT/sparskit.html.

[85] Victor Eijkhout, "Distributed sparse data sturctures for linear algebra operations (UT-CS-92-169)," University of Tennessee, Knoxville, May 1992. http://www.netlib.org/lapack/lawns/downloads/lawn50.pdf.

[86] Roldan Pozo, Karin A. Remington and Andrew Lumsdaine, "SparseLib++ v.1.5, Sparse Matrix Class Library Reference Guide," National Institute of Standards and Technology, and University of Notre Dame, April 1996.

[87] Iain S. Duff, Roger G. Grimes and John G. Lewis, "Sparse matrix test problems," *ACM Transactions on Mathematical Software*, vol. 15, no. 1, pp. 1-14, March 1989.

[88] David R. Kincaid, John R. Respess, David M. Young and Roger G. Grimes, "Algorithm 586 - ITPACK 2C: A Fortran package for solving large sparse linear systems by adaptive accelerated iterative methods," *ACM Transactions on Mathematical Software*, vol. 8, no. 3, pp. 302-322, September 1982.

[89] Thomas C. Oppe, Wayne D.Joubert and David R. Kincaid, "NSPCG User's Guide Version 1.0, A Package for Solving Large Sparse Linear Systems by Various Iterative Methods," Center for Numerical Analysis, University of Texas at Austin, April 1988. http://rene.ma.utexas.edu/CNA/NSPCG/manuals/usernsp/

[90] Alan George and Joseph W. H. Liu. , "Computer solution of large sparse positive definite systems," Englewood Cliffs, N.J. : Prentice-Hall, 1981.

[91] Matlab, The Language of Technical Computing, Version 6.0.0.88, Release 12, The Mathworks, Inc.

[92] "Iterative Solvers for System of Linear Equations," Joint Institute for Computational Science, Computer Science and Mathematics Division, Oak Ridge National Laboratory, the University of Tennessee, USA, Sept. 97. http://www-jics.cs.utk.edu

[93] Jack Dongarra, Andrew Lumsdaine, Roldan Pozo and Karin A. Remington, "IML++ v.1.2, Iterative Methods Library Reference Guide," Oak Ridge National Laboratory and The University of Tennessee, University of Notre Dame, National Institute of Standards and Technology, April 1996.

[94] J. Mizia, K. Adamiak, A. R. Eastham and G. E. Dawson, "Finite element force calculation: comparsion of methods for electric machines," *IEEE Transactions on Magnetics*, vol. 24, no. 1, pp. 447-450, Jan. 1988.

[95] Eugene A. Aronson and John R. Brauer, "Magnetic torque or force calculation by direct differentiation of finite element coenergy ," *IEEE Transactions on Magnetics*, vol. 25, no. 5, pp. 3578-3580, Sept. 1989.

[96] J. L. Coulomb, "A methodology for the determination of global electrical quantities from a finite element analysis and its application to the evaluation of magnetic forces, torques and stiffness," *IEEE Transactions on Magnetics*, vol. MAG-19, no. 6, pp. 2514-2519, Nov. 1983.

[97] Tang Renyuan, "Modern permanent magnet machines - theory and design," Mechanical Industry Publishing, Beijing, P. R. China, 1997 (in Chinese).

[98] N. Sadowski, Y. Lefevre, M. Lajoie-Mazenc and J. Cros, "Finite element torque calculation in electrical machines while considering the movement," *IEEE Transactions on Magnetics*, vol. 28, no. 2, pp. 1410-1413, March 1992.

[99] T. Tarnhuvud and K. Reichert, "Accuracy problems of force and torque calculation in FE-systems," *IEEE Transactions on Magnetics*, vol. 24, no. 1, pp. 443-446, Jan. 1988.

[100] A. A. Abdel-Razek, J. L. Coulomb, M. Feliachi and J. C. Sabonnadiere, "The calculation of electromagnetic torque in saturated electric machines within combined numerical and analytical solutions of the field equations," *IEEE Transactions on Magnetics*, vol. MAG-17, no. 6, pp. 3250-3252, Nov. 1981.

[101] A. A. Abdel-Razek, J. L. Coulomb, M. Feliachi and J. C. Sabonnadiere, "Concept of an air-gap element for the dynamic analysis of electromagnetic field in electric machines," *IEEE Transactions on Magnetics*, vol. MAG-18, no. 2, pp. 655-659, March 1982.

[102] A. M. Knight and J. C. Salmon, "Using a finite element eddy-current formulation to simulate the performance of a single-phase line-start permanent magnet machine," *Proceedings of the 1999 IEEE Canadian Conference on Electrical and Computer Engineering*, pp. 306-311, Shaw Conference Center, Edmonton, Alberta, Canada, May 9-12, 1999.

[103] S. J. Salon and J. M. Schneider, "A hybrid finite element-boundary element integral formulation of the eddy current problem," *IEEE Trans. on Magnetics*, vol. 18, no. 2, pp. 461-466, Sept. 1982.

[104] T. Onuki, S. Wakao and T. Hattori, "Hybrid finite and boundary element method applied to nonlinear magnetic field analysis," *IEEE Trans. on Magnetics*, vol. 30, no. 5, pp. 2908-2911, Sept. 1994.

[105] D. Rodger, H. C. Lai and P. J. Leonard, "Coupled elements for problems involving movement," *IEEE Trans. on Magnetics*, vol. 26, no. 2, pp. 548-550, March 1990.

[106] O. J. Antunes, J. P. A. Bastos and N. Sadowski, "Using high-order elements in problems with movement ," *IEEE Trans. on Magnetics*, vol. 40, no. 2, pp. 529-532, March 2004.

[107] Remy Perrin-Bit and Jean Louis Coulomb, "A three dimensional finite element mesh connection for problems involving movement," *IEEE Trans. on Magnetics*, vol. 31, no. 3, pp. 1920-1923, May 1995.

[108] Y. Marechal, G. Meunier, J. L. Coulomb and H. Magnin, "A general purpose tool for restoring inter-element continuity," *IEEE Trans. on Magnetics*, vol. 28, no. 2, pp. 1728-1731, March 1992.

[109] S. L. Ho, Shiyou Yang, M. Rahman and H. C. Wong, "Transient analysis of PWM inverter-fed AC motor dirves using finite element method coupling with external circuit model," *IEEE 1999 International Conference on Power Electronics and Drive Systems, PEDS'99*, pp. 591-596, Hong Kong, July 1999.

[110] Igor A. Tsukerman, "Overlapping finite elements for problems with movement," *IEEE Trans. on Magnetics*, vol. 28, no. 5, pp. 2247-2249, Sept. 1992.

[111] B. Davat, Z. Ren and M. Lajoie-Mazenc, "The movement in field modeling," *IEEE Trans. on Magnetics*, vol. MAG-21, no. 6, pp. 2296-2298, Nov. 1985.

[112] D. Deas, P. Kuo-Peng, N. Sadowski, A. M. Oliveira, J. L. Roel and J. P. A. Bastos, "2-D FEM modelling of the tubular linear induction motor taking into account the movement," *IEEE Trans. on Magnetics*, vol. 38, no. 2, pp. 1165-1168, March 2002.

[113] Mauricio V. Ferreira da Luz, Patrick Dular, Nelson Sadowski, Christophe Geuzaine and J. P. A. Bastos, "Analysis of a permanent magnet generator

with dual formulations using periodicity conditions and moving band," *IEEE Trans. on Magnetics*, vol. 38, no. 2, pp. 961-964, March 2002.

[114] T. W. Preston, A. B. J. Reece and P. S. Sangha, "Induction motor analysis by time-stepping techniques," *IEEE Trans. on Magnetics*, vol. 24, no. 1, pp. 471-474, Jan. 1988.

[115] Tang Renyuan, Hu Yan, Lu Zhanhong, Yang Shiyou and Miao Lijie, "Computation of transient electromagnetic torque in a turbogenerator under the cases of different sudden short circuits," *IEEE Trans. on Magnetics*, vol. 26, no. 2, pp. 1042-1045, March 1990.

[116] Paul C. Krause, Oleg Wasynczuk and Scott D. Sudhoff, "Analysis of electric machinery and drive systems," New York : John Wiley and Sons ; Piscataway, N.J. : IEEE Press, 2002.

[117] N. N. Hancock, "Matrix analysis of electrical machinery," Oxford, New York, Pergamon Press, 1974.

[118] Hiroshi Asano, Syu Yamamoto, Takahiro Ara, Shouichi Oda and Kouki Matsuse, "An estimation method of starting performance of squirrel-cage induction motor on DC decay testing method," *Conference Record of the 34th IAS Annual Meeting*, vol. 3, pp. 1559-1564, Oct. 1999.

[119] Gordon R. Slemon, "Electric Machines and Drives," Addison-Wesley Publishing Company, INC., 1992.

[120] Jose C. Principe, Neil R. Euliano and W. Curt Lefebvre, "Neural and Adaptive Systems: Fundamentals Through Simulations," John Wiley and Sons, INC., 1999.

[121] J. J. Hopfield,"Neural networks and physical systems with emergent collective computational abilities," *Proceedings of National Academy Sciences of United States of America*, vol. 79, no. 8, pp. 2554-2558, 1982.

[122] J. J. Hopfield,"Neurons with graded response have collective computational properties like those of two-state neurons," *Proceedings of National Academy Sciences of the United States of America*, vol. 81, no. 10, pp. 3088-3092, 1984.

[123] J. J. Hopfield and D. W. Tank,"Neural computation of decisions in optimization problems ," *Biological Cybernetics*, vol. 52, pp. 141-152, 1985.

[124] D. W. Tank and J. J. Hopfield,"Simple neural optimization networks: an A/D converter, signal decision circuit, and a linear programming circuit," *IEEE Trans. on Circuits and Systems*, vol. CAS-33, no. 5, pp. 533-541, 1986.

[125] S. Reynold Chu, Rahmat Shoureshi and Manoel Tenorio,"Neural networks for system identification," *IEEE Control System Magnize*, vol. 10, no. 3, pp. 31-35, 1990.

[126] Marc Karam and M. Sami Fadali,"System identification sing a Fourier/Hopfield neural network," *Proceedings of the 44th IEEE 2001 Midwest Symposium on Circuits and Systems (MWSCAS 2001)* , vol. 2, pp. 878-883, 2001.

[127] T. G. Park and K. S. Lee,"SMC-base adaptive input-output linearising control of induction motors," *IEE Proc. Control Theory Appl.*, vol. 145, no. 1, pp. 55-62, 1998.

[128] J. R. Raol,"Neural network based parameter estimation of unstable aerospace dynamic systems ," *IEE Proc. Control Theory Appl.*, vol. 141, no. 6, pp. 385-388, 1994.

[129] Rahmat Shoureshi and S. Reynold Chu,"Hopfield-based adaptive state estimators," *IEEE International Conference on Neural Networks*, vol. 3, pp. 1289-1294, 1993.

[130] Wang Lei, Xiao Yunshi, Zhou Guoxing and Wu Qidi,"Further discussion of Hopfield neural network based DC drive system identification and control," *Proceedings of the 4th World Congress on Intelligent Control and Automation*, pp. 1990-1993, June 10-14, Shanghai, P. R. China, 2002.

[131] Lei Wang, Guo-xing Zhou, Li-hong Xu and Qi-di Wu,"Hopfield neural network based identification and control of induction otor drive system - part I: identification," *Proceedings of the 14th World Congress, International Federation of Automatic Control (IFAC)* , vol. O, pp. 279-283, Beijing, P. R. China, 1999.

[132] Lin, Ching-Fang, "Advanced control systems design," Englewood Cliffs, N.J. : PTR Prentice Hall , c1994.

[133] N. A. Demerdash, F. A. Fouad,"Determination of winding inductances in ferrite type permanent magnet electic machinery by finite elements," *IEEE Trans. on Magnetics*, vol. MAG-18, no. 6, pp. 1052-1054, Nov. 1982.

[134] N. A. Demerdash, T. M. Hijazi and A. A. Arkadan"Computation of winding inductances of permanent magnet brushless DC motors with damper windings by energy perturbation ," *IEEE Trans. on Energy Conversion*, vol. 3, no. 3, pp. 705-713, Sept. 1988.

[135] N. A. Demerdash and T. W. Nehl,"Electric machinery parameters and torques by current and energy perturbation from field computation - part I: theory and formulation ," *IEEE Trans. on Energy Conversion*, vol. 14, no. 4, pp. 1507-1513, Dec. 1999.

[136] Zhu Z. Q., Howe D. and Mitchell J. K., "Magnetic field analysis and inductances of brushless DC machines with surface-mounted and non-overlapping stator windings ," *IEEE Trans. on Magnetics*, vol. 31, no. 3, pp. 2115-2118, July 1996.

[137] Francis Piriou and Adel Razek,"Calculation of saturated inductances for numerical simulation of synchronous machines," *IEEE Trans. on Magnetics*, vol. MAG-19, no. 6, pp. 2628-2631, Nov. 1983.

[138] Liuchen Chang,"An improved FE inductance calculation for electric machines ," *IEEE Trans. on Magnetics*, vol. 32, no. 4, pp. 3237-3245, July 1996.

[139] Jack F. Gieras, Ezio Santini and Mitchell Wing,"Calculation of synchronous reactances of small permanent-magnet alternating-current motors: comparison of analytical approach and finite element method with measurements," *IEEE Trans. on Magnetics*, vol. 34, no. 5, pp. 3712-3720, Sept. 1998.

[140] dSPACE, *Floating-Point Controller Board - DS1102, User's Guide*, v.3.3.1, 1996.

[141] Advanced Technical Information of IGBT Module-MUBW 10-12A7 (IXYS),1999.

[142] Liang Zhihong, *Integrated Electric Drive Platform, User's Guide*, National University of Singapore, Dec. 2000.

[143] Texas Instruments, *TMS320C31 - User's Guide*, 1998.

[144] "YOKOGAWA 700937 High Frequency Current Probe," YOKOGAWA Electric Corporation, 2002.

[145] "ONO SOKKI Torque Detecotr SS Series Standard Type (SS-200)," Ono Sokki Co. Ltd..

[146] Philip L. Alger, "Induction Machines, Their Behavior and Uses," 2nd Edition, New York: Gordon and Breach, 1970.

[147] R. Fletcher, "Conjugate Gradient Methods for Indefinite Systems," *Proceedings of Dundee Conference on Numerical Analysis 1975*, Lecture Notes in Mathematics 506, G. A. Watson, ed., Springer-Verlag, Berlin, pp. 73-89 (1976).

[148] D. A. H. Jacobs, "A generalization of the conjugate-gradient method to solve complex systems," *IMA Journal of Numerial Analysis*, vol. 6, pp. 447-452, 1986.

[149] Charles H. Tong, and Qiang Ye, "Analysis of the finite precision Bi-conjugate gradient algorithm for nonsymmetric linear systems," *Mathematics of Computation*, vol. 69, no. 232, pp. 1559-1575, August 1999.

[150] Enrico Levi, "Polyphase Motors - A Direct Approach to Their Design," John Wiley and Sons, 1984.

[151] S.L.Ho, H.L.Li, W.N.Fu and H.C.Wong, "A novel approach to circuit-field-torque coupled time stepping finite element modeling of electric machines," *IEEE Trans. on Magnetics*, vol. 36, no. 4, pp. 1886-1889, July 2000.

List of Publications

1. Dong Jing, M. A. Jabbar and Liu Zhejie, "Dynamic analysis of interior permanent magnet synchronous machines," in *Proc. of the International Conference on Electrical and Computer Engineering (ICECE 2002)*, Dhaka, Bangladesh, Dec.26 - 28, 2002.

2. M. A. Jabbar, Zhejie Liu and Jing Dong, "Time-stepping finite element analysis for the dynamic performance of a permanent magnet synchronous motor," in *Proc. of the International Magnetics Conference (INTERMAG 2003)*, FP-08, Boston, Massachusetts, March 30 - April 3, 2003.

3. M. A. Jabbar, Jing Dong and Zhejie Liu, "Dynamic analysis of a permanent magnet synchronous motor under different starting schemes," in *Proc. of the 11th International Symposium on Applied Electromagnetics and Mechanics (ISEM 2003)*, Versailles, France, May 12 - 14, 2003.

4. M. A. Jabbar, Zhejie Liu and Jing Dong, "Time-stepping finite-element analysis for the dynamic performance of a permanent magnet synchronous motor," in *IEEE Transactions on Magnetics*, vol. 39, no. 5, pp. 2621-2623, Sept. 2003.

5. M. A. Jabbar, Jing Dong and Zhejie Liu, "Dynamic analysis of a permanent magnet synchronous motor under different starting schemes," in *International Journal of Applied Electromagnetics and Mechanics*, Vol. 19, pp. 79 - 85, 2004.

6. M. A. Jabbar, Jing Dong and Zhejie Liu, "Determination of machine parameters for internal permanent magnet synchronous motors," *Second International Conference on Power Electronics, Machines and Drives (PEMD 2004)*, University of Edinburgh, UK, March 31 - April 2, 2004.

7. M. A. Jabbar, Jing Dong and Zhejie Liu, "Determination of parameters for internal permanent magnet synchronous motors," accepted by *International Electric Machines and Drives Conference (IEMDC 2005)*, San Antonio, TX, May 15-18, 2005.

8. M. A. Jabbar, Jing Dong and Zhejie Liu, "Parameter determination for internal permanent magnet synchronous motors," submitted to *IEE Proceedings - Electric Power Application*, August, 2004.

Appendix A

The Newton-Raphson Method

A.1 Application to Single Nonlinear Equation

Given a nonlinear function

$$f(u) = k(u) \cdot u = p, \tag{A.1}$$

where u is the unknown variable, k is the function of u, and p is a constant. To find the root of this equation, and initial value $u^{(0)}$ is assumed as the estimate of the solution. Expanding equation (A.1) by a Taylor's series about $u^{(0)}$ and ignoring higher order terms, we can get

$$f(u) = p = f(u^{(0)}) + \frac{\partial f(u^{(0)})}{\partial u}(u^{(1)} - u^{(0)}) \tag{A.2}$$

or,

$$\frac{\partial f(u^{(0)})}{\partial u}(u^{(1)} - u^{(0)}) = p - f(u^{(0)}). \tag{A.3}$$

Therefore,

$$u^{(1)} = u^{(0)} + [\frac{\partial f(u^{(0)})}{\partial u}]^{-1}[p - f(u^{(0)})] \tag{A.4}$$

Using the above equation, we can get the first approximate solution to equation (A.1). Repeat the calculation at point $u^{(1)}$, the second iteration can be done as

$$\frac{\partial f(u^{(1)})}{\partial u}(u^{(2)} - u^{(1)}) = p - f(u^{(1)}). \tag{A.5}$$

The similar computation can be done continually. After k times iterations, we get the approximate solution $u^{(k)}$, then the following equation can be used to calculate $u^{(k+1)}$

$$\frac{\partial f(u^{(k)})}{\partial u}(u^{(k+1)} - u^{(k)}) = p - f(u^{(k)}). \tag{A.6}$$

or

$$J^{(k)}(u^{(k+1)} - u^{(k)}) = p - f(u^{(k)}). \tag{A.7}$$

Such a process of iteration can be seen very clearly in Fig. A.1. After several iterations, the right hand side of equation (A.7) will be very close to zero, which means that the $u^{(k+1)}$ value will be very close to the accurate solution also. To control the accuracy of the computation, a small tolerance ε is set beforehand as the threshold. If the following condition is satisfied,

$$[p - f(u^{(k)})]^2 \leqslant \varepsilon \tag{A.8}$$

we consider that the satisfactory solution has obtained, and the iteration can be stopped.

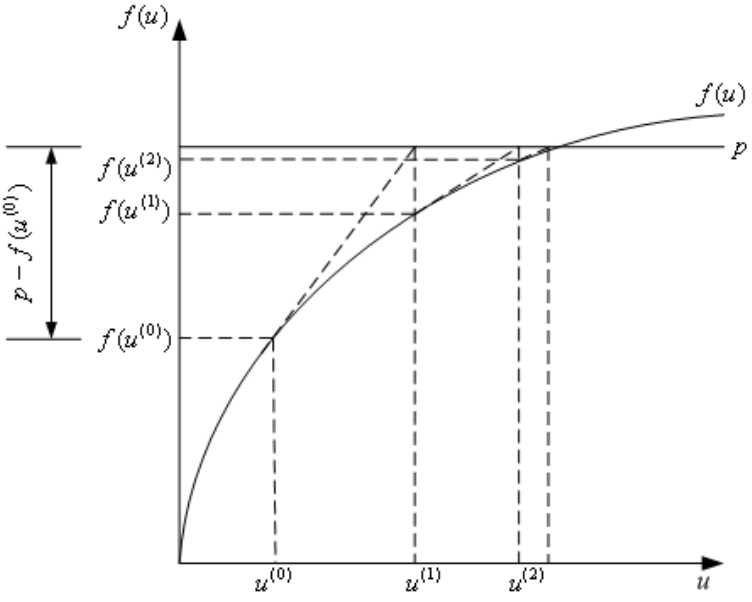

Figure A.1: Illustration of Newton-Raphson Method

A.2 Application to a System of Equations

Based on the implementation of Newton-Raphson method to single nonlinear equation introduced above, we extend the application to a system of equations. Consider a set of equations

$$[f] = [K][X] = [Q], \tag{A.9}$$

where $[K]$ is the coefficient matrix, [X] is the matrix unknown variables and $[Q]$ is the matrix of known values. Then equation (A.9) can be rewritten as a group of functions, which are

$$\begin{cases} f_1 = K_{11}X_1 + K_{12}X_2 + \ldots + K_{1n}X_{1n} = Q_1 \\ f_2 = K_{21}X_1 + K_{22}X_2 + \ldots + K_{2n}X_{1n} = Q_2 \\ \qquad\qquad \cdots \\ f_n = K_{n1}X_1 + K_{n2}X_2 + \ldots + K_{nn}X_{1n} = Q_n \end{cases} \tag{A.10}$$

Setting the initial value of $[X]$ as $[X]^{(0)}$, then we have

$$f_i^{(0)} = \sum_{j=1}^{n} K_{ij}X_j^{(0)}, (i = 1, 2, \ldots, n). \tag{A.11}$$

Expanding every row of $[f]$ by a Taylor's series and ignoring higher order terms, following equations can be obtained

$$\begin{cases} f_1 = f_1^{(0)} + \frac{\partial f_1^{(0)}}{\partial X_1}(X_1^{(1)} - X_1^{(0)}) + \frac{\partial f_1^{(0)}}{\partial X_2}(X_2^{(1)} - X_2^{(0)}) + \ldots + \frac{\partial f_1^{(0)}}{\partial X_n}(X_n^{(1)} - X_n^{(0)}) = Q_1 \\ f_2 = f_2^{(0)} + \frac{\partial f_2^{(0)}}{\partial X_1}(X_1^{(1)} - X_1^{(0)}) + \frac{\partial f_2^{(0)}}{\partial X_2}(X_2^{(1)} - X_2^{(0)}) + \ldots + \frac{\partial f_2^{(0)}}{\partial X_n}(X_n^{(1)} - X_n^{(0)}) = Q_2 \\ \qquad\qquad \cdots\cdots\cdots\cdots\cdots \\ f_n = f_n^{(0)} + \frac{\partial f_n^{(0)}}{\partial X_1}(X_1^{(1)} - X_1^{(0)}) + \frac{\partial f_n^{(0)}}{\partial X_2}(X_2^{(1)} - X_2^{(0)}) + \ldots + \frac{\partial f_n^{(0)}}{\partial X_n}(X_n^{(1)} - X_n^{(0)}) = Q_n \end{cases} \tag{A.12}$$

When rewritten into matrix form it will become

$$\begin{bmatrix} \frac{\partial f_1^{(0)}}{\partial X_1} & \frac{\partial f_1^{(0)}}{\partial X_2} & \cdots & \frac{\partial f_1^{(0)}}{\partial X_n} \\ \frac{\partial f_2^{(0)}}{\partial X_1} & \frac{\partial f_2^{(0)}}{\partial X_2} & \cdots & \frac{\partial f_2^{(0)}}{\partial X_n} \\ \vdots & \vdots & \vdots & \vdots \\ \frac{\partial f_n^{(0)}}{\partial X_1} & \frac{\partial f_n^{(0)}}{\partial X_2} & \cdots & \frac{\partial f_n^{(0)}}{\partial X_n} \end{bmatrix} \begin{bmatrix} X_1^{(1)} - X_1^{(0)} \\ X_2^{(1)} - X_2^{(0)} \\ \vdots \\ X_n^{(1)} - X_n^{(0)} \end{bmatrix} = \begin{bmatrix} Q_1 - f_1^{(0)} \\ Q_2 - f_2^{(0)} \\ \vdots \\ Q_n - f_n^{(0)} \end{bmatrix} \tag{A.13}$$

or

$$[J]^{(0)}([X]^{(1)} - [X]^{(0)}) = [Q] - [f]^{(0)}, \tag{A.14}$$

where

$$[J] = \frac{\partial [f]}{\partial [X]} = \begin{bmatrix} \frac{\partial f_1}{\partial X_1} & \frac{\partial f_1}{\partial X_2} & \cdots & \frac{\partial f_1}{\partial X_n} \\ \frac{\partial f_2}{\partial X_1} & \frac{\partial f_2}{\partial X_2} & \cdots & \frac{\partial f_2}{\partial X_n} \\ \vdots & \vdots & \vdots & \vdots \\ \frac{\partial f_n}{\partial X_1} & \frac{\partial f_n}{\partial X_2} & \cdots & \frac{\partial f_n}{\partial X_n} \end{bmatrix} \tag{A.15}$$

is the Jacobian matrix. Using equation (A.14), we can get the value of $([X]^{(1)} - [X]^{(0)})$, thereby the value of $[X]^{(1)}$

$$[X]^{(1)} = [X]^{(0)} + \{[J]^{(0)}\}^{-1}\{[Q] - [f]^{(0)}\} \tag{A.16}$$

Take the value of $[X]^{(1)}$ as initial value and repeat the above process described in equations (A.12)-(A.16), the value of $[X]^{(2)}$ can be calculated as

$$[X]^{(2)} = [X]^{(1)} + \{[J]^{(1)}\}^{-1}\{[Q] - [f]^{(1)}\} \tag{A.17}$$

Repeat the similar calculation process and after k iterations, the value of $[X]^{(k+1)}$ can be obtained by the following equation

$$[X]^{(k+1)} = [X]^{(k)} + \{[J]^{(k)}\}^{-1}\{[Q] - [f]^{(k)}\} \tag{A.18}$$

After several iterations, the term of $\{[Q] - [f]^{(k)}\}$ on the right hand side of equation (A.18) will approach zero, which means the value of $[X]^{(k+1)}$ will be very close to the real solution. To control the accuracy of the approximate solution, a small tolerance ε is set. At the k_{th} iteration, when the criteria in equation (A.19) is met, we think the result of this iteration is satisfactory for the approximation of solution and the iteration can be stopped.

$$\sum_{i=1}^{n} (Q_i - f_i^{(k)})^2 \leqslant \varepsilon \tag{A.19}$$

Appendix B

The Derivation of $\frac{\partial B}{\partial A}$

Recalling equation (4.19) and (4.20), the x and y component of the flux density in one element are

$$B_x = \frac{1}{2\Delta}(b_1A_1 + b_2A_2 + b_3A_3) \tag{B.1}$$

$$B_y = -\frac{1}{2\Delta}(c_1A_1 + c_2A_2 + c_3A_3) \tag{B.2}$$

and the flux density over the element is

$$B = \sqrt{B_x^2 + B_y^2}. \tag{B.3}$$

Then the partial derivation of B with respect to $A_i, (i = 1, 2, 3)$ is

$$\begin{aligned}
\frac{\partial B}{\partial A_i}|_{i=1,2,3} &= \frac{1}{2}(B_x^2 + B_y^2)^{-\frac{1}{2}}(2B_x\frac{\partial B_x}{\partial A_i} + 2B_y\frac{\partial B_y}{\partial A_i}) \\
&= \frac{1}{B}(B_x\frac{\partial B_x}{\partial A_i} + B_y\frac{\partial B_y}{\partial A_i}) \\
&= \frac{1}{B}(B_x\frac{b_i}{2\Delta} - B_y\frac{c_i}{2\Delta}) \\
&= \frac{1}{B}\left[\frac{1}{2\Delta}(b_1A_1 + b_2A_2 + b_3A_3)\frac{b_i}{2\Delta} + \frac{1}{2\Delta}(c_1A_1 + c_2A_2 + c_3A_3)\frac{c_i}{2\Delta}\right] \\
&= \frac{1}{4\Delta^2}\cdot\frac{1}{B}\left[(b_1b_i + c_1c_i)A_1 + (b_2b_i + c_2c_i)A_2 + (b_3b_i + c_3c_i)A_3\right]
\end{aligned} \tag{B.4}$$

Therefore,

- when $i = 1$,

$$\frac{\partial B}{\partial A_1} = \frac{1}{4\Delta^2}\cdot\frac{1}{B}\left[(b_1^2 + c_1^2)A_1 + (b_2b_1 + c_2c_1)A_2 + (b_3b_1 + c_3c_1)A_3\right] \tag{B.5}$$

- when $i = 2$,

$$\frac{\partial B}{\partial A_2} = \frac{1}{4\Delta^2} \cdot \frac{1}{B} \left[(b_1 b_2 + c_1 c_2) A_1 + (b_2^2 + c_2^2) A_2 + (b_3 b_2 + c_3 c_2) A_3 \right] \tag{B.6}$$

- when $i = 3$,

$$\frac{\partial B}{\partial A_3} = \frac{1}{4\Delta^2} \cdot \frac{1}{B} \left[(b_1 b_3 + c_1 c_3) A_1 + (b_2 b_3 + c_2 c_3) A_2 + (b_3^2 + c_3^2) A_3 \right] \tag{B.7}$$

Recall equation (4.32) where

$$\begin{array}{lll} S_{11} = b_1^2 + c_1^2; & S_{12} = b_1 b_2 + c_1 c_2; & S_{13} = b_1 b_3 + c_1 c_3; \\ S_{21} = b_2 b_1 + c_2 c_1; & S_{22} = b_2^2 + c_2^2; & S_{23} = b_2 b_3 + c_2 c_3; \\ S_{31} = b_3 b_1 + c_3 c_1; & S_{32} = b_3 b_2 + c_3 c_2; & S_{33} = b_3^2 + c_3^2; \end{array}$$

then equations (B.5)-(B.7) become

$$\begin{array}{rcl} \dfrac{\partial B}{\partial A_1} & = & \dfrac{1}{4\Delta^2} \cdot \dfrac{1}{B} \cdot (S_{11} A_1 + S_{12} A_2 + S_{13} A_3) \\ \dfrac{\partial B}{\partial A_2} & = & \dfrac{1}{4\Delta^2} \cdot \dfrac{1}{B} \cdot (S_{21} A_1 + S_{22} A_2 + S_{23} A_3) \\ \dfrac{\partial B}{\partial A_3} & = & \dfrac{1}{4\Delta^2} \cdot \dfrac{1}{B} \cdot (S_{31} A_1 + S_{32} A_2 + S_{33} A_3) \end{array} \tag{B.8}$$

Let

$$\begin{cases} f_1 = \frac{\nu}{4\Delta}(S_{11} A_1 + S_{12} A_2 + S_{13} A_3) \\ f_2 = \frac{\nu}{4\Delta}(S_{21} A_1 + S_{22} A_2 + S_{23} A_3) \\ f_3 = \frac{\nu}{4\Delta}(S_{31} A_1 + S_{32} A_2 + S_{33} A_3) \end{cases} \tag{B.9}$$

or

$$\begin{pmatrix} f_1 \\ f_2 \\ f_3 \end{pmatrix} = \frac{\nu}{4\Delta} \begin{pmatrix} S_{11} & S_{12} & S_{13} \\ S_{21} & S_{22} & S_{23} \\ S_{31} & S_{32} & S_{33} \end{pmatrix} \begin{pmatrix} A_1 \\ A_2 \\ A_3 \end{pmatrix}, \tag{B.10}$$

then equation (B.8) can be rewritten as

$$\begin{array}{rcl} \dfrac{\partial B}{\partial A_1} & = & \dfrac{f_1}{B\nu\Delta} \\ \dfrac{\partial B}{\partial A_2} & = & \dfrac{f_2}{B\nu\Delta} \\ \dfrac{\partial B}{\partial A_3} & = & \dfrac{f_3}{B\nu\Delta} \end{array} \tag{B.11}$$

Appendix C

The Representation of Nonlinear $B-H$ Curve

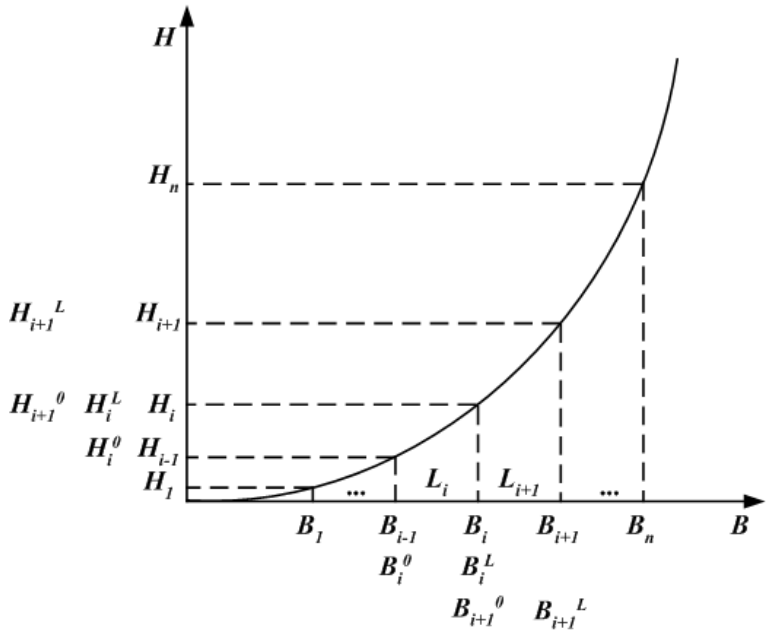

Figure C.1: The Cubic Splines

As shown in Fig. C.1, H is the function of B. Based on the n pairs of input data, the $x-$coordinate is subdivided into n segments, and their length on $x-$coordinate are $L_1, \ldots, L_i, L_{i+1}, \ldots, L_n$ separately. For a segment L_i and $\forall B \in [0, L_i]$, we can write H as a polynomial of B, which is

$$H = c_0 + c_1 B + c_2 B^2 + c_3 B^3, \tag{C.1}$$

where c_0, c_1, c_2 and c_3 are constants to be determined. Taking the first derivation

on the both sides of the above equation, we can get

$$\frac{dH}{dB} = c_1 + 2c_2B + 3c_3B^2. \tag{C.2}$$

Substituting $B = 0$ and $B = L_i$ into equation C.1 and C.2 respectively and solving the resulted 4 equations together, constants $c_0 \sim c_3$ can be obtained as

$$\begin{pmatrix} c_0 \\ c_1 \\ c_2 \\ c_3 \end{pmatrix} = \begin{pmatrix} 1 & 0 & 0 & 0 \\ 1 & L_i & L_i^2 & L_i^3 \\ 0 & 1 & 0 & 0 \\ 0 & 1 & 2L_i & 3L_i^2 \end{pmatrix}^{-1} \begin{pmatrix} H_i^0 \\ H_i^{L_i} \\ dH_i^0/dB \\ dH_i^{L_i}/dB \end{pmatrix}. \tag{C.3}$$

Therefore,

$$\begin{aligned} H &= (1 - \frac{3B^2}{L_i^2} + \frac{2B^3}{L_i^3})H_i^0 + (\frac{3B^2}{L_i^2} - \frac{2B^3}{)}L_i^3)H_i^{L_i} \\ &+ (B - \frac{2B^2}{L_i} + \frac{B^3}{L_i^2})\frac{dH_i^0}{dB} + (-\frac{B^2}{L_i} + \frac{B^3}{L_i^2})\frac{dH_i^{L_i}}{dB} \end{aligned} \tag{C.4}$$

Taking the second derivation on the above equation yields

$$\begin{aligned} \frac{d^2H}{dB^2} &= (-\frac{6}{L_i^2} + \frac{12B}{L_i^3})H_i^0 + (\frac{6}{L_i^2} - \frac{12B}{L_i^3})H_i^{L_i} \\ &+ (-\frac{4}{L_i} + \frac{6B}{L_i^2})\frac{dH_i^0}{dB} + (-\frac{2}{L_i} + \frac{6B}{L_i^2})\frac{dH_i^{L_i}}{dB}. \end{aligned}$$

As

$$\frac{d^2H_i^{L_i}}{dB^2} = \frac{d^2H_{i+1}^0}{dB^2}$$

and

$$\begin{aligned} H_i^0 &= H_{i-1}, H_i^{L_i} = H_i \\ H_{i+1}^0 &= H_i, H_{i+1}^{L_{i+1}} = H_{i+1} \end{aligned}$$

the following equation can be obtained

$$\frac{2}{L_i}\frac{dH_{i-1}}{dB} + \frac{4}{L_i}\frac{dH_i}{dB} + \frac{4}{L_{i+1}}\frac{dH_i}{dB} + \frac{2}{L_{i+1}}\frac{dH_{i+1}}{dB} = \frac{6}{L_i^2}(H_i - H_{i-1}) + \frac{6}{L_{i+1}^2}(H_{i+1} - H_i) \tag{C.5}$$

Consider boundary conditions

$$\frac{d^2H_1^0}{dB^2} = 0, \frac{d^2H_n^{L_n}}{dB^2} = 0,$$

finally we can get equation C.6 from which the derivative coefficients dH/dB can be calculated in terms of the values of H and B.

$$[LHS][dH/dB] = [RHS][H], \tag{C.6}$$

where

$$[LHS] = \begin{bmatrix} \frac{4}{L_1} & \frac{2}{L_1} & 0 & \dots & \dots & \dots & \dots \\ \frac{2}{L_1} & (\frac{4}{L_1} + \frac{4}{L_2}) & \frac{2}{L_2} & \dots & \dots & \dots & \dots \\ \vdots & \vdots & \vdots & \vdots & \vdots & \vdots & \vdots \\ \dots & \dots & \frac{2}{L_i} & (\frac{4}{L_i} + \frac{4}{L_{i+1}}) & \frac{2}{L_{i+1}} & \dots & \dots \\ \vdots & \vdots & \vdots & \vdots & \vdots & \vdots & \vdots \\ \dots & \dots & \dots & \dots & \frac{2}{L_{n-1}} & (\frac{4}{L_{n-1}} + \frac{4}{L_n}) & \frac{2}{L_n} \\ \dots & \dots & \dots & \dots & 0 & \frac{2}{L_n} & \frac{4}{L_n} \end{bmatrix}$$

$$[RHS] = \begin{bmatrix} -\frac{6}{L_1^2} & \frac{6}{L_1^2} & 0 & \dots & \dots & \dots & \dots \\ -\frac{6}{L_1^2} & (\frac{6}{L_1^2} - \frac{6}{L_2^2}) & \frac{6}{L_2^2} & \dots & \dots & \dots & \dots \\ \vdots & \vdots & \vdots & \vdots & \vdots & \vdots & \vdots \\ \dots & \dots & -\frac{6}{L_i^2} & (\frac{6}{L_i^2} - \frac{6}{L_{i+1}^2}) & \frac{6}{L_{i+1}^2} & \dots & \dots \\ \vdots & \vdots & \vdots & \vdots & \vdots & \vdots & \vdots \\ \dots & \dots & \dots & \dots & -\frac{6}{L_{n-1}^2} & (\frac{6}{L_{n-1}^2} - \frac{6}{L_n^2}) & \frac{6}{L_n^2} \\ \dots & \dots & \dots & \dots & 0 & -\frac{6}{L_n^2} & \frac{6}{L_n^2} \end{bmatrix}$$

$$[dH/dB] = \begin{bmatrix} dH_0/dB & dH_1/dB & \dots & dH_{i-1}/dB & \dots & dH_{n-1}/dB & dH_n/dB \end{bmatrix}^{tr}$$

$$[dH/dB] = \begin{bmatrix} H_0 & H_1 & \dots & H_{i-1} & \dots & H_{n-1} & H_n \end{bmatrix}^{tr}$$

After getting the values of $[dH/dB]$, for a specific flux density value of B, the corresponding value of $d\nu/dB$ can be calculated by

$$\frac{d\nu}{dB} = \frac{d\frac{H}{B}}{dB} = \frac{1}{B}\frac{dH}{dB} - \frac{H}{B^2}. \tag{C.7}$$

Appendix D

The Method of BICG

After the assembly process of the finite element method, a large system of equations is generated. The number of unknowns involved in this system equations is often several thousand. The bandwidth of the matrices is so large that the classical Gauss elimination algorithm and its modern variants are not efficient methods. This suggests that the iterative methods should be used. The method used in this work is the biconjugate gradient method (BICG). The method of BICG was firstly described by Fletcher [147] for real nonsymmetric matrices and by Jacobs for complex matrices [148]. The method has evolved many variations, such as CGS, BiCGSTAB and QMR, each of which was specially designed to overcome some of its inherent difficulties. However, BICG may still be competitive in terms of convergence and convergence rates when compared with other methods [149].

Our concern is to get the solution of a system of real or complex linear algebraic equations

$$Ax = b, \tag{D.1}$$

where A is a nonsingular $N \times N$ matrix. $x = (x_1, \ldots, x_N)^{tr}$ is the vector of unknowns, $b = (b_1, \ldots, b_N)^{tr}$ and $()^{tr}$ represents the transpose operation of a matrix.

The BICG algorithm for solving the linear system described in equation (D.1)

is implemented as

1. Input initial approximation x_1;

2. Initialize

$$r_1 = p_1 = \tilde{r}_1 = \tilde{p}_1 = b - Ax_1; \tag{D.2}$$

and

$$\rho_1 = \tilde{r}_1^{tr} r_1 \tag{D.3}$$

3. For $n = 1, 2 \ldots$

$$\sigma_n = \tilde{p}_n^{tr} A p_n \tag{D.4}$$

$$\alpha_n = \frac{\rho_n}{\sigma_n} \tag{D.5}$$

$$r_{n+1} = r_n - \alpha_n A p_n \tag{D.6}$$

$$x_{n+1} = x_n + \alpha_n p_n \tag{D.7}$$

$$\tilde{r}_{n+1} = \tilde{r}_n - \alpha_n A^{tr} \tilde{p}_n \tag{D.8}$$

$$\rho_{n+1} = \tilde{r}_{n+1}^{tr} r_{n+1} \tag{D.9}$$

$$\beta_{n+1} = \frac{\rho_{n+1}}{\rho_n} \tag{D.10}$$

$$p_{n+1} = r_{n+1} + \beta_{n+1} p_n \tag{D.11}$$

$$\tilde{p}_{n+1} = \tilde{r}_{n+1} + \beta_{n+1} \tilde{p}_n \tag{D.12}$$

end For

The sequence generated by the algorithm satisfies the following conditions:

$$\tilde{r}_n^{tr} r_m = 0, \tilde{p}_n^{tr} A p_m = 0, for(m \neq n) \tag{D.13}$$

r_{n+1} is called the computed residual and it is equal to $b - Ax_{n+1}$. The iteration process of BICG method described in equations (D.4)-(D.12) continues until the residual is small enough.

Appendix E

The flowchart of the Field-Circuit Coupled Time Stepping Finite Element Method

In Chapter 3, details of the time stepping finite element computation of the line-start permanent magnet synchronous machine have been presented. The whole process can be summarized by the flowchart shown in Fig. E.1.

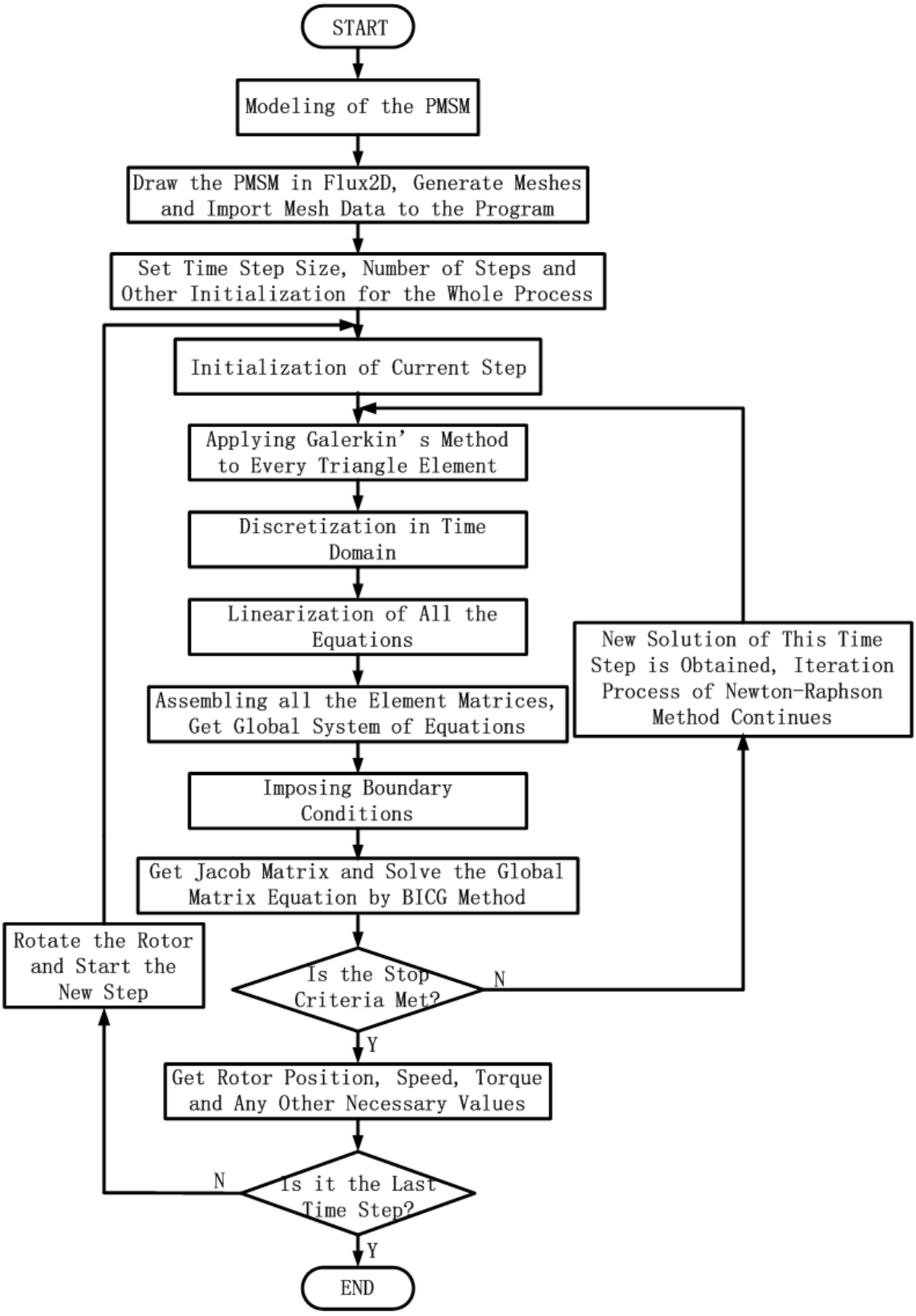

Figure E.1: Flow Chart of the Field-Circuit Coupled Finite Element Computation Process

Appendix F

Motor Specifications and Dimensions

1. **PMSM Specifications**

Table F.1: Ratings of the PMSM Used in This Research Work

Rated power (kW)	2.2
Rated speed (rpm)	1500
Rated voltage (line-to-line V_{rms})	200
Rated current (A_{rms})	8.1
Number of phases	3
Number of poles	4
Number of stator slots	48
Number of rotor cage bars	40
Number of series turns per phase N_s	240
Winding connection	Y
Winding layout	Single layer

2. **Dimensions of the PMSM**

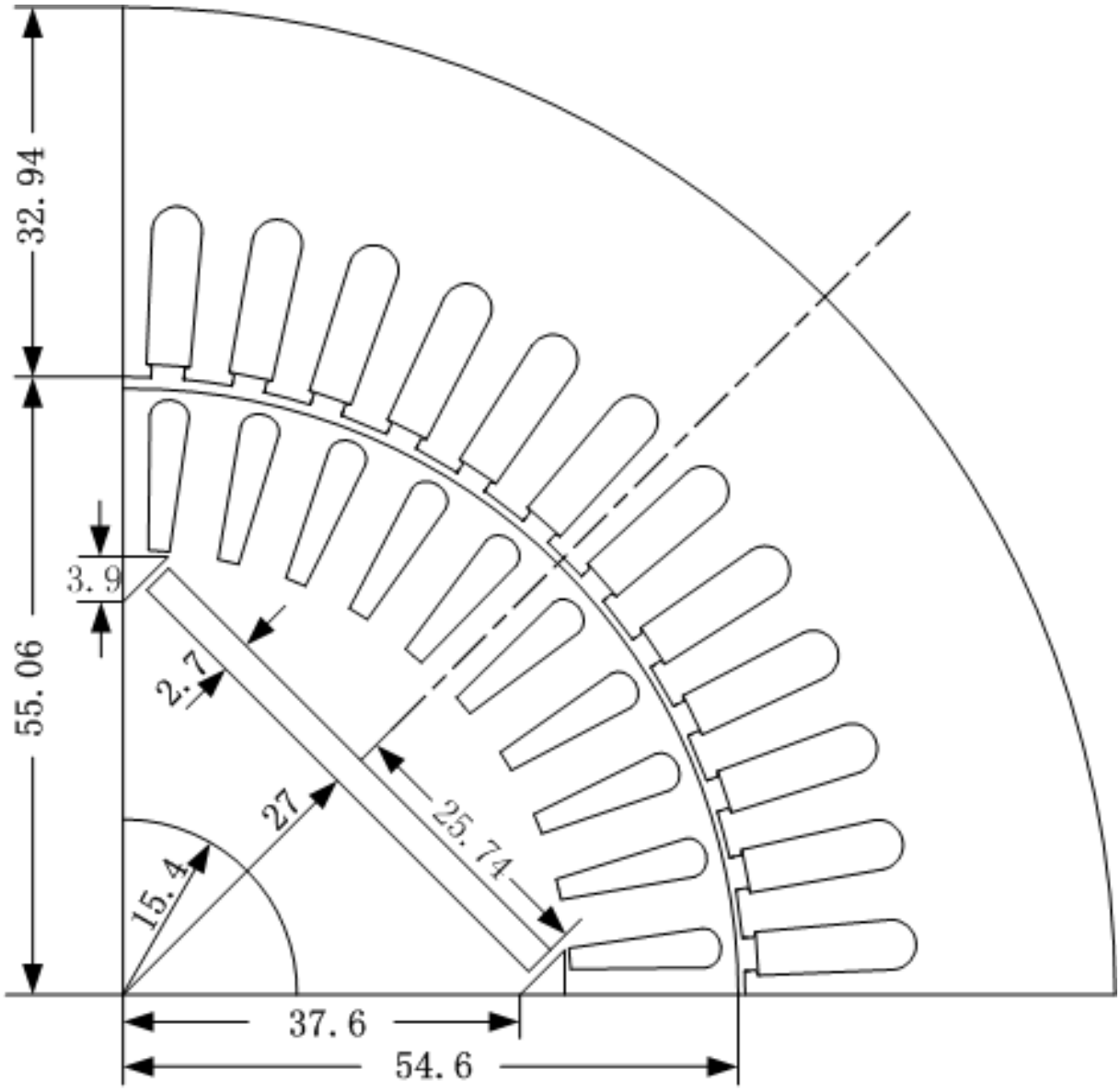

Figure F.1: Dimensions of the PMSM Used in this Research Work (unit: mm)

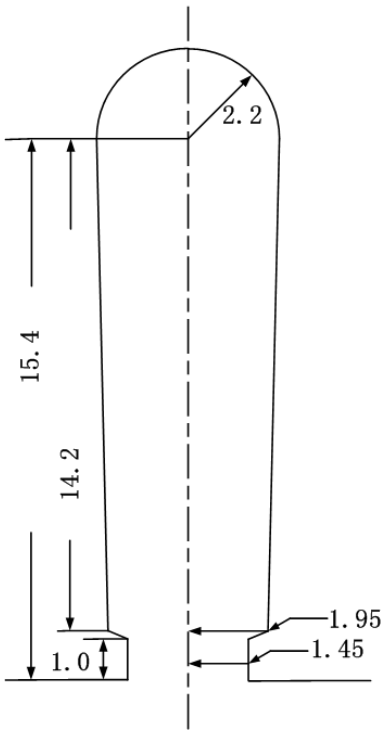

Figure F.2: Stator Slot Dimensions of the PMSM (unit: mm)

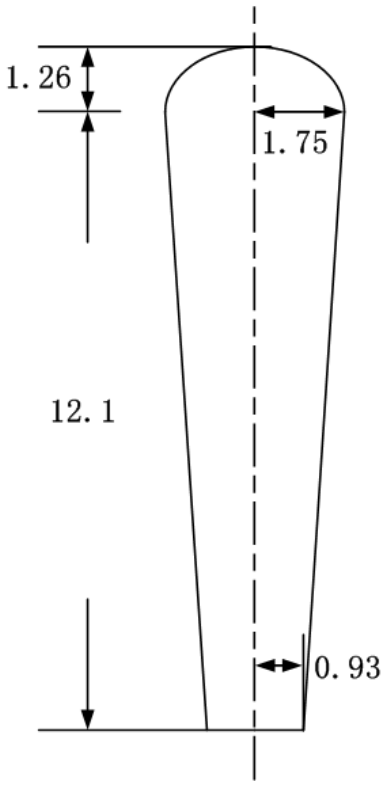

Figure F.3: Rotor Cage Bar Dimensions of the PMSM (unit: mm)

Appendix G

Determination of the $B - H$ Characteristic of the Stator Iron

The finite element solution program requires input material characteristics for all magnetic materials in the part of pre-processing. All linear materials (air gap, spacers, rotor bars and stator windings) are assigned the permeability of free space. The solid rotor shaft is made by aluminium and has the permeability of free space. The $NdFeB$ permanent magnet is modelled with a straight line BH curve in the second quadrant. The remanent flux density B_r is 0.8 Tesla and the relative permeability μ_r is 1.05.

Fig. G.1 shows the totoidal transformer used for testing BH characteristic of motor core. The number of turns for primary winding is $N_1 = 576$, the number of turns for secondary winding is $N_2 = 116$. The experimental data of I_1 and V_2 are shown in Table G.1. The computed BH data are shown in Table G.2.

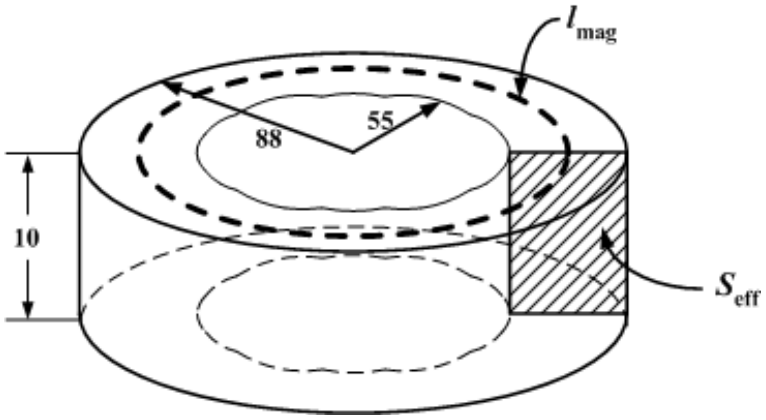

Figure G.1: Wound Motor Core for Testing of BH Characteristics (unit: mm)

Table G.1: Experimental Data for Testing of BH Characteristics

Primary Current (I_1: amps)	Secondary Voltage (V_2: volt)
0.110	1.477
0.130	1.849
0.150	2.443
0.200	3.655
0.240	4.320
0.260	4.770
0.320	5.930
0.400	6.900
0.630	8.630
0.750	9.070
0.950	10.100
1.630	10.910
2.010	11.300
2.440	11.810
2.830	12.080
3.250	12.410
3.650	12.730
4.100	12.980
5.440	13.910
5.010	13.660
6.200	14.330
6.740	14.590
7.610	14.990
8.130	15.250
8.560	15.440
8.920	15.640
9.370	15.790
10.570	16.260
11.020	16.400

Table G.2: Stator Lamination BH Characteristics

Flux Density (B: Tesla)	Field Intensity (H: amps/meter)
0	0
0.176	141.531
0.221	167.263
0.292	192.996
0.435	257.328
0.516	308.794
0.570	334.527
0.708	411.725
0.825	514.657
1.029	810.585
1.083	964.982
1.206	1428.571
1.302	2097.227
1.350	2586.151
1.410	3139.407
1.443	3641.197
1.482	4181.587
1.521	4696.244
1.551	5275.232
1.632	6446.077
1.662	6999.333
1.710	7977.181
1.743	8671.968
1.791	9791.346
1.821	10460.400
1.839	10846.393
1.866	11476.847
1.884	12055.836
1.941	13599.807
1.959	14178.796

Appendix H

Experimental Data Tables for Parameter Determination

Table H.1: Experimental Data of Sensorless No-Load Test Method

Terminal Line-Line Voltage (V: volt)	Phase Current (I: amps)
100.920	2.298
105.59	1.922
111.201	1.545
115.749	1.251
121.670	0.885
127.289	0.622
133.540	0.525
137.241	0.600
140.238	0.718
146.347	1.068
152.652	1.454
157.591	1.749
160.571	1.922
166.106	2.270
171.746	2.628
176.916	2.928
181.495	3.168
187.615	3.472
192.641	3.695
197.250	3.912

Table H.2: Experimental Data of Load Test Method - Voltage and Current

	Phase Voltage (volt)		Phase Current (amps)	
	V	V'	I	I'
1	102.595	102.596	2.675	2.679
2	102.517	102.567	2.730	2.729
3	102.586	102.515	2.889	2.871
4	102.356	102.207	3.100	3.074
5	102.159	102.259	3.365	3.338
6	102.158	102.131	3.671	3.639
7	102.025	101.968	3.985	3.949
8	101.996	102.041	4.322	4.276
9	101.8201	101.8401	4.666	4.618
10	101.566	101.641	5.014	4.961
11	101.519	101.502	5.368	5.285
12	101.292	101.333	5.714	5.640
13	101.139	101.229	6.064	5.968
14	101.084	101.107	6.392	6.297
15	101.017	100.851	6.723	6.594

Table H.3: Experimental Data of Load Test Method - Input Power

	Torque Angle (deg)	Input Power I (Kw)		Input Power II (Kw)	
	δ	P_1	P_2	P_1'	P_2'
1	26.11	0.023	0.348	0.0195	0.345
2	30.34	0.105	0.383	0.101	0.381
3	33.84	0.178	0.432	0.175	0.428
4	35.97	0.249	0.485	0.239	0.479
5	38.67	0.317	0.533	0.305	0.532
6	41.44	0.382	0.588	0.377	0.581
7	43.02	0.450	0.637	0.439	0.633
8	44.74	0.504	0.700	0.495	0.691
9	45.88	0.566	0.753	0.552	0.748
10	46.56	0.619	0.810	0.610	0.800
11	48.82	0.672	0.863	0.658	0.856
12	49.46	0.726	0.922	0.710	0.908
13	54.29	0.773	0.975	0.755	0.963
14	55.21	0.811	1.037	0.794	1.022
15	56.02	0.846	1.093	0.836	1.070

Table H.4: Results of Load Test Method

	Stator Current (ampere)	X_d (ohm)	X_q (ohm)	E_0 (volt)
1	2.677	2.060	21.771	87.090
2	2.729	6.960	21.153	78.701
3	2.880	12.256	20.467	75.083
4	3.087	-11.041	19.484	82.557
5	3.352	7.898	18.959	79.008
6	3.655	11.651	18.605	81.856
7	3.967	3.708	17.937	75.587
8	4.299	1.770	17.414	71.849
9	4.642	2.540	17.025	71.491
10	4.988	26.807	15.689	124.160
11	5.327	12.048	15.783	94.074
12	5.677	1.247	15.240	65.586
13	6.016	6.254	16.170	77.437
14	6.345	3.459	15.778	67.111
15	6.658	13.123	15.210	106.678

Table H.5: Results of Regression Model

	Stator Current (ampere)	L_d (mH)	L_q (mH)	E_0 (volt)
1	2.674	30.128	60.901	76.011
2	2.734	32.926	58.478	75.800
3	2.889	31.657	55.651	77.520
4	3.098	27.530	53.683	79.258
5	3.365	23.770	51.187	79.723
6	3.674	19.925	49.102	79.524
7	3.985	18.049	47.474	78.797
8	4.320	15.590	46.316	77.406
9	4.664	14.636	45.551	76.341
10	5.011	13.031	44.284	74.624
11	5.367	12.440	43.272	73.283
12	5.709	12.084	42.741	71.957
13	6.066	11.450	41.721	70.451
14	6.385	10.811	41.040	68.840
15	6.722	11.020	40.593	67.081

Table H.6: Results of Hopfield Neural Network

	Stator Current (ampere)	X_d (ohm)	X_q (ohm)	E_0 (volt)
1	2.673	12.600	21.154	69.806
2	2.737	10.652	20.440	74.098
3	2.889	9.775	19.698	76.175
4	3.097	8.774	18.980	77.624
5	3.364	8.078	18.324	78.041
6	3.674	7.366	17.734	78.226
7	3.986	7.180	17.214	78.127
8	4.321	6.358	16.732	77.196
9	4.663	5.987	16.262	76.430
10	5.011	5.343	15.874	74.979
11	5.368	5.150	15.505	73.983
12	5.709	4.981	15.170	72.911
13	6.065	4.759	14.864	71.740
14	6.383	4.451	14.598	70.208
15	6.722	4.136	14.357	68.531

Appendix I

The Inverter Circuit

1. **Specifications**

   - **Input**: 3-phase, 380-415 V, 50-60 Hz
   - **Output**: 3-phase, 0-380/415 V
   - **Power**: up to 2.2 kW (3 HP)

2. **Description**

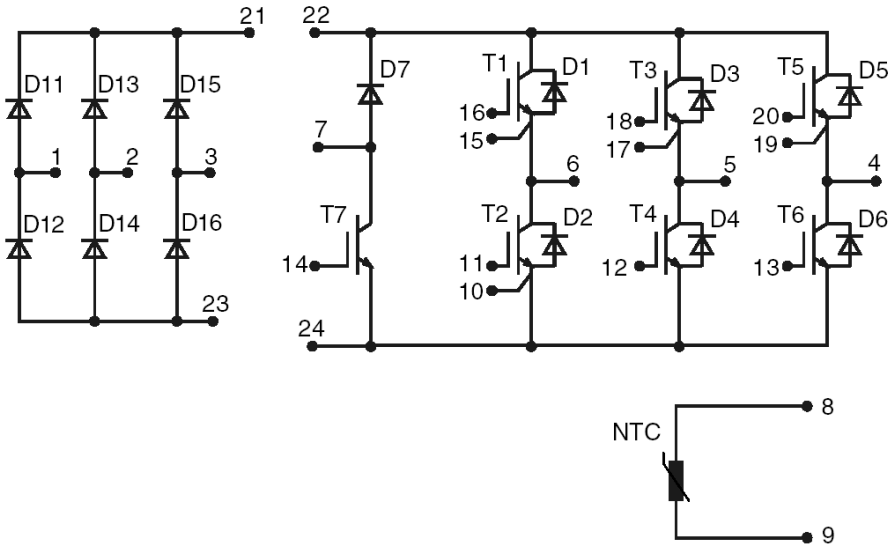

Figure I.1: Schematic diagram of MUBW 10-12A7.

- **IGBT module–MUBW 10-12A7 (IXYS)**

  The IGBT module comprises a 3-phase uncontrolled rectifier, six IGBT switches, one IGBT for braking and a built-in NTC thermistor for temperature sensing.

- **DC-link capacitors & transformer board**

  Fig. I.1 shows the schematic diagram of IXYS module. The DC-link capacitor is connected across pins 22-23. An NTC thermistor is connected in between pins 21-22 to limit the in-rush current. A low ohmic shunt is connected in between pins 23-24 for over-current sensing. Two resistor are connected in series across pins 22-24 as a voltage divider for over-voltage sensing. The transformers are powered from single-phase mains and provide floating power sources to the driver board.

- **Driver board**

  The driver board comprises voltage regulators (78L15), opto-couplers (HCPL4503, H11L1), gate drivers (TC4429), braking control and protection circuits. The connections in between the driver board and the IGBT module or transformer board are made by wires of twisted pairs. The driver board is connected with the Control-PWM Card via a shield flat-ribbon cable.

Appendix J

Parameters of PMSM

1. Equivalent Stator Resistance R_s

   In this thesis work, the input values for R_s are required. R_s is calculated by the following equation [97] (Page 223):

$$R_s = \rho \frac{2 l_{av} N_s}{\pi (\frac{d_w}{2})^2} \tag{J.1}$$

   where

$$\begin{aligned} l_{av} &= l_{ef} + l_e \\ l_e &= 2(d + l'_e) \\ l'_e &= 0.6\tau_y \\ \tau_y &= \frac{\pi(D_{i1} + h_{01} + h_{s1} + h_{12} + r_1)}{2p} \end{aligned}$$

The definition of h_{01}, h_{s1}, h_{12} and r_1 were shown in Fig. J.1, and

ρ	resistivity of stator windings
d_w	diameter of the coil
l_{ef}	axil length of stator
N_s	equivalent number of turns per phase
p	number of pole pairs
d	extension length of windings
D_{i1}	inner diameter of the stator

The calculated R_s value for the PMSM is 1.1430Ω per phase. The measured R_s value is 0.8Ω per phase.

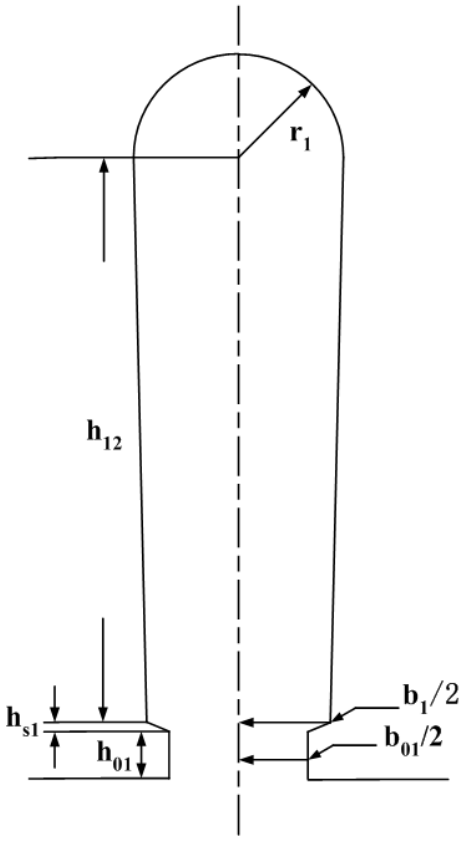

Figure J.1: A Stator Slot

2. Inductance of Stator End-Windings L_e

The reactance of stator end-windings X_{e1} was calculated first and $L_e = X_{e1}/\omega_e$, where ω_e is the angular synchronous speed of the PMSM. X_e was calculated by the following equation [97] (Page 225):

$$X_{e1} = 0.67(\frac{l_e - 0.64\tau_y}{l_{ef}K_{dp}^2})C_x \tag{J.2}$$

where

$$\begin{aligned} C_x &= \frac{4\pi f \mu_0 l_{ef}(K_{dp}N_s)^2}{p} \\ K_{dp} &= K_d \cdot K_p \cdot K_s \end{aligned}$$

and

μ_0	magnetic permeability in free space
f	synchronous frequency
K_d	winding distribution factor
K_p	winding pitch factor
K_s	skew factor

The calculated value of end-winding inductance is

$$L_e = 8.496 \times 10^{-4} H \tag{J.3}$$

3. End-Ring Resistance R_{ek}

The end-ring resistance R_{ek} is calculated by [150] (Page 395):

$$R_{ek} = \frac{\rho_R l_R}{A_R} \frac{1}{(2 \sin \frac{\pi p}{Q_2})^2} \tag{J.4}$$

where

$$l_R = 0.7 \frac{\pi D_R}{Q_2}$$

and

Q_2 number of rotor slots

ρ_R resistivity of the end ring

D_R average diameter of the end ring

A_R cross section area of the end ring

The calculated value of end-ring resistance is

$$R_{ek} = 4.536 \times 10^{-6} \Omega \tag{J.5}$$

4. End-Ring Inductance L_{ek}

The end-ring inductance is calculated by [150] (Page 389):

$$L_{ek} = \mu_0 \frac{Q_2}{m_1 p} \times \frac{2}{3}[(l_B - l_2) + \varsigma \frac{\pi D_R}{2p}] \tag{J.6}$$

where

m_1	number of phases
l_B	axil length of the rotor bar
l_2	axil length of rotor iron core
$\varsigma = 0.18$	for $p > 1$

The calculated value of end-ring inductance is

$$L_{ek} = 8.994 \times 10^{-8} H \tag{J.7}$$

Appendix K

Determination of Moment of Inertia and the Coefficient of Friction

The movement of the rotor is governed by :

$$J_r \frac{d\omega_m(t)}{dt} = T_{em} - T_f - D\omega_m(t), \tag{K.1}$$

where J_r is the moment of inertia of the rotor, ω_m is the mechanical motor speed, T_{em} is the electromagnetic torque, T_f is the load torque, D is friction coefficient and t is time. In order to compute the dynamic performances of the PMSM involving the rotor movement, the parameters of J_r and D have to be determined. In this work, both of these two parameters are determined by simple experiments.

1. Determination of D

   Under no load condition, equation K.1 can be rewritten as

   $$J_r \frac{d\omega_m(t)}{dt} = T_{em} - D\omega_m(t). \tag{K.2}$$

   With the initial condition of $\omega_m(0) = 0$, the solution of equation K.2 is

   $$\omega_m(t) = \frac{T_{em}}{D}(1 - e^{-\frac{D}{J_r}t}). \tag{K.3}$$

   Therefore, when $t = \infty$, $\omega_m(t) = T_{em}/D$. In other words, mathematically, if we apply a torque of T_{em} to the rotor, with infinitely long time, the final speed of the rotor is T_{em}/D. So if we can know T_{em} and $\omega_m(t = \infty)$, D will be attainable.

In order to realize the above process in the experiment, the PMSM is run to rated speed of $1500rpm$. When the machine is running at the steady state, the motor torque T_{em} is recorded. With the values of T_{em} and ω_m, the friction coefficient D can be calculated as

$$D = \frac{T_{em}}{\omega_m}. \tag{K.4}$$

The motor torque T_{em} at the speed of $1500rpm$ in steady state is shown in Fig. K.1.

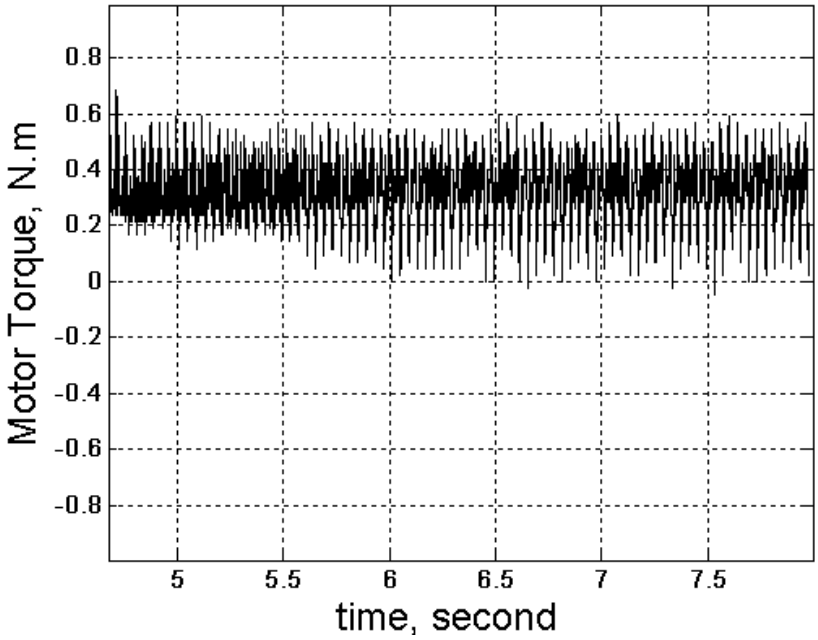

Figure K.1: Motor Torque at the Speed of $1500rpm$ in Steady State

From Fig. K.1, we can get the average motor torque under this condition was $T_{em} = 0.3242$N.m. Therefore, the friction coefficient is

$$D = \frac{0.3242}{157.0796} = 0.00206393N.m/rad \tag{K.5}$$

2. Determination of J_r

Referring to equation K.1, when $T_{em} = 0$ and $T_f = 0$, it can be rewritten as

$$J_r \frac{d\omega_m(t)}{dt} = -D\omega_m(t). \tag{K.6}$$

With the initial condition of $\omega_m(t = 0) = \omega_m^0$, the solution of equation K.6 is

$$\omega_m(t) = \omega_m^0 \cdot e^{-\frac{D}{J_r}t}. \tag{K.7}$$

Therefore, when $t = J_r/D$, $\omega_m(t) = \omega_m^0 \cdot e^{-1} = 0.3679\omega_m^0$. In other words, if we know the initial speed ω_m^0 and time point of t when $\omega_m(t) = 0.3679\omega_m^0$, the value of J_r/D is attainable, hence the value of J_r can be determined.

In the experiment, the PMSM is run to its rated speed of $1500rpm$ under no load condition. So we have $\omega_m^0 = 1500rpm$ and the condition of $T_f = 0$ is satisfied. Then the power supply of the machine is cut off, the condition of $T_{em} = 0$ is met and the rotor speed gradually decrease to zero. The time point of $\omega_m(t) = 0.3679\omega_m^0$ is found and J_r is determined. The rotor speed after deceleration is plotted in Fig. K.2. Since

$$\omega_m(t) = 0.3679\omega_m^0 = 0.3679 \times 1500 = 551.82rpm,$$

the time point corresponding to this speed is $t = 4.4s$. Therefore

$$\frac{J_r}{D} = 4.4 \tag{K.8}$$

Substituting equation K.5 into equation K.8, we can get that the moment inertia of the rotor was

$$J_r = 4.4 \times 0.00206393 = 0.009081292kg \cdot m^2 \tag{K.9}$$

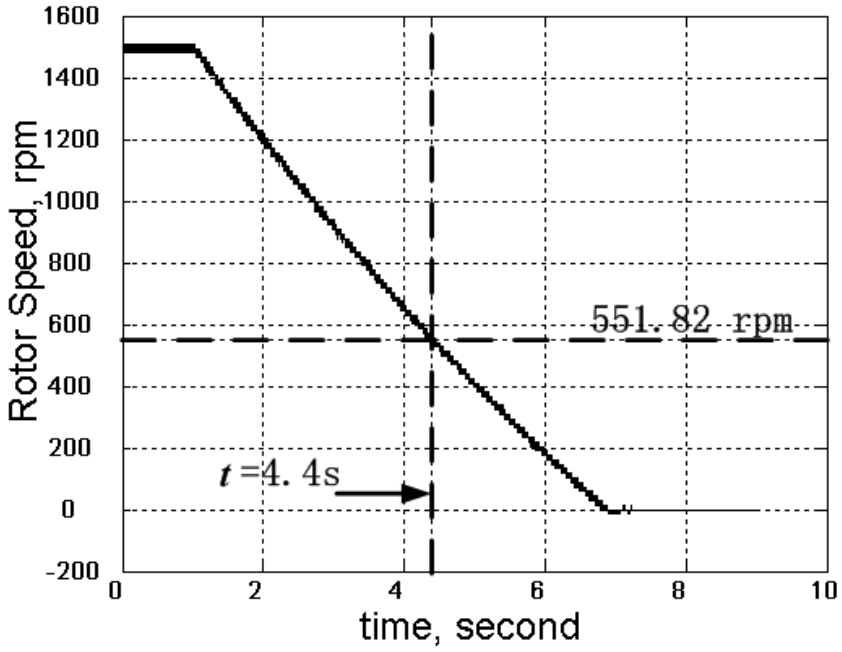

Figure K.2: Rotor Speed after Deceleration

Appendix L

Equations used in the Mid-symmetrical PWM Generation

To improve the performance of PWM, it is always preferred to adopt mid-symmetrical PWM generation to make the pulse symmetrical to the center of the PWM period, as shown in Fig. L.1.

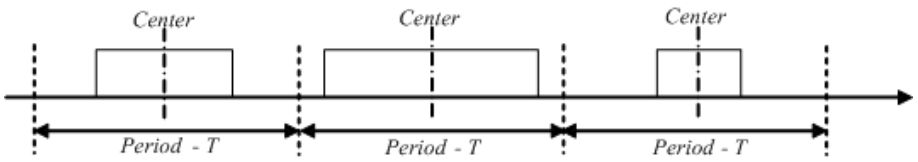

Figure L.1: Pulses Symmetrical to the Center of the PWM Period

Due to the technical limitation, dSPACE DSP card always generates the pulse at the starting edge of the PWM period and hence is unable to do mid-symmetrical PWM generation itself. However, a pulse symmetrical to the center of the period can be generated by an 2-input EX-OR gate with the two pulses shown in Fig. L.2 as the input. These two pulses are generated at the starting edge of the period and hence can be generated by the DSP card.

Suppose the duty ratio of pulses 1 and 2 is D_1 and D_2, respectively, and the duty ratio of the mid-symmetrical pulse is D, as shown in Fig. L.2. It is evident

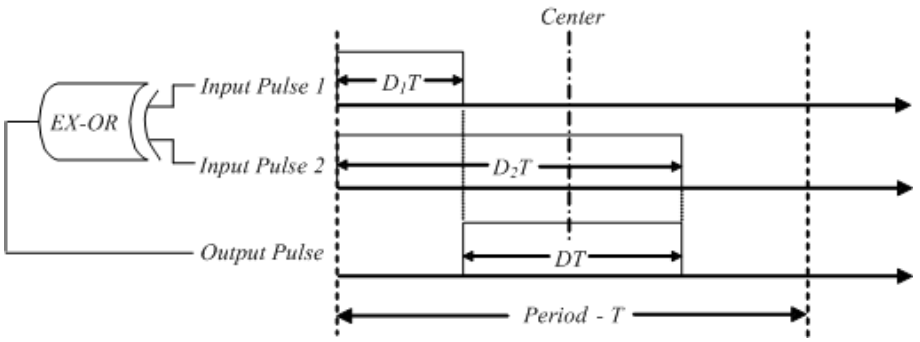

Figure L.2: Generation of a Pulse Symmetrical to the Center of the Period by an 2-Input EX-OR Gate

that D_1 and D_2 can be computed as follows:

$$D_1 = (1 - D)/2 = 0.5 - 0.5D \tag{L.1}$$

$$D_2 = D_1 + D = 0.5 + 0.5D \tag{L.2}$$

To generate a mid-symmetrical pulse with duty ratio D, two PWM channels of the DSP card are employed to generate pulse 1 with duty ratio D_1 and pulse 2 with duty ratio D_2, respectively. An external EX-OR gate is used to EX-OR pulses 1 and 2 to generate the mid-symmetrical pulse.

As far as the gating signal for the Top Switch of the inverter is concerned, if its duty ratio D is of $0 \sim 100\%$, then correspondingly the output phase voltage V is of $-V_{max} \sim V_{max}$, where V_{max} is the maximum output phase voltage of the inverter. Since V is the desired voltage and V_{max} is known, then the question becomes how to use V and V_{max} for the mid-symmetrical PWM generation.

It should be noted that dSPACE provides two C functions for PWM generation. One function is for fixed-frequency PWM generation and the other is for variable-frequency PWM generation. Input to both functions must be a down-

scaled value, but the ranges of the scaling for the two functions are different.

For fixed-frequency PWM generation, the input to the C function should be scaled down within $-1 \sim 1$, which is corresponding to duty ratio of $0 \sim 100\%$. For variable-frequency PWM generation, the input to the C function should be scaled down within $0 \sim 1$, which is corresponding to duty ratio of $0 \sim 100\%$. The Simulink block for PWM channels given by RTI of dSPACE is for variable-frequency PWM generation, hence requires its input to be scaled down within $0 \sim 1$.

To use V and V_{max} for PWM generation, define a variable u in terms of V and V_{max}. For fixed-frequency PWM generation, $u = V/V_{max}$ so that u is within $-1 \sim 1$. For variable-frequency PWM generation, $u = 0.5(1 + V/V_{max})$ so that u is within $0 \sim 1$. If conventional PWM generation would be used, then u could directly be used by the C function/Simulink block as input. The duty ratio D is hence as follows:

- For fixed-frequency PWM generation:$D = 0.5(1 + u)$
- For variable-frequency PWM generation: $D = u$

However, to carry out mid-symmetrical PWM generation, u is not used directly as the input but split into two components, which are then used by the C function / Simulink block as the inputs. Let them be u_1 and u_2 corresponding to duty ratio D_1 and D_2, respectively.

1. For fixed-frequency PWM generation, since the input of $-1 \sim 1$ is corresponding to duty ratio of $0 \sim 100\%$, then it can be known that:

$$D_1 = 0.5(1 + u_1) \tag{L.3}$$

$$D_2 = 0.5(1 + u_2) \tag{L.4}$$

Substituting equations (L.3) and (L.4) into equations (L.1) and (L.2), we can get

$$u_1 = -0.5 - 0.5u \tag{L.5}$$

$$u_2 = 0.5 + 0.5u \tag{L.6}$$

2. For variable-frequency PWM generation, since the input of $0 \sim 1$ is corresponding to duty ratio of $0 \sim 100\%$, then it can be known that:

$$D_1 = u_1 \tag{L.7}$$

$$D_2 = u_2 \tag{L.8}$$

Substituting equations (L.3) and (L.4) into equations (L.1) and (L.2), we can get

$$u_1 = 0.5 - 0.5uu_2 = 0.5 + 0.5u \tag{L.9}$$